Università degli Studi di Palermo (UNIPA)
Dipartimento di Ingegneria (DI)
Université du Quebec
Institut National de la Recherche Scientifique (INRS)
Centre Énergie, Matériaux et Télécommunications (EMT)

DEVELOPMENT OF A NOVEL *IN VITRO* SYSTEM FOR BIOMEDICAL APPLICATIONS

by
Maria Elena Lombardo

Thesis or dissertation submitted to obtain the double Degree of
Philosophy Doctor (Ph.D.)
in Energy and Materials Science (EMT), Varennes, Quebec
and
in Information and Communication Technologies (DI), Palermo, Italy

Jury d'évaluation

Président du jury	Prof. Antonella Motta University of Trento, Italy
Examinateur interne	Prof. Andrea Cipollina University of Palermo, Italy
Examinateur externe	Prof. Antonio D'Amore University of Pittsburgh, PA, US
Directeur de recherche	Prof. Federico Rosei INRS-EMT, QC, Canada
Codirecteur de recherche	Prof. Vincenzo La Carrubba University of Palermo, Italy

A Mirko,

“il mio secondo cuore”.

Sempre e per sempre

&

Ad Andrea,

“un essere speciale”.

Forever in my heart

ACKNOWLEDGMENTS

My Ph.D. was a long trip full of many expected and un-expected moments. It was not an easy journey, and surrounded by obstacles both in the personal and professional life, but thanks to the hard work, the perseverance and the passion, I can say now to be a different and new woman.

First and foremost, I would like to thank my supervisors, Prof. Vincenzo La Carrubba, at the University of Palermo (UNIPA, Italy), and Prof. Federico Rosei, at INRS-EMT center of Varennes (Quebec, CA), for their professional guidance, the inspiration and support they gave me for realizing this Ph.D. project. Particularly, I'm grateful to **Prof. Vincenzo La Carrubba** for showing me the fascinating world of Tissue Engineering and teaching me that being a chemical engineer does not necessarily mean being only an industrial engineer, but we are also and first researchers. I'm very thankful to **Prof. Federico Rosei** who more than anyone believed in me and my potential, and gave me the chance to arrive in Canada and improve my knowledge in different fields, but especially to grow as a person and as scientist.

A special acknowledgement goes to **Dr. Francesco Carfì Pavia** who taught me what it means loving scientific research and putting passion into everything you do. It was inspiring working with him during all the master and Ph.D. studies. Without his help, in and out of the lab, this work would have never been possible, and I am deeply grateful for this. My dear "Fra", thank you also for your enormous patience, your encouragement words and reassurance when I needed it; your friendship and support, also during the long time I spent in Canada, always helped me not to feel alone and go forward when I felt lost.

Throughout my Ph.D., I had the pleasure and honour to collaborate with great people that empowered me to always move forward and never stop being curious and learning. I wish to express my thank to everyone I had the opportunity to work with during the time spent at UNIPA:

- **Prof. Valerio Brucato** for his precious intellectual support and feedback on the engineering issues;

- **Prof. Gennara Cavallaro** and **Dr. Emanuela Fabiola Craparo** of the Laboratory of Biocompatible Polymers, Department of "*Scienze e Tecnologie Biologiche, Chimiche e Farmaceutiche*" (STEBICEF) for supplying the polymeric fluorescence nanoparticles (FNPs) used in this work;
- **Prof. Fabrizio Messina** e **Dr. Alice Sciortino** of the Physic and Chemistry Department-Emilio Segrè for providing the Nitrogen-doped Carbon Dots used in this work;
- **Prof. Maurizio Leone** and **Prof. Valeria Vetri** for giving me the access to their laboratory of Microscopy and Bioimaging at Aten Center of Palermo and the opportunity to carry out the optical characterization of nanoparticles;
- **Prof. Carla Giordano** and **Dr. Giovanni Zito** for supplying the C643 tumor cell line, the equipment and their precious collaboration for the realization of a section of this project, about polymeric scaffold application as 3D supports for studying thyroid tumor biology;

I'm extremely thankful to **Prof. Giulio Ghersi** and his staff at the Department of "*Scienze e Tecnologie Biologiche, Chimiche e Farmaceutiche*" (STEBICEF) of the UNIPA for making possible all the biological experimentation of the project. He gave me the opportunity to work by myself and learn the complex biological world. I would particularly like to thank **Simona** and **Silvia** for their knowledgeable inputs, all the practical help in the bio-lab, the lunches and the kind words in the dark moments.

A big thanks goes to **Sumitra Rajagopalan**, Founder and CEO of Bioastra Technologies Inc (Montreal, Quebec, CA), who allowed me to collaborate with her research group in the framework of MITACS Accelerate project about COVID-19 prevention. Thanks to her I experienced the non-academic research, I learned that if you strongly believe in your ideas you can win against all the obstacles, and especially I learned what means being a business woman.

I wish to thank my colleague and friend **Ilenia** from the Biomaterials and Tissue Engineering Lab of Palermo, that shared with me all the happy and sad moments, helped and encouraged me during the hard Ph.D. years and made experimental work and long hours in the lab more fun.

I want to thank all the people I met during my Canadian period at the **INRS-EMT** center in Varennes, from professors to administration staff. With a simple smile in the corridor or a

nice word every day, all of them allowed me to find another family and feel safe even if in a foreign country and far from my loved ones.

I wish to thank all the members of my research group NanoFemto Lab at INRS-EMT. Especially my positive, friendly and outgoing colleagues **Xin, Faying and Li** who were always there to support and help me. I would like particularly thank my group-leader **Dr. Daniele Benetti** at NanoFemto Lab, who guided me inside the nanotechnology world, completely new for me when I arrived for the first time at Varennes. Thanks to his enthusiasm, positivity and encouragement, together with very interesting discussions and suggestions, I spent a really great time working in that lab.

A deep thanks goes to my friend **Dr. Emek Goksu Durmusoglu** that I had the pleasure to meet when I started my experience at the INRS-EMT center. We shared many moments on the crazy rollercoaster of lab research, but thanks to your constant support, my dear Emek, I was able to strongly believe in myself as scientist.

I want also to mention my lovely friend **Ilknur**. In January 2018, we were sitting at the same table at INRS for the safety test which would allow us to finally start our scientific trip. Thanks for being such a special friend, taking care of me every time I needed it. We were able to fill the emptiness left in our hearts by our loved ones far away, and warmed the cold Montreal winters.

During the past five years I changed a lot, personally and professionally, thanks to all the people that I found on my way and shared with me part of their life. This international Ph.D. gave me the chance to discover different cultures. So, I would like to thank all my African, Arabic, Azerbaijan, Canadian, Chinese, French, German (especially **Dominik**, almost Italian), Indian, Italian (especially **Alessandro**, **Andrea**, **Andrea Aura**, **Cristina**, **Giacomo**, **Gianluca**, **Luca**, **Luigi**, **Stefania**), Lithuanian, Mexican, Tunisian, Turkish friends/colleagues around the World, and everyone I forgot. I love you guys and I will remember each one of you forever as my second big family.

Outside of work, I would like to acknowledge the contribution of all my housemates who have endured my up-and-down moods, particularly **Marta** and **Daniela** in Palermo's house. And I also want to thank my non-biological sister **Eleonora** who stayed by my side for 27 long years as classmate, housemate, confident, crazy friend, that taught me the joy of life.

Special thanks to my precious Montrealer/Neapolitan housemate **Ylenia** who filled my sad days with her joyfulness, my stomach with her delicious food, my mind with her knowledge and my soul with her love. This was only the beginning for us, my new little Sis.

Y gracias a INRS he conocido una persona muy especial. **Uriel**, my colleague, my special friend, my partner in many inspiring discussions about science, my lover! Thanks for strongly believing in my ideas and encouraging me to follow my dreams, always, no matter how difficult it could be. Mi vida, mi cielo, mi mundo, mi todo. Te quiero amorcito corazón.

And finally, I wish to thank my parents, **Anna** and **Giuseppe**, and my sister **Vita** who have always supported me throughout the years and kept me going on. Thank you for your endless love and for being there when I needed you and made me the person I am today. I can't imagine my life without you. I love you!

Lastly, I want to thank **ME** for not being scared 5 years ago for accepting this Ph.D. program and leaving my country, and for never giving up during the years despite the issues, the diseases, the deaths and the worldwide pandemic. ALWAYS BE STRONG!

“Do what you can, with what you have, where you are.”

(Theodore Roosevelt)

ABSTRACT

The use of animals in science and medicine research has significantly benefited human beings. Although their physiology does not identically mimic the human body, they act as perfect “models” for studying human diseases and developing potential new drugs and medical treatments. However, according to the U.S. Food and Drug Administration (FDA), just 8% of drugs tested on animals are considered safe and effective for human use, 92% are not. These extremely high failure rates together with dramatically rising costs in drug development have led many researchers to re-evaluate the value of animal studies. Because of that, over the past three decades scientists worked hard for finding valid alternatives to *in vivo* animal testing that could be more effective, more reliable, and more humane.

The development and use of *in vitro* models, which involve growth of cells outside the body in a closed and controlled environment, quickly became a very popular alternative to animal experiments in pharmaceutical and biomedical research. Among the variety of *in vitro* approaches studied during the years, 3D *in vitro* cell culture was proposed by Regenerative medicine and Tissue engineering as a crucial and essential step for bridging the gap between the *in vitro* and *in vivo* outcomes in pre-clinical testing. Particularly, dynamic cell culture using bioreactors was considered a good intermediate step between the conventional *in vitro* static approach and *in vivo* animal studies. The design of a bioreactor should be inspired by observations of the native environment trying to reproduce the numerous and complex stimuli on cell behaviour in a controlled and scalable way. All these aspects still make the design and operation of bioreactors a big challenge for bioengineers.

In the meantime, Nanotechnology and nanomaterials came into play helping and improving the life sciences with the manipulation of matter over the scale of a nanometer. The subsequent implementation of nanotechnology in biology and medicine fields showed an

enormous positive impact on human health. Nanobiotechnology held enormous potential for healthcare, by using nanoparticles as new probes for bioimaging, potential biosensors and vehicles for delivering drugs more effectively in cellular systems, and *in vitro* diagnosing diseases more rapidly and sensitively.

This study is focused on the design and development of an advanced dual-flow perfusion bioreactor, in which an efficient and tunable radial flow perfusion is applied to enable the diffusion of nano-systems through micro-porous polymeric matrices. At the same time, the proposed work presents a wide investigation concerning the synthesis of "*ad hoc*" polymeric structures for achieving the most performant 3D *in vitro* model for cell culture, together with the production of powerful and versatile nanoparticles useful for multiple applications as probes for bioimaging or vectors for drug-delivery. With the combination of micro- and nano-structures in a controlled environment, the bioreactor is suggested here as a potential *in vitro* apparatus for new drug pre-screening testing and for studying new human therapies with less cost/time consuming and less ethical concerns compared to *in vivo* animal models.

RÉSUMÉ

L'utilisation d'animaux dans la recherche scientifique et médicale a considérablement profité aux êtres humains. Bien que leur physiologie n'imite pas identiquement le corps humain, ils agissent comme de « modèles » parfaits pour étudier les maladies humaines et développer des nouveaux médicaments et traitements médicaux. Cependant, selon la "Food and Drug Administration (FDA)", seulement 8% des médicaments testés sur les animaux sont réputés être sûrs et efficaces pour un usage humain, tandis que 92% ne le sont pas. Ces taux d'échec extrêmement élevés ainsi que les coûts en augmentation pour le développement de médicaments ont conduit des nombreux chercheurs à remettre en question la valeur des études animales. Pour cette raison, au cours des trois dernières décennies, les scientifiques ont travaillé pour trouver des alternatives valables aux tests *in vivo* sur les animaux qui pourraient être plus efficaces, plus fiables et plus humaines.

Le développement et l'utilisation de modèles *in vitro*, qui impliquent la croissance de cellules dans un environnement clos et contrôlé, sont rapidement devenus une alternative très populaire à l'expérimentation animale dans la recherche pharmaceutique et biomédicale. Parmi la variété d'approches *in vitro* étudiées au fil des ans, la culture cellulaire *in vitro* 3D a été proposée par la médecine régénérative et l'ingénierie tissulaire comme une étape cruciale et essentielle pour combler l'écart entre les résultats *in vitro* et *in vivo* dans les tests précliniques. En particulier, la culture cellulaire dynamique à l'aide de bioréacteurs a été considérée comme un bon intermédiaire entre l'approche statique *in vitro* conventionnelle et les études animales *in vivo*. La création d'un bioréacteur devrait se baser sur des observations de l'environnement natif, tout en essayant de reproduire, de manière contrôlée et évolutive, les nombreux et complexes stimuli sur le comportement cellulaire. Tous ces aspects rendent la création et l'utilisation des bioréacteurs un grand défi pour les bioingénieurs.

En attendant, la nanotechnologie et les nanomatériaux entrent en jeu pour aider et améliorer les sciences de la vie au travers de la manipulation de la matière à l'échelle nanométrique. L'application de la nanotechnologie dans les domaines de la biologie et de la médecine a montré un impact positif énorme sur la santé humaine. La nanobiotechnologie a un potentiel extraordinaire pour les soins de santé: des nanoparticules peuvent être utilisées en tant que nouvelles sondes pour la bio-imagerie; en tant que biocapteurs potentiels; enfin, comme véhicules pour délivrer des médicaments plus efficacement et pour diagnostiquer les maladies *in vitro* plus rapidement et avec plus de sensibilité.

Cette étude porte sur la conception et le développement d'un bioréacteur de perfusion à double flux avancé, dans lequel une perfusion à flux radial efficace et contrôlable est appliquée pour permettre la diffusion de nano-systèmes à travers des matrices polymères microporeuses. Au même temps, le travail proposé présente une vaste recherche concernant la synthèse de structures polymères "ad hoc" pour obtenir le modèle 3D in vitro le plus performant, ainsi que la production de nanoparticules puissantes et polyvalentes utiles pour de multiples applications en tant que sondes pour la bio-imagerie ou vecteurs de délivrance de médicaments. Avec la combinaison de micro- et nano-structures dans un environnement contrôlé, le bioréacteur est recommandé ici comme un potentiel appareil *in vitro* pour les tests de présélection de nouveaux médicaments et pour l'étude de nouvelles thérapies humaines avec moins de coûts/temps et moins de préoccupations éthiques par rapport aux modèles animaux *in vivo*.

SOMMARIO

Nella ricerca scientifica e medica, l'uso degli animali ha apportato notevoli benefici all'uomo. Sebbene la loro fisiologia non imiti perfettamente il corpo umano, essi agiscono come perfetti "modelli" per lo studio delle malattie umane e lo sviluppo di nuovi farmaci e trattamenti. Tuttavia, secondo la Food and Drug Administration (FDA), solo l'8% dei farmaci testati sugli animali è considerato sicuro ed efficace per l'uso sull'essere umano, il 92% non lo è. Questi tassi di fallimento estremamente elevati nello sviluppo di farmaci, insieme ai costi in forte aumento, hanno portato molti ricercatori a rivalutare il valore degli studi *in vivo* sugli animali. Questo è stato il motivo per cui, negli ultimi tre decenni, gli scienziati hanno lavorato duramente per trovare valide alternative alla sperimentazione animale *in vivo*, che potessero essere più efficaci, più affidabili e più umane.

Lo sviluppo e l'uso di modelli *in vitro* sono diventati rapidamente un'alternativa molto popolare agli esperimenti sugli animali nella ricerca farmaceutica e biomedica. Essi coinvolgono la crescita di cellule al di fuori del corpo (umano o animale) in un ambiente chiuso e controllato. Tra i diversi tipi di approcci *in vitro* studiati nel corso degli anni, la medicina rigenerativa e l'ingegneria dei tessuti hanno proposto la coltura cellulare 3D come un passaggio cruciale per colmare il divario tra i risultati *in vitro* e *in vivo* nei test preclinici. In particolare, la coltura cellulare in ambiente dinamico, attraverso l'utilizzo di bioreattori, è stata considerata un valido passaggio intermedio tra l'approccio statico convenzionale *in vitro* e gli studi sugli animali *in vivo*. La progettazione di un bioreattore dovrebbe ispirarsi alle osservazioni dell'ambiente nativo, cercando di riprodurre i numerosi e complessi stimoli che agiscono a livello cellulare, in modo controllato e modulabile. Tutti questi aspetti rendono ancora oggi lo sviluppo e l'utilizzo dei bioreattori una grande sfida per i bioingegneri.

Nel mondo della ricerca, nel frattempo, hanno fatto la loro comparsa le nanotecnologie e i nanomateriali, aiutando e migliorando le scienze attraverso la manipolazione della materia su scala nanometrica. L'implementazione della nanotecnologia nei campi della biologia e della medicina ha avuto un impatto positivo sulla salute umana. La nanobiotecnologia possiede un enorme potenziale per le scienze mediche, grazie all'utilizzo di nanoparticelle come nuove sonde per il "bioimaging", come potenziali biosensori e mezzi per la somministrazione di farmaci in modo più efficace a livello cellulare, e infine per diagnosticare le malattie *in vitro* in modo più rapido e sensibile.

Il seguente studio è centrato sulla progettazione e lo sviluppo di un bioreattore a perfusione dotato di doppio flusso, in cui un'efficiente e regolabile perfusione a flusso radiale viene applicata per consentire la diffusione di nano-sistemi attraverso matrici polimeriche microporose. Il lavoro proposto mostra anche un'ampia sperimentazione riguardante la sintesi di strutture polimeriche al fine di realizzare un modello 3D *in vitro* altamente performante per le coltura cellulari. Tutto questo, insieme alla produzione di potenziali nanoparticelle utili per molteplici applicazioni, come sonde per bioimaging o vettori per la somministrazione di farmaci. Con la combinazione di micro- e nano-strutture in un ambiente controllato, il bioreattore è proposto come un potenziale apparato *in vitro* per nuovi test pre-screening di farmaci e per studiare nuove terapie, con più benefici costi/tempo e meno problemi etici rispetto a modelli animali *in vivo*.

TABLE OF CONTENTS

LIST OF FIGURES

LIST OF TABLES

LIST OF ABBREVIATIONS AND SYMBOLS

2D	two-dimensional
3D	three-dimensional
3DD	3D dynamic
AB	Alamar Blue
Al	Aluminium
ATC	Anaplastic Thyroid Carcinoma
AWA	Animal Welfare Act
B	Boron
BE	Binding Energy
BSE	Backscattered Electrons
C	Carbon
CAD	Computer Aided Design
CCK-8	Cell Counting Kit-8
Cd	Cadmium
CDs	Carbon Dots
Co	Cobalt
CS	Chitosan
DAPI	4’,6-diamidino-2-phenylindole
DCM	Dichloromethane
DIPS	Diffusion Induced Phase Separation
DMEM	Dulbecco’s modified Eagle’s medium
Dox	Doxorubicin
EAB	Ethyl Alcohol Bath
ECM	Extra-cellular matrix

EDX	Energy-dispersive X-ray spectrometer
ELS	Electrophoretic Light Scattering
EPC	External Perfusion Circuit,
EPR	Electron Paramagnetic Resonance
ES	Electrospinning
ESB	European Society for Biomaterials
ESCs	Embryonic Stem Cells
ES-NF	Electrospun nanofibers
EU	European Union
FDA	Food and Drug Administration
FE	Filtration efficiency
FNPs	Polymeric Fluorescent Nanoparticles
FTIR	Fourier-transform Infrared Spectroscopy
GF	Gas foaming
H	Height
H/S	Hydrothermal/Solvothermal
HA	Hydroxyapatite
HDPE	High-Density Poly-Ethylene
HNO_3	Nitric Acid
HOMO	Highest-energy Occupied Molecular Orbital
HRTEM	High-resolution TEM
HTS	High throughput screening
ID	Internal Diameter
IF	in-flow
IPC	Inner Perfusion Circuit
iPSCs	induced Pluripotent Stem Cells
L-L	Liquid-Liquid
LUMO	Lowest-energy Unoccupied Molecular Orbital
MB	Methylene Blue
Mg	Magnesium
MM	Melt Molding
MRI	Magnetic resonance Imaging
N,B-CDs	Nitrogen-Boron co-doped CDs

N,Co-CDs	Nitrogen-Cobalt co-doped CDs
N-CDs	N-containing CDs
NHPs	Non-Human Primates
NIR	Near-Infrared
NPs	Nanoparticles
O	Oxygen
OD	Outside Diameter
OF	out-flow
PAN	polyacrylonitrile
PBS	Phosphate buffered saline
PCL	poly (caprolactone)
pD	phenylenediamine
PDLA	poly-D-lactic acid
PEG	poly (ethylene-glycol)
PESU	Polyethersulfone
PET	polyacrylonitrile
PGA	poly (glycolic acid)
PHEA	α,β-Poly(N-2-hydroxyethyl)-D,L-aspartamide
PL	Photoluminescence
PLA	poly (lactic acid)
PLE	Photoluminescence Excitation Spectroscopy
PLGA	poly (lactic-co-glycolic acid)
PLLA	poly-L-lactic acid
PP	Polypropylene
PPE	Personal Protective Equipment
PS	Phase separation
PTFE	Polytetrafluoroethylene
PVA	poly (vinyl alcohol)
QDs	Quantum Dots
qRT-PCR	quantitative real-time PCR
QY	Quantum Yield
R&D	Research and Development
RhB	Rhodamine B

ROS	Reactive Oxygen Species
RP	Rapid Prototyping
RPM	Revolutions per minutes
SC/PL	Solvent casting/particulate leaching
SD	Standard deviation
SEM	Scanning Electron Microscopy
SEs	Secondary electrons
S–L	Solid–Liquid
t	time
T	Temperature
TE	Tissue Engineering
TEM	Transmission Electron Microscopy
TIPS	Thermally Induced Phase Separation
TME	Tumor Microenvironment
TWB	Thermostatic Water Bath
U.S.	United States
UV	Ultraviolet
UV-vis	Ultraviolet–visible
WHO	World Health Organization
XPS	X-ray Photoelectron Spectroscopy
Z	Zinc
ZP	Zeta potential
λem	emission wavelength
λex	excitation wavelengths

CHAPTER 1

INTRODUCTION

1.1. Moving from *in vivo* to *in vitro*

The world of drug discovery is exciting and challenging at the same time. The trip from a new compound discovery to its commercialization is complex, long and expensive and usually takes 10-12 years and over $775 million for the Research and Development (R&D) [1]. Unfortunately, the efficiency of the drug discovery and development process has decreased significantly since the mid-20th century and the number of new drugs approved per billion US dollars used for R&D has halved almost every 9 years. Usually, around 250 new compounds selected from a million compounds start pre-clinical testing, 10 of them proceed to clinical trials, and only one will be approved by the Food and Drug Administration (FDA). These inefficiencies in the targeted drug discovery and development process are motivating the pharmaceutical industry to employ new and more cost-effective systems which can supply accurate and predictive information on the effects of chemicals on the human body [2].

High throughput screening assays (HTS Assays) have changed scientific research and biological testing, allowing for greater efficiency and lower costs. The concept of HTS first appeared in the mid-1980s and has evolved over the past 25 years to serve the changing needs of pharmaceutical research. It is important to understand that HTS almost never identifies a new drug but rather a chemical starting point or cluster of chemicals around which a chemistry process can be initiated [3]. The HTS is a methodology for scientific experimentation based on an automatic process that allows the collection of a large amount of experimental data in less time. It can test hundreds of thousands of compounds per day from large chemical, genetic, or

biological libraries [4]. HTS utilizes nowadays 96-, 384-, or 1536-well microplates to contain the cell cultures subject to treatment, robotics, liquid handling devices, sensitive detectors, and automatic data-processing machines to identify a small number of effectors of a particular biological mechanism (active compounds, antibodies, or genes) from collections that can contain up to two million drug candidates or leads [5]. However, the multi-well system suffers from a substantial issue that may affect the significance of a test: the environment divergence problem. The environment discrepancy problem lies in the fact that the wells in which the tissue grows is only able to approximate the real physiologic culture environment [6]. Moreover, if fewer compounds could be tested without compromising the probability of success, the cost is still high and the data quality would be greatly improved [7].

Another relevant problem related with the actual drug testing is an ethical problem related to the enormous number of animals that have to be killed every year. Animal experimentation is an essential component of biomedical and behavioral research. Each year around the World a big portion of laboratory animals are involved both in research and testing. Research and testing are not always separable, but generally for evaluating the safety and efficacy of new consumer products, such as drugs, chemicals, and cosmetics, testing involves the use of animals, especially rats and mice [8]. The use of animals in pharmaceutical and biomedical industrial research dates back to approximately the 6^{th}-5^{th} century BC with more prominent references in the texts of Aristotle, Diocles, Praxagoras in the 4^{th} century BC and Erasistratus and Herophilus in the 4^{th}-3^{rd} century BC [9]. Animal Testing is still playing a large role in research and drug development in each part of the World. Under Directive 2010/63/EU1, The European Union (EU) member states have an obligation to collect statistical data on the use of animals in scientific research and publish a report every five years to increase transparency and understanding of the current number of animals used in scientific research and testing across Europe. In the last report released on the 14 July 2021 the total number of animals used in scientific research across the 28 EU member states (including UK and Norway) in 2018 was around 10.5 million per year [10]. As shown in Figure 1.1, among the 10 million animals, 54.1% are mice, 26.2% fishes and 9.5% rats. According to this report, it is worrying that there has been a 4% increase in the use of non-human primates (NHPs) compared to 2017. France has the highest number of animals used, recorded at 1.75 million, followed by UK and Germany, both

at around 1.6 million uses of animals, while the rest of the member states falling significantly below this number. In 2013, the EU implemented a prohibition on all animal testing for cosmetic products and cosmetic ingredients under the Cosmetics Regulation 1223/2009. Nevertheless, in Europe there are areas of scientific research where animal testing still seems "unnecessarily high", such as biomedical testing (especially for human cancer research) and toxicity testing for drugs and various other substances.

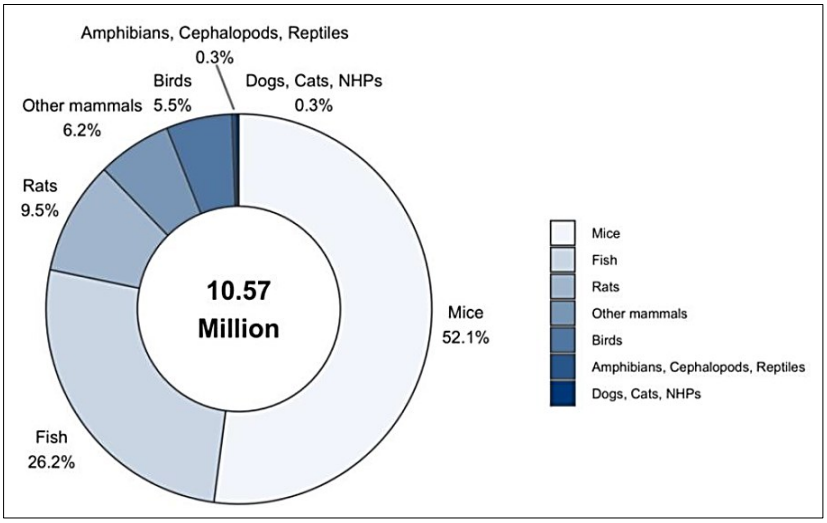

Figure1.1: Numbers of animals classified by main classes of species used in research in EU in 2018. Source: [10].

Since 1996, in the United States (U.S.) the Animal Welfare Act (AWA) is the only Federal Law that regulates the treatment of animals in research, exhibition, transport, and by dealers. The AWA is not intended to regulate how animals are used for research purposes, but only to set standards for how they are obtained and treated at a facility. Among the animals covered by this Act there are: live dogs, cats, monkeys (NHPs- mammals), guinea pigs, hamsters, and rabbits. According to the U.S. annual report of Apr. 2021, 797.546 animals were used in labs for research experiments, testing, and education in the United States and Puerto Rico in 2019, with an increase of 2.2% from 2018 [11]. Unfortunately, only animals covered by the AWA are included in this report. Therefore, this is only an approximation because under current law, labs

in the U.S. are not required to disclose data about the animals most often used in experimentation (rats, mice, birds, and fish) that comprise almost 90 percent of all animals used. Consequently, the real number of animals employed in the US for experimentation every year is more than 100 million, however, there are no published statistics to confirm this. Unlike the U.S., Canada provides regulatory and legal protection for the animals included in science, and the Annual Report of Canadian Council on Animal Care for 2020 declared around 5 million animals used in experimentation in the country [12]. A worse scenery is noticeable in China, where laws regarding laboratory animal welfare are very low and the transparency in the Chinese laboratory animal industry is non-existent. Moreover, there are no concrete enforcement or punitive mechanisms for laboratories that break the rules. Statistically each year, Chinese laboratories use around 12-13 million animals in scientific research, and China exports approximately 40.000 laboratory primates annually to Western institutions [13].

Despite the extreme use of animal models for the purposes of research, teaching, and testing, numerous studies confirmed that most of the time animal testing does not achieve its intended results. Over the last couple of decades, the chances of success for a compound to progress from Phase I via Phases II and III clinical trials till FDA approval it's still slightly under 10% [14]. Moreover, laboratory animal models can only be useful but show many limitations for predicting effects in human progress or on understanding the human diseases which need to be treated. Consequently, many researchers accepted the challenge to focus on new methodologies as valid alternatives to animal testing and avoiding the unethical procedures [15]. Over the past three decades, thanks to the innovations in science and the tremendous progress in preclinical development across the pharmaceutical industry, researchers can now use techniques that allow them to obtain a sufficient level of information with a smaller number of animals [16]. *In vitro* models and cell cultures, computer models, and new imaging/analyzing techniques are only a few examples of good ways to screen the compounds at early stages in drug development that could help to eliminate unsuitable compounds in preliminary stages and minimize the use of animals in further testing [17]. Particularly, conventional *in vitro* technologies offer new opportunities to improve modeling of the human condition and they can act both as a valuable helper to and a potential replacement for modeling in animals. Beside the decrease of animals testing, the advantages of *in vitro* systems are undoubted and include:

- controlled testing conditions;
- reduction of variability between experiments;
- request of a small amount of tested material;
- a limited amount of toxic waste products;
- same dose range can be tested in a variety of test systems.

There are also limitations in using *in vitro* cultures, such as the difficulty to estimate systemic effects and side effects; limitations in cell metabolism; pharmacokinetic effects that cannot be evaluated [18]. Nevertheless, at present experimental investigations of both drug development and toxicology start with *in vitro* studies (Figure 1.2). Since animal studies still represent the only factor in human studies necessary for providing the final proof for the effectiveness of a new drug in humans, they represent the big second step after *in vitro* tests. In many countries, *in vitro* cell cultures have completely replaced the use of animals, for example, for the skin irritancy test and Draize eye irritancy test [19]. The hope for the future is the availability to obtain more accurate and informative *in vitro* assays that will represent an important challenge for the applications in research, toxicity testing and safety screening [20].

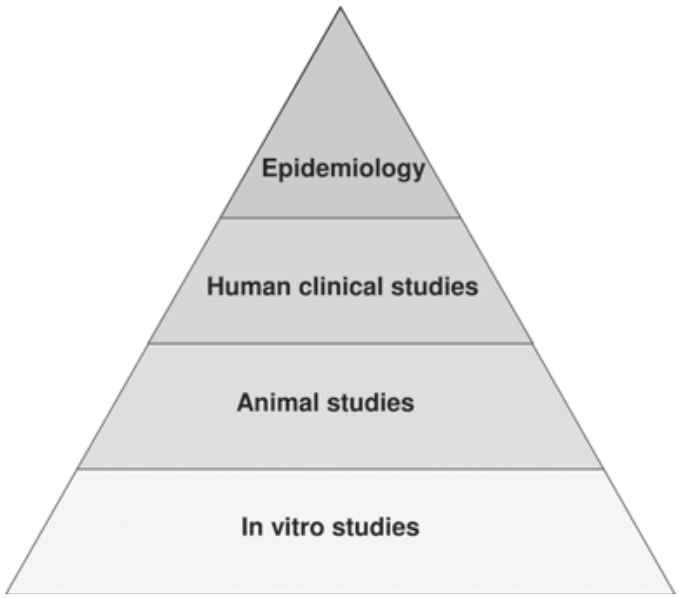

Figure 1.2: The role of in vitro studies in pharmacology and toxicology. [18]

1.2. *In vitro* cell culture systems

Cell culture is an important and necessary process in drug discovery, cancer research, as well as stem cell study. It is the process by which a scientist grows and maintains cells under carefully controlled conditions outside of a living organism [21]. In the 21st century, *in vitro* cell/tissue culture has become an indispensable step in the preclinical drug discovery process, mainly for *in vitro* toxicity studies. Compared to the expensive *in vivo* animal models, cell-based assays using cultured cells are simple, fast and less cost-intensive and the most important thing is that they require fewer animals as well as they are versatile and easily reproducible [22]. Moreover, presently cell culture is widely used also into basic research such as biomedical research, tissue engineering, regenerative medicine, and industrial practices to help discover fundamental biophysical and biomolecular mechanisms by which cells assemble into tissues and organs, how these tissues work, and how their specific functions become disrupted in disease [23]. The global market for cell-based assays in drug discovery was evaluated at USD 13.9 billion in 2019, and is projected to increase at an annual growth rate of 6.3% to reach nearly USD 18.9 billion in 2024. While North America dominated the market in 2019, Asia Pacific is expected to register the highest annual growth rate in the market during the forecast period (Figure 1.3). This is largely driven by the increasing R&D investment by the government and increasing infrastructural development in that region [24].

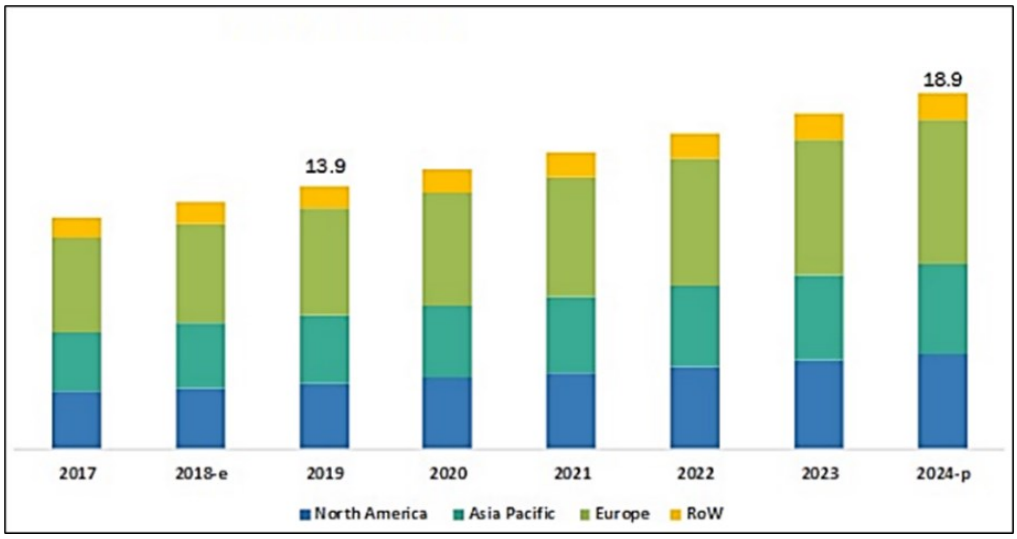

Figure 1.3: Global forecast of cell-based assays market in drug discovery to 2024 by region (USD billion): North America, Europe, Asia Pacific, and the Rest of the World (RoW). [24]

A first conception of cell culture can be traced back to Roux in the late 19th century, who showed that it could be possible to maintain alive outside the animal body embryonic chick cells using a saline solution [25]. Currently, cells removed from an animal/human organ or tissue can be kept outside the body in a laboratory environment, in suitable growth medium, for a few days to several months or even for a few years. Usually, *in vitro* culture of animal/human cells start from their isolation from each other and subsequently they are grown as a monolayer over the surface of culture plates/flasks [17]. The main components of a cell-based assay include cells, device for culturing the cells, and detection system for quantification of cells or cellular activities. Various types and sources of cells have been used in cell-based assays for drug screening during the years. They should be sensible to the assays, faithfully represent the system and express the necessary factors and signaling intermediates. Cell lines widely used for drug screening assays are the "Immortalized cell lines" that continue to grow and divide *in vitro* indefinitely times under optimal culture conditions [26]. The advantages of using these cells include cheapness, easy growing, reliable and reproducible tests. However, they are usually derived from a well-known tissue type, sometimes also a tumor tissue, and artificially manipulated, so they suffer significant mutations and their biological characteristics might be

altered after several passages, becoming more different from those of the native or normal cells [21]. Another kind of cells very common are the "Primary cells" which derived directly from healthy tissue and maintained under *in vitro* culture. They retain the morphological and functional characteristics of their tissue of origin so scientists can easily obtain more representative responses for specific cellular behaviours investigated. The major disadvantage of using primary cell lines is that these cells have a limited lifetime and will always be more heterogeneous than a culture of immortalized cells [27]. Human cancer cell lines represent the cancer of origin and are widely used for anticancer drug screening in pharmaceutical research. Nevertheless, they can contain mutations that might affect the experimental results and the response to treatment [28]. Recent advances in stem cell research have revolutionized the drug discovery process. Embryonic Stem Cells (ESCs) can provide an unlimited source of normal human cells that can be expanded for drug screening and toxicological studies. However, ESCs present some moral issues since the embryos are destroyed during the process for obtaining the cells. More recently, the development of induced Pluripotent Stem Cells (iPSCs) has revolutionized the stem cell field. These cells are pluripotent cells artificially derived from somatic cells (e.g., fibroblasts and other adult cell types) and genetically reprogrammed to an embryonic stem cell–like state. iPSCs can be derived from patients with specific diseases and could be used as a new tool in drug discovery [29].

1.3. 2D vs 3D *in vitro* cell culture models

Since the beginning of the cell culture *era*, a two-dimensional (2D) monolayer cell culture model was mostly used, which involved cultures under an adherent condition [30]. An artificial plastic or glass substrate (flask or flat petri dish) is used for carrying out this culture, where cells are adherent and in contact with other cells only from at their periphery (Figure 1.4i A) [20]. For over a century, 2D cell cultures have been used as *in vitro* models to study cellular responses to stimulations from biophysical and biochemical signals and due to its simplicity and low-cost it is still the most commonly model used in drug discovery for the research of cell-based assays in order to obtain preliminary results [23]. However, adherent cultures also have

various drawbacks and limitations. The first disadvantage is the failure to accurately mimic the *in vivo* architectures and microenvironments. As a consequence, 2D-cultured cells possess many differences compared with *in vivo* cells such as shape and morphology, proliferation and differentiation potentials, cell-cell and cell-surrounding matrix interactions, signal transduction [31]. Another drawback of 2D cell culture is that the cells in the monolayer have unlimited access to the ingredients of the medium such as oxygen, nutrients, metabolites and signal molecules, but also an increasing amount of waste products. On the contrary, in the *in vivo* state, the cells are maintained in an environment characterized by a constant fresh supply of nutrients thanks to the removal of waste products via a complex dynamic transport. Furthermore, in case of *in vivo* cancer cells the availability of nutrients and oxygen is more variable due to the natural multicellular architecture of the tumour mass [32]. The unnatural microenvironment and the incapacity of cells to form a multi-dimensional structure, alter the responses to a variety of chemical and physical stimuli which particularly affect drug metabolism and so cell drug sensitivity, finally causing the failure in drug validation and approval processes. This indicates that 2D cell culture models are unreliable predictors of *in vivo* drug efficacy and toxicity and so could be an inaccurate model for drug development [33]. Such concerns inspired the development of novel models to solve the inconsistency between the 2D cell culture systems and clinical trials. The three-dimensional (3D) *in vitro* cell culture systems proved to be the perfect candidates by providing novel cell-based assays with more relevance for clinical studies [30]. 3D cell culture refers to the culture of living cells inside an artificial environment in which they are permitted to grow or interact with its surroundings in all three dimensions (Figure 1.4i B). Thus, the 3D model more accurately imitates the *in vivo* cell environment compared to the classic flat, unnaturally thin, monolayer cell cultures. Growth of cells in their 3D physical shape allows improvements of the basic biological mechanism, like: proliferation and differentiation, cell-cell interaction, response to stimuli, drug metabolism, gene expression and protein synthesis, and all the general cell functions and *in vivo* relevance [34]. Furthermore, cells grown in a 3D culture have greater stability and longer life cycles than cells cultured in 2D. Also, it allows to generate 3D tissue-like aggregates which can be cultured for longer, at least up to 4 weeks, as compared to almost one week with 2D monolayer culture due to cell confluency. Therefore, they might be more appropriate for long-term studies and surviving cells and for

demonstrating long-term effects of a drug [35]. Thanks to the production of highly fidelity models and the several advantages compared to the traditional 2D cell cultures, 3D cell culture is a method more popular today than ever with many and various applications, including cancer research, stem cell research, drug discovery, and research about new human diseases and their treatments [36]. In the 90s, the number of publications about 3D models reached just 10 per year, during the last 10 years, there was an exponential increase that has brought to almost 1000 publications in 2016 alone (Figure 1.4ii) [37].

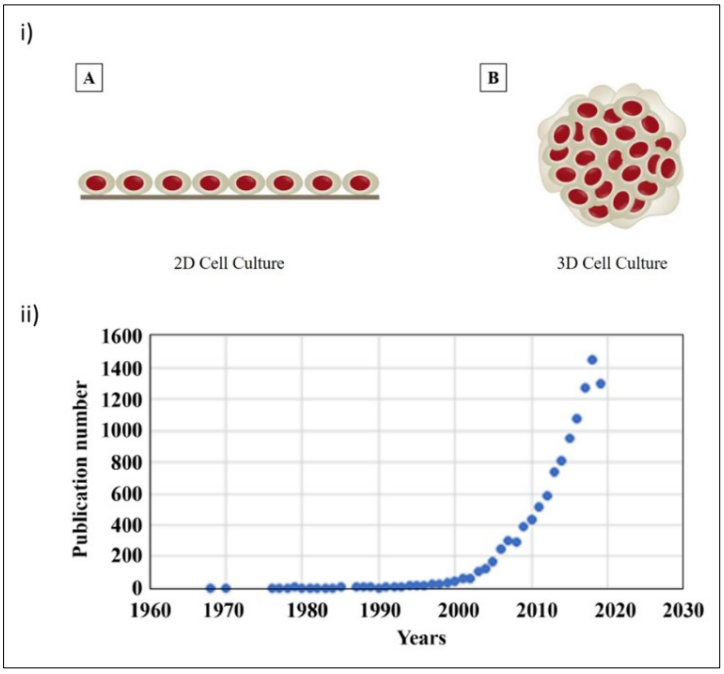

Figure 1.4: i) Graphic representation of (A) 2D monolayer of cell culture and (B) 3D cell culture environment. ii) Number of publications per year (1968–2020) about 3D in vitro cell cultures. [36]

Recent advances in cell biology, microfabrication techniques, and tissue engineering have enabled the development of a wide range of 3D cell culture technologies, such as: multicellular aggregates formation, hydrogel-based cultures and scaffolds, 3D bioprinting, and more recently organs-on-chips [38]. 3D multi-cellular aggregates, commonly known as spheroids, are aggregates of cells grown in suspension or embedded in a 3D matrix [39]. They represent one of the first approaches to 3D cell culture, initially developed by Sutherland and coworkers in

1970 to recapitulate the functional phenotype of human tumor cells and their responses to radiotherapy [40, 41]. Since then, this culture method has been applied to a wide range of cell types, including hepatocytes [42], endothelial cells [43] and stem cells [44]. The generation of spheroids is based on the common basic biological principle of self-assembly that allows cells to form complex tissue with 3D architecture and intensive cell–cell contacts [45]. Some important examples are hanging-drop cultures [46, 47], microfluidics devices [48], or cultures on low-adhesive substrates [49]. Most of the current multicellular spheroid models are applied for pre-clinical uses in anti-cancer research due to the possibility to faithfully reproduce *in vitro* the physiological conditions of tumors in human body, that appears as spheroid with diameter more than 400-500 μm and a typical "hollowed-heart" structure consisting of an exterior layer of reproducing cells and an internal necrotic core. As a result, this 3D architecture allows the generation of substantial barriers for drug penetration with a more proper evaluation of drug efficiency [50]. Despite the success of these models, they still present inherent limitations. Specifically, it has been demonstrated that microenvironmental conditions influence cell behaviours and also control tumorigenesis [51]. Spheroids are entirely cell-based, so they do not offer enough flexibility for engineering the surrounding environment [52].

A more recent approach for creating realistic *in vitro* cell/tissue models is the use of scaffolds-based cell culture [34] that involves employing hydrogel-based support, polymeric hard material-based support, hydrophilic glass fiber, and organoids. Each alternative provides advantages and disadvantages for applications in different research areas [22]. Among these methods, scaffolds and hydrogels are unique because of their ability to mimic the 3D structure of the *in vivo* Extra-cellular matrix (ECM) for each particular cell type and specific tissue [36]. Hydrogels are a class of highly hydrated polymer materials (water content ≥30% by weight) [53] with a gel-like structure, composed of crosslinked hydrophilic polymer chains that allows an efficient transport of nutrients and oxygen within the 3D porous network [54]. Although hydrogels have properties such as soft and rubbery consistency [55] which are properly for tissue repair, their use for in vitro 3D cell culture is limited by various practical drawbacks, including gel preparation and consistency, expenses for the entire process and the supply of chemicals, shelf-life and storage [56]. On the contrary, in a solid-scaffold cells can grow and proliferate into a hard 3D space that is easy to design with different shapes, porosity, stiffness

and permeability for helping the generation of natural 3D tissue-like structures [57]. Figure 1.5 shows a general appearance of solid scaffold and its microstructure. Indeed, one of the main advantages of solid scaffolds is their ability to create *in vitro* organized placement of cells using controllable and reproducible steps [34].

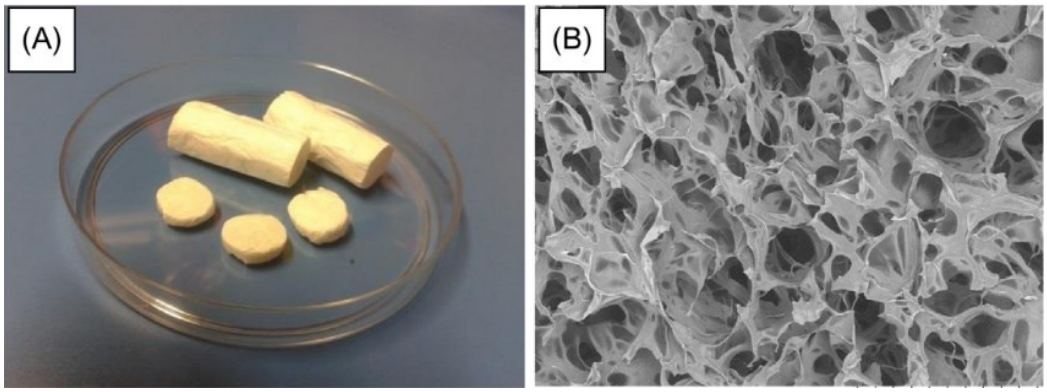

Figure 1.5: (A) General macroscopic appearance of scaffolds; (B) SEM micrograph of scaffold cross section. [58]

1.3.1. Scaffolds

The use of scaffolds for 3D models has increased considerably in the past twenty years. For obtaining a scaffold with characteristics similar to that of native tissue and supporting the cell attachment and organisation, the synthesis of complex 3D polymeric matrices needs a wide number of parameters to consider [59]. Important criteria for choosing an appropriate scaffold include the biological aspect, chemical composition, structure and physical-mechanical features [60].

1.3.1.1. Scaffold requirements

A crucial property for scaffold is its biocompatibility and nontoxicity allowing attachment of cells, ECM secretion and tissue formation without the induction of an inflammatory or toxic response [61]. To ensure this property, the first important choice for the scaffold development is the biomaterial selected. Biomaterial is defined by the European Society for Biomaterials

(ESB) as “a material intended to interface with biological systems to evaluate, treat, augment or replace any tissue, organ or function of the body” [62]. The most common biomaterials used for scaffold fabrication are polymers, called biopolymers, due to the easy control of their chemical and structural properties, important for ensuring the adhesion and spreading of living cells and protein adsorption and so the cellular attachment [63]. They are typically grouped into natural and synthetic derivatives.

- Natural biopolymers

Natural biopolymers can be considered as the first biomaterials used for clinical purposes [64]. They include alginate, proteins, collagens, gelatin, fibrins, albumin, elastin, hyaluronic acid, cellulose and chitosan (Figure 1.6 A). Natural polymers offer the first significant advantage of being very similar, often identical, to macromolecular substances of the biological environment recognized by cells, that means excellent biocompatibility [65]. Furthermore, intrinsic bioactivity, availability on the market, easy processing, and more closely mimicking of the natural ECM of tissues make natural polymers perfect candidates for providing support to cells and regulating cellular activity including growth, proliferation, differentiation and migration [66]. The use of natural materials, however, owns limitations, such as: short supply for commercial use, excessive expenses, large variation between one batch to another one, tendency to denature or decompose if the temperature is below their melting point that limits their fabrication into different sizes and shapes, susceptibility to contamination and as they are often derived from non-human tissue, they carry the risk of an immunological reaction and/or transferring pathogens if implanted *in vivo* [67].

- Synthetic biopolymers

Synthetic biopolymers represent the largest group of biopolymers used to fabricate 3D supports. Although relatively biologically inactive, they posses many advantages compared to natural polymers, including: easily manageable physicochemical properties, no immunogenicity, processability with various techniques to obtaining different shapes and morphologies, consistent supply of large quantities, mechanical properties and biostability that could be well modified depending the desired application [68]. Generally, the surface chemical

properties of a biomaterial are essential for controlling the adhesion and spreading of living cells [63]. Another relevant advantage of synthetic polymers is exactly the possibility to easily modulate their surface properties through attachment of specific functional groups/proteins by coating or using specific surface modification techniques such as plasma vapour phase deposition. Surface coating and functionalization has been proved to improve cell seeding efficiency, wettability and diffusion of proteins/nutrients through microporous structures [59]. A wide range of polymers can be selected to fit the desired biological, physical, chemical, and biomechanical properties of the tissue to be mimicked. The most used synthetic polymers for scaffold fabrication are: poly (lactic acid) (PLA), poly (glycolic acid) (PGA), poly (caprolactone) (PCL), poly (lactic-co-glycolic acid) (PLGA), poly (ethylene-glycol) (PEG), and poly (vinyl alcohol) (PVA) (Figure 1.6 B) [69]. Frequently, the combination of synthetic polymers with natural components to produce composites is considered as a promising way to simultaneously achieve high biological activity as well as manageable mechanical properties and so improving annoying issues associated with hydrophilicity, cell attachment, and biodegradability [70]. Among the synthetic polymers, PLA and its stereoisomers (poly-L-lactic acid (PLLA) and poly-D-lactic acid (PDLA)) have been used widely in biomedical research and pharmaceutical applications for the past five decades. They received attention in biopolymer research due to the unique properties, such as biodegradability, biocompatibility, and environmental sustainability [71]. The most attractive aspect of PLA is its high biocompatibility that makes it a natural choice for biomedical applications. As a biocompatible material, it doesn't produce toxic or carcinogenic local effects as well as its degradation products (if at lower concentration). Compared to other biopolymers, such as PEG and PCL, PLA has a high strength and high modulus thermoplastic so has better processability through conventional processing by following cooling and heating cycles without losing its properties to obtain different shapes for the final products [72]. Biodegradability is generally considered as an indispensable property for scaffolds used for tissue engineering and organ regeneration as they are used as temporary templates which would support cell attachment, proliferation and ECM secretion before the new tissue formation. Indeed, it should degrade in time with tissue regeneration, so that once the tissue is matured the scaffold no longer exists as such and the created tissue can perform the function of the lost tissue [73]. On the contrary, biodegradability

is not necessarily an attractive feature for all the *in vitro* cell cultures especially for long period testing in drug discovery, where the degradation can lead to changes in the properties of such biopolymers and so variation of results. In addition, biodegradation during an *in vitro* experiment introduces another variable that may influence how cells behave and is therefore not always a desirable requirement [56]. PLA and its stereoisomers possessed a slow degradation rate which leads to a long *in vivo* life time, that could be up to years in some cases (mostly 3– 5 years), as a consequence of the additional methyl group in the PLA repeating unit that makes it more hydrophobic than other synthetic polymers [74]. This represent a limit for PLA scaffold applications in different sectors of biomedical research, but make them a perfect choice for many long-term drug delivery systems and *in vitro* pre-clinical investigations in drug testing, where stable physical dimension, chemical structure, and biological activity over a prolonged period of time are crucial necessities [75].

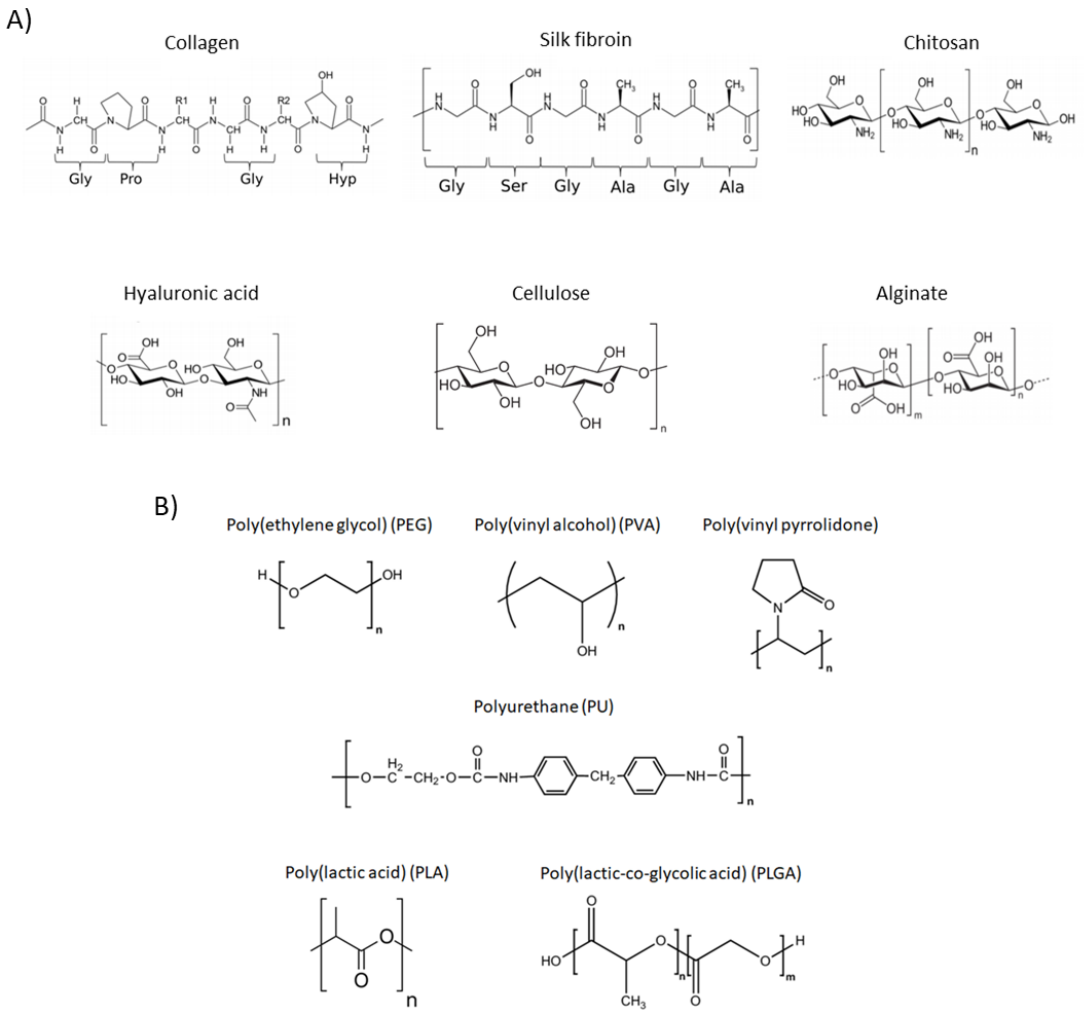

Figure 1.6: Chemical structure of (A) natural polymers and (B) synthetic polymers used as biomaterials.

The biological aspects (biocompatibility and nontoxicity properties) and the chemical composition (natural or synthetic polymers) belong to the minimum requirements for an ideal scaffold. Since biological tissues are incredibly complex 3D structures with complex mechanical functions, the design of the scaffold is another crucial issue [60]. The mechanical properties (stress and strain) are key factors to consider during the scaffold fabrication and each application needs a different acceptable range to guarantee the mimic of a specific native tissue/organ structure. Mechanical strength is identified as the impact resistance of scaffold in order to maintain its integrity during the implantation in the human/animal body. The most

common mechanical tests to evaluate scaffold quality include tensile and compressive tests [76]. Very often the mechanical properties depend on the nature or chemical bonds of the materials. Among the biomaterials, the synthetic polymers have the advantage of generating desired mechanical properties only by changing the chemical structure of the polymer by different methods of synthesis and using cross-linking agents [77]. Furthermore, they possess higher mechanical performances with mechanical strength and stiffness closer to native soft/hard tissues compared to the other biomaterials (Table 1.1) [66]. The mechanical properties to support cell growth can be also improved through the porosity and appropriate pore size of the scaffold framework [60]. Porosity represents the percentage of empty volume in a scaffold and it's a desirable factor for a good cell migration and proliferation. Additionally, the porous structure aids nutrient supply, oxygen, and waste product exchange during tissue generation. The preferred porosity for a good cell penetration is generally between 60%-90% [78]. However, since the degree of porosity also influences other properties of the scaffolds such as its mechanical stability, its value should always be balanced with the mechanical needs of the particular tissue that is going to be replicated [79]. Similarly, scaffold pore size and geometry are fundamental issues for assisting cell biological activities, including cellular penetration, ECM production, and neovascularization of the inner areas of the scaffold [64]. In order to facilitate cell migration and proliferation, the pore size of the scaffold must be comparable to the physical cellular size (10–100 μm). Pore sizes smaller than the size of cells prevent cell infiltration and migration. However, larger pore size also limits cell migration due to the insufficient points to generate traction [58]. Beside porosity and pore size, pore interconnectivity is also a critical issue during scaffold fabrication. Even if the matrix porosity is high, cell migration and mass transfer of oxygen and nutrients within the scaffold network can be inhibited if the pores are not sufficiently interconnected [80]. Hence, high porosity, appropriately sized open pores and a well interconnected geometry must be considered among the scaffold design criteria to improve diffusion throughout the scaffold inner area [35].

Table 1.1: Mechanical properties of hard tissues, soft tissues, biomaterials (metallic, ceramic, polymeric).

Material	Young's Modulus (GPA)	Tensile Strength (MPa)
Cortical bone	7-30	50-150
Cancellous bone	0.05-0.5	10-20
Articular cartilage	10.5	27.5
Skin	0.1-0.2	7.6
Stainless steel	200	540-1000
Co-Cr alloys	230	900-1540
Alumina	400	450
Bioglass	35	42
Hydroxyapatite	30-100	60-190
Polyethylene (PE)	1	30
Polyurethane (PU)	0.02	35
Polyethilenglicole (PEG)	0.13	2.4-4.2
Poly-lactic-acid (PLA)	2-3	32.8

1.3.1.2. Scaffold fabrication techniques

After selecting the adequate biopolymer, the next step is to choose a suitable processing technique in order to generate 3D scaffolds fulfilling all the requirements described above. Several polymeric scaffold fabrication methods have been developed and evolved in the last decades for producing increasingly complex structures [81]. The conventional techniques for scaffolding can be roughly classified into two categories: wet methods (i.e., solvent casting/particulate leaching, phase separation, electrospinning) and solvent-free methods (i.e., gas foaming, melt molding, rapid prototyping). In the wet methods, polymers are dissolved in a solvent to form a solution which is further processed and finally the solvent is removed to

form a porous polymeric structure. Since most organic solvents used are harmful to cells, one of the big issues of these techniques is the residual solvent in the scaffolds [82]. These methods are briefly described below and the micrographs of the scaffold structure obtained with each technique are shown in Figure 1.8.

- Solvent casting/particulate leaching

Solvent casting/particulate leaching (SC/PL) is one of the most traditional techniques used to fabricate scaffolds. In principle, the polymer is dissolved in an appropriate organic solvent and then an insoluble salt (porogen) of a certain size is mixed with the polymer solution or the homogeneous polymer solution is cast into the porogen-filled mold. The solvent evaporation creates a salt-polymer composite which is finally washed in the bath to remove the salt particles and obtain a network of interconnected pores [83]. Sodium Chloride particles, glucose, and paraffin spheres are generally used as porogen agents to create pores in the polymer matrix. The content of the added porogens and their size/shape allow to control the microporous structure of the scaffold in terms of porosity, pore size and interconnectivity. While, the macro-geometry of the scaffold is determined by the casting mold cavity. Huang and coworkers have demonstrated that, if the polymer solution is diffused in a stable salt stack and an appropriate thermal treatment is performed before leaching, even the crystallinity of the porous foam can be controlled closely [84]. Highly porous scaffolds with porosity range from 50% to 90% can be prepared using this technique (Figure 1.8 a). SC/PL technique is relatively simple to carry out, easy to manipulate and low cost. One of the drawbacks of this fabrication technique is the high residual content of organic solvents involved in the process, which takes a lot of time to evaporate (days or weeks) and limits as-produced scaffold applications in biomedical research due to the toxicity of the residual solvent for the cells. Moreover, some authors question the homogeneity and interconnection of the pores, thickness limitations and limited mechanical properties intrinsic to the SC/PL process [85].

- Electrospinning

Electrospinning (ES) is known as a technique for making fibers from a solution by using electricity. In recent ten years, ES has been introduced and became an indispensable technique

for preparation of nanofibrous scaffolds [86]. It has a very complicated mechanism in which a polymer droplet is held at the tip of a metal needle by surface tension. Under high voltage (10–20 kV), the droplet becomes charged and the strength of the electric field exceeds the surface tension of the droplet to produce a jet of polymer solution that is then extended and whipped continuously by electrostatic repulsion until it is deposited on a grounded collector. Before reaching the collector, the solvent evaporates and the jet solidifies into thin fibers that generate the porous scaffold (Figure 1.8 b) [82, 87]. The most attractive characteristic of electrospinning is the possibility to produce polymer fibers with diameter ranging from tens of nanometres to tens of micrometres with a specific orientation that can be adjusted using different collection devices. Another advantage of this technique is that the ultrafine fibers in the electrospun scaffolds possess suitable high surface-to-volume ratios and porosity for cellular growth both *in vitro* and *in vivo* and subsequent tissue organization by mimicking the natural ECM of body tissues [66]. Moreover, the ES setup is very simple, inexpensive and with high efficiency. The main drawbacks of this fabrication method are: the nanoscale pore size, which is not sufficient for cell seeding and penetration, the lack of control on the porosity and pore size, and solvent residues in the scaffold which may be dangerous for cells and organs [79]. Therefore, scaffolds with complex structures and homogeneous distribution of pores are still a challenge for this technique, that limit many applications in biomedicine [60].

- Phase separation

Phase separation (PS) is a versatile technique for 3D scaffold designing in which the formation of porous structure depends upon the induced phase separation of a homogeneous polymeric solution [88]. In the process, a polymer is dissolved in solution by using a specific solvent and the phase separation is induced, either thermally (Thermally Induced Phase Separation, TIPS) or through the addition of a non-solvent to the polymer solution (Diffusion Induced Phase Separation, DIPS). The polymer solution under this condition becomes thermodynamically unstable and tends to separate into two phases [89]. The advantage of the phase separation process is that it is a relatively simple procedure and requires minimal apparatus. The main drawback instead is that this is a small-scale technique that is suitable only for certain polymers that are susceptible to phase separation, such as thermoplastic polymers

[90]. In the last decades, TIPS has been widely adopted in different fields from biomedical to pharmaceutical one. It is one of the most effective processes to produce scaffolds with an intrinsically interconnected polymer network and tunable properties in one-single step by manipulating processing parameters and system composition [91]. It ensures a good control of the scaffold structure, especially porosity, pore diameter and interconnectivity, besides mechanical properties and biodegradability [92, 93]. Basically, the principle of TIPS is to induce the demixing of a homogeneous polymer solution, or polymer–solvent–non-solvent solution, at elevated temperature by cooling the system to a lower temperature and obtaining a polymer-rich phase and polymer-lean phase. After the solution saturation, which leads to polymer precipitation followed by polymer organization, the as-obtained structure is frozen and finally the solvent is removed by extraction, evaporation, or freeze-drying, forming a porous structure (Figure 1.8 c) [82]. As a function of polymer-solvent affinity, the TIPS process can follow two typical mechanisms: Solid–Liquid (S–L) phase separation and Liquid-Liquid (L-L) phase separation. In case of good compatibility of the polymer-solvent couple, the S-L phase separation occurs with the crystallization of the solvent part that governs the structuration of the scaffold matrix, and a final irregular 3D network structure with relatively small pores is formed. On the contrary a L-L phase separation occurs when the polymer-solvent affinity is too weak. In this case, the addition of a non-solvent lowers interactions between the polymer and the good solvent and induces the demixing. Moreover, L-L separation needs a higher temperature than the own solvent freezing temperature [91]. A typical schematic representation of L–L phase separation for a binary polymer-solvent solution presenting an upper critical solution temperature is shown in Figure 1.7.

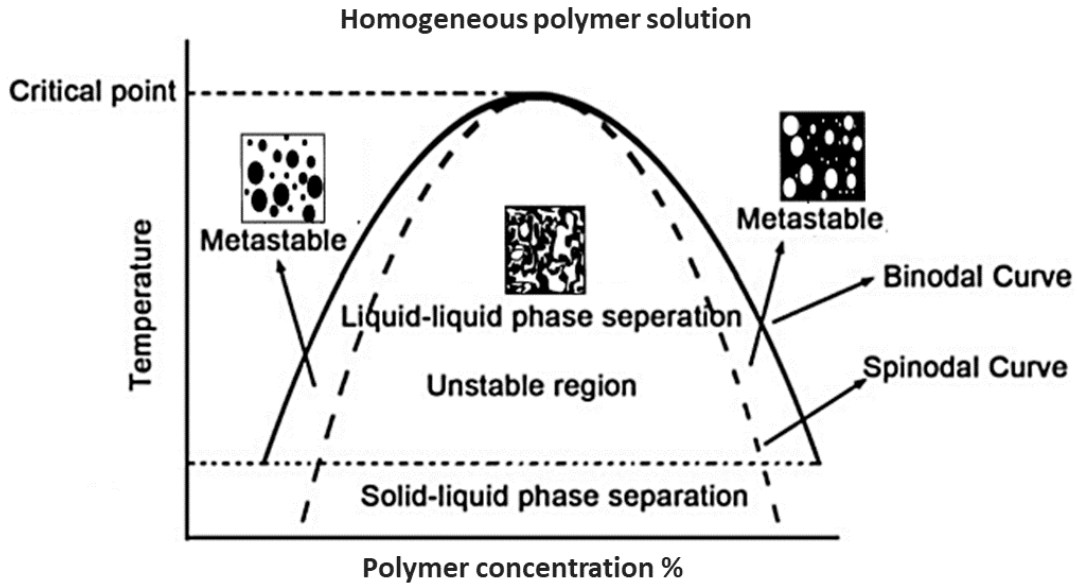

Figure 1.7: Schematic representation of a binary thermally induced phase separation in polymer solution by L-L phase separation. (Figure adapted from [82])

Briefly, the solid binodal curve represents the thermodynamic equilibrium of L–L demixing, which is often used to approximate the cloud point at which the clear solution becomes turbid. Immediately below this curve, in the metastable region, a first type of demixing takes place in which the two phases separate following nucleation and growth mechanisms. L–L demixing in the metastable region leads to spherical or pseudo-spherical pores poorly interconnected. In the unstable region crossing the dashed spinodal curve, a spinodal decomposition takes place with a 3D polymer network characterized by open porous and well-interconnected structure. A third scenario is possible if the temperature of the solution is decreased to or beyond the solution glass transition temperature (freezing point) before the L-L phase separation leading to a S-L phase separation [82, 94]. DIPS is a second type of PS technique which allows the production of porous membrane with a rather simple procedure. The main steps involved are: a dip coating by casting a polymer solution on a specific support and then the immersion into a coagulation bath composed by a nonsolvent. The exchange of solvent and nonsolvent modifies the composition of the casted solution, inducing the L-L or S-

L phase separation again following nucleation and growth and/or spinodal decomposition mechanisms [95]. Among all the fabrication techniques, the easy implementation due to the absence of required expensive specialised equipment makes TIPS and/or DIPS one of the most effective processes to produce scaffolds with tunable properties [96]. As it is well-known, an accurate control of scaffold architectural parameters (i.e., pore geometry, size, interconnectivity and orientation) is necessary to maximize nutrient diffusion, control cell growth and function, manipulate tissue differentiation, and mimic the mechanical properties of regenerated tissue [73]. For this reason, the principal advantage of PS is the easy control of scaffold morphology by changing parameters such as polymer type and concentration, type of solvent/non-solvent, freezing temperature and cooling rate for TIPS [97], while the composition and temperature of coagulation bath and the desiccation environment for DIPS [95]. Additionally, to improve cell adhesion on the scaffolds as well as their mechanical properties, composite scaffolds can be fabricated using different types of porogens, such as the bioactive ceramic Hydroxyapatite (HA) for bone regeneration [98]. However, long time for solvent sublimation, solvent residuals, possibility to use limited polymers, low mechanical stability, sensitivity of the technique (processing parameters have to be very well controlled) and small-scale production together with inadequate resolution are the main disadvantages of this methods [79].

- Gas foaming

Gas foaming (GF) method can be applied for highly porous foams fabrication by avoiding the use of organic solvents to dissolve polymers. This process involves high-temperature compression for molding the polymer into a solid disk-like structure. This structure is exposed to a high-pressure inert GF agent such as carbon dioxide (CO_2) or Nitrogen (N) for several days. At this point, the pressure is rapidly decreased and the bubbles created by gas expansion escapes the polymer, leaving a porous, sponge-like structure [99]. Up to 90% porosities and pore sizes up to 100 μm could be obtained using this technique (Figure 1.8 d) and pore size can be modulated varying the temperature, pressure, and rates of parameter reductions. However, the main disadvantage of GF is the poor interconnectivity of the foam that makes cell seeding and migration within the scaffold difficult, and usually the surfaces are mostly non-porous. Also,

even if organic solvents are not used, the high temperature which is involved in the disc formation prohibits the incorporation in the matrix of cells or bioactive molecules [100].

- Melt molding

Similar to GF technique, Melt Molding (MM) is a non-solvent scaffold fabrication process. Powder polymer mixed with a suitable porogen compound is filled into a mold and heated above its glass transition temperature while applying pressure. The polymer tends to bind together producing a scaffold with the shape of the mold. Finally, the mold is removed, and the porogen is leached out of the scaffold leaving behind a porous structure with specific surface morphology (Figure 1.8 e) [101]. Using this method, it is possible to construct scaffolds of any shape just by changing the mold geometry as well as to obtain the desired shape and pore size by varying the size and amount of the porogen particles. The drawbacks of MM include the difficulty of removing the porogen particles and high processing temperatures that preclude the ability to incorporate bioactive molecules as well as for GF technique [102].

- Rapid prototyping (3D printing)

Rapid Prototyping (RP) is a common name for a group of advanced manufacturing processes that can produce 3D objects through repetitive deposition and processing of material layers using directly computer data such as Computer Aided Design (CAD) data (Figure 1.8 f) [103]. One of the attractive uses of RP is associated to produce scaffolds with controlling over pore size, pore interconnectivity, porosity and spatial distribution of pores [104]. 3D printing was the first RP technique to be proposed for biomedical purposes. It uses ink-jet printing approach to accurately writes a ‘‘binder’’ solution like polymer latex or silica colloid, which moves uniformly with the CAD cross-sectional data through the ink-jet print head, on to metallic, ceramics or composites powder [105]. Although RP technologies have gained a lot of interest in the field of biomedical research, there are some challenges that need to be addressed before these methods can replace the conventional fabrication methods. The surface roughness of scaffolds is a very important factor that influences the cell-matrix interactions, and powder-based techniques produce rough surfaces that may enhance cell adhesion. The feasibility of scaffold fabrication by RP processes also depends on the resolution of the machines, that is a

consequence of several machine-specific parameters [106]. Due to the fact that cells cannot be directly assembled to the 3D structures, recently 3D bioprinting has been developed as a channel by simply providing a 3D cell assembly with printing. It needs to prepare a bio-ink, which can be defined as mixtures of hydrogels and cells with good printability for 3D cell assembling and realization of tissues and organs. Despite challenges, 3D bioprinting is poised to play a key role in future implementing biomedical research [107].

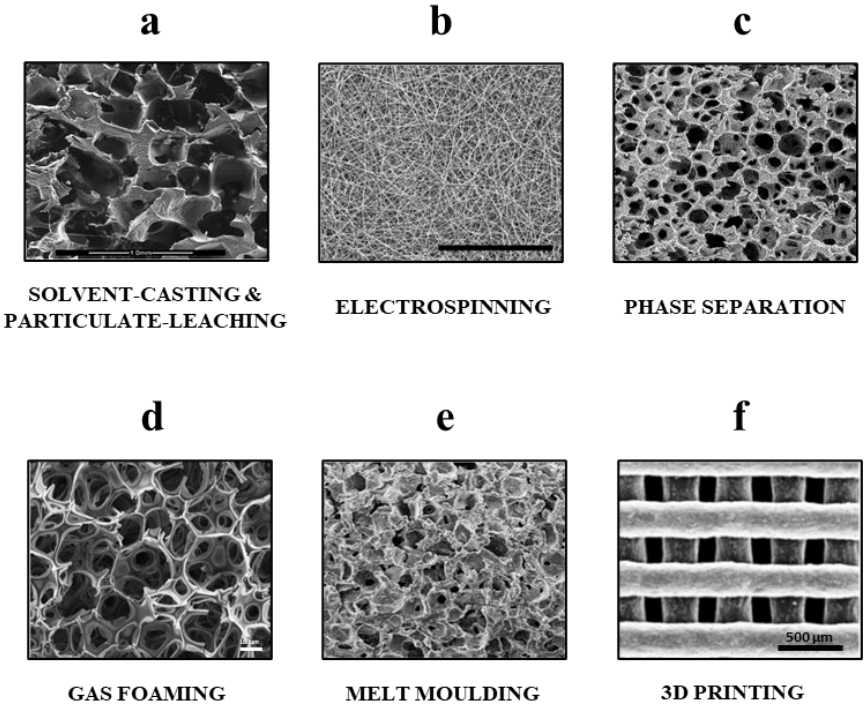

Figure 1.8: SEM micrographs of polymeric scaffolds produced with different techniques.

1.4. Static vs Dynamic 3D *in vitro* cell culture

Flat 2D surfaces like tissue culture flasks (T-flasks) are still "gold standard" [108] for many *in vitro* cell cultures at laboratory scale, even if it is well known that despite the simplicity, ease of handling and low cost, these static 2D culture systems present several and serious limitations [109]. As previously mentioned, 2D cultured cells do not mimic the natural structures of natural tissues because of the deficiency of cell-cell and cell-extracellular

environment interactions [32]. The need to overcome these issues inspired the emergence of 3D cell cultures systems, a promising approach to provide cell-based assays with more physiological importance, especially the behaviour similar to the *in vivo* cells. Although 3D culture models guarantee an optimal spatial organization of cells by mimicking tissue-like structures, the traditional 3D static condition of culture has received gradually less attention in the last years while in the meantime 3D dynamic (3DD) cell cultures have generated great interest in the scientific and medical communities [30]. Static technologies satisfy the external requirement for medium flow together with waste removal and nutrient transport by manually changing the medium about every two days (or on the base of the specific cell metabolism and activity) [110]. The medium in these systems follow the path of least resistance and prefers to circumnavigate the scaffold, consequently the poor convection of medium alone at the external surface does not guarantee nutrient transportation within the porous confines in the 3D volume [111]. Furthermore, static cultures have several other problems such as low seeding efficiencies, small number of cells that can be maintained in culture due to the limited available surface with the correct amount of nutrients, gas-liquid exchange (such as oxygen) occurring only at the medium/scaffold interface and leading to presence of concentration gradients (pH, dissolved oxygen, nutrients, metabolites, etc.) in the entire scaffold volume [112]. On the contrary, when the culture is carried out in dynamic conditions the mass transfer rates for gases, nutrients, metabolites and growth factors are improved and thus the formation of gradients is prevented, the transport of oxygen and nutrients is increased, and the sedimentation of cultured cells/constructs is avoided [113]. The most common 3DD cultures are based on bioreactor systems, where cells in a 3D scaffold environment are cultured and incubated in the presence of shear stress that can resemble the physiological relevant shear stress conditions. Thereby, this apparatus proved to have the potential to bridge the gap between the conventional *in vitro* static approach and *in vivo* studies by mimicking physiological key-features of organs and tissues [114].

1.4.1. Bioreactors

From a general point of view, bioreactor is the name given to any closed culture environment (typically mixed) that is designed to control at least one operating parameter of a

physio-chemical environment to obtain aseptic feeding and sampling and to improve reproducibility and automatization of a process [115]. In biomedical and pharmaceutical industry, bioreactors are essentially used in three ways: to mimic the *in vivo* state of cells thus to better understand normal cell and molecular physiology or to study the pathophysiology of a disease; to expand cells for potential clinical use such as in gene and cell therapies or transplantation; to create new therapeutic targets and test potential new treatments and drugs in a more realistic environment than simple *in vitro* conventional static culture. Thus, a better drug design is allowed and simultaneously a potential way to reduce the numbers of animals in research is proposed [116]. There are complex stimuli *in vivo* that a cell may be exposed to, both chemical and mechanical stimuli, that impact cell performance. As a consequence, for cell growth by using bioreactor devices, a precise measure and control of the *in vitro* physiological environment is essential during culture [115].

Bioreactor design is complex and includes key requirements as follows: increased cell-seeding efficiency maintaining a desired uniform cell concentration within the scaffold; microenvironmental parameters control (i.e., temperature, pH, pressure, oxygen tension, metabolites, regulatory molecules, shear stress); improved mass transfer (i.e., nutrient and oxygen supply and removal of waste products and toxic metabolites) and physiological stimuli. Contemporary bioreactor design may incorporate biological, mechanical, or electrical stimuli in order to apply greater influence over cellular differentiation and development into functional tissue constructs and specific tissue phenotypes [117]. Furthermore, each type of tissue structure (e.g., skin, bone, blood vessel, liver, kidney, cartilage, myocardium) requires a unique kind of bioreactor design in which both biological and engineering conditions have to be approached along with reliability, reproducibility, scalability, and safety issues [118]. For example, the performance of blood vessels depending on their role: the make-up of a vein usually delivering low pressure flow at low shear stress, compared with an artery responsible for high flows at much higher pressures which are designed with thicker musculature in vessel walls and more elastic. This means that for modelling blood vessels in a bioreactor, not only the correct cell type is necessary but also the mechanical structures capable of delivering specific functions [116]. Among the design parameters described above, the mass transfer and mechanical stimuli represent the major obstacles for a 3DD culture of cell seeded constructs which also impact on

cell physiology and limit application of bioreactors in different research areas [119]. Mass transfer in 3D culture systems involves the transport of nutrients and gases from the place that they are supplied to the site of the cells distributed throughout porous scaffolds (opposite path for waste products elimination). Thus, there is an external mass transfer, from the bulk culture medium to the scaffold surface, and an internal mass transfer to the cells within the tissue construct [118]. Commonly, two processes govern mass transfer of nutrients to cells: convective mass transfer in the bulk motion of the media flow that will get the nutrients to the surface area of the scaffold and the cells; and diffusion, that involves the movement of species down a concentration gradient through the porous network. The ratio between convective transport and diffusive transport is a key design parameter for bioreactors [115]. External mass transfer rates depend primarily on hydrodynamic conditions in the bioreactor. In contrast, internal rates may depend on a combination of bioreactor configuration and the scaffold structure and porosity, the overall cell or scaffold construct size, and the diffusion rate through the biomaterial [120]. Amongst mass transfer mechanisms, oxygen transfer is a big challenge due to its poor solubility in aqueous culture medium with a diffusive penetration depth within *in vivo* tissues in the range of only 100 to 200 μm for fully oxygenated culture medium at 37°C. Consequently, maintaining a good equilibrium between oxygen delivery to cells and their oxygen consumption is a critical issue, considering the diffusive distance. Therefore, the oxygen tension and level adjustment are important biochemical parameters that need to be closely monitored for a successful design process of any bioreactor [121]. Biomechanical stimuli management, such as shear stress, are another important requirement in bioreactor design, particularly for musculoskeletal tissue engineering, cartilage formation, and cardiovascular tissues [122–124]. During tissue growth under 3DD culture, mechanical interactions between different components, that is cells, medium, and scaffold material, can influence the final generation of cell aggregates or a dispersion throughout the scaffold. Indeed, it is widely accepted that shear stress has a dominant impact on tissue function and viability. Different values for the maximum tolerable shear stress for different types of cells are reported in literature. For example, high shear stress on the scaffold surface due to the flow of fluid, can peel off attached cells and reduce the speed of tissue growing compared with static cultures [118]. Usually, biomechanical stimuli can be applied throughout the bioreactor by the culture medium flow and so nutrient and waste transfer

are automatically regulated. Other types of mechanical stimuli can also be applied to tissue constructs using a bioreactor, including axial compression or tensile forces [125, 126].

1.4.1.1. Common types of Bioreactors

Over the years, several types of bioreactors have been developed and employed in biomedical research areas to induce different types of physiological and biomechanical stimulation to cells *in vitro* dynamic culture [127]. Recently, bioreactors have been also applied in the pharmaceutical industry as systems for investigating the response of tissues and cells to potential new drugs during pre-screening tests [128]. The most common are: spinner flask, rotating wall vessel and perfusion bioreactor. Simple systems, such as spinner flasks and rotating vessels, in which the culture medium is exchanged at appropriate intervals, minimize the nutrient gradient and metabolite concentration around the construct; while perfusion chambers directly perfuse media inside the scaffold with a continuous medium recirculation, thus guaranteeing a good mass transport within the porous matrix [129].

- Spinner flask

The spinner flask and rotary vessel use convection to ensure that the media surrounding the scaffolds is well-mixed. Within spinner flasks (Figure 1.9 A), cell seeded scaffolds are attached at the end of needles hanging from the lid of the flask and immersed in the culture medium. A magnetic stirrer bar forms vortex fluid flows in the superficial pores, providing dynamic mixing of the medium and mass transfer between the medium and the scaffold surface. It is via the generated vortexes that nutrient diffusion is allowed and cell proliferation is promoted throughout the porous network in comparison to static condition [62]. However, these bioreactors suffer from some drawbacks that limit their upscaling and standardization of the process. First, mass transfer in these flasks is not good enough to deliver homogeneous cell distribution throughout scaffolds and cells mostly reside on the construct periphery. Furthermore, the shear stresses acting on the constructs are very high and heterogeneous, which prevents homogenous tissue development. These adverse conditions can affect cell growth rate and metabolism limiting efficiency and reproducibility of the culture process [113].

- Rotating wall vessel

A low-shear stress culture environment, allowing to partially overcome the limitations of stirred tanks, is generated in the rotating wall bioreactors (Figure 1.9 B). They were originally developed by NASA in order to protect cell culture from high forces during experiments in space. In these devices, the scaffolds are free to move in a vessel and they are suspended in the medium due to the balance between hydrodynamic drag force, provided by the wall rotation, and the downward gravitational force. Indeed, to ensure the scaffold remains in suspension, the rotational speed must be increased during tissue growth to balance the gravitational force [62].

In these systems, a dynamic laminar flow enhances external mass transfer bypassing the diffusion limitations for the delivery of nutrients and removal of waste products. As compared to the turbulent flow within stirred flasks, the laminar flow condition provides a more uniform distribution of the cells and better metabolism [130]. Additionally, it also protects fragile tissues from cracking because of the reduced levels of mechanical stresses experienced by cells on the construct [131]. A weakness of these devices is the complexity of the technological solutions adopted for rotation that make them not easily scalable and unsuitable for continuous medium replacement and real-time monitoring. The potential critical limitation of both stirrer flasks and rotating systems is the insufficient mixing on scaffold surface to deliver the necessary nutrients and gases, especially oxygen, to the core of the foam and so compromising development and survival of tissues during *in vitro* culture [132]. Due to mass transfer limitations within scaffolds in the as mentioned bioreactors, high concentrations of viable cells and deposits of ECM are exhibited on the external portion of the scaffold leaving the interior almost empty of cells. Moreover, necrosis occurs if an adequate amount of oxygen is not delivered to the cells throughout the entire scaffold that leads to engineered tissues developed with inhomogeneous cellular distributions.

- Perfusion Bioreactor

The improvement of mass transport and maintaining a uniform cell distribution throughout porous networks is guaranteed by the design and employ of perfusion bioreactors [133]. Commonly, the term perfusion bioreactor refers to a system consisting of a pump and a scaffold chamber connected by flexible tubes with an open or closed loop (Figure 1.9 C). In a

closed loop, a medium reservoir is also present and the medium after perfusing the interior of the scaffold can be recycled. Thus, the growth factors, cytokines, matrix proteins, and other signals that are secreted by the cells during tissue development can be helpful to tissue generation. With these systems the circulation of medium and a constant aeration throughout the culture chamber is allowed [130]. In the last twenty years, culture using flow perfusion bioreactors has been shown to provide more homogeneous cell distribution through scaffolds in comparison to the traditional static culture and other bioreactor models. For example, J. S. Greenberger and co-workers [134] showed that collagen scaffolds seeded with bone marrow stromal cells and cultured in a flow perfusion bioreactor display greater cellular infiltration within the scaffold, implying that better nutrient exchange occurs due to the perfusion flow. Another incredible advantage due to the medium flow throughout the construct during the perfusion mechanism, is the flow-induced shear stress at which cells may be exposed. As described before, shear stress is a beneficial mechanical stimulus for tissue development and for maintaining its normal structure and function during 3DD culture. However, nowadays the cellular mechanisms underlying the responses to mechanical stresses are still not well understood [124]. Flow perfusion bioreactors have been also designed to mimic physiologically relevant levels of shear stress, thus offering an environment more favourable to tissue development than scaffolds cultured in the absence of mechanical stimuli [135].]. In the end, the perfusion bioreactor seems to be the most convenient for *in vitro* dynamic cell culture on solid porous scaffolds between the different types of bioreactors, since it offers both convection and diffusion mechanism for mass transfer and can provide *in vivo*-like physicochemical and environmental stimuli for engineered tissue constructs [118]. One of the limitations with the perfusion systems is their relative complexity and difficulty in assembling and operating. Nevertheless, comparison of it with the other system issues is sufficient to justify its utility [132].

- Magnetic and Ultrasonic Bioreactors

The bioreactors described above mainly use direct application of mechanical stimuli on a macroscopic scale to seeded scaffolds. However, recent studies have demonstrated how microscale mechanobiological stimuli, such as magnetic forces and ultrasounds, can positively

affect tissues and cells growth and proliferation. Traditionally, magnetic bioreactors (Figure 1.9 D) consist of one or more permanent magnets which influence cell behaviour through static or dynamic magnetic field strengths [136]. An advanced high-throughput magneto-mechanical stimulation bioreactor for cartilage TE was developed from M. Brady et al. [137]. They showed how their device was able to provide a novel platform for studying the effects of both electromagnetic phenomena and mechanical stimulation on chondrocyte culture. Subramanian's research group [138] realized an ultrasound (US) assisted bioreactor (Figure 1.9 E) that stimulate chondrocyte proliferation and differentiation through the polyurethane-polycarbonate/chitosan-based scaffold under low-intensity continuous US stimulation during long-term culture periods. They placed a 6-wells plate with cell-seeded scaffolds above the transducer array and a US signal was applied. Their results showed that the bioreactor had positive effects on cell proliferation, viability and the gene expression of specific chondrocyte markers. However, many questions about the cell response to magnetic fields and ultrasound stimulation remain unsolved and more studies should be performed in the future.

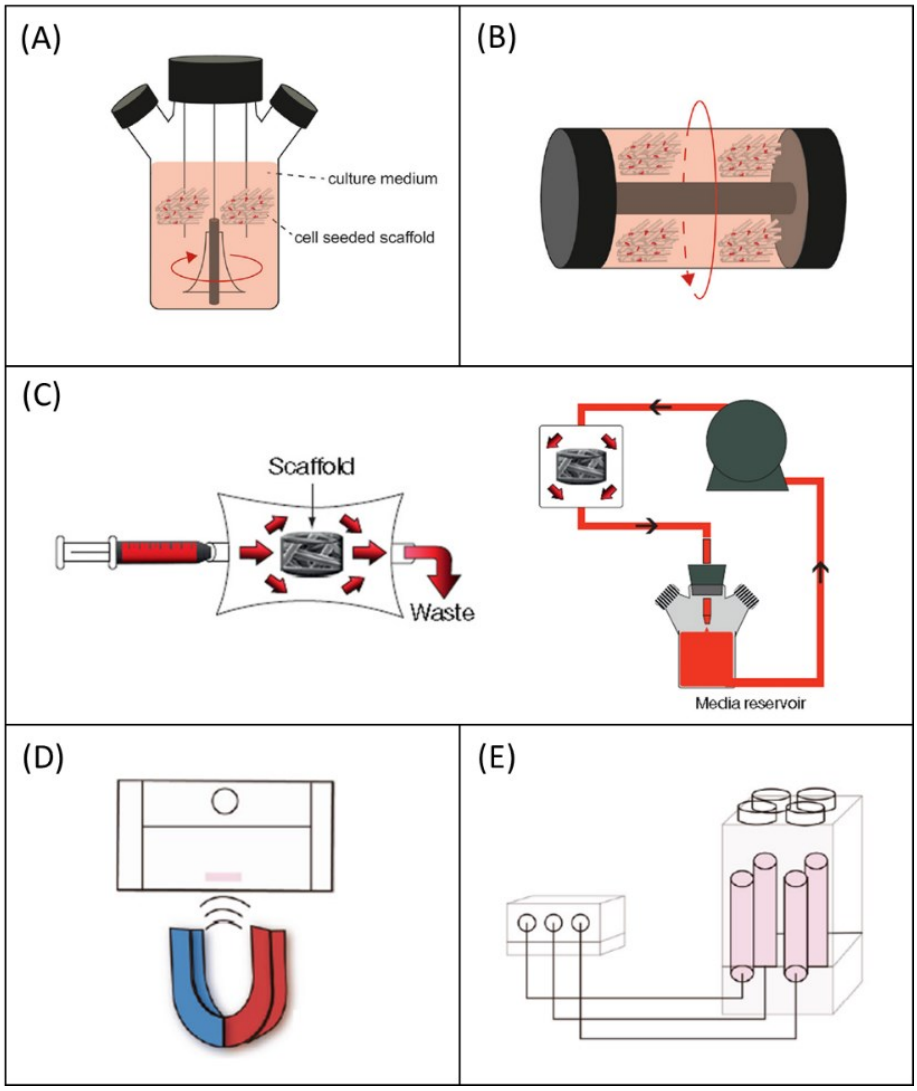

Figure 1.9: Schematic of the most common bioreactor used for 3D dynamic cell culture. (A) spinner flask; (B) rotating wall vessel; (C) perfusion bioreactor with a direct waste disposal at the outlet (open flow loop) (left) and a perfusion bioreactor with a medium reservoir between the culture chamber and the pump (closed flow loop) (right); (D) Magnetic bioreactor; (E) Ultrasonic bioreactor. (Figure adapted from [129, 133, 136])

1.5. Nanoparticles: from micro to nano

Nanotechnology represents one of the most interesting fields of modern science, which deals with the manipulation of matter with at least one dimension of size from 1 to 100 nanometres (Figure 1.10) [139]. It possesses a highly interdisciplinary character by including different doctrines like chemistry, biology, physics and engineering and taking advantage of their principles and their processes [140]. In the last years, nanotechnology products have become increasingly useful in biomedicine and have led to the advent of a hybrid science named "nanobiotechnology" [141]. The two big applicative areas of nanobiotechnology are: tissue engineering (TE) and biomedicine. In TE, metallic, ceramic, and polymeric materials with improved material properties at the nanometer scale dimension, such as increased surface area and finer surface roughness, have been investigated as new scaffolds that may produce better biological cell responses and effective tissue-implant mechanical interaction [142]. Nanotechnology products have revolutionized the biomedical sciences in different areas from disease diagnosis and treatment to monitoring and control of biological systems (bioimaging and biosensing) to drug design and drug delivery [143].

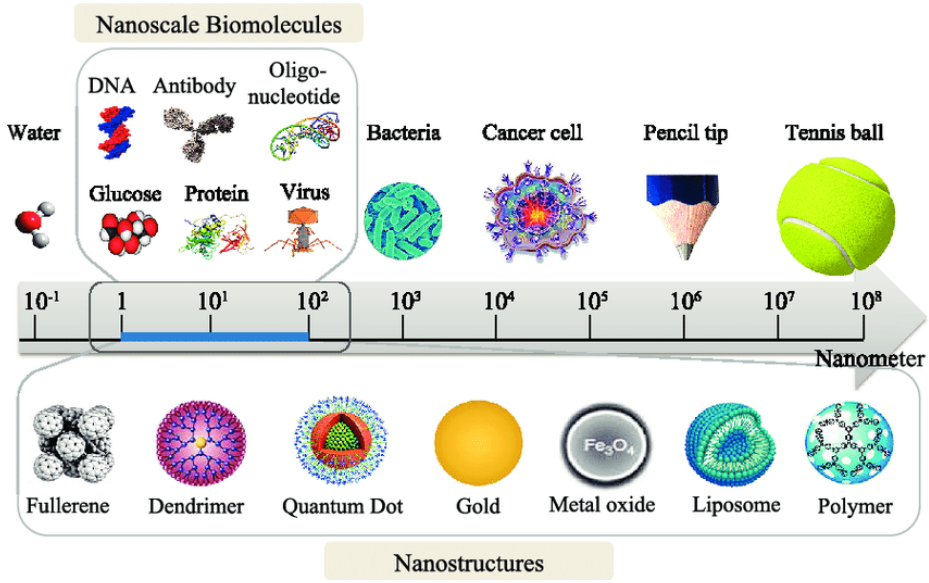

Figure 1.10: Dimensional scale from nanoscopic to macroscopic. [144]

Nanoparticles (NPs) are a wide class of materials with unique properties derived from inorganic, organic, metallic or semiconductive compounds [145]. Depending on their physical (morphology, size) and chemical properties, NPs can broadly be divided into various categories. Some of the common classes are: metal NPs, Ceramic NPs, Semiconductor NPs, and Polymeric NPs [146]. One of the major advantages of NPs over larger sized particles are the high surface-to-volume ratio that means higher surface energy, unique optical and electronic properties and also excellent magnetic properties. Usually, these size-dependent properties have been observed to be very useful for biomedical applications. For example, the magnetic properties of nanoparticles are utilized to develop drugs for targeted drug delivery systems as well as Magnetic resonance imaging (MRI) contrast agents in place of conventional gadolinium-based contrast agents [147]. NPs optical properties are mainly utilized to find alternatives to organic dyes for imaging and diagnostic purposes since bio-optical imaging still suffers from problems such as resolution, sensitivity, speed, and penetration depth [148].

1.5.1. Quantum Dots (QDs)

Quantum Dots (QDs) are one of the first nanotechnologies to be integrated with the biological sciences [149]. QDs are nearly spherical semiconductor particles composed of groups I-VII, II-VI, or III-V elements and with diameter range from 2 to 10 nm, comprising of approximately 200-100,000 atoms [150]. They are defined as particles with physical dimensions smaller than the exciton Bohr radius, which is the distance between the electron (negatively charged) and the hole (positively charged) left in the valence band by the electron after exciting and jumping to higher energy levels. From quantum mechanical point of view, when the radii of the particles are smaller than the bulk exciton Bohr radius there is a "confinement quantum regime" in which the energy levels that the electrons inhabit become discrete, with a finite separation between them, in place of continuous valence and conduction bands typical of macroscopic semiconductors [151]. Due to this regime, the optical properties, such as absorbance and Photoluminescence, and electronic properties of QDs are size-dependent and can be easily controlled [152]. The effect of changing size on the electronic structure of QDs is shown in Figure 1.11: the larger a quantum dot becomes, the more continuous its electronic structure becomes and the closer its band gap becomes to that of the

bulk material. Consequently, bigger QDs with shallow and small band gaps require less energy to excite the electron and emit photons in the red-orange wavelengths. Similarly, smaller size QDs have larger bandgaps and emit in blue wavelengths [153]. Moreover, changing the nanocrystal composition influence the wavelength range over which the optical properties can be tuned, since the lowest wavelength at which the nanocrystal will absorb and emit, is dictated by the bulk band gap of the semiconductor. For example, switching from Cadmium (Cd) to Zinc (Zn) will lead to bluer nanocrystals due to the wider bandgap of Zn [149]. An essential parameter to evaluate the emission properties and the efficiency of this process is the fluorescence Quantum Yield (QY), which is described as the ratio of the number of emitted photons divided by the number of absorbed photons [154].

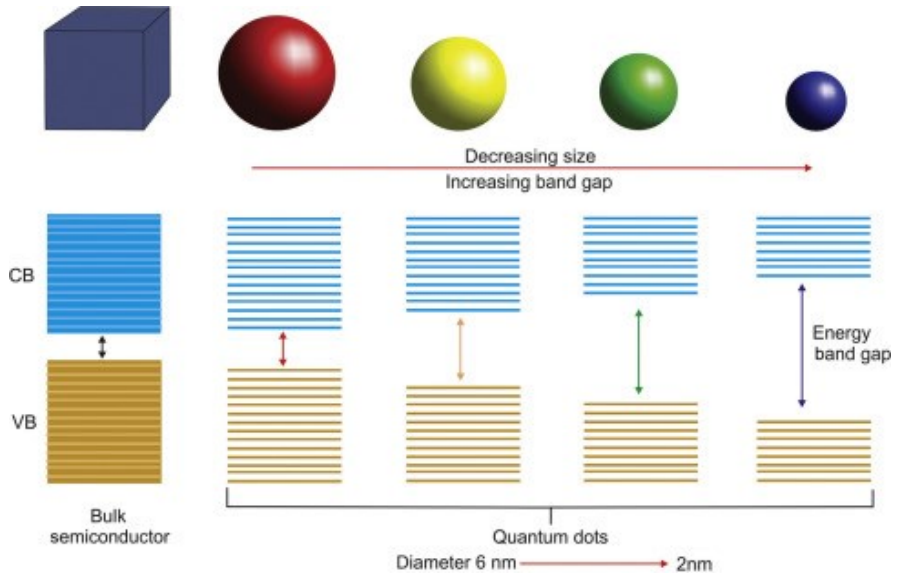

Figure 1.11: Schematic representation of energy band gap variation and color in quantum dots with the size variation. [153]

Due to the unique optical and electronic properties size-tunable, improved signal brightness, high fluorescence QY, resistance against photobleaching and simultaneous excitation of multiple fluorescence colours, QDs have gained considerable attention in the last decade in biology and medicine as novel biological agents and a valid competitor for the conventional fluorescence dyes for being applied where they have failed [155]. Conventional

fluorophores are inclined to photobleaching, which means they lose their fluorescence in a short amount of time in high-intensity studies and long-term imaging, like confocal microscopy or laser irradiation. Additionally, properties that particularly influence fluorophore behaviour, and thus their applicability to different situations, include the width of the absorption and emission spectra which makes it difficult to effectively and simultaneously detect multiple signals, photostability, and the decay lifetime [156]. QDs, in comparison, offer superior photophysical properties and several advantages over organic dyes. First, they have a broad absorption spectrum, enabling excitation by a wide range of wavelengths, and their emission spectra are symmetric and narrow (Figure 1.12). Consequently, multicolor nanocrystals of different sizes can be excited by a single wavelength shorter than their emission wavelengths, with minimum signal overlap [157].

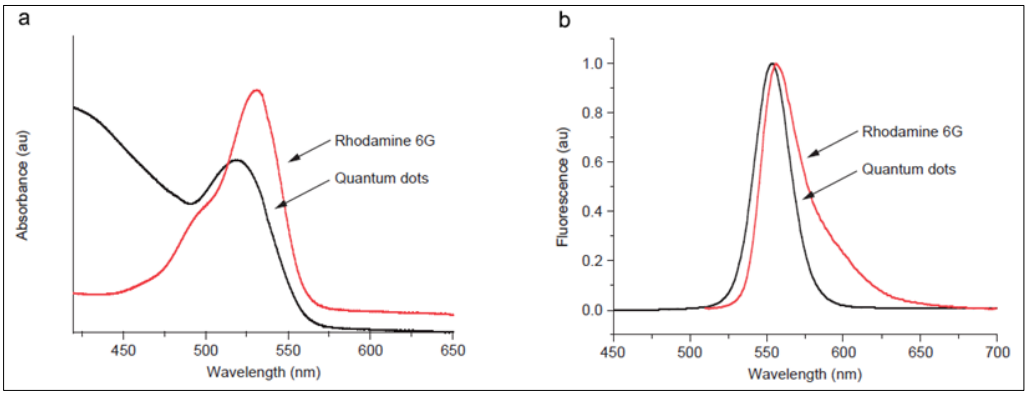

Figure 1.12: The absorption (a) and emission (b) spectra of an organic dye (rhodamine 6G, red line) and quantum dots (black line). [157]

QDs are also extremely stable light emitters, due to their inorganic composition, and can undergo repeated cycles of excitation and fluorescence for hours with a high level of brightness (10-20 times brighter than organic dyes) and photobleaching threshold. QDs have been shown to be more photostable than a number of organic dyes, including rhodamine and fluorescein [158]. Another interesting characteristic of QDs is their fluorescence lifetime after excitation, typically five to hundreds of nanoseconds, which is significantly longer than typical organic dyes or auto-fluorescent proteins that decay on the order of a few nanoseconds. The fast

fluorescence emission of organic dyes upon excitation coincides with short-lived autofluorescence background from many naturally occurring species, thus in time-gated analysis they are often disregarded to decrease background noise and increase sensitivity. Contrariwise, QDs comparatively long decay time at room temperature, enables clear temporal discrimination of the signal from cellular autofluorescence and scattered excitation light in time-gated measurements, enhancing the sensitivity [159].

Despite their several advantages, QDs applications in clinical practice are limited because of their high toxicity for the living system. Several toxicological studies have demonstrated that toxicity increases with decreasing size of the particles, generally less than 100 nm, because of its easy penetration across bio-membranes and interference with basal metabolic reactions within the cell. Also, these particles are easily translocated throughout the body not only through the circulatory system, but also the neural network (nerve cells) and they also tend to accumulate in the body that could lead to deadly diseases with the passage of time [147]. Furthermore, the presence of heavy metals, such as cadmium or lead, are the cause of toxic manifestations since they can leak out of the QDs over time, upon Ultraviolet (UV) irradiation or oxidation that potentially cause degradation of the particles and release intracellularly toxic ions. A direct way to avoid the possible toxicity of QDs is to make them well coated and so become biologically inert. Addiction of organic biopolymers (e.g. PEG) or inorganic silica (SiO_2) and ZnS shell can reduce oxidation and toxicity levels, and improve QY by passivizing nonradioactive recombination sites [160]. However, both oxidation and toxicity are unable to be totally eliminated under exposure to UV light and/or oxidative conditions [155, 161].

1.5.2. Carbon Dots (CDs)

From the beginning of this century, a new subclass of fluorescence nanoparticles called Carbon Dots (CDs) have received significant attention worldwide and provide a promising alternative to conventional toxic metal QDs in traditional fields, such as biosensing, biomedicine, bioimaging, optoelectronics, energy conversion and photocatalysis [162]. They show several advantages over the traditional QDs, including high water solubility, remarkable biocompatibility, robust chemical inertness, good thermal and optical photostability, simple and inexpensive preparation methods from renewable sources, high conductivity and abundant

functional groups and so easy surface functionalization [163]. Since when they were first discovered by Scrivens's research group in 2004 [164] as fluorescence impurities isolated from the purification of single-walled carbon nanotubes, the research interest in such carbon-based nanomaterials increased during the years as clearly showed in Figure 2.13, which report the constant increase in publishing of scientific literature studies related to CDs [165].

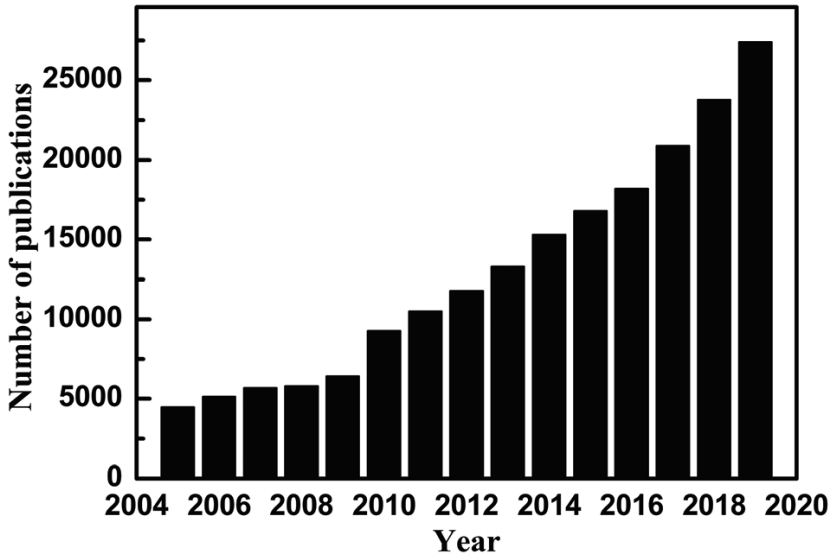

Figure 1.13: Google Scholar search results about the number of published literature studies using "carbon dots" as keyword. [165]

CDs are typically described as fluorescent carbon-based zero-dimensional nanomaterials with sizes less than 10 nm and quasi-spherical shape, consisting of a nanocrystal core (conjugated sp^2 -domains) embedded within an amorphous carbon (C) matrix, containing defects, which are stabilized by surface functional groups (e.g., carbonyl, carboxyl, hydroxyl, and amine groups). Due to this specific structure CDs show tunable physical, chemical, electronic and optical properties [166]. In general, they display a strong absorption band in the UV region (200-400 nm) and moderate in the visible range (400-700 nm). The absorption in the first UV band located around 230-280 nm is often suggested to be ascribed to the π–π^* transition of C=C bond of the carbon core, while the second band around 300-340 nm is due to n-π^* transitions of C=O surface groups. Ultraviolet–visible (UV-vis) absorption peaks at longer

wavelengths were also reported at 440-450 nm which could be associated with the trapping of excited state energy by certain surface states [167].

One of the most interesting optical properties of CDs is their tunable Photoluminescence (PL) across the entire visible spectrum. The fascinating PL phenomenon occurs upon the energetic relaxation of photoexcited electrons from a series of higher states when they return to their ground states. However, the exact origin of CD's PL and the explanations behind the mechanism responsible for that, still remain unclear and contradictory. Typically, CDs show excitation-dependent PL. This may be attributed to the surface states created on CDs, particularly the surface defects generated by surface oxidation that could trap more excitons during the excited stage and would subsequently result in radiative recombination of the trapped excitons to generate fluorescence emissions [168]. CDs have also been reported to exhibit solvent-dependent PL [169] and/or concentration-dependent PL [170]. The local pH value [171] and temperature [171] can also influence the PL properties. Relatively low QYs of CDs (approximately 0.10) compared to those of commercially organic compounds and semiconductor QDs limit the general use of CDs as luminescent materials [172]. Moreover, a majority of CDs exhibit intense emission into blue or green visible light regions under UV excitation, while the long wavelength emissions are very weak [173]. This behaviour limits their applications, especially for *in vitro* and *in vivo* biomedical tests, due to blue auto-fluorescence of biological matrix that reduces the contrast between the area tagged with CDs and the biological matrix, together with severe photodamage of UV excitation light [174]. CDs with long-wavelength emissions (far-red and near-infrared (NIR) (≥600 nm) region) are rare but more attractive for applications dealing with *in vivo* biological environment [168], especially as probes for bioimaging, thanks to their superior properties, such as deep tissue-penetration and low interference with biological tissues strong blue auto-fluorescence [175].

Numerical approaches have been developed for modulating both the absorption spectrum and PL emissions of CDs to obtain red shifts and high QYs. Degree of surface oxidation, selected precursors and/or solvents nature, especially nitrogen source, and specific synthetic routes controlling reaction temperature and time, are only some factors that have been already demonstrated to red shift CDs fluorescence [173, 176]. Several surface states mean different energy levels which may result in a series of emissive traps leading to numerous electronic

transition possibilities and diverse PL properties [177]. It has been reported that surface passivation and functionalization with carboxyl groups also help to enhance the fluorescence intensity. Among the nitrogen-containing groups, amines are known to be the best passivating agents by affecting the absorption and emission properties of CDs by modulating the HOMO (Highest-energy Occupied Molecular Orbital) -LUMO (Lowest-energy Unoccupied Molecular Orbital) gap of the aromatic C domains [178]. Moreover, the presence of small aliphatic diamine molecules has been demonstrated to increase the nitrogen content and generate surface passivation with an enhancement of the PL and QY of the functionalized CDs [179]. The isomers of phenylenediamine (pD) (*o*-, *m*-, *p*-pD) can easily lead to heterocyclic compounds and polymers by oxidation which covalently linkage onto the CDs' surface leading to improvement of PL intensity [180]. Among the pD, *p*-pD has been studied and proposed as a C source for preparing red-emissive CDs since 2015, while blue and green CDs can be prepared from *o*- and *m*-PD, respectively [180–182]. J. Joseph and coworkers [183] prepared CDs from *p*-PD by hydrothermal method for obtaining high fluorescence emission at a longer wavelength and additionally they demonstrated the potential of these red color-emitting/amine-functionalized dots for the determination of Cystine levels in human blood plasma and urine samples. Two-photon photoluminescence and excitation-wavelength-independent fluorescence are the properties of the red-emitting CDs proposed by Tan et al. [182], obtained from *p*-PD water solution with the assistance of the strong acid H_2SO_4 and tested as probes for bio-imaging. HNO_3 is the acid used from Yang's research group [184] for the hydrothermal synthesis of highly efficient red emissive CDs by using *o*-PD as C source. Their results demonstrated the importance of acid-assistance for obtaining red emissive CDs not only because the acid acts as a catalyst for the reaction rate but also could react with the polymer and affect the structure of the dots under high temperature and high-pressure conditions, with consequent effects on the optical properties.

Recent research advances proposed Hetero-atom doping as an alternative robust technology to adjust the chemical structure and optical properties of CDs. By replacing few components of the host's surface and/or interior with substitutional atomic impurities (e.g., nitrogen, boron, sulfur, phosphorus, zinc, nickel, etc.), the electronic structure related to the energy gap of the CDs is strongly influenced by introducing new energy/electronic states [185].

The impurities may be non-metal and metal ions which it is believed that affect the interaction between p- and n-states by the extent of orbital overlap and electron withdrawing/donating abilities. The introduction of extra electrons (n-type doping) or extra holes (p-type doping) determines variation in the emission may be caused by an increase in the radiative recombination of electron–hole pairs that many studies attested as origin of the observed CDs bright PL. The non-metal-based doping showed tremendous potential and, among various non-metals, Nitrogen-doping is the most adopted, due to the easy doping process and the atomic size of nitrogen comparable to C atoms. Compared to most non-metallic heteroatoms, in the metal ions there are more electrons easy to lose and unoccupied orbitals outside and larger atomic radius. Hence, the metallic heteroatom doping not only improves the optical properties of CDs giving more opportunities for changing charge density and charge transition forms between the metal ions and graphene matrix of CD, but can also impart novel functionalities [162]. For example, Zou and co-workers [186] designed gadolinium-doped carbon dots (Gd-doped CDs) for magnetic resonance imaging (MRI) and as novel agents for radiotherapy of tumors. By Gd capsulation into carbonaceous dots they overcame the intrinsic unstable characteristic and considerable biological toxicity of Gd-based compounds and at the same time they introduced for CDs a new feature of radio-sensitization. One concern for metal atom doping is the associated increase in biotoxicity that affects their potential in bio-applications [187]. In recent years, the combination of different dopants (called co-doping) has also been proposed to improve the optical properties of CDs. Barman et al. [188] demonstrated that phosphorus co-doping with nitrogen containing carbon dots (N-P-doped CDs) favors the photophysical properties (i.e. radiative decay rate and average decay time) compared to nitrogen containing carbon dots (N-doped CDs) and also boron co-doped nitrogen carbon dots (N-B-doped CDs). Although the as-mentioned CDs can emit red fluorescence, their emissions are always accompanied by intense decreases in PL intensity and QYs which limit their application in the biomedical field. Therefore, it is still a great challenge for the researchers to prepare highly efficient pure red emissive CDs with good biocompatibility [173].

1.5.2.1. CDs fabrication techniques

Another key factor in CDs development is the synthesis approach. Numerous routes have been investigated and proposed in the past decade. Generally, the manufacturing approaches can broadly be classified into two categories, namely top-down and bottom-up, which basically differ in degrees of quality, speed and cost [189].

- Top-down approach

The top-down is essentially the "breaking down" of larger carbon structure into smaller nano-size particles through hard and strong conditions. It mainly includes arc-discharging, laser ablation, electrochemical etching or chemical oxidation [190]. Both arc-discharging and laser ablation methods involve the condensation of C atoms generated from evaporation of solid carbon sources. In arc-discharge, high currents pass through opposing C anode and cathode and C atoms are evaporated by the generation of an energetic plasma of helium gas. In the case of laser ablation C nanoparticles are detached from the C target by the irradiation with a laser beam energy. All these approaches are integrally easy and with simple set-up but don't have a good control of the particle size and structure, resulting in CDs with quite heterogeneous size and many surface imperfections [191].

- Bottom-up approach

The bottom-up methods synthesize CDs from small organic molecules or polymer precursors under suitable and relatively facile conditions, such as Hydrothermal/Solvothermal (H/S), thermal combustion, template-assisted, microwave assisted pyrolysis, ultrasonic, and so on [192]. Microwave synthesis routes and H/S treatments are the most common bottom-up approaches used for CDs synthesis. In the microwave-assisted synthesis the electromagnetic energy given by the microwaves is converted into heat by the substances, allowing the reaction between the precursors and solvents, passing through the polymerization, the carbonization and finally the generation of the CDs [193]. H/S method brings to carbon-based materials by sealing in an autoclave environment a solution of selected precursors that react at high temperature and high pressure. A wide range of solvents (polar and non-polar) and organic precursors of different nature (molecular or polymeric) can be involved in the reaction path, even if water is

the green solvent widely used in hydrothermal synthesis [191, 194]. Both these techniques are cheap, eco-friendly and low-cost routes. Microwave is faster than H/S thanks to the reaction acceleration due to the microwave energy source, however the allowed reaction volumes are small and the pressure of the system is limited, limiting the use of solvents with lower boiling points [193].

Bottom-up approaches have noticeable advantages, compared with top-down methods, in producing nanostructures with less defects and more homogeneous chemical composition by controlling the deposition parameters and the careful selection of diversified organic precursors and carbonization conditions. However, with most of the bottom-up methods it is still difficult to control the morphology and size distribution of CDs since the strong surface tension of these quantum-sized particles leading to random conglomeration during the carbonization process [195]. Adopting one of the top-down approaches may solve some issues of the other techniques, even if many other drawbacks persist, including the requirement of expensive materials, severe reaction conditions, and long reaction time [196]. Thus, it is urgent to establish novel bottom-up and top-down methods that can provide an opportunity to fabricate CDs with defined morphology and properties [195].

1.5.2.2. CDs for biomedical applications

Biocompatible CDs appear to be the new promise in nanomedicine and healthcare applications (Figure 1.14). They have demonstrated that they are safe for both *in vitro* and *in vivo* studies and a wide range of cells, even in the case of bioimaging when high concentrations are required. Moreover, CDs can be rapidly excreted from the body, thanks to their ultrasmall-scale, without any significant alterations of many biochemical tissue parameters [197]. Efficient and smart bioimaging tools are extremely useful for an early diagnosis of diseases. Over the past decades, Fluorescence Imaging (FI) has emerged as a potential method for medical diagnosis due to its low cost, easy operation and non-invasiveness.

Among various fluorescent probes, CDs emerged as a next-generation probe for *in vitro* and *in vivo* bioimaging thanks to unique properties, such as good photostability, excellent biocompatibility, water solubility, and multicolor emission [166]. The scientific literature is full of studies about the use of CDs as fluorescent bio-probes for photomediated imaging and their

wide versatility and superiority to conventional fluorophores in biomedical and healthcare fields. As shown in the work of Jiang et al. [180], full-color emissive CDs were developed by using Phenylenediamines as precursors, and the as-prepared CDs could emit bright and stable red (*p*-PD), green (*o*-PD) and blue (*m*-PD) colors of luminescence and work as multiplexed cell bioimaging reagents. Eco-friendly multi-functional nitrogen/sulfur co-doped CDs were developed by Wei et al. [198] by hydrothermal treatment of *Allium fistulosum*. They showed great biocompatibility and were explored for multicolor imaging in MCF-7 and K562 cell cytoplasm, without adoption of any surface passivation. In addition to the CDs' intrinsic properties as new platforms for FI, their elevate photonic performances have been applied in many other nanomedicinal and healthcare applications. For example, Yang et al. [199] proposed Mg-doped CDs as a new kind of osteogenic biomaterials for promoting osteoblastic differentiation by improving alkaline phosphatase (ALP) activity and upregulation related mRNA expression and maybe promising nanodrugs for bone loss therapy. Moreover, due to the multicolor fluorescence properties the as-mentioned Mg-CDs showed cell labeling abilities. N-S-co-doped red-emitting CDs were synthesized by a green and facile hydrothermal method by Sun's group [200]. The doping with N and S created functional groups on the dot surface by giving a unique behaviour for rapid identification and quantification of Ferric ions (Fe3+ ions) and L-cysteine (L-Cys) traces in the human body, mainly involved in biological processes that lead to various diseases. Unlike the as-mentioned works, Zhang and co-workers [201] followed a novel green microwave-assisted method for CDs synthesis. Essentially, they prepared red-emissive CDs by an easy carbonization of *p*-PD in an ethanol/H_2O solution by microwave irradiation. The CDs were used first as fluorescent chemosensors for the detection of glutathione (GSH). Furthermore, they discovered that the CNDs–GSH mixture could be utilized as a "turn-on" fluorescence sensor (off–on) for the determination of temperature through the fluorescence quenching and recovery processes, respectively. The GSH interaction with the surface group on CDs quenched the fluorescence, but this interaction could be destroyed by increasing temperature and the quenched fluorescence could be recovered. A novel "turn-on" carbon-dot-based fluorescent nanothermometer device and a perfect candidate for cellular imaging and temperature sensing at a molecular level was developed.

In recent years, the extraordinary optical/physicochemical properties and unique biocompatibility with low toxicity have guaranteed to CDs promising applications not only for bioimaging, chemical sensing, fingerprint detection and so on, but also as new non-invasive agents in cancer diagnosis and treatment [202]. The integration of diagnosis and therapy into a single nanoplatform, so called Nanotheranostics, have attracted growing interest for cancer treatment. In comparison with traditional anticancer models, this integration makes it possible to collect more detailed information and monitor the metastasis and relapse of tumor to obtain high therapeutic efficacy [203]. A tumor microenvironment (TME) stimuli-responsive nanoplatform for FI and cancer therapy was developed by Prof. Hengwei Lin's group [204]. Red-emissive CDs were first derived from citric acid and PEG through a facile one-pot solvothermal method. The incorporation of the photosensitizer Chlorine e6 conferred them a superior photostability and bright red emission, guaranteeing an efficient cell penetration and excellent TME stimuli-responsive for FL imaging. Furthermore, the introduction of Cu^{2+} provided Photodynamic therapy (PDT) functions which can destroy tumor cells just reacting with hydrogen peroxide (H_2O_2) and enhanced the production of cytotoxic reactive oxygen species (ROS). Therefore, doping transition-metal (e.g. Cu, Fe) into carbon dots can widely increase their near-infrared absorption and thus allow their applications in photodynamic and photothermal cancer therapy. Recently, Yue et al. [205] fabricated ruthenium-containing carbon dots (Ru-CDs) via the partial pyrolysis of ruthenium complexes and the carbonization of citric acid. The as-prepared Ru-CDs exhibited interesting features as bioimaging agent for cancer cells and zebrafish thanks to the good biocompatibility and strong red luminescence in aqueous solution. They also acted as photodynamic nano-agents for cancer therapy due to the efficient ROS generation. Finally, their results showed that Ru-CDs and light can damage plasmid DNA, giving to the doped-CDs good prospects and wide range of biological applications. Although in-depth studies on CDs have gained rapid development, numerous unsolved issues are still a big challenge for researchers. For this reason, further studies on CDs in terms of their basic studies (chemo-physical properties, optical properties and photoactive capability) and practical applications will continue to be a hopeful and challenging field for the future [206].

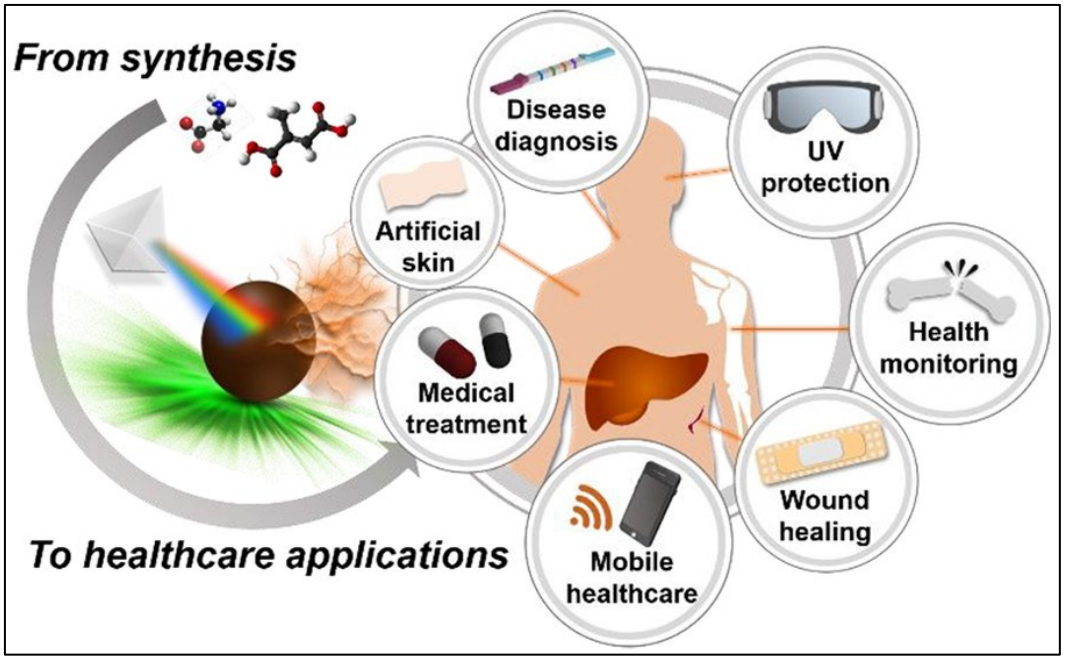

Figure 1.14: CDs in various Biomedical and Healthcare Applications. [166]

CHAPTER 2

GENERAL MOTIVATION AND AIM OF THE PROJECT

2.1. Overview

On 16th October 2021, the European Commission approved a motion about the urges of plans and actions "to accelerate the transition to innovation without the use of animals in research" [207]. Starting from 2010, one of the main goals of the European Union (EU) is the gradual phasing out the use of animals for scientific purposes by following the 3Rs principle of Replacement, Reduction and Refining. Currently, the use of animals in research still remains necessary since non-animal methods are not yet available across all scientific research areas. For this reason, the Reduction of the number of animals used to obtain precise information, and the Refining as "to reduce to a minimum value the amount of stress imposed on animals in each experiment", remain the only two options to minimise the impact of the use of animals in scientific procedures [208, 209].

As already mentioned in Chapter 1, i*n vitro* technologies and applications of *in vitro* models have received an exponential increase in the last decade. Scaffold-based platforms and bioreactors are driving the global market of 3D cell culture and their application is expected to rise by the end of 2026 (Figure 2.1). Over the past 10 years there was a remarkable increase in the use of 3D polymeric scaffolds, particularly for cancer cell culture [210]. The state-of-the-art has shown that the tumor microenvironment is complex and dominates cancer cell behavior with tumor formation, progression, and metastasis [211]. Understanding the connection between tumors and the

microenvironmental conditions and correctly mimicking *in vitro* the complexity of the tumor microenvironment, represent fundamental aspects for the development of more realistic *in vitro* models for drug-screening and cancer biology studies [212, 213]. 3D scaffolds applied in biomedical and cancer research are predominantly fabricated by using synthetic polymers, such as PLGA, PCL, and PEG. Here are some examples of polymeric scaffolds used as tumor models in the last years. Nowadays, breast cancer is one of a few cancers for which an effective prevention, detection, and treatment is available. However, it is still a major cause of cancer-related mortality in women worldwide [214]. Rijal et al. [215] have cultured mammary epithelial cells on PLGA or PCL scaffolds fabricated by using a modified GF approach. They observed a distinct behaviour of the breast cancer cells in terms of morphology, proliferation, responses to anticancer drugs and also development into tumors compared to those cultured on 2D polymeric surfaces. More recently, Puig and colleagues [216] suggested electrospun-PLA scaffolds as suitable 3D supports for Triple-negative breast cancer cell culture in short culture periods with no breast cancer stem cells-enrichment. Among the numerous cancer types already studied, only a small proportion of patients with brain cancer (glioblastoma) achieve 5-year survival. Furthermore, glioblastoma tumor cells quickly become resistant to current chemotherapies and radiation techniques [217]. In order to create this lethal tumor in *in vitro* environment for improving studying on molecular mechanisms of cancer development, identifying therapeutic targets, and testing drug candidates, Kievit et al. [218] have produced chitosan-alginate 3D scaffolds and developed an artificial *in vitro* model for studying the tumor microenvironment. They showed how altering the tumor microenvironment *in vitro* affects tumor growth and malignancy and alters the expression of glioblastoma stem-like cell markers that play a significant role in tumor aggressiveness and progression. Despite the progress in utilizing 3D models for studying cancer cell biology and screening/testing of potential anticancer drugs, developing a 3D tumor model that more closely mimics the *in vivo* tumor microenvironment, particularly for rare tumors, remains a formidable challenge and unsatisfied need [219].

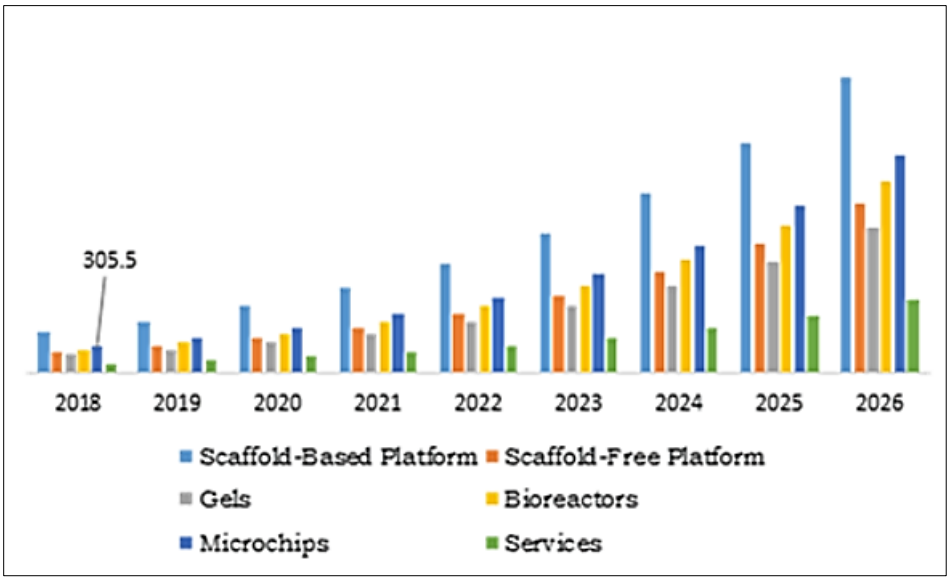

Figure 2.1: 3D in vitro cell culture market trend, by product (*https://www.researchdive.com/73/3d-cell-culture-market*)

The use of bioreactor devices is also a promising approach for long-term *in vitro* cell culture enabling high-throughput screening in drug development and toxicity tests [220]. Compared to the different existing bioreactors, in the perfusion mode higher cell density is sustained for much longer periods, by constantly feeding fresh media and by supplying the appropriate nutrients and removing toxic waste products. Within the pharmaceutical industry perfusion bioreactors represent a valid platform to overcome the common drawbacks to study *in vitro* drug efficacy and toxicity, by offering the closest *in vitro* model of natural physiological state, lightening the problems of the 3D static culture, maintaining 3D architecture and extending the functionality, heterogeneity, structural complexity and cell-cell interactions during the dynamic culture [221]. For example, a novel perfused bio-fabricated 3D ovarian cancer spheroid model was designed in Woodfield's lab [222] to demonstrate the potential of perfusion system for anticancer drug screening and the capacity to support *in situ* non-destructive computer tomography imaging. Starting from a 96-well microplate, the 3D printed bioreactor can support a large number of samples at the same time, and guarantee both fluid transport and mechanical stimulation on the constructs. A perfusion microbioreactor was realized by Huber and coworkers [223] using 3D

printing technology. The system consists of up to four independent-operating parallel bioreactors and integrated microsensors to measure the oxygen concentration during the cultivation period. In addition, an automated cell seeding procedure facilitates the distribution of cells within the scaffold before the culture. More recently, Talò G. et al. [224] developed and validated a perfusion bioreactor to culture decellularized tendon matrices after cell reseeding. Multiple independent chambers are able to combine a bidirectional perfusion with a programmable uniaxial strain to obtain a local alignment of the new collagen fibers.

2.2. Aim of the project

Despite the continuing advancements in the field, there remains a constant need to develop, enhance and implement *in vitro* systems [225]. The use of bioreactors in the pharmaceutical industry, especially for drug pre-screening testing, is still one of the big challenges for researchers. The combination of perfusion systems for 3D dynamic cell culture, and the generation of engineered new constructs, with the investigation on toxicity and drug-sensitivity using a single system could represent the next generation of *in vitro* technologies.

The principal aim of this research project is to develop a low-cost and compact *in vitro* apparatus that could be used for multiple purposes in both biomedical and pharmaceutical areas by reducing as much as possible the *in vivo* animal experimentations. An original dual-flow perfusion bioreactor is proposed as a potential candidate for stimulating *in vitro* diffusion of nano-systems throughout microporous matrices emulating the *in vivo* path of nutrients, growth factors or drugs in living organisms. To achieve this, polymeric porous scaffolds were also developed as perfect supports for 3D cell culture, together with the synthesis of promising nano-systems as future drug carrier models.

2.3. Experimental objectives

The thesis is based on 5 main experimental objectives:

- Synthesis and characterization of different polymeric microporous scaffolds to be used as 3D *in vitro* supports for cell culture and diffusion of nanoparticles.
- *In vitro* 2D and 3D cell culture to select the best scaffold structure acting as a model for growth and proliferation of living cells, particularly tumor cells.
- Design and fluid-dynamic characterizations of a dual-flow perfusion bioreactor, with a particular attention on its radial perfusion properties.
- Testing of the radial diffusion generated by the bioreactor throughout microporous matrices by using nanoparticles of different nature as potential nano-carriers.
- Synthesis and characterizations of Red-emitting Carbon Dots to be used as fluorescence probes for bioimaging/tumor tracking, biosensor or carriers for drug-delivery.

CHAPTER 3

MATERIALS AND METHODS

3.1. Part 1: Production and characterization of PLLA scaffolds

3.1.1. Scaffold for *in vitro* cell tests

PLLA (Resomer® L 209 S; supplied by Evonik Health Care) was chosen as a biopolymer to produce 3D porous scaffolds (Figure 3.1 A) and the adopted technique for the synthesis was the TIPS. Firstly, a ternary solution of PLLA-dioxane-water (polymer-solvent-nonsolvent) was prepared as described in Lombardo et al. (2019) [226]. The polymer at 4% (wt/wt) was dissolved into 1,4 dioxane (Merck KGaA, Darmstadt, Germany) by stirring at a temperature of 120 °C. After a complete dissolution, deionized water was added dropwise with a constant dioxane to water weight ratio of 87/13 (Step I). The final transparent solution was kept at 60°C. Next, 5 mL of the hot solution was poured into a High-Density Poly-Ethylene (HDPE) cylindrical sample holder (Figure 3.1 B) (inner diameter 17.6mm and 35.7mm height) that was immersed into a thermostatic water bath (TWB) at a well-defined temperature (demixing temperature), for a specific time interval (demixing time) (Step II). Subsequently, a quench by direct pool immersion at -20°C in an ethyl alcohol bath (EAB) was performed (Step III). The as-obtained foams were washed in deionized water and dried at 35°C under vacuum overnight, in order to completely remove any remaining solvent trace.

To obtain different porous structures, batches of scaffolds were prepared by varying demixing temperature and demixing time. A schematic representation of the steps followed for the

scaffold synthesis is provided in Figure 3.1 C. In the first case (Fig. 3.1 C, case 1), two demixing temperatures were investigated, 25 °C and 30 °C, keeping a constant demixing time of 30 min. In the second case, the sample-holder was directly placed at -20°C in a EAB for 20 min and subjected to Direct Quench (DQ) (Fig. 3.1 C, case 2); as reported in previous papers, according to this experimental route a spinodal decomposition takes place that deeply modifies the scaffold microstructure [227, 228]. Finally, in order to slow down the cooling rate and consequently control the scaffold porous structure, in the third case PLLA scaffolds were synthesized by using a demixing time of 20 °C and a demixing time of 15 minutes by embedding the sample holder in a Polytetrafluoroethylene (PTFE) shell (coating) for the immersion in the TWB and/or in the EAB (Fig. 3.1 C, case 3 a,b,c).

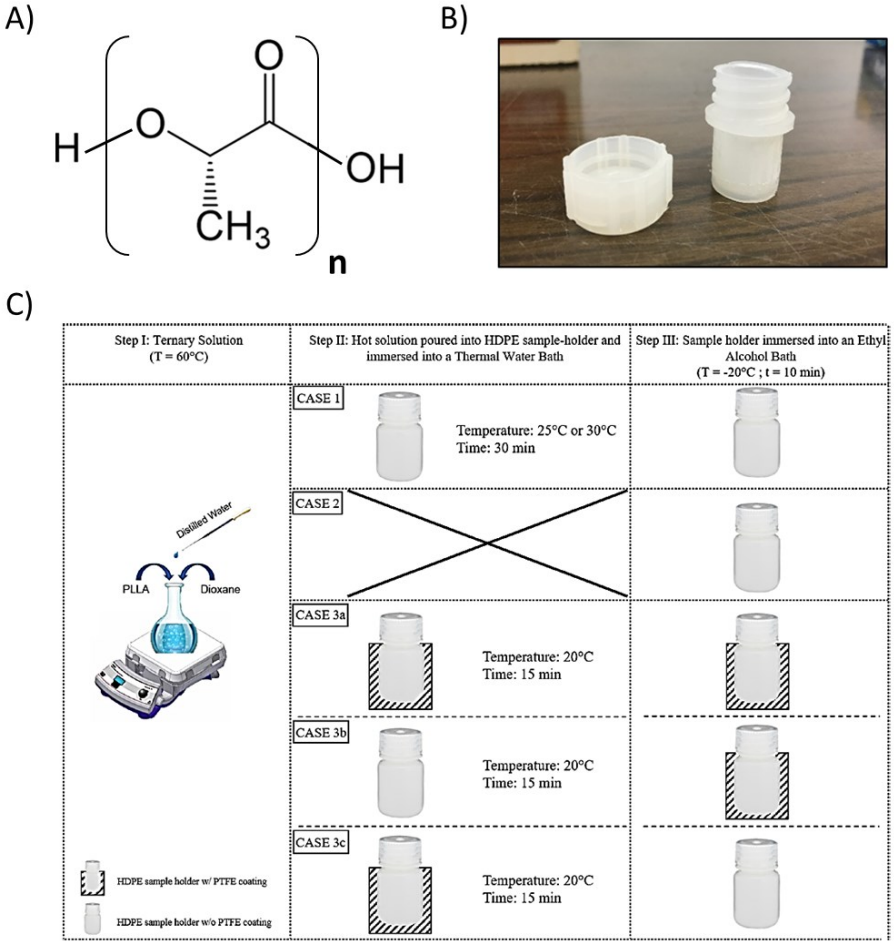

Figure 3.1: A) Chemical structure of PLLA. B) HDPE cylindrical sample holder. C) Schematic representation of the steps adopted for scaffold preparation via TIPS. [226]

3.1.2. Cylindrical 3D Scaffold for perfusion testing with the Bioreactor

In order to obtain an engineered construct that simulates a natural vascularised biological tissue, a double-structured polymeric scaffold was produced. It consists of a cylindrical porous matrix that is able to host cells. The inner structure, that emulates a blood vessel, is a porous tubular-shaped scaffold obtained via DIPS after a dip coating, around a support with a diameter of ~2 mm. Both Polypropylene (PP) and stainless steel AISI 316 supports were tested. Briefly, the support was first immersed into a homogeneous PLLA/dioxane (PLLA 8% wt/wt) solution kept at 30°C (dip coating bath, Figure 3.2i, left). Then, the support was slowly pulled-out from the solution

at a rate of 10 cm/min and immersed quickly into a second bath, at the same temperature, containing distilled water (DIPS bath, Figure 3.2i, right). During this step, a L-L phase separation and/or polymer crystallization is induced by the diffusion of the solvent from and to the casted solution that changes its composition [95]. Finally, the support was extracted from the bath and the samples were desiccated in an environment with controlled humidity for 24 h. Subsequently, the as-prepared vessel-like scaffold was incorporated into a 3D matrix by performing a TIPS around the vessel. The ternary solution described above, initially kept at 60°C, was hot poured into an "*ad hoc*" cylindrical Al sample holder shown in Figure 3.2 ii [229]. It consists of an empty cylinder with an outside diameter (OD) of 3.5 cm and height (H) of 4 cm, with a cover that perfectly closes off the system, thus preventing the communication between the inside and the outside environment. Both the base of the central hole cavity (internal diameter (ID) = 2.8 cm, H = 1.8 cm) and the cover incorporate a 0.2 cm hole, which allows fixing the support bringing the tubular-shaped scaffold. By pool immersion of the sample holder into a TWB, the temperature of the system was suddenly lowered to 0°C and kept at this temperature for 10 min. Afterwards, a quench by immersion in an EAB was performed for 20 min. Lastly, the polymeric structure obtained was removed from the sample-holder and also the support was gently pulled out from the foam. The sample was finally washed in deionized water for 24 hours and dried under vacuum overnight.

The morphology of all the as-obtained samples was analysed by SEM (Phenom ProX, Phenom-World, The Nederland) operating at an accelerating voltage of 10.0 kV. The dried samples were kindly cut crosswise into smallest pieces (thickness of around 0.5 cm) with a surgical scalpel. Then, they were mounted on a metal stub using a C tape and finally coated with gold (thickness ~4 nm) in a sputter coater under argon atmosphere for increasing the conductivity. The average pore size was determined by image analysis on the SEM micrographs using Image-J software.

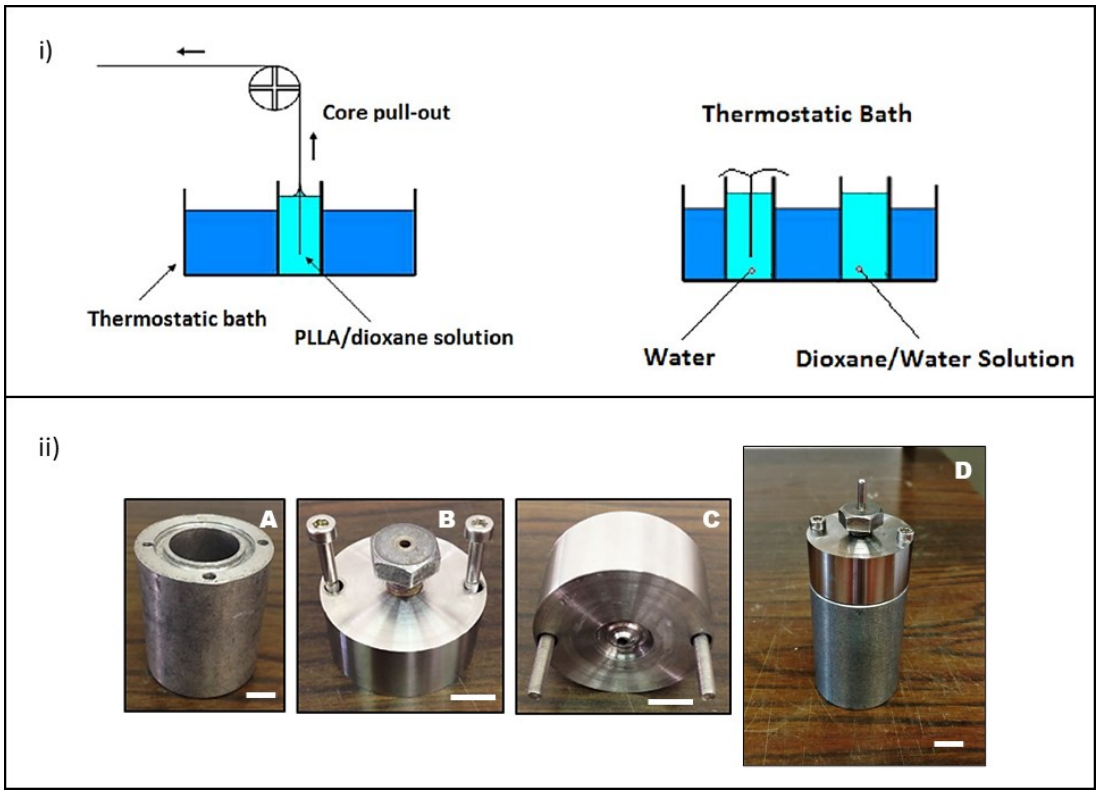

Figure 3.2: (i) Schematic illustration of dip-coating process (left) and a DIPS bath (right) [95]. (ii) Al sample holder for tubular scaffold production via TIPS: body (A), cover top view (B), cover bottom view (C), sample holder assembled (D). Scale bar 1cm. [229]

3.2. Part 2: Dual-flow perfusion bioreactor design and set-up

3.2.1. Bioreactor design

In this work, a novel dual-flow perfusion bioreactor was implemented and optimized. It is basically composed of two glass-made cylindrical tubes (a main column and a bubble column) connected to each other. As shown in Figure 3.3i, the main column presents an ID of 3.6 cm and H of 21 cm. A glass tube (ID = 0.5 cm and H = 3.5 cm) is located at the base of the column and allows fixing the bottom of the scaffold. The lid of the column is characterized by a unique configuration (Figure 3.3i A-B). A central hole is present through which a thin glass tube (ID = 0.5 cm) is inserted to block the upper part of the scaffold. The distance between the upper and

lower glass tubes can be adapted to accommodate scaffolds with different heights. In addition, a grid was realized inside the lid to break the bubbles generated during the recirculation of the culture medium, thus preventing foaming and leaking of the medium outside the device. The bubble column is a smaller glass tube (ID = 1.2 cm and H = 15 cm) that is connected to the main one and works as a conventional bubble column (Figure 3.3i).

The singular configuration of the device allows a separate control of two perfusion flows: the Inner Perfusion Circuit (IPC) and an External Perfusion Circuit (EPC). The IPC (Fig. 3.3ii, left) consist of the main column that works as a culture chamber and where the hollow cylindrical scaffold is located. To connect the scaffold to the two glasses tubes, standard biocompatible PP Luer-Lock connectors with 0.15 cm ID tubing were used (Figure 3.4). The fresh culture medium is pumped inside the lumen of the scaffold, from top to bottom, by a syringe pump (New Era Single Syringe Pump NE-1000) which allows infusion rates from 0.73 μL/hr to 2100 mL/hr and with a dispensing accuracy of +/-1%. A pipe system with silicone tubes (ID = 0.55 mm, OD = 0.65 mm) carries the medium from the pump to the top of the main column.

The EPC (Fig. 3.3ii, right) is integrated in the bubble column that is connected to the main column and to a peristaltic pump (Model M025; VerderFlex) by means a silicone tube (ID = 0.2 cm) and a syringe membrane filter (0.22μm) for the inlet air helping to maintain a good sterility of the system. The air bubbles rise through the column, and drag part of the liquid to the main column, thus allowing a recirculation of the medium. In addition, the gas phase that is bubbled vertically through the liquid phase promotes the gas–liquid mass transfer, as in a conventional bubble column [230], thus improving the oxygenation of the medium. The equipment was sterilized by steam autoclave and the apparatus was assembled under sterile conditions in a laminar flow biosafety cabinet. During operation, the entire system was placed in a standard cell-culture incubator at 37°C in a humidified atmosphere of 95% air and 5% CO_2 to maintain constant operating conditions for the future cell culture tests.

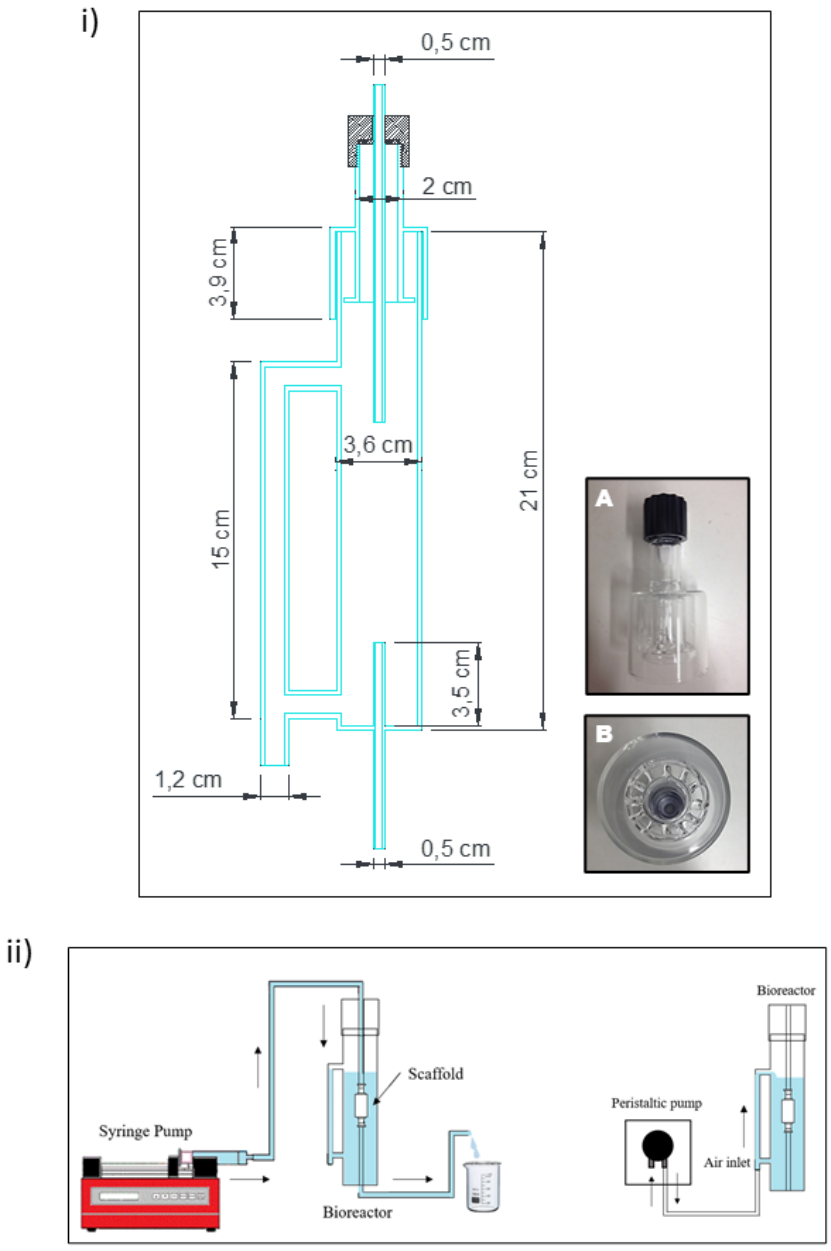

Figure 3.3: (i) Scheme and dimensions of the main column and the bubble column of the dual-flow perfusion bioreactor. (A) Photograph of the glass lid; (B) Bottom view of the glass lid. (ii) Scheme of the IPC (left) and the EPC (right). [229]

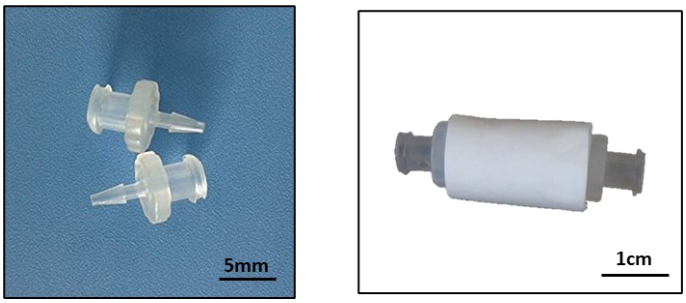

Figure 3.4: PP Luer-Lock connectors (left); real picture of tubular PLLA scaffold assembled with the connectors for being fixed inside the bioreactor (right).

3.2.2. Fluid-dynamic characterizations (IPC and EPC)

Upon completion of the device construction, evaluation of bioreactor fluid dynamics was carried out. An IPC flow analysis was first carried out to determine the best operating medium flow rate inside the lumen of the scaffold by evaluating the flow regime and the shear stresses on the lumen wall. For each flow rate delivered by the syringe pump, fluid velocity and Reynolds number were estimated. The shear stresses (dyne/cm^2) on the lumen surface were calculated by using the Hagen-Poiseuille equation (Eq. 3) which directly links the shear stress to the flow rate by considering a stationary laminar flow of an incompressible Newtonian fluid in a long rigid pipe with inelastic walls:

$$\tau = \frac{4*\mu}{\pi*r^3} * Q \qquad \text{Eq. 3}$$

where Q is the volumetric flow rate (cm^3/s), μ is the viscosity of the medium (Pa*s) and r is the radius of the lumen of the scaffold. An EPC flow analysis was also assessed to precisely control the air and liquid flow rates only by varying the RPM (revolutions per minutes) of the pump. The air flow rate was measured by using a bubble soap flowmeter shown in Figure 3.5. Briefly, the main column was connected to a volumetric glass tube containing a small amount of liquid soap on the base. While the peristaltic pump guarantees air circulation through the system, a flat soap bubble is interposed in the air flow path moving from one volume mark to another. Usually, the travel time of each single soap film can be measured with a stopwatch and together with the known

tube volume allow to directly calculate the flow rate. Here, I measured the distance covered by the rising bubble generated by the water soap solution after 1 minute, and consequently I were able to determine the air volume. A varied range of RPM (from 27 to 110) for the peristaltic pump was evaluated. This analysis was carried out for both empty (Figure 3.5A) and liquid-filled bioreactor (Figure 3.5B). Furthermore, the volume of liquid dragged in the main column by the rising air bubbles in the bubble column was also evaluated in order to confirm a good and uniform oxygenation and supply of nutrients to cells seeded in the scaffold. For this test, the main column was connected to a larger diameter reservoir which kept constant the liquid level inside the main column during the measurements (Figure 3.5C). The liquid volume dragged in 1 minute was collected in a silicone box and measured by weighting. A working range between 27 and 85 RPM for the peristaltic pump was investigated. The results were expressed as mean ± standard deviation (SD).

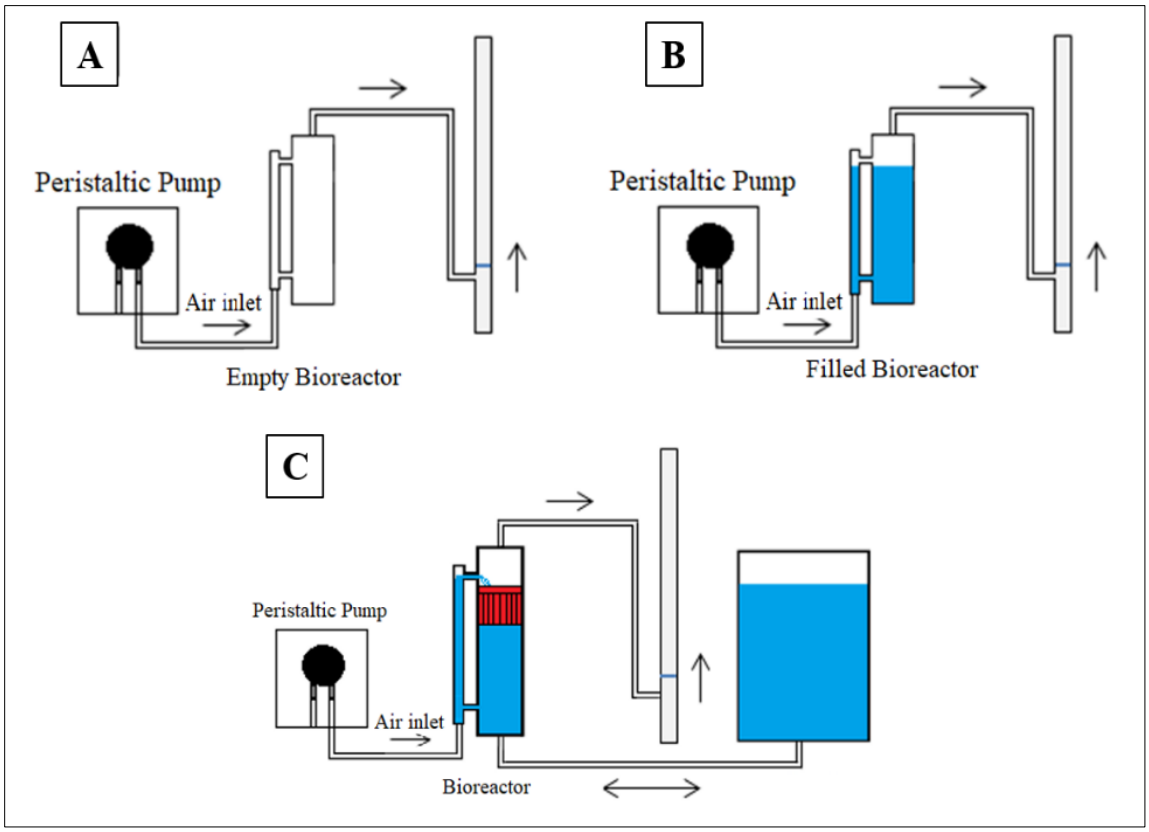

Figure 3.5: Illustration of the system used for the air flow rate investigation. The operations were conducted for both the empty (A) and filled (B) bioreactor. (C) Schematic diagram of the system used for liquid flow rate analysis. [229]

3.2.3. Perfusion system characterization

For evaluating the efficacy of the perfusion system of the bioreactor and the potential of the device to manage the direction path of the radial flow throughout a 3D microporous matrix, permeability tests were performed. First a qualitative test was carried out adding an organic dye (toluidine blue) to the deionized water (0.1% v/v) in order to visibly observe the staining of the scaffold. A known volume of the aqueous solution (60 mL) was pumped inside the lumen of the scaffold with a constant flow rate of 1 mL/min which corresponds to a superficial linear velocity of 10 mm/s. After 30 minutes, the cross-sections of the as-treated scaffold were observed both macroscopically and under stereo-microscope (Euromex, Holland).

To investigate the possibility to control the radial perfusion, in terms of flow direction and flow rate, a second test was performed. Via the IPC, deionized water at a constant flow rate (0.5 ml/min and 1 ml/min) was dispensed by a syringe pump (New Era Single Syringe Pump NE-1000) inside the lumen of the scaffold located inside the water-filled main column. The water coming out from the circuit was weighted at specific time points. The radial flow through the scaffold was calculated by subtracting the mean weight of the water outflowing from the syringe pump (measured independently previously) from the mean reading of three measurements. Several tests were conducted by varying the height level H defined as the distance between the bottom of the scaffold and the outlet of the IPC tube, and depicted in Figure 3.6. Five different levels were investigated with ΔH of 5 centimeters among each level. The distance between the outlet of the IPC tube (S2), and the bottom of the scaffold (S1) was assumed as Level 0. The resulting values were plotted by using Origin Lab Software.

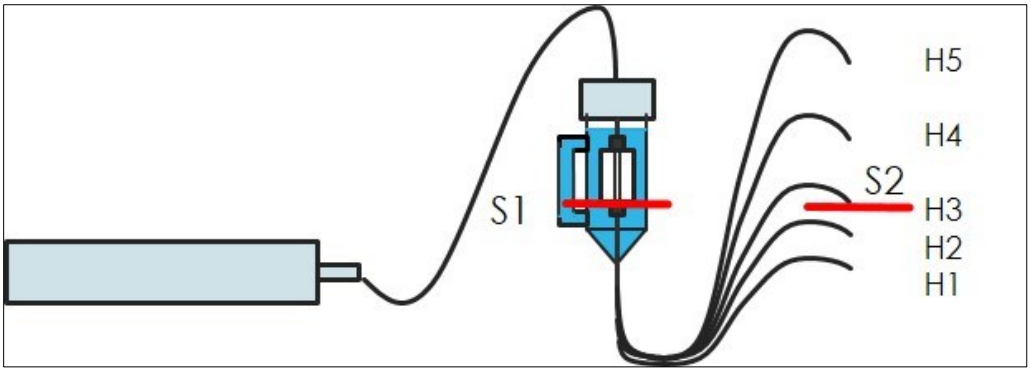

Figure 3.6: Experimental apparatus for efficacy of perfusion system. The level S1-S2 was assumed as Level 0. [229]

3.3. Part 3: 2D and 3D *in vitro* cell culture

3.3.1. Cell culture and scaffold seeding

Human invasive breast cancer cell line MDA-MB 231 was grown in high-glucose (4.5 g/l) Dulbecco's modified Eagle's medium (DMEM) supplemented with 10% (v/v) FBS (Euroclone,

Celbar), 100 units per ml penicillin G, 100 µg ml-1 streptomycin (Euroclone, Celbar) and 2 mM L-glutamine (Euroclone, Celbar). The cells were cultivated at 37°C, in a humidified atmosphere of 5% CO_2 and maintained in sterile conditions. For the 2D culture, cells were grown in tissue culture Polystyrene (PS) T-flasks inside a conventional cell-culture incubator. Instead, the 3D culture was performed by using the as-prepared PLLA scaffolds as support. As a preliminary study, a static culture was carried out to select the best scaffold morphology allowing to reproduce a tumor microenvironment. After being cut into 6 mm diameter (2 mm thickness) circular discs, the scaffolds were sterilized by immersion in 70% ethanol overnight under vacuum. Then, the samples were washed several times with Phosphate buffered saline (PBS) by shaking at 100 rpm on an orbital shaker to remove any remaining ethanol traces. This was followed by a pre-treating the scaffold with acidic type-I collagen solution to improve cell adhesion on the hydrophobic polymeric structure. After achieving a confluence up to 80%, cells were trypsinized, counted by a hemocytometer and 4 x 10^4 cells were seeded on each scaffold placed inside 12-well plates. The PLLA discs were incubated for 1 h in 100 µL DMEM to allow cells to migrate through and adhere to the porous structure. Then the samples were immersed in 1 mL DMEM and incubated at 37°C with 5% CO_2 for 14 days with regular media changes.

3.3.2. Cell viability and proliferation rate

The cell viability and proliferation rate were evaluated with the CCK-8 assay at several time points during the incubation period. For the assessment, samples were incubated for 3 hours at 37°C in 10% CCK-8 reagent solution in fresh DMEM in order to permit its reduction by mitochondrial dehydrogenases of the living cells into soluble formazan dye that is directly proportional to the number of living cells. After this period, 100 µL of the reagent solution was transferred to a 96-well plate and the absorbance at a wavelength of 460 nm was measured using a microplate DU-730 Life Science spectrophotometer (Beckman Coulter). The viability was expressed as percentage respect to the negative control (100% of cell viability). A blank scaffold without cells was used as control. Three parallel replicates were read for each sample for a statistical evaluation.

3.3.3. Cell migration inside the PLLA scaffold

Cell migration and distribution inside the 3D porous polymeric matrix were investigated. At different time points the samples were rinsed twice with PBS and then treated with 100 mL of 10% formaldehyde for 30 min for cell fixation. After washing three times with PBS, few drops of 4',6-diamidino-2-phenylindole (DAPI; Sigma Aldrich) (dilution of 1: 10000 in water) were added to each scaffold and kept for 5 min at room temperature in the dark for cell nuclei staining. The cell morphology was observed under a fluorescence microscope (Leica DM 2500, Leica MicroSystems) equipped with a charge-coupled device camera. All tests were performed in duplicate.

3.3.4. Cell morphology

The evaluation of cell morphology was performed by SEM analysis. Cell-seeded scaffolds were fixed in a 50/50 (v/v) solution of 4% glutaraldehyde in 1X PBS at 4 °C for 30 min. Samples were then dehydrated in a series of ethanol washes (15%, 35%, 50%, 70%, 95%, and 100%), dried and covered with gold under Argon atmosphere using a sputter coater. The images were obtained from the FEI VERSA 3D (FEI) SEM microscope.

3.4. Part 4: Diffusion tests and biocompatibility of nanoparticles

In this work, two different types of nanoparticles were used as models for fluorescent drug/colloidal carriers. The synthesis of the tested nanoparticles, characterized by different chemical, physical and optical properties, are reported below.

3.4.1. Polymeric Fluorescent Nanoparticles (FNPs)

Professor Gennara Cavallaro's research group (Laboratory of Biocompatible Polymers, Department of "*Scienze e Tecnologie Biologiche, Chimiche e Farmaceutiche*" (STEBICEF)) of the University of Palermo, synthesized Polymeric Fluorescent Nanoparticles (FNPs) starting from the multifunctional polymer α,β-Poly(N-2-hydroxyethyl)-D,L-aspartamide (PHEA). Fluorescent

amphiphilic graft copolymers were first synthesized by covalently linking on PHEA other three molecules: Rhodamine B (RhB) moieties, PLA and PEG chains [231, 232]. The chemical structure of the obtained PHEA-RhB-PLA-PEG copolymer is reported in Figure 3.7A. The graft copolymer was used to realize FNPs by following the well-known high-pressure homogenization (HPH)-solvent evaporation method [233]. Finally, the FNPs were diluted with NaCl aqueous solution to obtain an isotonic aqueous dispersion (milli-Q water with 0.9% NaCl) at a concentration of 0.1 mg/ml.

3.4.2. Nitrogen-doped Carbon Dots (N-CDs)

N-CDs were developed and characterized by Professor Fabrizio Messina's research group (Physic and Chemistry Department- Emilio Segrè) of the University of Palermo. The N-containing CDs are composed of a hexagonal β-C3N4 crystalline core structure and a high amount of amide groups grafted on the surface (Figure 3.7B). The nanoparticles were synthesized by microwave-induced decomposition of an aqueous solution of citric acid and urea in a standard household microwave oven [234].

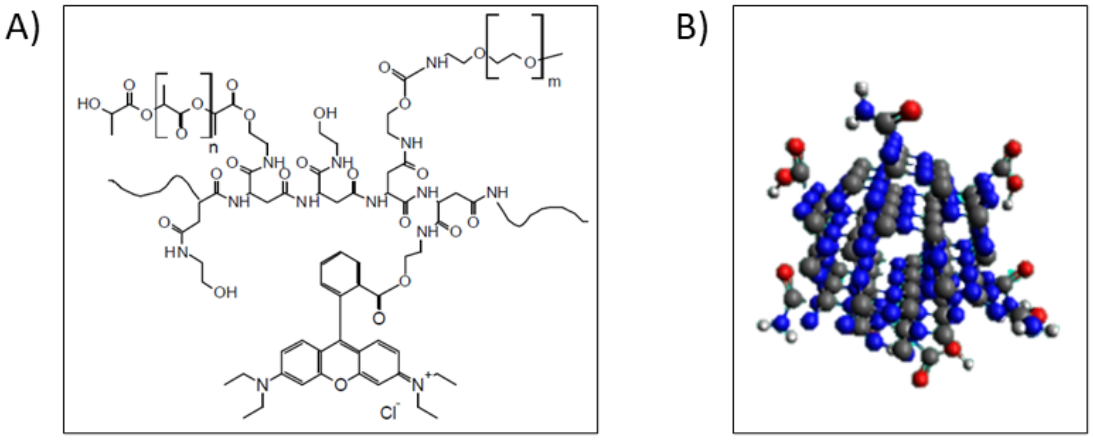

Figure 3.7: (A) Chemical structure of PHEA-RhB-PLA-PEG graft copolymer (m=44, n=194) [235]; (B) Crystalline structure of a hexagonal β-C3N4 core of N-CDs (Figure adapted from [236])

3.4.3. Diffusion testing

A diffusion test was carried out to study the ability of the apparatus in the distribution of the drug colloidal carriers inside a 3D polymeric scaffold. Firstly, a fixed volume (40 ml) of an isotonic aqueous FNPs solution at a concentration of 0.1 mg/mL was pumped inside the lumen of the scaffold, with a constant flow rate of 1 mL/min. To ensure a complete permeation of the entire scaffold volume and a diffusion of the solution till the external surface of the construct, the circulation loop was repeated three times. Afterwards, the scaffold was extracted from the bioreactor, dried overnight at room temperature and processed for further analyses. Different cross sections were prepared as described above and observed by SEM to verify the presence and distribution of the FNPs among all the polymeric matrices. Three areas were focused: lumen surface, polymeric matrix close to the lumen and polymeric matrix far from the lumen. Other dried cross sections were used for the fluorescence analysis. After locating on a standard glass microscope slide, they were observed with an inverted fluorescence microscope (Leica DM 2500) equipped with a charge-coupled device camera. A 530-550 nm band-pass excitation filter was selected for detecting the red emission of the organic dye Rhodamine B and blocking any possible green emission. Both a qualitative and a quantitative analysis were performed for studying the FNPs radial distribution into the scaffold. The fluorescence distribution was qualitatively evaluated for 4 regions (moving from the lumen to the external surface) of the polymeric matrix.

The fluorescence images were also used for the quantitative analysis by determining the fluorescence signal intensity by Image-J Software. Three different pictures were analysed per each region and at least 20 squares of the same area were examined for each picture. The results were expressed as mean ± standard deviation (SD). A statistical test was performed using Origin2021 and ANOVA with Tukey's correction for the comparison between different groups. A p-value < 0.05 was accepted as statistical significance.

A second diffusion test was conducted by pumping inside the lumen of the scaffold an aqueous N-CDs dispersion at a concentration of 0.1 mg/mL and following the same operating conditions described above. The overnight-dried cross sections were observed by the inverted fluorescence microscope selecting a different band-pass excitation filter of 450−480 nm and 330−385 nm for detecting the green and blue emission, respectively.

3.4.4. Cytotoxicity studies

MDA-MB-231 cells were seeded into a 96-well plate at the density of $5x10^4$ cell/well and grown in the appropriate medium for 24 hr at 37°C under a humidified atmosphere of 5% CO_2. Therefore, they were incubated with 100 µL of media containing N-CDs at different concentrations (0.01875–0.6 mg/mL) for 48 hr. The untreated cells were considered as positive control. Cytotoxicity assay was conducted using the colorimetric assay AB. In particular, AB mixture with fresh medium was added to each sample (90/10 v/v ratio) and incubated for 3 hr at 37 °C for the reduction process. The fluorescence of the reduced resorufin was determined at the excitation and emission wavelength of 540 and 590 nm using a microplate reader DU-730 Life Science spectrophotometer (Beckman Coulter). The cell viability was assessed by the ratio of the AB fluorescence values between the experimental and control group and was expressed as mean ± SD. Three independent experiments with three replicates per experiment (3x6 well plates) were carried out. The cell viability was expressed as percentage, assigning the viability of non-treated cells as 100%. A statistical analysis of the data was performed using a One-way ANOVA test followed by Tukey's test for the comparison between the cell viability at different N-CDs concentration and the positive control for both 24 and 48h. Results with a p-value < 0.05 were considered statistically significant.

3.4.5. *In vitro* bioimaging of MDA-MB 231 cells

For *in vitro* cell imaging, MDA-MB 231 cells were seeded in 12-well plates containing sterile coverslips at a density of $5x10^3$ cells per well and grown for 10 days at 37°C under humidified 5% CO_2 condition. The medium was changed frequently. Therefore, cells were incubated with two different concentrations of CDs (0.1 and 0.3 mg/mL) for 72 hr. At the end of this period, the samples were washed with complete PBS to remove the excess of particles, fixed with 3.7 wt % formaldehyde for 5 minutes and washed again with PBS. Images of the breast cancer cells were obtained by an inverted fluorescence microscope using excitation wavelengths of 450−480 and 330−385 nm respectively for emission in green and blue regions of the visible spectrum.

3.5. Part 5: Doped and co-doped Red-emitting Carbon Dots

In this work, a novel class of fluorescence nanoparticles were developed as potential substitute for the conventional organic dye and fluorophores in biological applications, including bioimaging, sensoring, targeting, drug delivery.

3.5.1. CDs Synthesis

Different batches of CDs were prepared in the NanoFemtoLab of the Énergie, Matériaux et Télécommunications center, part of the research institute *Institut national de la recherche scientifique* (INRS), located in Varennes (Québec, Canada). *p*-phenylenediamine (*p*-pD) (Figure 3.8A) was selected as a carbon precursor and solvothermal method as synthetic route.
A first batch was synthesized mixing 10 mg of *p*-pD into 10 mL of three different solvents: ethanol (e-CDs), dimethylformamide (DMF) (d-CDs) and ultrapure water (w-CDs). Each mixture was transferred into a 50 mL Teflon-lined stainless-steel autoclave and kept at 200 °C for 6 h. Subsequently, the reaction solutions were cooled down at room temperature naturally and filtered by polyethersulfone (PESU) membrane filter (0.22 μm) to remove the large particles.

For the second batch, a solvothermal/acid-assisted method was used for the synthesis of doped and co-doped CDs. Briefly, for nitrogen doped CDs (N-CDs) 1.5 mmol of *p*-pD were dissolved in 10 mL of ultrapure water with ultrasonic stirring for 5 min. 5%wt of Boric Acid (Figure 3.8B) and Cobalt (II) acetate tetrahydrate (Figure 3.8C) were added to the solution and mixed with the assistance of ultrasonic for 5 min, for the synthesis of nitrogen-boron co-doped CDs (N,B-CDs) and nitrogen-cobalt co-doped CDs (N,Co-CDs), respectively. Then, 200 μl of 70% HNO_3 (Sigma) was added to each solution that was transferred into a 50 ml Teflon-lined stainless-steel autoclave and heated at 200°C for 2h. After natural cooling at room temperature, the dark-red solutions were collected and filtered with a 0.22 μm PESU filter. In the end, all the purified CDs from the two batches were lyophilized for 2 days to obtain the solid powder, stored at 4°C and dissolved in pure water for further studies.

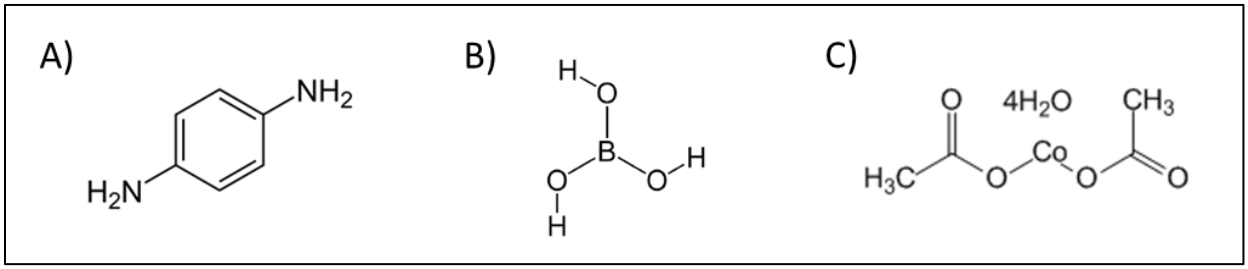

Figure 3.8: Chemical structures of (A) p-phenylenediamine (p-PD), (B) Boric Acid and (C) Cobalt(II) acetate tetrahydrate.

3.5.2. CDs characterizations

The surface morphology and the dimension of all the as-produced CDs was determined using a JEM-2010 TEM. The samples were prepared by drop casting the solution on C-coated copper grids and dried in air at room temperature. XPS analysis was carried out by using a Thermo Fisher VG (Escalab 220i XL) X-ray photoelectron spectrometer. FTIR spectra were recorded with a Thermo Fisher Nicolet 6700 FTIR spectrometer. For the investigation of the optical properties, UV-vis absorption spectra were measured using a UV-Visible-NIR Spectrometer (Lambda 750, Perkin Elmer). A fluorescence spectrometer (LS45, Perkin Elmer) was used for performing both the PL and PLE measurements. The absorption, PL and PLE of CDs was measured using 3 mm optical path length quartz fluorescence cuvette and an aqueous solution at the CDs concentration of 1mg/mL.

The fluorescence QY of CDs was determined according to the reference point method. Rhodamine 6G in water (literature QY 0.92) was used as standard. The absorbance of the solutions at 520 nm was kept below 0.1 to prevent the reabsorption phenomenon. The relative QY values were calculated by the following equation (Eq. 4):

$$\Phi_S = \Phi_R \left(\frac{Grad_S}{Grad_R}\right)\left(\frac{\eta_S^2}{\eta_R^2}\right) \qquad \text{Eq. 4}$$

where the subscripts S and R stand for sample and reference respectively, Φ is the Quantum Yield, $Grad$ represents the gradient of the curve from the plot of integrated fluorescence intensity vs absorbance, η is the refractive index of the solvent. The refractive index of water is 1.333.

The ZP was measured for all the samples of the second batch in aqueous solution at room temperature using BrookHaven ZetaPlus equipment. The electron paramagnetic resonance (EPR) was performed on a Bruker Elexsys E580 X-band EPR Spectrometer set as follow: center field 333.33 mT, sweep width is 10 mT, sweep time is 20.97 s, modulation amplitude is 0.3 mT, modulation frequency is 100 KHz, and microwave power is 30 mW.

Finally, the stability of the doped and co-doped CDs was evaluated recording the fluorescence intensity at various pH values (3 to 12) and after a prolonged exposure to UV light (up to 24 hours) using a 18W lamp with long wavelength of 365 nm. For all the stability experiments a concentration of 1 mg/ml CDs in ultrapure water was adopted.

CHAPTER 4

RESULTS AND DISCUSSION

To find an efficient treatment method for diseases is not easy and certainly more reliable drug testing platforms could help. *In vitro* pre-clinical studies on drug development would be improved and successful by using engineered 3D models and bioreactor systems for controlling the culture environment. For this purpose, in this work a dual-flow perfusion bioreactor was developed and improved together with "*ad hoc*" 3D polymeric supports as potential apparatus for *in vitro* drugs pre-screening. A second part of the experimentation involved the synthesis of new kinds of fluorescence nanoparticles as potential future carriers for multiple biomedical applications, involving fluorescence bioimaging, tumor tracking and drug delivery testing.

4.1. Part 1: Development of 3D polymeric scaffolds

In the first part of this project, 3D polymeric scaffolds were produced to create a solid platform for cell growth, morphology, metabolism, and differentiation studies. Two of the most important requirements for these porous devices are: acceptable biocompatibility and adequate porosity for the optimal interaction with cells [66]. Among the different categories of biopolymers commonly used for scaffold synthesis, PLLA was selected. PLLA is a non-linear poly (a-hydroxy ester) which has been used in different medical and pharmaceutical applications [237]. It exhibits beneficial properties including biocompatibility, biodegradation to harmless lactic acid mainly by hydrolysis in water, an appropriate strength and modulus, as well as the capacity to improve cell attachment and proliferation [238]. The high hydrophobicity of this crystalline polymer allows cell

adhesion thanks to a nonspecific adsorption of the proteins of the medium as well as an easy cell detachment [239].

The degradation time is one of the key features for scaffold applications as support for *in vitro* testing. PLLA degradation is slow and the complete loss of strength often takes years [240]. In addition, as a thermoplastic polymer, PLLA can be easily processed and tuned by following cooling and heating cycles without losing its properties to obtain different final shapes [241]. In order to produce porous scaffolds with different porous structures, PS technique was chosen. The advantage of the phase separation technique is that the morphology of the scaffold can be controlled just by changing parameters such as polymer type and concentration, freezing temperature, and use of different types of porogen, solvent and non-solvent [97].

A first experimentation was focused on selecting the best microporous structure for 3D polymeric scaffolds in order to recreate an *in vitro* microenvironment allowed to stimulate cellular processes as close as possible to the *in vivo* ones. Particularly, the aim of this work was to create a 3D *in vitro* model for mimicking the complex TME since it appears crucial for the development of effective treatment strategies and for studying the molecular mechanisms behind tumor formation, progression, and metastasis. In addition, these models are extremely useful for improving the efficacy of pre-clinical studies on cancer drug development [242]. Several batches of 4% (wt/wt) PLLA scaffolds were synthesized via TIPS by using different temperature (T) vs time (*t*) protocols in order to obtain various morphologies and pore sizes/shapes. A ternary polymeric solution PLLA/dioxane/water, well above the cloud point temperature (T=60°C), was hot poured inside a HDPE sample holder and kept into a TWB at a lower temperature than previous one. As it is widely reported in literature, through the temperature changing it is possible to induce the demixing of a homogeneous polymer solution, by entering inside the metastable/unstable region, and obtain a multi-phase system [243]. As result, porous structures with high degree of interconnection and a specific pore size, related to the T/time pathway chosen, were obtained. The cross sections of all the as-synthesised samples were analysed by SEM. In the case 1 illustrated in Figure 3.1C (Chapter 3: Materials and Methods), a time of 30 min was kept constant and two temperatures (25°C and 30°C) were selected. With this residence time and temperature, the phase separation takes place in the metastable region according to a binodal demixing, characterized by nucleation and growth [227]. From SEM micrographs shown in Figure 4.1, two different average

pore sizes can be observed: 100 μm for the sample 25°C/30min (Figure 4.1 A); 150 μm for the sample 30°C/30min pore size of (Figure 4.1 B). An increment of only 5 degrees in the T of phase separation led to an increase in the pore size of about 50 μm which highlighted the high susceptibility of the system to the process parameters. In a second set of experiments, the porous structure of the scaffolds produced were assayed by reducing T and *t* used for the phase separation. In this case, the PLLA scaffolds prepared by Direct Quenching from 60 °C to -20 °C inside the EAB (case 2 of Figure 3.1C) exhibited an average pore size of around 25-30 μm (Figure 4.1 C). The structure obtained with very small highly interconnected pores is in agreement with the results related to a "spinodal phase separation route", as reported in a previous study [228]. Finally, for controlling the porous structure and producing foams with an average pore size in-between the previous ones, the physical and chemical parameters of the TIPS were kept unchanged while the sample-holder was embedded into a cylindrical PTFE coating to tune the heat transport during the phase separation process. At a T/*t* path of 20°C/15 min, three slightly different protocols were adopted (case 3, Figure 3.1 C). In a first step, the samples were produced by maintaining the PTFE coating around the sample holder both in TWB and in EAB (case 3a, Figure 3.1 C). SEM micrograph of these as-produced scaffolds revealed a pore size of ~60 μm (Figure 4.1 D). In a second experimental pathway, the insulation PTFE coating was placed around the sample holder during the cooling phase at -20 °C inside the EAB (case 3b, Figure 3.1 C). The average pore size obtained with this protocol was in the range of 40–50 μm (Figure 4.1 E). Finally, the ternary polymeric solution was brought from the initial temperature of 60 °C to 20 °C in the presence of the PTFE coating and subsequently to -20 °C without the coating (case 3c, Figure 3.1 C). In this case, SEM micrograph revealed a pore size of ~30 μm (Figure 4.1 F). These data clearly reveal how it is possible to tune up the morphology of the scaffolds (pore shape and pore size, network interconnection) using TIPS as synthesis technique simply by varying some experimental parameters such as the residence time and temperature in the metastable/unstable state, and the condition of the cooling phase.

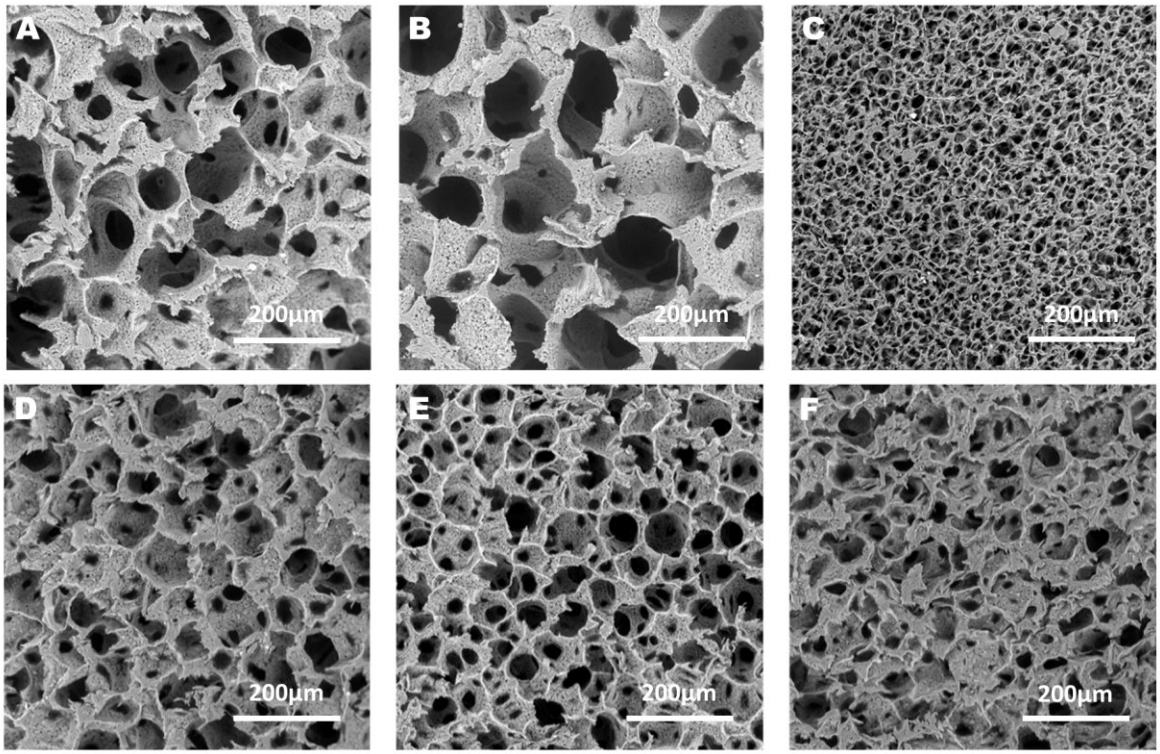

Figure 4.1: SEM micrographs of PLLA scaffolds produced via TIPS using different temperature/time pathways, with/without an insulating PTFE coating shell. (A) 25°C/30min; (B) 30°C/30min; (C) Direct Quenching; (D) 20°C/15min with PTFE coating both in the TWB and the EAB; (E) 20°C/15min with PTFE coating only in the EAB; (F) 20°C/15min with PTFE coating only for the TWB. Scale bar, 200µm.

For simulating the natural drug release process through a vascularized tissue, by using a dual-flow perfusion bioreactor, a "*ad hoc*" vessel-integrated scaffold was designed. PS was adopted again for the production of a double-structured polymeric scaffold, with two different morphologies in order to mimic a vascularised biological tissue under physiological conditions. It consists of a "pseudo-vascular" structure that was embedded into a cylindrical porous matrix which is able to lead cell spreading. The structure that mimics a blood vessel is a porous tubular scaffold and was prepared by following a two-step experimental protocol, including a dip-coating of a viscous PLLA/dioxane binary solution around a cylindrical support and a DIPS by immersion into an antisolvent bath (deionized water). Firstly, a PP rod with a diameter of ~2mm was chosen as support. PP is widely used in various applications due to its excellent chemical and high

temperature resistance, good mechanical properties, highly available and cost-effective [244]. The dip-coating step allowed to generate a tubular structure with a specific wall thickness depending on the extraction rate. In this work, a rate of 10 cm/min was selected. In the second stage (DIPS), the PP rod was immersed into the bath where the phase separation took place, owing to the diffusion of the antisolvent from the bath to the polymeric solution and the solvent (dioxane) in the opposite sense. This process is responsible for the surface microporosity necessary for nutrients and metabolites transport from the inner of the artificial vessel (lumen) outwards and *vice versa*. The SEM micrograph of the cross section of the as-obtained scaffold is shown in Figure 4.2 A which reveals a porous wall with a uniform thickness of ~200 µm. However, the lumen surface exhibited a non-uniform surface with an evident macro-porosity (Figure 4.2 B-C). To overcome this problem, the PP rod was first replaced with a stainless steel AISI 316 rod, keeping the operation conditions unchanged. The SEM analysis of the tubular scaffold obtained showed that the morphology of the scaffold did not undergo significant changes about the wall thickness and both the surface (internal and external) showed a uniform microporosity with an average pore size of ~10µm (Figure 4.3).

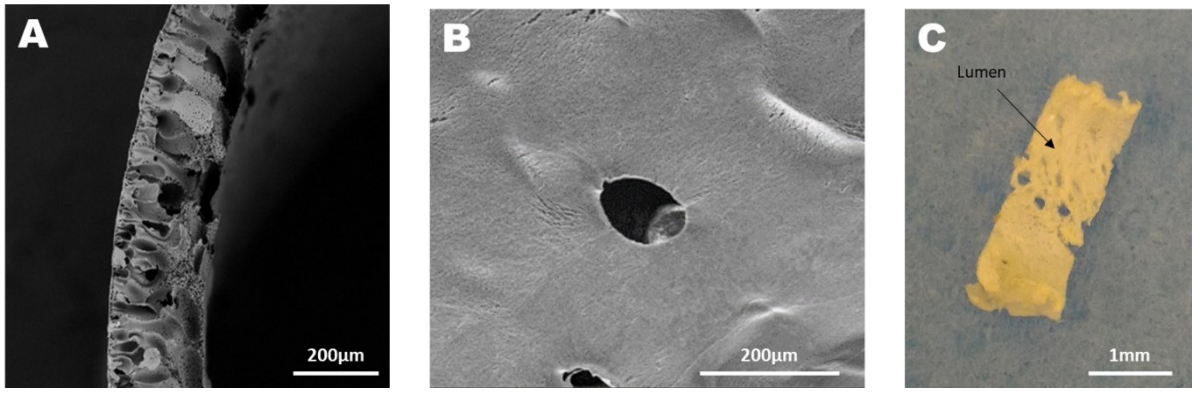

Figure 4.2: (A) SEM micrograph of a cross section of a vessel-like scaffold prepared via DIPS using PP rod for the dip-coating with an extraction rate of 10 cm/min. Scale bar, 200µm. (B) SEM micrograph of tubular scaffold lumen surface with the presence of a macro-pore. Scale bar, 200µm. (C) Photograph of a cross section of tubular scaffold after DIPS using PP rod with an evident non-uniform lumen surface. Scale bar, 1mm.

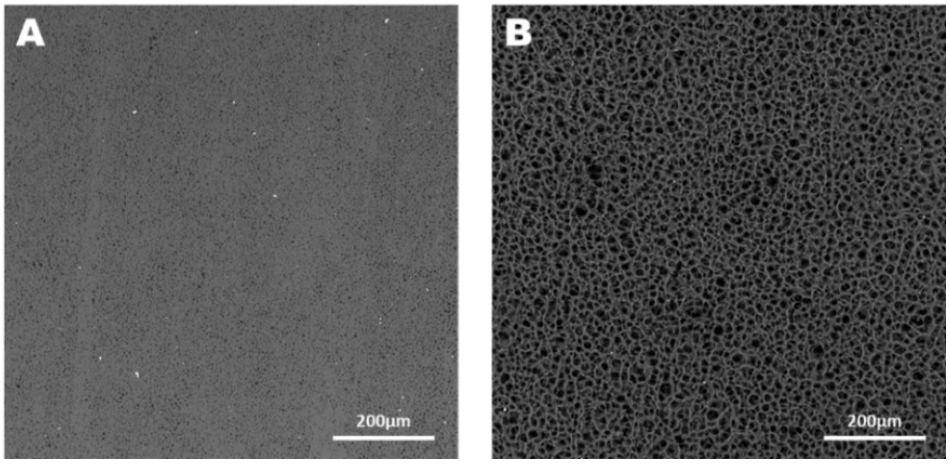

Figure 4.3: SEM micrographs of PLLA tubular scaffolds prepared via DIPS using stainless steel rod as support for the dip-coating. (A) Lumen surface; (B) external surface. Scale bar, 200µm.

At this point, the as-prepared vessel was incorporated into a three-dimensional matrix, prepared by TIPS. Particularly, the vessel-like scaffold was placed perpendicularly into a cylindrical Al sample holder and the TIPS protocol, described above, was followed. A hot ternary polymeric solution (PLLA/dioxane/water) was poured into the sample holder which was placed in a TWB at 0°C for 10 min and then in the EAB for a quick quench. The foam obtained was gently pulled out from the aluminum structure and washed in deionized water to eliminate the residual dioxane. From the SEM micrographs (Figure 4.4 A-B) of the cross sections it is easy to observe that the vessel-like scaffold is totally embedded into the porous structure produced by TIPS with a thickness of ~200µm (Figure 4.4 A). Moreover, a continuous porous matrix is well connected to the vessel-like structure and presents a high porosity (about 95%) and an average pore size of ~10µm in many areas (Figure 4.4 B). The morphology of this construct which is easy-tunable in terms of pore size, porosity and thickness makes it adaptable to various cell culture or tissue types. Furthermore, the peculiarity of this multifunctional scaffold makes it usable as a real route to mimic a vascularised biological tissue under physiological conditions inside a device like the bioreactor that allows cell growth under dynamic conditions.

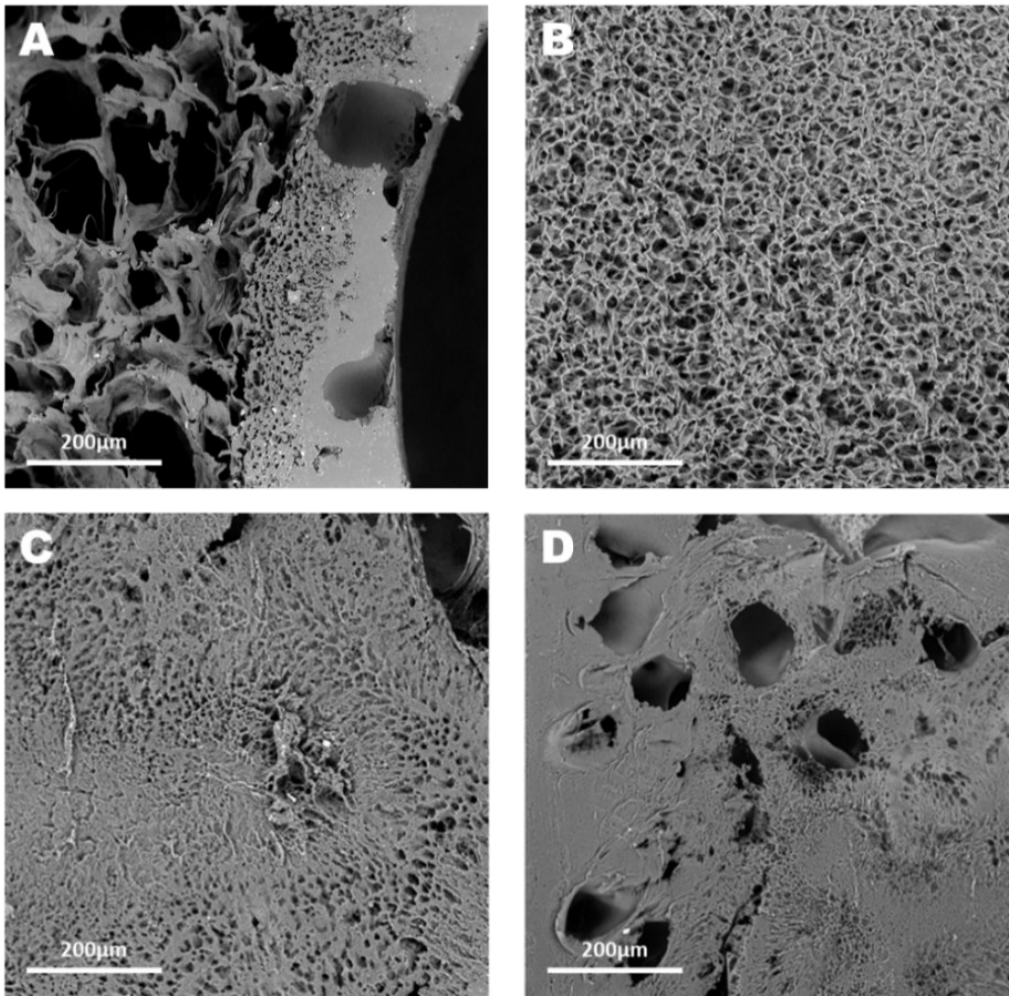

Figure 4.4: SEM micrographs of double-structure PLLA scaffolds synthesized via DIPS+TIPS (temperature/time path 0°C/10 min). (A) detail of embedding zone; (B) external porous matrix; (C) and (D) details of a non uniform lumen surface. Scale bar, 200µm.

Despite the excellent results obtained in terms of wall thickness, the homogenous microporosity of the matrix around the vessel-like scaffold and the lumen surface after TIPS appeared non-uniform (Figure 4.4 C) and with different areas of macropores (Figure 4.4 D). Moreover, from Figure 4.4 A it is evident how the wall of the embedded tubular scaffold lost its microporosity. The solution adopted in this work was to skip the synthesis of the vessel-like scaffold via DIPS and try to realize a single porous tubular scaffold just using the TIPS method.

Keeping the cylindrical Al sample holder and the stainless-steel rod, the ternary polymeric solution at 60°C was gently hot poured inside the sample holder and put in the TWB at 0°C for 10 minutes. The macroscopic shape of the final foam extracted from the sample-holder (OD = 2.5 cm, ID = 0.2 cm, H = 3.5 cm) is shown in Figure 4.5 i. To verify the homogeneity of the sample structure, thin slices (thickness 0.5 cm) from different areas of the as-obtained scaffold were analyzed. From SEM images it is possible to observe a well-interconnected porous structure with a uniform microporosity (Figure 4.5 ii A). SEM micrograph of the external polymeric matrix reveals an average pore size of about 30–40 μm (Figure 4.5 ii B). The surface of the lumen was also microporous, with a pore size of 20–30 μm, as observed in Figure 4.5 ii C.

All the previous results prove that the as-obtained PLLA scaffolds can sufficiently support a cell co-culture thanks to both inner and outer highly microporous surfaces. In addition, the interconnected porous matrix allows to promote a good diffusion throughout the scaffold during a dynamic culture inside a bioreactor.

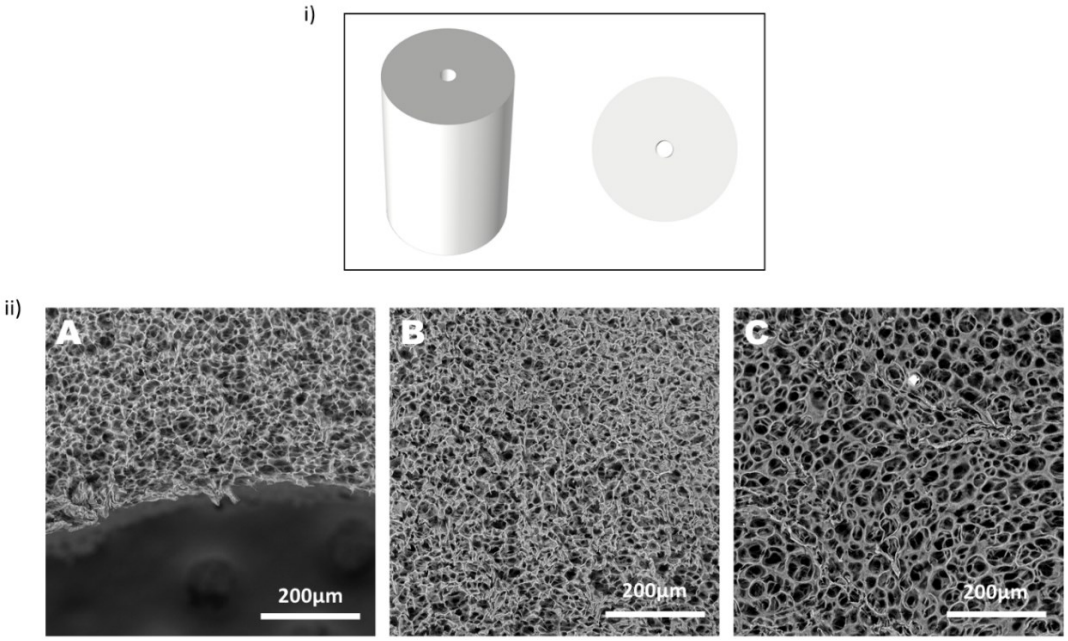

Figure 4.5: (i) 3D macroscopic image of a PLLA scaffold produced via TIPS (0°C/10min) using a cylindrical Al sample holder and a stainless-steel rod. (ii) SEM micrographs of cross sections of PLLA scaffold obtained via TIPS (0°C/10min) using a cylindrical Al sample holder and a stainless-steel rod. (A) Detail of area close to the central channel; (B) external porous matrix; (C) lumen surface. Scale bar, 200 μm.

4.2. Part 2: Dual-flow perfusion Bioreactor design and characterization

In the last couple of decades, bioreactor systems have been proposed as a key factor in the manufacture of standardized and cost-effective engineered products in several different industry areas [245, 246] and research, especially for clinical applications such as the progress of the 3D dynamic cell cultures for human health research [247, 248]. However, the implementation of new bioreactor-based apparatus for *in vitro* preclinical studies in the pharmaceutical industry, identification of disease mechanisms or therapeutic solutions have not yet broadly investigated [128].

In this work, a novel custom-made device is presented as an improvement of the common perfusion bioreactors. As it is well known, flow perfusion culture offers several advantages, notably the ability to improve mass transfer through the interconnected porous network of the seeded scaffold [249]. The culture medium is forced through the entire scaffold and allows to mitigate both external and internal diffusional limitations to enhance nutrient or potential drug delivery systems for the cells [223]. The goal of this project was to design and implement a perfusion bioreactor which expanded the traditional use of the bioreactor as *in vitro* 3D dynamic cell culture platform for TE applications to pharmaceutical purpose, including the *in vitro* pre-screening testing of new drugs. To this end, a novel dual-flow perfusion apparatus was developed consisting of two independent perfusion circuits, whose operating principles (Figure 4.6) allow both the radial perfusion through a porous polymeric matrix (IPC circuit) and a continuous circulation of culture medium, at a fixed flow rate, inside the device (EPC circuit). One of the primary key elements of a bioreactor design are ease of use and assembly [250]. The height of less than 30 cm guarantees an easy assembly, quick handling and stability during the operations, easily location into a common cell-culture incubator, and reduced volume of culture medium sufficient for long-term cell cultures. Moreover, the bioreactor is totally glass-made which grants a complete and fast sterilization of each component into a conventional autoclave.

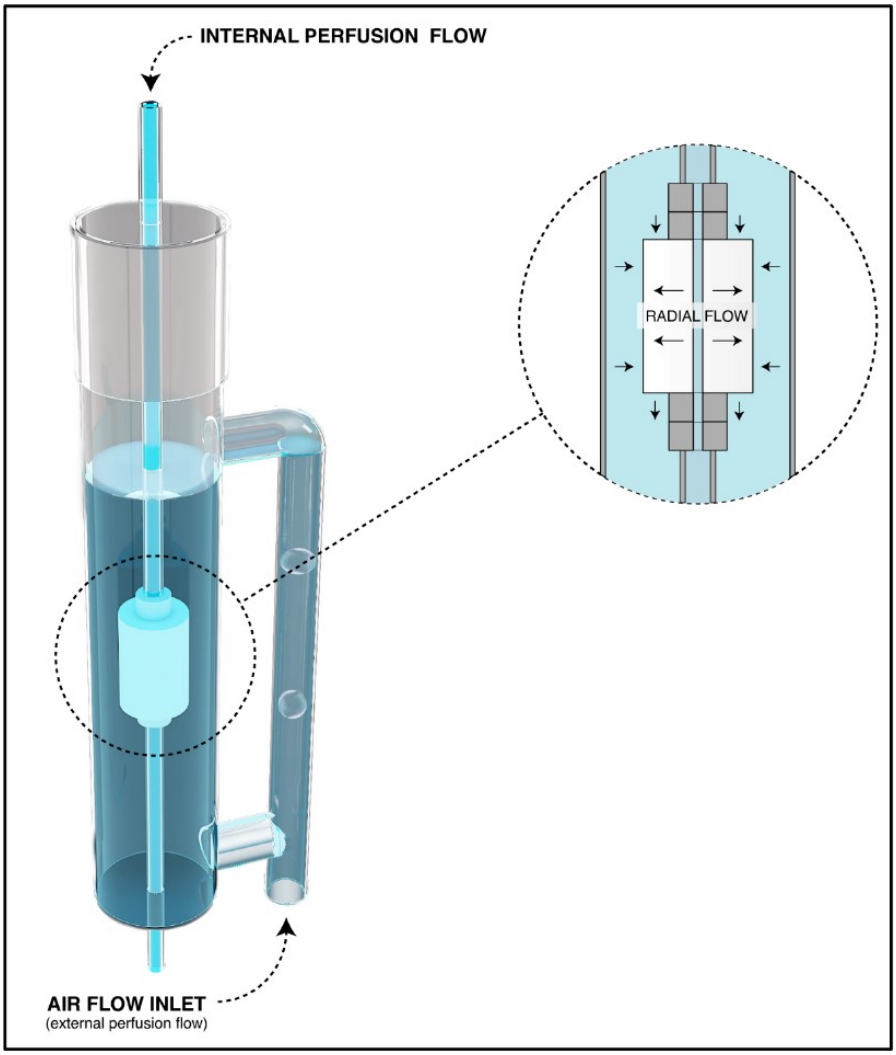

Figure 4.6: Illustration of the operating principle of the double-flow perfusion bioreactor. An internal perfusion flow and an external air perfusion flow generate a "radial flow" throughout the scaffold placed inside the main column of the bioreactor.

4.2.1. Fluid-dynamic characterization

One of the important aspects in developing bioreactors consists of the investigation on engineering parameters, such as fluid profile and hydrodynamic conditions, which can influence the final performance [118, 251].

Here, the fluid dynamic of both IPC and EPC were investigated. The data presented in Table 4.1 show a constant laminar flow regime in the system inside the IPC, with Reynolds numbers from 2 to 170, despite an increase in the liquid flow rate and fluid velocity inside the lumen of the scaffold. These results provide a range of shear stresses in agreement with the literature values related to cylindrical vessels with diameter between 1-5 mm [252–254] to enable cell attachment and growth on polymeric surfaces.

Table 4.1: Volumetric Flow rate (ml/min) and fluid velocity (cm/s) of the circulating fluid inside the PLLA tubular scaffold. Reynolds number and Shear Stress (dyne/cm^2) were calculated by using the equations reported in "Materials and Methods" section.

Flow rate [ml/min]	Fluid velocity [cm/s]	Reynolds number	Shear Stress [Dyne/cm^2]
0.15	0.08	2	0.04
0.50	0.27	5	0.13
1.00	0.53	11	0.27
5.00	2.65	53	1.33
6.00	3.18	64	1.59
8.00	4.24	85	2.12
10.00	5.31	106	2.65
11.00	5.84	117	2.92
12.00	6.37	127	3.18
14.00	7.43	149	3.71
16.00	8.49	170	4.24

The fluid-dynamic investigation of the EPC allowed it to demonstrate the capability of controlling the airflow in a reliable and reproducible way. The flow rates of the EPC were measured for both empty and filled bioreactor with a fixed volume of culture medium, and the data were plotted as a function of the peristaltic pump speed in terms of RPM (Figure 4.7). As expected, no significant differences were observed between the two conditions. Figure 4.7 B shows the liquid

flow rate circulating from the bubble column to the main column, thanks to the rising air bubbles, as a function of the pump speed (RPM). A direct proportion was found between the air and liquid flow rates (Figure 4.7 C) by comparing the two results. Together these results demonstrated the wide range of liquid and air flow rate coverable with this device (10-40 ml/min), maintaining both stability of the system and sufficient liquid recirculation, and underline the significant reliability of the entire system.

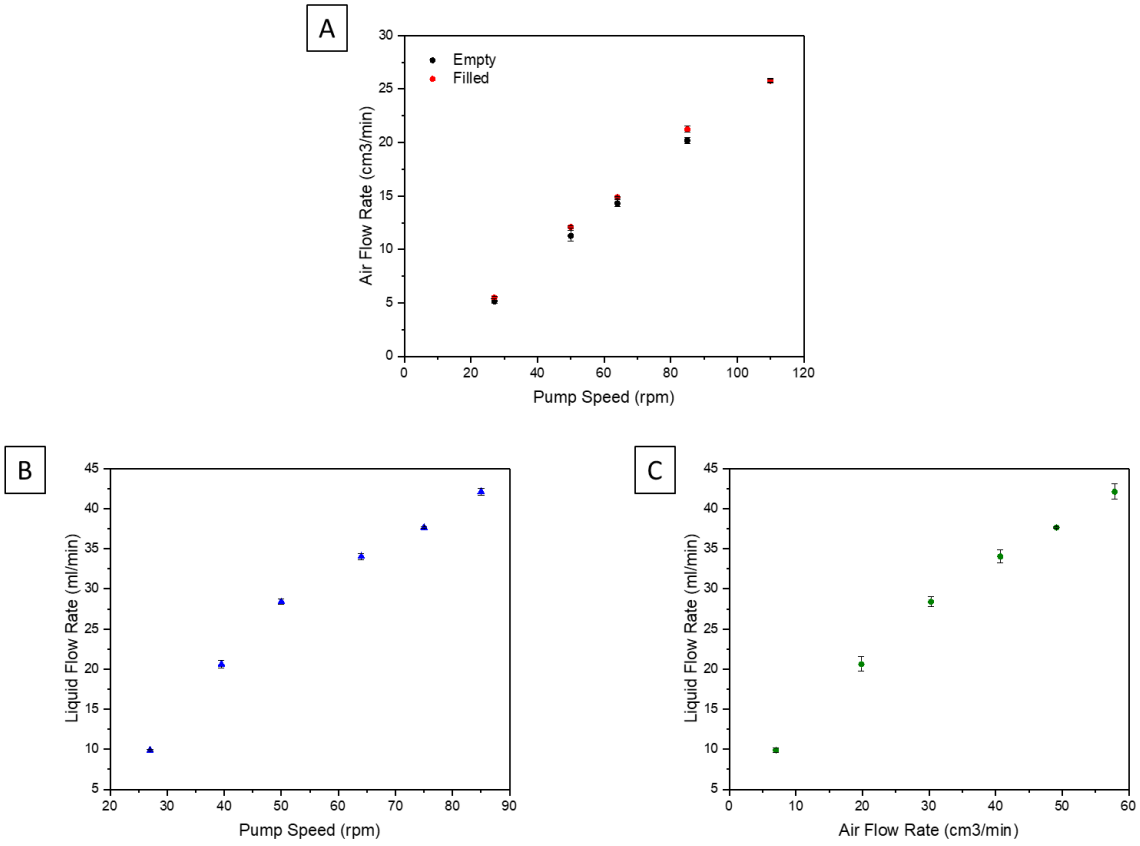

Figure 4.7: Fluid-dynamics of the external perfusion circuit (EPC) of the bioreactor. Air flow rates plotted as a function of pump speed (RPM) (A); Liquid flow rate plotted as a function of the pump speed (RPM) (B); Air flow rates Vs Liquid flow rates (C). Data represent mean ± SD.

4.2.2. Efficacy of the radial perfusion system

One of the most crucial cell cultivation parameters into 3D polymeric scaffolds is the continuous supply of nutrients, oxygen and the removal of waste products. In comparison with other conventional systems, perfusion represents the most promising method for a greater control of the cell microenvironment and cell viability during 3D *in vitro* dynamic cell cultures [255, 256]. In this work, the efficacy of the radial perfusion flow through the porous scaffold was evaluated.

A qualitative diffusion test was first carried out adding an organic dye (toluidine blue) to the deionized water (0.1 % v/v). After 30 min of circulation inside the bioreactor at a fixed flow rate of 1 ml/min, the scaffold was recovered and cut in different slices from the upper, center and bottom part. In Figure 4.8 (A-C) a clear radial staining of the matrix can be appreciated. From the cross sections it is possible to confirm that the blue dye permeated uniformly inside the microporous structure from the lumen to the external surface of the scaffold and from top to bottom.

An interesting result came out from a second permeability test. In this experiment, radial flow rates through the hollow cylindrical scaffold were measured at different IPC flow rates (0.5 ml/min-1.0 ml/min) and for different heights (*H*) (Figure 3.6 Chapter 3: Material and Methods, Part 2). In Figure 4.8 D the calculated radial flow rates are plotted. By convention, the flux from the external surface to the inner channel of the scaffold (in-flow, IF) was assumed as a negative flow, while for the opposite flow direction (out-flow, OF) a positive sign was adopted. For all the tested flow rate, when *H* was below the level 0 (the outlet of the tube at the same height of the scaffold) a radial flow from the outside towards the inner surface of the scaffold was observed (IF). On the contrary, when the outlet of the tube was raised, the flow rate decreased as long as it turned zero and then a change of flow direction was observed with the fluid running radially from the inner channel to the outside (OF). For all the tested IPC flow rates, the flow increased when increasing *H*. The findings of the permeability tests revealed the possibility to manage the direction of the radial flow simply by changing the height of the outlet of the IPC tube. Consequently, according to the desired application, it can be possible to precisely set the direction of the radial flow rate in a cheap and simple way, without the use of specific devices [257] or the more approximating results of a computational simulation [258, 259].

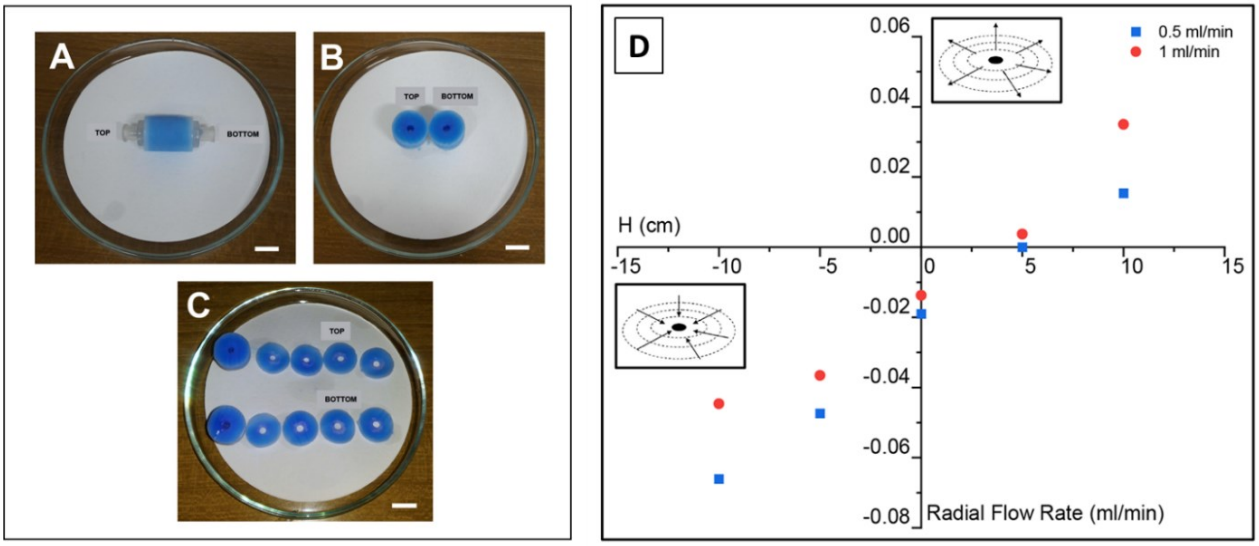

Figure 4.8: Photograph of the PLLA scaffold post perfusion inside the dual-flow bioreactor for 40 min using an aqueous solution added with a blue dye: entire scaffold (A); top and bottom (B), slices from top and bottom part (C). Scale bar 1 cm; (D) Radial Flow rate (ml/min) across the PLLA scaffold inside the bioreactor as function of the height (cm) of an outlet silicon tube. [229]

4.3. Part 3: 3D *in vitro* cell culture using PLLA scaffolds as support

In the previous sections, we already discussed about the 3D *in vitro* models as a valid alternative in drug development and toxicity testing for many diseases varying from cancer to neurological disorders [22], compared to traditional 2D *in vitro* cultures, which are not able to mimic faithfully the 3D tissue microenvironment, and *in vivo* studies, influenced by low reproducibility and ethical issues [260].

In this work, human triple negative breast cancer MDA-MB 231cells were seeded on PLLA scaffolds in order to verify the ability of the as-produced PLLA foam to support cancer cells growth, adhesion and proliferation until bringing to an *in vivo*-like tumour mass generation. MDA-MB 231 cell line belongs to the more aggressive basal-like subtype of breast tumor cells [261] and

it is widely used as a standard *in vitro* breast cancer model with applications in the study of tumor mechanobiology, metastasis, and cell invasion [262, 263].

4.3.1. Cell proliferation and migration inside the PLLA scaffold

To investigate the PLLA foam proliferative capability, a viability assay was carried out for over 2 weeks of culture at different time points. For these tests scaffolds with three different average pore sizes were selected: 20µm (PLLA-20), 50µm (PLLA-50) and 100µm (PLLA-100), in order to evaluate the influence of the microporous structure of the foam on cell growth and proliferation. The results showed a comparable proliferation trend for all the samples investigated (Figure 4.9 A). However, an increased proliferation rate was observed on Day 7 of culture for the cells grown on PLLA scaffold with an average pore size of 50 µm.

To visualize the cells grown and migrate inside the polymeric structure under the fluorescent microscope, nucleus specific DAPI fluorescent stain was used. It produces a strong blue fluorescence, when binds with DNA, due to the displacement of water molecules from both DAPI and the minor groove of the DNA. As shown in Figure 4.9 B, after 7 and 14 days of 3D culture the DAPI stained MDA-MB-231 cells show bright blue fluorescence under the DAPI filter in all the PLLA scaffolds analyzed. A complete colonization of the scaffold surface is clearly evident. However, because of the nature of the staining and imaging method, some of the cells grown on the 3D scaffolds appear to be out of focus increasing evidence of the growth of cells at different focal planes/depths.

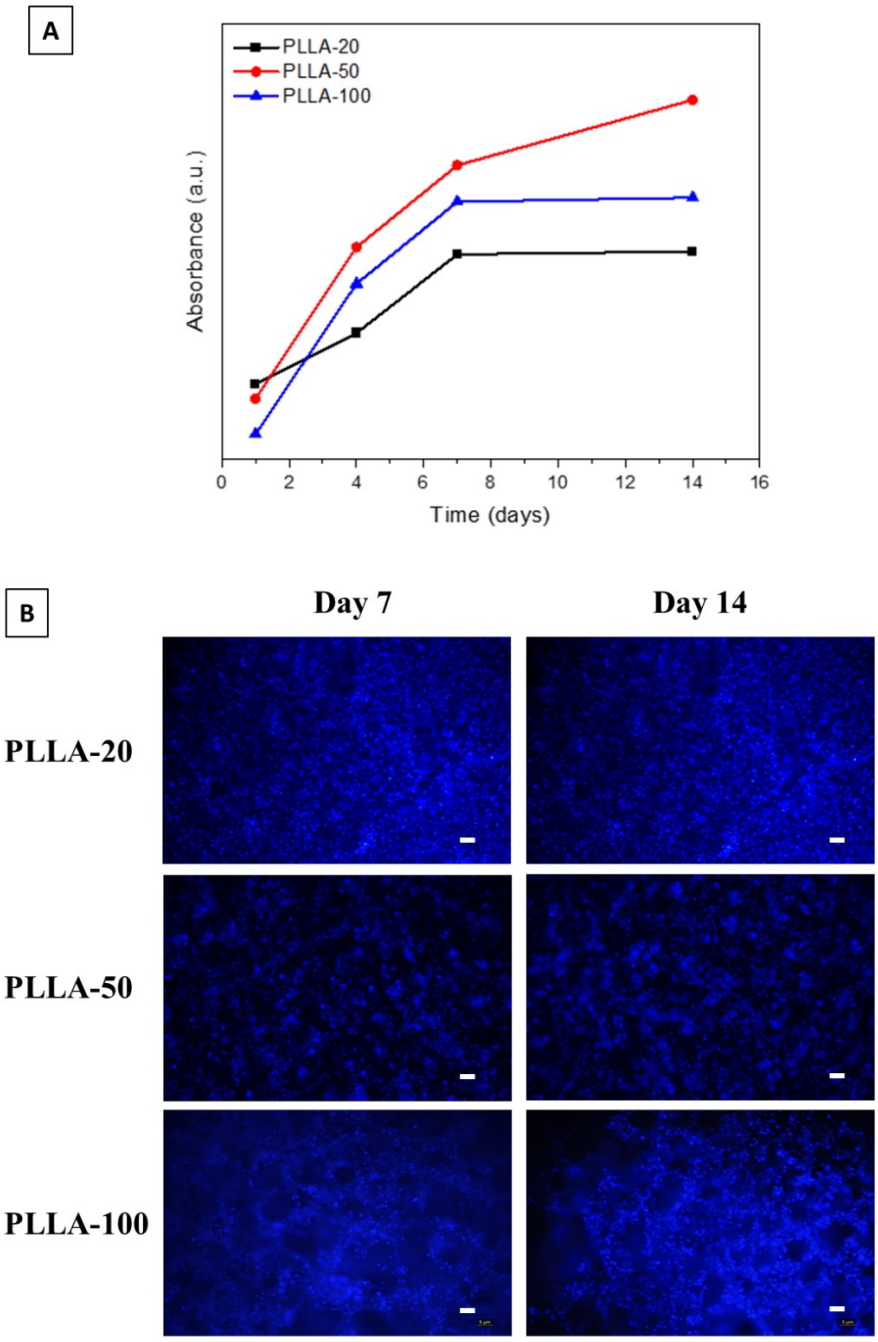

Figure 4.9: (A) Proliferation rates of MDA-MB 231 cells on three PLLA scaffolds with different pores size: 20 µm (PLLA-20), 50 µm (PLLA-50) and 100 µm (PLLA-100); (B) Examination of MDA-MB 231 cell growth on three different porous scaffolds at two time points by staining the nuclei of the cells with DAPI (blue). Scale bar, 50µm.

4.3.2. Cell morphology on PLLA scaffold

The morphological properties of cancer cells within 3D microenvironments could be a fundamental factor contributing to cancer cell growth, motility, tumor development, and also resistance to therapeutic drugs [215].

In this experimentation, scaffolds with different pore size were compared and, in the end, the microarchitecture seemed to influence 3D cell culture efficiency. SEM micrographs in Figure 4.10 show MDA-MB-231 cells cultured on PLLA scaffold discs pre-treated with a collagen solution. The cells grown on the samples with low average pore size (PLLA-20) exhibit round shapes and form cell clusters starting from Day 4 of culture (Figure 4.9 A). However, 7 days post-seeding the cells appeared to populate the entire surface areas leading to the formation of a uniform epithelium-like layer (Figure 4.10 B). The effect of the microporous structure on tumor cell morphology was more emphasized in the scaffold with an average pore size of 40-50 μm (PLLA-50). As can be seen from Figure 4.9 C-D, distinct multicellular aggregates are recognizable with a "stellate" irregular morphology, typical of the highly invasive phenotype of these breast cancer cells, in agreement with a previous study [264]. Furthermore, from the observation of these 3D cellular spatial organization it's evident how emitted protrusions anchor the cells to the fibers of collagen rather than directly to the polymeric porous matrix. Finally, an increased pore size led to a decrease in the number of cell colonies. In fact, the MDA-MB-231 cells cultured on the scaffolds with an average pore size of ~100 μm (PLLA-100) were not well-spread and located principally inside the big pores (Figure 4.10 E-F). These data are consistent with previous studies that showed how *in vitro* aggregates of cancer cells (tumoroids) can be commonly achieved in 3D cultures [212, 219, 265]. The network structure of the scaffold provides a physical support for cell growth as well as playing a major role in improving multidirectional interactions of the living cells with the surrounding matrices or/and other cells at all directions. Moreover, the cell morphological differences evinced between the three types of investigated microarchitectures suggest to take into account an average pore size of ~50 μm to make the PLLA scaffolds suitable as potential *in vitro* tumor models including also a better 3D distribution of the collagen fibers around and within the cellular aggregates, thus stabilizing the spatial architecture of the cells and acting as a topological stimulus to their aggregation.

All the previous results propose the as-obtained 3D polymeric scaffolds as a valid support for tumor cell culture and for studying certain aspects of cancer biology which involves either biomedical or bioengineering applications.

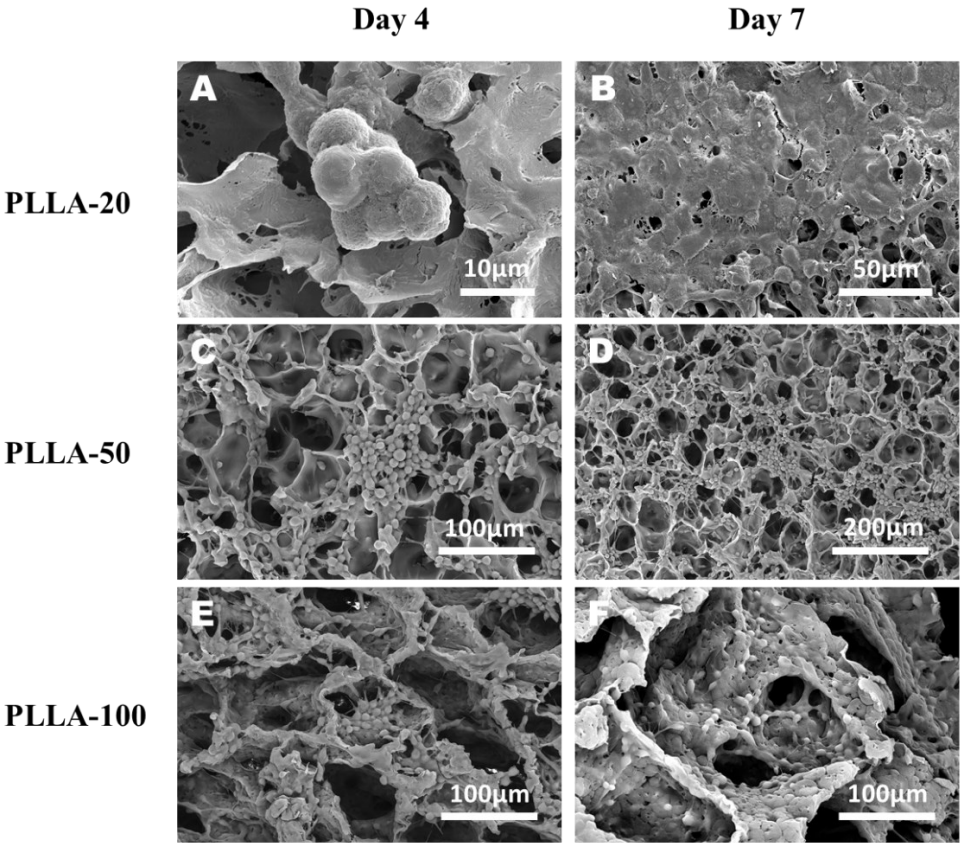

Figure 4.10: SEM micrographs of MDA-MB 231 cells grown for 7 and 14 days on (A-B) PLLA-20, (C-D) PLLA-50 and (E-F) PLLA-100. Scale bars: (A) 10 µm, (B) 50 µm, (C-E-F) 100 µm, and (D) 200 µm.

4.4. Part 4: Diffusion of nanoparticles through polymeric structures

In the last decade, understanding the diffusion of macro-, micro- and nano- particles within porous matrices has become of great interest in many biological and medical applications, including drug delivery [266]. Undoubtedly, radial diffusivity assures an optimal spatial distribution of particles inside a porous support.

At this regard, once established the dual-flow bioreactor capacity to guarantee an adequate perfusion system and the diffusion flow throughout the polymeric scaffold, the efficacy of the radial flow of the apparatus related to the migration of particles inside the scaffold was investigated. Preliminary studies were conducted using two different types of nanoparticles as potential carrier models.

4.4.1. Polymeric fluorescent nanoparticles (FNPs)

The first nanocarrier tested was synthetized by Prof. G. Cavallaro research group (Laboratory of Biocompatible Polymers, Department of "Scienze e Tecnologie Biologiche, Chimiche e Farmaceutiche" (STEBICEF)) of the University of Palermo. A derivative of PHEA was used as a starting copolymer. The biocompatible protein-like copolymer PHEA was chosen as precursors for the FNPs since its good water solubility, absence of toxicity, antigenicity and teratogenicity. It has been already successfully utilized as starting material to generate different graft copolymers for several biomedical and pharmaceutical applications [96]. A first functionalization of PHEA with RhB it was a valid way to introduce a fluorescent probe, with high absorption coefficient and photostability, permanently conjugated on the polymeric backbone. For making it suitable for the preparation of nanoparticles, the PHEA-RhB was grafted with PLA, biodegradable hydrophobic chains for obtaining an amphiphilic copolymer, and finally a derivation with biocompatible PEG allowed to reduce particle aggregation phenomena, to increase the biocompatibility of the resulting copolymer and to confer stealth properties. The resulting FNPs exhibited colloidal size of ~200 nm and slightly negative ZP (-2.44 mV) [267, 268].

In SEM micrographs reported in Figure 4.10, the FNPs are clearly identifiable within the polymeric structure. As predicted, the nanoparticles population is predominant in the lumen surface (Figure 4.11 A), since it is directly in contact with the circulating flow. A wide population of particles is also evident in the region near the lumen, as shown in Figure 4.11 B. Then, the particle's front radially decreases when moving from the lumen to the external surface (Figure 4.11 C). These results were confirmed both qualitatively and quantitatively using the fluorescence images of the scaffold cross sections, where FNPs are marked by the dye RhB, under an excitation of 530-550 nm (Figure 4.12 i). An intense red emission was observed in the area close to the lumen surface with a relative intensity decreasing up to the external surface. Directly referring to the

fluorescence signal, a quantitative analysis allowed us to evaluate the radial distribution of the nanoparticles after the perfusion process using ImageJ software. A high signal intensity was obtained in the region A near the lumen. The closed region B showed a slight decrement which resulted stronger for the subsequent two region C and D (Figure 4.12 iii). Nevertheless, statistically no significant differences were evaluated between the 4 regions, indicating a uniform diffusion and distribution of the FNPs within the polymeric matrix.

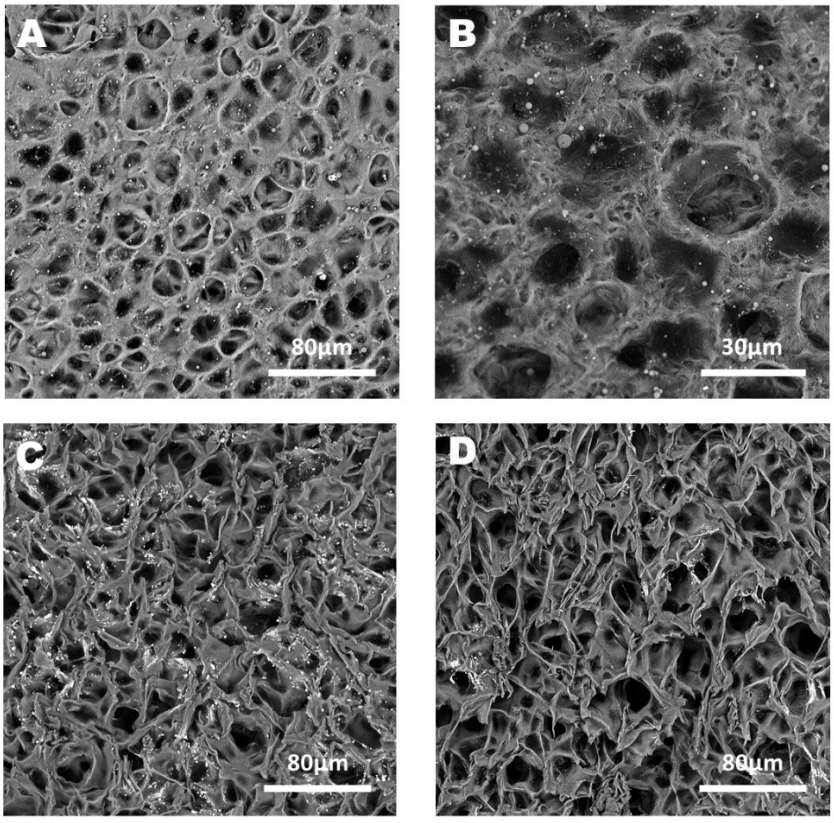

Figure 4.11: SEM micrographs of PLLA scaffold cross-sections after the perfusion of a solution with PHEA-RhB-PLA-PEG nanoparticles (FNPs) (100µg/ml) inside the bioreactor. SEM images of (A-B) lumen surface, (C) polymeric matrix portion close to the lumen, (D) polymeric matrix far from the lumen. Scale bar 80 µm (A-C-D), scale bar 30 µm (B).

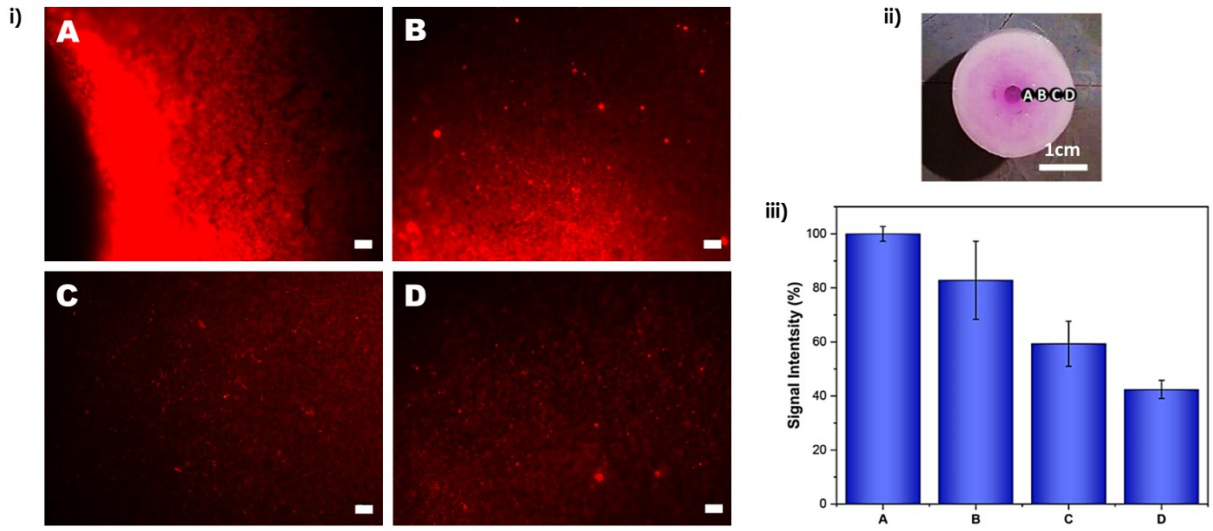

Figure 4.12: (i) Fluorescence microscopy images of PLLA scaffold cross section after the perfusion of FNPs diffused inside the bioreactor. Scale bar: 50 μm. (ii) Real picture of the PLLA scaffold cross section with the 4 areas analyzed: A lumen, B close to lumen, C far from lumen and D external surface. Scale bar 1 cm. (iii) Fluorescence signal intensity (%) of the 4 different areas of the scaffold post perfusion. Data represent mean ± SD. There is no statistically significant different between the samples ($p > 0.05$)

4.4.2. N-doped Carbon Dots (N-CDs)

To investigate the flexibility of the apparatus in the diffusion of nano-carriers inside the polymeric matrix, a second kind of nanoparticles was tested. Since the great attention in the last decade as a novel class of fluorophores [269] and their remarkable significance in various biomedical areas of application such as *in vitro* and *in vivo* bio-imaging, bio-sensor and drug delivery [270], CDs were chosen for the diffusion tests. Prof. Fabrizio Messina's research group (Physic and Chemistry Department- Emilio Segrè) of the University of Palermo synthesized N-CDs demonstrating how the high-nitrogen-content modifies the crystalline structure and induced dual emission (blue and green). The particles obtained by microwave-induced decomposition of an aqueous solution of citric acid and urea in a standard household microwave oven, showed diameters less than 7 nm [235]. In this second diffusion test, the fluorescence images of the scaffold cross-sections were obtained using an excitation of 450−480 nm and 330−385 nm for the green

and blue emission, respectively. From the results shown in Figure 4.13, it is immediately evident a strong emission of the N-CDs even with the presence of the scaffold. Moreover, a reliable reproduction of the characteristic porous microstructure of the scaffold is guaranteed. These results could be attributed both to an absence of interference on the particle optical properties by the polymer and a stable interaction between nanoparticles and polymeric matrix.

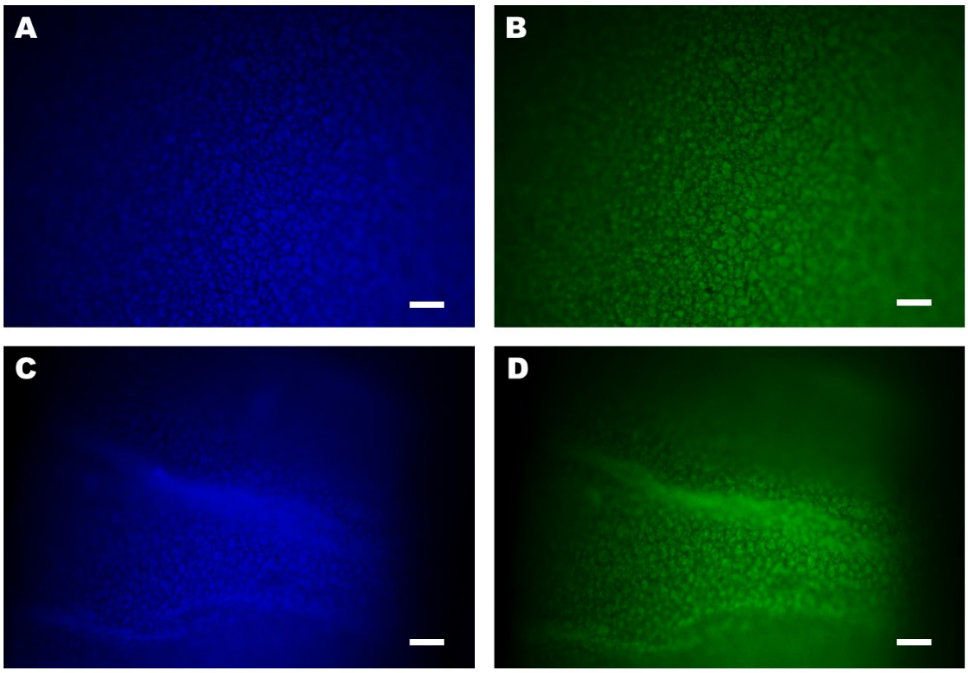

Figure 4. 13: Fluorescent images of PLLA scaffold cross sections after perfusion inside the bioreactor with an aqueous CDs dispersion (0.1 mg/ml) for 40 min. External porous matrix (A-B); lumen surface (C-D). The excitation wavelength is (A-C) 450−480 nm and (B-D) 330−385 nm. Scale bar 100 μm.

To sum up, all the data shown above provide undoubtedly supports to the main idea of using the dual-flow perfusion bioreactor as a platform for *in vitro* therapeutic pre-screening system, thanks to the good perfusion and effective radial flow guarantying diffusion of nano-carriers inside 3D polymeric microporous porous structures.

4.4.3. *In vitro* cytotoxicity study and bioimaging of living cells treated with N-CDs

Since CDs biocompatibility is one of the most important properties to consider for their applications in cell labeling and imaging [271], a specific cytotoxic effect of N-CDs was evaluated by performing a viability assay in the cancer cell line MDA-MB 231. After the incubation with different concentrations of N-CDs, a no significant inhibition in cell proliferation is individuated, with a viability over 80% for all the concentrations tested (Figure 4.14 i). No statistically significant differences were found for both the data at 24h and 48h of culture at concentrations less than 0.075 mg/ml compared to the positive control. Concentrations higher than 0.075 mg/ml showed instead a significant difference ($p<0.05$) with the control.

Once the absence of cytotoxicity was established, a preliminary study was carried out in order to analyse the particles localization inside the cells. For this purpose, MDA-MB 231 cells were incubated for 72 hr with two different N-CDs concentrations (0.1 and 0.3 mg/mL). Both blue and green signals are evident in Figure 4.14 ii. However, the fluorescence inside the cells treated with a concentration of 0.1 mg/mL appears feeble, muffled and punctuate (Figure 4.14 ii A-B) maybe due to the presence of the particles still in the media and partially inside the cells. Stronger blue and green signals are observed with an increase in N-CDs concentration (Figure 4.14 ii C-D). In this case, the N-CDs seem clearly presented in the nuclei and cytoplasm of MDA-MB 231 cells that also show a good morphology. Nevertheless, in both cases the two fluorescence signals are sufficiently localized inside the tumor cells probably due to the N-CDs internalization into the cells through a diffusion process, as already demonstrated for many nano-systems [272].

All the above results suggest that the N-CDs are biocompatible and can be employed as future fluorescence probes in biomedical applications thanks to the high fluorescent signals.

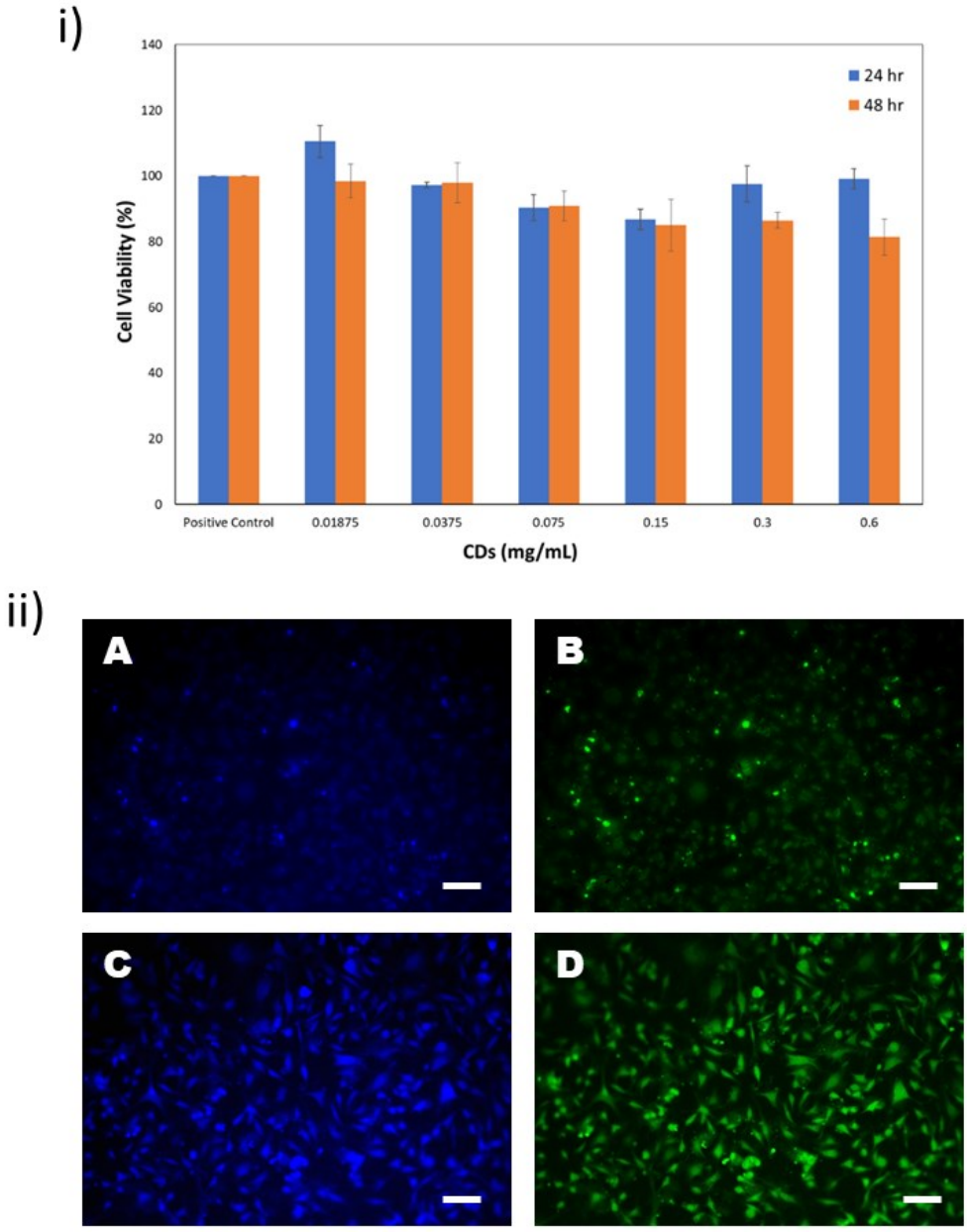

Figure 4.14: (i) Viability of MDA-MB 231 cells treated with CDs at various concentrations for 24 and 48 hr. The error bars are the standard deviations of triplicate samples. * = statistically significant differences compared to the positive control ($p < 0.05$). (ii) Fluorescence microscopy images of MDA-MB 231 cells labeled with CDs for 24 hr under excitation wavelength of 330−385 nm (blue A-C) and 450−480 nm (green B-D). The CDs concentration is 100 mg/mL (A-B) and 0.3 mg/mL (C-D). Scale bar, 50µm.

4.5. Part 5: Green-synthesis of Red-emitted doped and co-doped CDs

The efforts during the synthesis of carbon nanostructures, especially with long-wavelength emission and excellent PL properties, combined with the long/complex purification processes and the difficulties in easily manageable processes are only some of the major obstacles in moving CDs applications from the laboratory level to the global market for large-scale preparations [273]. Furthermore, the origin and mechanism of CDs optical properties, particularly the control of red emissions, and the relation with their structure are still not fully understood and represent an important challenge for the future CDs' use for biomedical applications.

In this work, the synergic contribution of different factors, such as precursors and solvents, production technique and hetero-doping, were exploited to synthesize new Red-emissive CDs with improved optical properties useful for future application in biomedical imaging and sensing. *p*-pD was chosen as Carbon (C)/Nitrogen (N) source and the solvothermal bottom-up approach as synthesis technique.

Numerous works in literature show a significant PL band shift from blue to red spectral region with the increase in solvent polarity [274–276]. Thus, in this work, the influence on CDs synthesis of three different solvents with different polarity (DMF 0.386, ethanol 0.654, and ultrapure water 1) were investigated and compared. The primary method of characterization concerned the evaluation of their optical properties. All the samples did not show a strong red PL with the excitation wavelength increasing from 310 to 540 nm. In addition, an excitation wavelength-dependent is evident for all these CDs (Figure 4.15). As expected, since water relative polarity is higher than ethanol (e-CDs) and DMF (d-CDs), w-CDs (water) exhibited a PL red shift toward higher wavelengths (Figure 4.15 C).

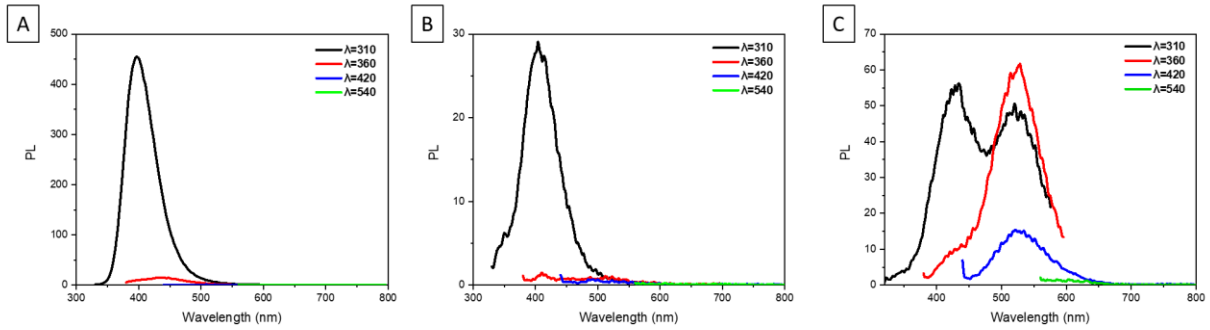

Figure 4.15: Photoluminescence (PL) emission spectra of p-pD CDs synthesised using with different solvents (A) DMF (d-CDs) (B) ethanol (e-CDs) water (w-CDs). Excitation wavelength range 310-540 nm.

For the formation of highly efficient red fluorescent CDs, a second batch was synthesized starting from *p*-pD as precursor and using water as solvent. Since the presence of a strong acid, especially nitric acid (HNO_3), was found to be efficient to prepare red C-dots, an acid-assisted solvothermal method was carried out for CDs synthesis [181, 277]. In addition to the N doping due to the presence of *p*-PD, the impact on the electronic structure and the fluorescence properties of the CDs was studied using the simultaneous co-doping of more than one heteroatom. Particularly, boron (B) and cobalt (Co) were selected as co-doping agents for the synthesis of N,B-CDs and N,Co-CDs. It is well-known that N doping acts as an electron-donor dopant forming significant surface defects into doped CDs. On the contrary, doping of electron-deficient heteroatom such as B, which should provide p-type doping characteristics, is comparatively a less explored method even if B-doped CDs demonstrated extraordinary solid-state fluorescence properties and excellent biocompatibility [278]. Here N and B co-doping was investigated for exploiting the simultaneous positive effects of n-type and p-type doping on CDs performance. Among the metal heteroatoms, the transition metal ion Co_2^+ has been widely selected for doping in the last years, due to its greater biological safety and good magnetic property. The combination of magnetic and fluorescence features allows their applications in both magnetic resonance and FI, suggesting them as excellent diagnostic probes or theranostic agents [279]. Nevertheless, synthesis of fluorescent magnetic N and Co co-doped CDs are still rare as well as their biological applications [280].

4.5.1. Structure characterizations

The structural and optical properties of the as-prepared CDs were checked by various characterizations approaches. Firstly, the morphology of the CDs was investigated by TEM. Figure 4.16 (a-c) shows quasi-spherical and well dispersed particles with uniform sizes. According to a statistical analysis of around 200 particles using ImageJ software, the average sizes of N-CDs, N,B-CDs and N,Co-CDs are 2.4 ± 0.6, 2.9 ± 0.5 and 3.2 ± 0.6 nm, respectively (Figure 4.16 d-f).

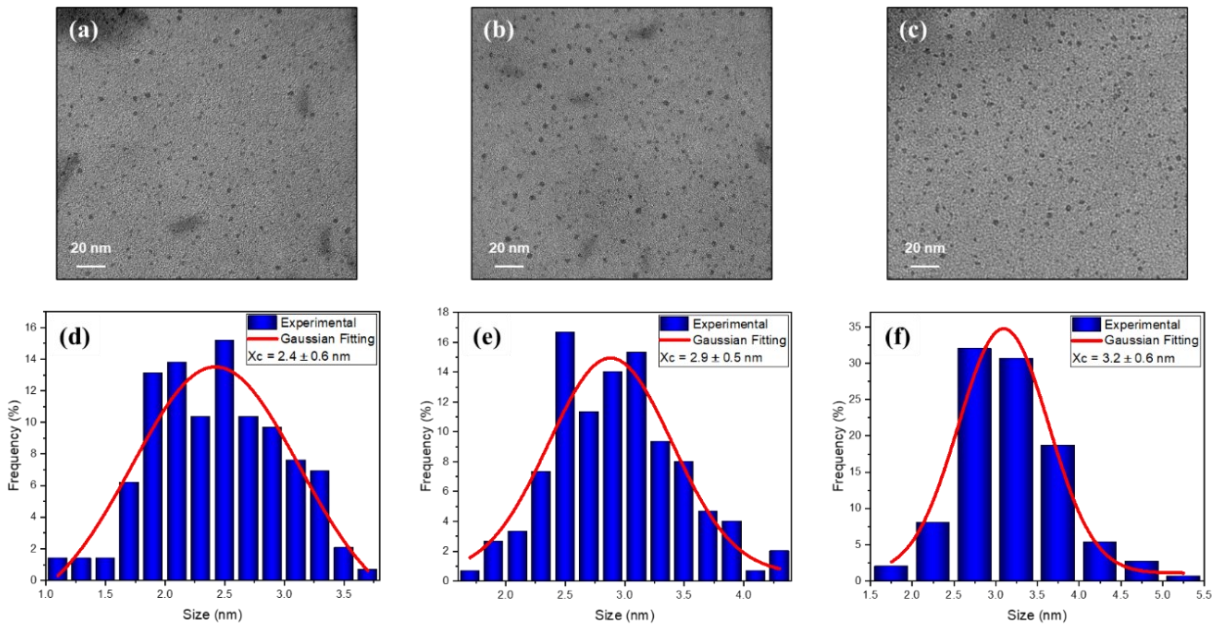

Figure 4.16: TEM images (a-c) and particle size distribution histograms (d-f) of N-CDs (a,d), N,B-CDs (b,e) and N,Co-CDs (c,f).

The chemical structure and functional groups were characterized by FTIR. As indicated in Figure 4.17, a broad peak centred at 3264-2736 cm-1 indicates the presence of the O-H vibration stretch of the carboxylic group, amide -N-H stretch and C-OH bond, while the sharper peak at 2604 cm-1 could be attributed to the covalent C-H bond [280, 281]. The absorption peaks located at 1608, 1540, and 1503 cm-1 are associated with the stretching vibrations of C=O, =C−H, and multiple C=C/C=N bonds, respectively [280], while the 1390 cm-1 is ascribed to the vibration of C-N-C, suggesting that N atoms has been successfully introduced into the CDs structure for all the

samples analysed. Furthermore, the C-O-C stretching vibration peak at 1070 cm-1 can be found in the spectra of the three synthesized CDs. Finally, a strong absorption peak is observed at 1290 cm-1 owing to -NO2 probably due to the reaction of HNO_3 with p-PD through the electrophilic reaction under hydrothermal conditions [277]. No significant differences were found in the chemical structure of all the three samples analysed.

Detailed surface composition and elemental contents of the doped and co-doped CDs were investigated by XPS. The XPS survey spectra (Figure 4.18 A-E-I) suggest that all the CDs are mainly composed of carbon, nitrogen and oxygen with the characteristic peaks of C1s at c.a. 284.9 eV, N1s at c.a. 400.0 eV and O1s at c.a. 531.8 eV [280], confirming the success of the Nitrogen doping. Furthermore, the co-doping in the N,B-CDs and N,Co-CDs is also confirmed by the existence of the characteristic peaks of B1s at c.a. 192.1 eV and Co2p at c.a.782.5, respectively. The amounts of the different elements in N-CDs, N,B-CDs, and N,Co-CDs are displayed in Table 4.1. In the high-resolution XPS of the three representative CDs samples (Figure 4.18 B-F-L), their C1s spectra are divided into four Gaussian peaks corresponding to C-C/C=C (284.6 eV), C-N (285.2), C-O (286.2 eV) and C=O/C=N (287.6 eV) [281, 282]. The N1s spectra (Figure 4.18 C-G-M) show four peaks at 398.7, 399.8, 401.6, and 406.7 eV, which could be assigned to Pyridinic N, Pyrrolic N, Graphitic N and N oxide bonds, respectively [283, 284]. The presence of $-NO_2$ could be a direct consequence of the reaction between HNO_3 and *p*-pD through electrophilic reaction under high temperature and high pressure [283]. Moreover, the O1s spectra (Figure 4.17 D-G-N) are de-convoluted into three significant peaks at 530.9 eV (C=O), 531.9 eV (C–O-C) and 533.0 eV (C-O-H), reveling the formation of oxygen functional groups on the surface [285]. The high resolution XPS spectrum of B1s (Figure 4.19 A) demonstrated the presence of three dominant peaks attributed to B-N bond (188.9 eV), which suggests the successful substitution of boron for the carbon next to the nitrogen and the doping in CDs [286], B-O bond in $B\text{-}C_2O$ (192.33) and B-O bond in $B\text{-}CO_2$ (192.77) [188, 287, 288]. The high-resolution spectrum of Co2p (Figure 4.19 B) consists of two relevant peaks: Co 2p3/2 at 782.80 eV and Co 2p1/2 at 795.5 eV which are assigned to its spin−orbit splitting with their satellite peaks at 785.8 eV and 802.8 eV, respectively [199, 280, 281].

Collectively, FTIR and XPS results confirm the successful doping of N element for all the as-synthesised CDs and the presence of the dopant B and Co in the co-doped N,B-CDs and N,Co-

CDs which can explain their strong red PL (as discussed later) due to the introduction of more surface defects and the reduction of nonradiative recombination [289]. Furthermore, the presence of various surface oxygenated and nitrous bonds/groups such as OH, C-OH, -N-H, C-C/C=C, C-N/C-O, C=O, and quaternary N may explain the high water dispersibility and stability [290, 291].

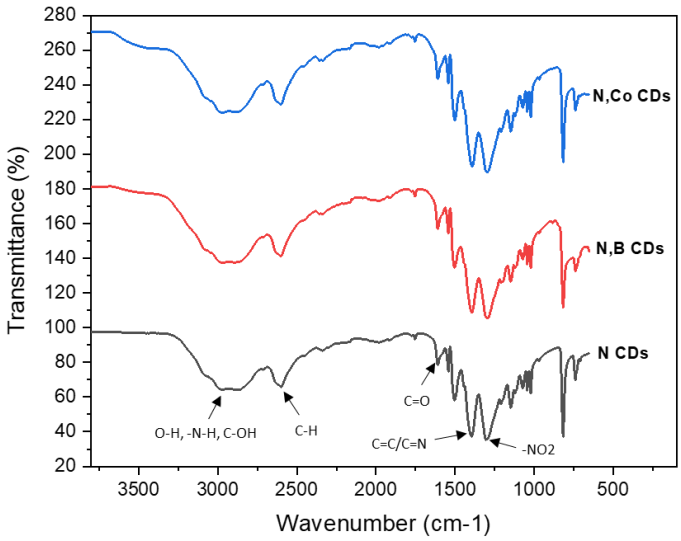

Figure 4.17: FTIR spectra of N-CDs (black line), N,B-CDs (red line) and N,Co-CDs (blue line).

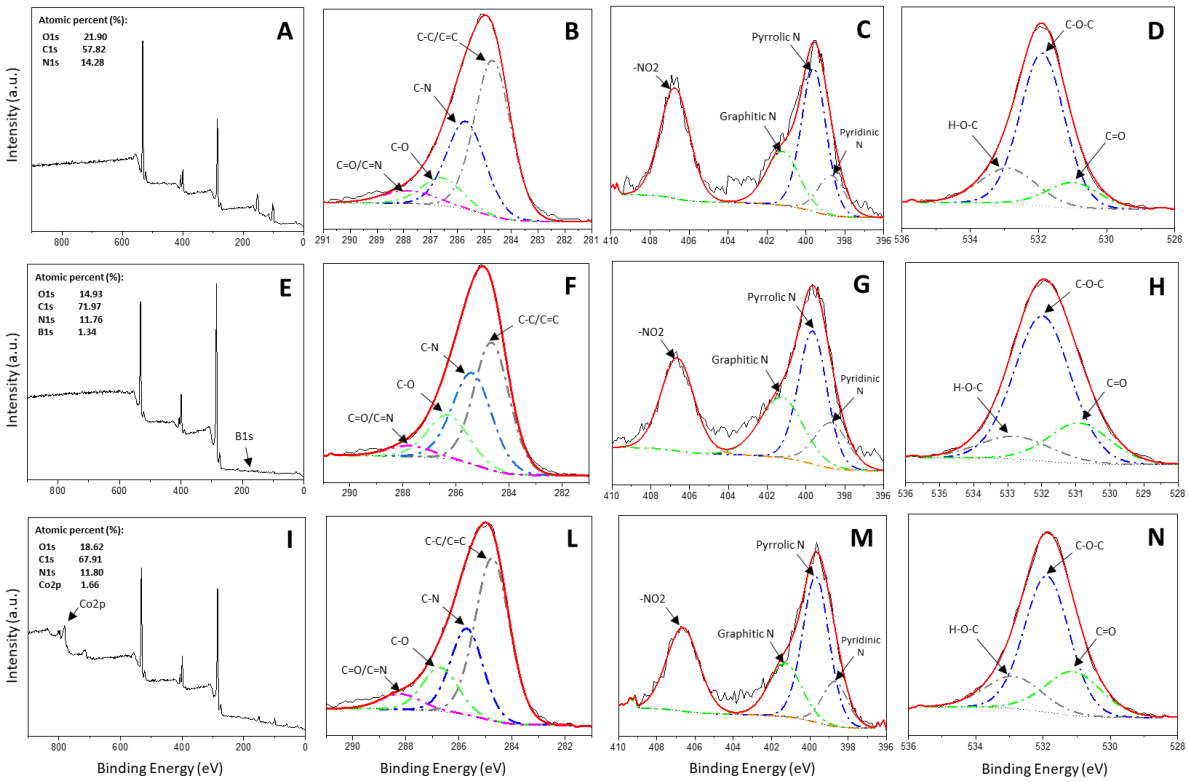

Figure 4.18: XPS survey and high-resolution spectra of N-CDs (A-D), N,B-CDs (E-H) and N,Co-CDs (I-N).

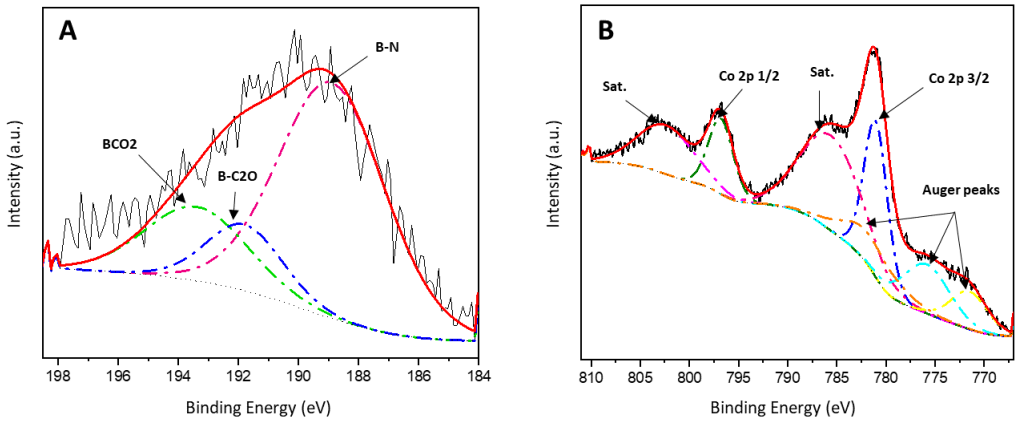

Figure 4.19: XPS High-resolution spectra of B1s (A) for N,B-CDs and Co2p (B) for N,Co-CDs

Table 4.2: The element analysis of N-CDs, N,B-CDs and N,Co-CDs, respectively.

Sample	Elements	Atomic Percentage (%)
N-CDs	C1s	57.82
	N1s	14.28
	O1s	21.90
N,B-CDs	C1s	71.97
	N1s	11.76
	O1s	14.93
	B1s	1.34
N,Co-CDs	C1s	67.91
	N1s	11.80
	O1s	18.62
	Co2p	1.66

4.5.2. Optical, electrical and magnetic properties

Uv-vis absorption (abs) and photoluminescence (PL) spectroscopy were used to study the optical properties of the CDs.

All the Uv-vis abs spectra (Figure 4.20) show an intense peak around 282 nm corresponding to the electronic transition $\pi \rightarrow \pi^*$ of aromatic sp^2 carbon core [277, 289]. The N-CDs exhibit a peak around 398 nm (Figure 4.20 A) which can be assigned to the $n \rightarrow \pi^*$ electronic transition of the surface groups -C=O, -C=N [277, 278], confirming the success of the doping. A red shift of this peak is observed upon N,B- and N,Co-CDs (Figure 4.19 B-C), which is probably due to some structural effects as a consequence of the co-doping. Moreover, an absorption band around 520 nm is displayed in all the UV-vis abs spectra which can be ascribed to the numerous surface states

corresponding to a small bandgap [292]. From Figure 4.20 D is evident a stronger absorption for the co-doped CDs, compared to N-CDs, at the same concentration of 1mg/ml.

In contrast to the CDs of the first batch and other traditional CDs [293–295], an excitation-independent PL was observed. The emission spectra of all the CDs in the second batch revealed a strong red emission with a maximum at around 600 nm within the range of the excitation wavelengths (λex) from 420 to 560 nm (Figure 4.21 A-B-C). This peak were more intense for both N,B-CDs and N,Co-CDs, compared to N-CDs. The single doped CDs exhibited a different behaviour showing a multiple-peak at 600 nm and 680 nm when excited with λex between 460 and 560 nm (Figure 4.21 A).

In addition to PL, PLE measurements were carried out in order to identify the origin of the emission peaks together with providing more detailed information on the origin of the absorption peaks. In figure 4.21 D-E-F are reported the PLE spectra of the three CDs analysed. By monitoring the maximum emission at λem= 600 nm, for all the CDs samples, two main excitation peaks can be observed at 430 and 520 nm (Figure 4.21 D-E-F). These features are more accentuated in the N-CDs spectrum. N-CDs also showed a decrease in the emission intensity after λex=520 nm, supporting the aforementioned observations seen for the different UV-vis abs and PL behaviour.
The relative QYs of N-CDs, N,B-CDs and N,Co-CDs were measured using Rhodamine 6G as standard and calculated by Eq. 4 (Chapter 3: Materials and Methods, Part 5) to be 8%, 17% and 18% (Table 4.2), respectively, indicating a beneficial effect of the co-doping . The different optical properties exhibited by the samples can be attributed to the remarkable differences in chemical microstructure and surface chemical states. First of all, the common strong red emission of all the CDs obtained with the acid treatment (second batch) could be explained by the presence of the H^+ and NO_3^- during the reaction which could act as a catalyst to speed up reaction rate [283]. Upon co-doping with both metal and non-metal ions, the different absorption/emission/excitation features and the higher QYs of N,B- and N,Co-CDs compared to the N-CDs, suggests that simultaneous doping with more than one atom can positively affect CDs optical properties due to the structural and surface changes generated.

The zeta potential of the N,CDs, N,B-CDs and N,Co-CDs in water solution was evaluated to be +30.7 mV, +35.7 mV and +47.6 mV, respectively (Table 4.2). The strong positive charge of these CDs is due to the presence of abundant nitrogenous and amino groups on the surface,

conferring a high stability in solution [290, 296–298]. These data are in agreement with the XPS and FTIR results.

Table 4.3: Quantum Yield (QY) and Zeta potential values for1mg/ml of N-CDs, N,B-CDs and N,Co-CDs in ultrapure water.

Sample	Quantum Yield (%)	Zeta potential
N-CDs	8	+30.7
N,B-CDs	17	+35.7
N,Co-CDs	18	+47.6

As a direct consequence of the doping with N and Co elements, the as-prepared CDs may possess magnetic properties. To verify that, electron paramagnetic resonance (EPR) was performed at room temperature. Figure 4.22 depicts the EPR spectra of N-CDs, N,B-CDs and N,Co-CDs. It can be seen that N-CDs show a single signal at g=1.995 which reveals a singly occupied orbital in ground-state carbon dots [299] (Figure 4.22 A). N,B-CDs exhibited a single signal at the same position of the N-CDs but in this case no symmetry along the axis is present, maybe due to the presence of the B^+ on the surface of the CDs (Figure 4.22 B). Notably, the EPR spectrum of N,Co-CDs (Figure 4.22 C) presents hyperfine splitting lines and a shifted *g*-value at 2.001. A possible explanation for the rising *g*-value and the multiple hyperfine signal in the EPR spectrum could be a filling of vacancies and the induced paramagnetic defects on CDs surface due to the incorporation of Co(II) ions [300]. However, since the electronic structure and behaviour of several transition metals, including Co and Cu, remains unclear so far [301], further experimental and theoretical investigations should be done. Nonetheless, these preliminary results demonstrated how doping with Co ions can induce strong magnetic properties and provided an informative viewpoint on the potential of N,Co-doped CDs for disease diagnosis, such as magnetic resonance, and clinical therapy.

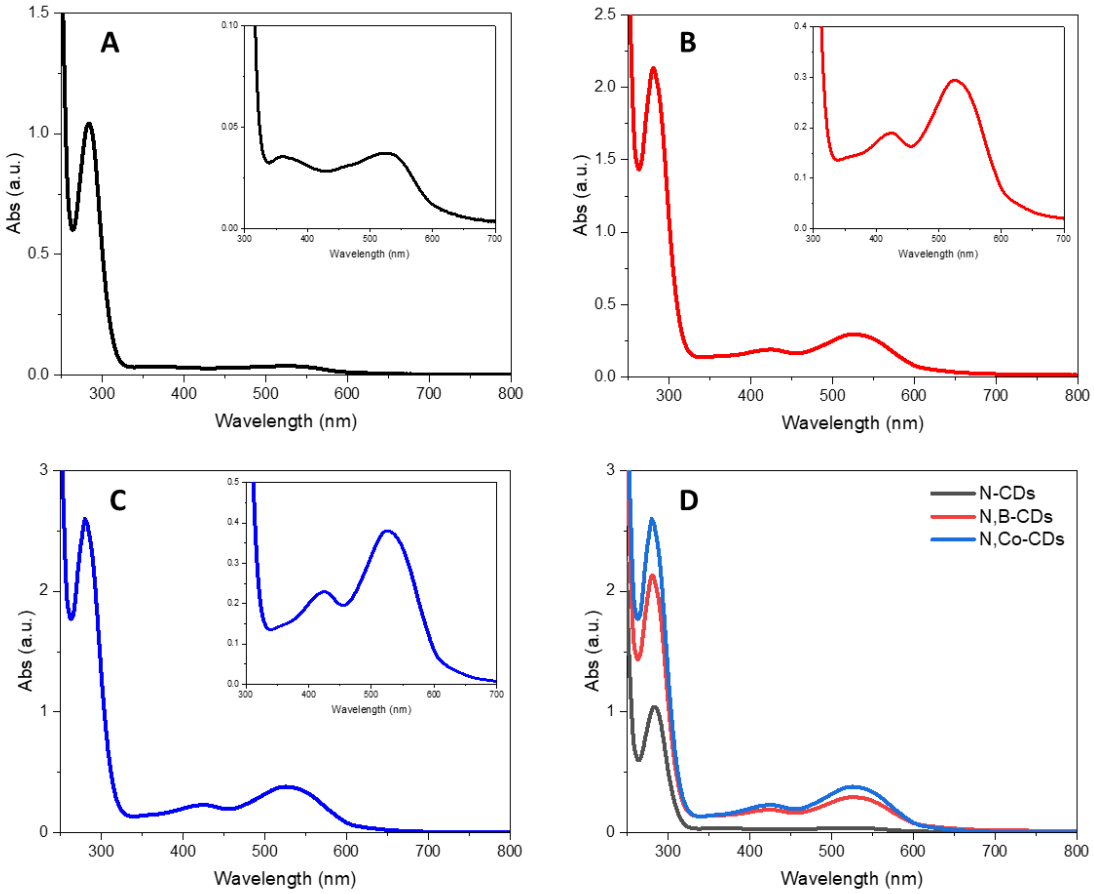

Figure 4.20: UV-vis absorption spectra of N-CDs (A), N,B-CDs (B) and N,Co-CDs (C). The corresponding insets in each graph show a zoomed area between 300 nm and 700 nm of the absorption spectrum. Comparison of Uv-vis abs spectra of N-CDs (black line), N,B-CDs (red line) and N,Co-CDs (blue line) at 1mg/ml in aqueous solution.

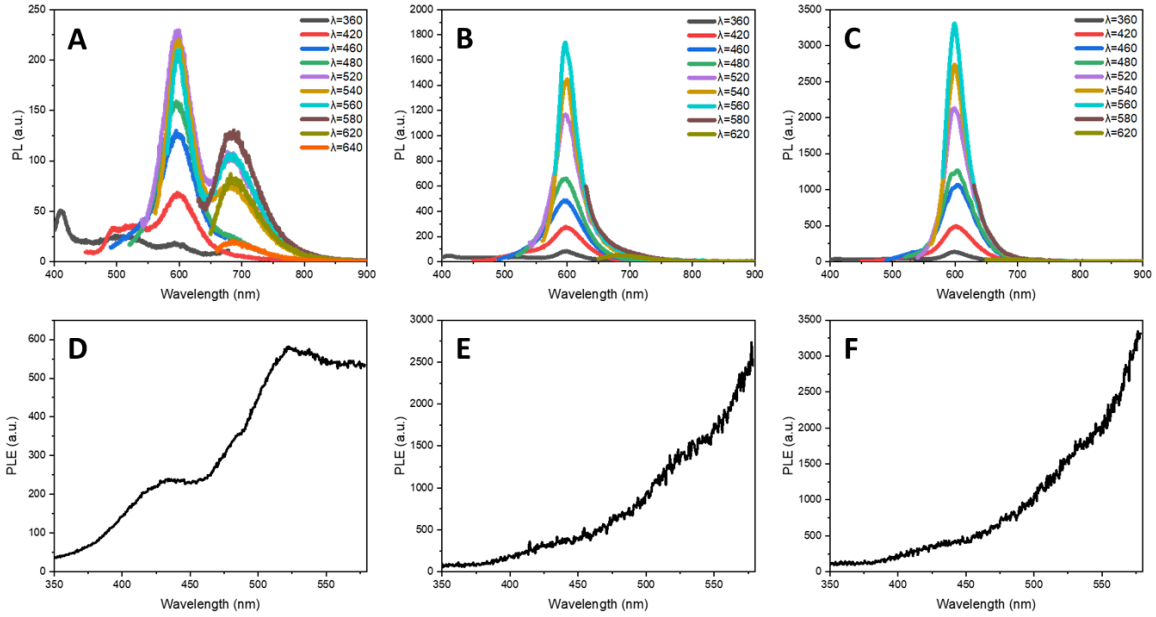

Figure 4.21: PL (A-B-C) (λex between 360 and 620 nm) and PLE (D-E-F) (λem=600nm) spectra of N-CDs (A-D), N,B-CDs (B-E) and N,Co-CDs (C-F).

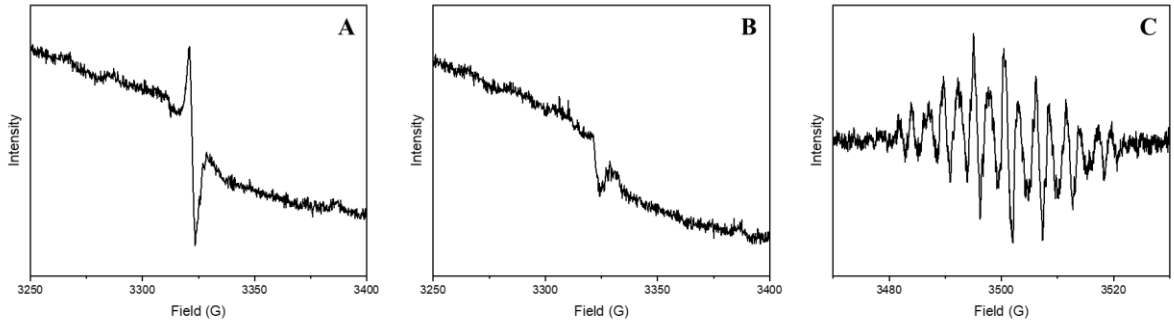

Figure 4.22: EPR spectra of N-CDs (A), N,B-CDs (B) and N,Co-CDs (C).

4.5.3. Photostability investigation

The high stability is one of the significant properties of nano-size fluorescence materials which plays an important role in making them suitable for applications in various fields, especially for chemical and biological applications [302, 303]. In this project, the effects of parameters such

as different pH values and exposure under long time UV light irradiation (24h) on the photo-stability of the CDs were examined.

A key factor which still greatly limits CDs practical application into large scale is the PL-pH sensitivity. As shown in Figure 4.23 A, the fluorescence intensity of N-CDs, N,B-CDs and N,Co-CDs, with the maximum peak at c.a. 600 nm, remains almost unchanged in solutions within the wide pH range from 3.0 to 10.0. However, the PL intensity quickly decreased under strong alkaline conditions (pH =12.0), with a blue shift for both N-CDs and N,B-CDs while complete quenching of the emission was observed in N,Co-CDs. From the histogram in Figure 4.23 B, it is possible to note that the intensity of the red peak remains almost unchanged for all the samples with pH values less than 12. A possible explanation for the as-described behaviour could be the pH-induced aggregation of CDs with the pH variation as a consequence of the protonation or deprotonation of carboxylic/amino functional groups on the CDs surface [304]. Under strong alkaline conditions, noncovalent molecular interactions, such as hydrogen bonds between the carboxyl groups, can induce CDs aggregation and consequently a PL quenching [305, 306]. Moreover, the protonation or deprotonation of amino groups on the surface could also lead to CDs aggregation as the pH rises. In fact, as previously reported, CDs with high content of amino functional groups have a positive charged surface and are stable under strong acidic conditions. In contrast, under an alkaline environment, the deprotonation of amino groups promotes the decrease of CDs charge causing their aggregation [304]. However, a general consensus on the mechanism of CDs PL-pH sensitivity has still not been reached.

The stability of doped and co-doped CDs against photobleaching was evaluated by exposing them to long UV irradiation. After 24 hours of irradiation under UV light (λem=365nm, intensity 1W/cm^2) the PL intensity of the peak centred at 600nm was almost unchanged for all the samples (Figure 4.23 C, orange bars). A different behaviour can be observed for the PL intensity of the peak at 698 nm (Figure 4.23, blue bars). In this case, no variation in intensity was observed for N,B-CDs and N,Co-CDs, while for the N-CDs a steady decrease can be seen until almost complete quenching after 24 h of irradiation. Such behaviour could indicate the presence of molecular fluorophores on the surface of the CDs or in solution. According to recent studies, the hydrothermal/solvothermal methods for CDs synthesis bring to the co-existence of carbon dots and organic molecular fluorophores which have significant impact on the optical properties of CDs

but are extremely sensitive to photobleaching [307]. This suggests that the presence of fluorophores is responsible for the NIR emission peak, while B and Co co-dopant elements show a higher emission at 600 nm (without a secondary emission at 680 nm). The presence of these dopants can probably help the reorganization of the CDs structure by protecting the carbon core and increasing the CDs stability, avoiding the formation of by-products.

All these results showed the great photochemical stability of the doped and co-doped CDs under different environmental conditions promoting their potential for providing solutions within the scientific research for environmental, pharmaceutical and also *in vivo* applications.

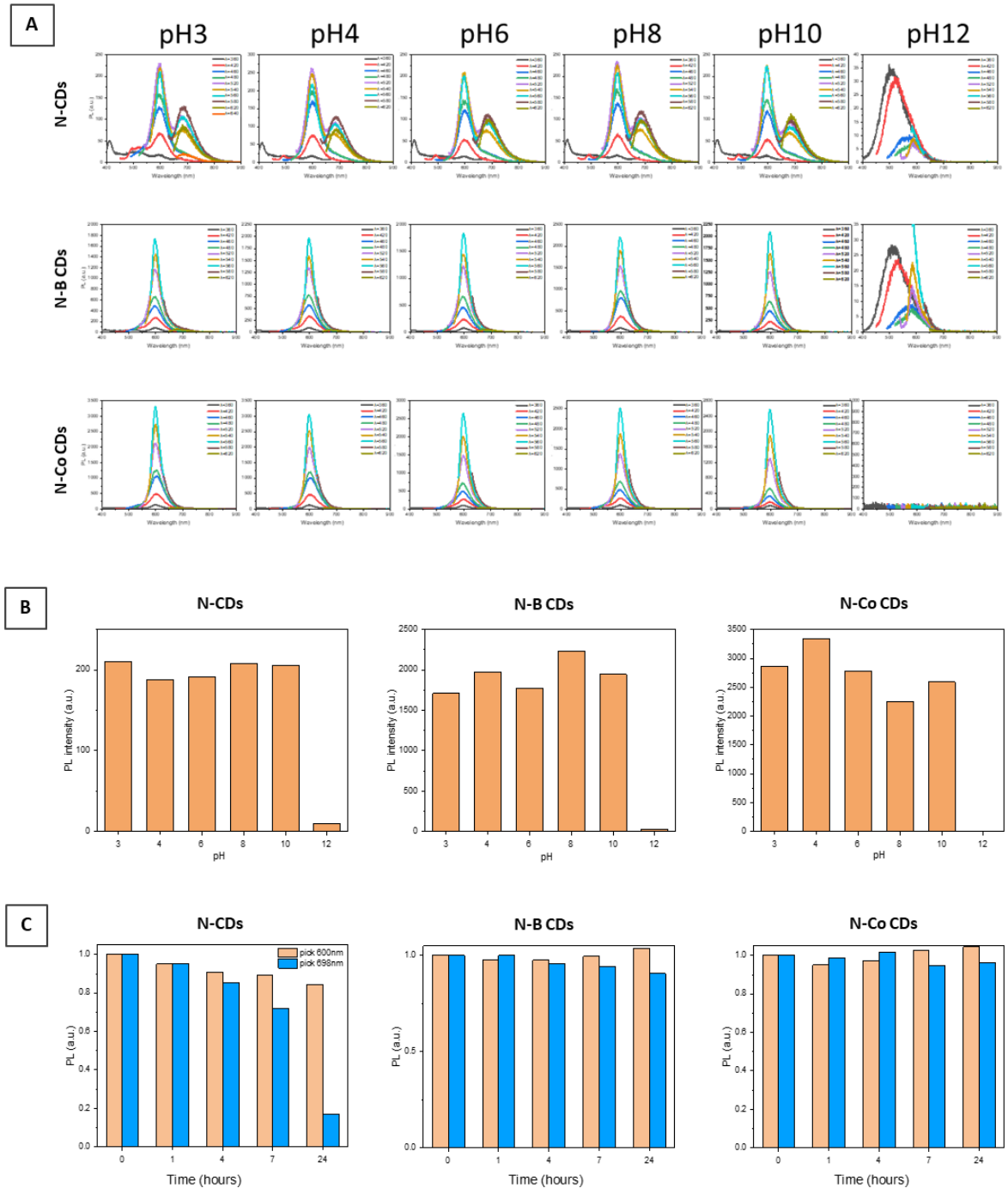

Figure 4.23: Photostability of N-CDs, N,B-CDs and N,Co-CDs. Influence of the solution pH on the (A) fluorescence emission and (B) emission intensity of the main peak at 600nm. (C) Effect of exposure under UV irradiation for 24 h on the emission intensity. Orange bars correspond to the main emission peak at 600nm, while the blue bars are related to the NIR peak.

The results presented in Part 1 (Figure 4.1) and in Part 3 (Figure 4.8, 4.9) have been reported in the paper “PLLA scaffolds with controlled architecture as potential microenvironment for in vitro tumor model” published by M. E. Lombardo, F. Carfì Pavia, I. Vitrano, G. Ghersi, V. Brucato, F. Rosei, V. La Carrubba in Tissue and Cell, April 2019.

The results presented in Part 1 (Figure 4.5 B-C), Part 2 (Figure 4.6, 4.7, 4.8) and in Part 4 (Figure 4.10, 4.11) have been reported in the paper “Novel dual-flow perfusion bioreactor for in vitro pre-screening of nanoparticles delivery: design, characterization and testing” published by M. E. Lombardo, F. Carfì Pavia, E. F. Craparo, E. Capuana, G. Cavallaro, V. Brucato, V. La Carrubba in Bioprocess and Biosystems Engineering, June 2021.

The results presented in Part 5 (Fig. 4.16 - 4.23) are present in the paper “Solar photocatalytic degradation of Methylene Blue dye using red-emitted doped CDs”, co-authored by M.E. Lombardo, D. Benetti, F. Rosei. (Manuscript in preparation)

CONCLUSION AND FUTURE PERSPECTIVES

The aim of this work was the design and the development of an *in vitro* apparatus for biomedical and pharmaceutical applications trying to limit the massive abuse of *in vivo* animal testing. There is no doubt that the use of animals in science and medicine has significantly benefited human beings. However, testing certain substances first on cellular models allows to exclude directly certain compounds if results are not favorable, before moving to animal models, or at least reduce the number of *in vivo* experimentations. Although the 3D culture method has not yet replaced the traditional 2D models on a large scale, it has become easier to use and routinely applicable, allowing researchers to switch to this technology in order to obtain better cell culture models and *in vitro* alternatives to animal models more human and time/cost effective.

In this thesis, I have shown the development and validation of a dual-flow perfusion bioreactor as a potential system for pre-screening *in vitro* tests. Its original design offers several significant advantages over existing bioreactors. First, the device allows a separate control of two perfusion flows through an “ad hoc” hollow cylindrical porous scaffold. The external perfusion flow guarantees both a good recirculation and oxygenation of the medium, whereas the inner perfusion flow guarantees a radial diffusion through the entire scaffold volume. The direction of this radial flux and the perfusion flow rate can be accurately regulated, according to the desired application. Therefore, the dual-flow design certainly allows maximizing the efficacy of the perfusion dynamic cell culture inside the 3D device. Moreover, thanks to the tunable radial flow from the inner to the outer surface of the scaffold and vice versa this system is able to control migration/diffusion of nanoparticles across a hollow scaffold, while mimicking flow conditions

suitable for drug release from nano-carriers. Different models of nanocarriers were presented in this work. Both polymeric and carbon-based nanoparticles were tested via diffusion tests with the intention to demonstrate the flexibility of the apparatus and good flow diffusion of nano-systems throughout 3D polymeric microporous structures.

Nowadays, cancer is a primary cause of death worldwide, with almost 9.6 million deaths in 2018, especially because of lack of efficient approaches for early cancer detection and a deep knowledge about their biology [308]. In this thesis, to make the presented system suitable for cancer biology studies, chemotherapics pre-screening and development of new therapies, PLLA scaffolds were synthesised via TIPS with different architectures of the porous matrix. A scaffold with highly interconnected porous matrix, an average pore size of 40-50 μm, and a collagen coating resulted an appropriate support for both MDA-MB 231 (breast cancer) cells growth and proliferation inducing the formation of multicellular tumor aggregates rather than a monolayer with a typical tumoroid morphology.

To complete the studies, an easy, rapid and environmentally friendly synthesis of red-emitting CDs was reported. Red-emitting CDs present promising potential in cell imaging, *in vitro*/*in vivo* imaging, and *in vivo* labeling and diagnosis, however it is still very challenging to fabricate CDs with strong long-wavelength emission through a facile and cost-effective strategy [309]. Three different hetero-atoms were chosen to prepare doped CDs (N-CDs, N,B-CDs, N,Co-CDs) which showed uniform morphology, abundant functional groups and a strong red emission with a typical excitation-wavelength-independent emission. The co-doping improved the QY and the stability of the CDs, showing a high photostability under visible light irradiation and different pH values. Overall, the as-synthesized CDs showed promising optical features for their future use as alternatives fluorescence probes to conventional organic dyes and potential nano-carriers for future clinical trials.

This dissertation demonstrated the great potential of the dual-flow perfusion bioreactor as a versatile device with impact in numerous fields, including biomedical and pharmaceutical applications. However, improvements of the existing system design as well as its performance are necessary to have major opportunities of further utilizations. In this final section some suggestions for further enhancements of the whole apparatus are listed:

- the bioreactor design should be simplified into a small-scale reactor with multiple independent culture chambers for reducing the experimental and operating time and costs;
- implementation of some sensors, such as mixing speed, radial perfusion flow direction, oxygen concentration, pH control, could be potential solutions to expand the information level obtained per each experiment;
- a deeper investigation on the morphology of the hollow cylindrical scaffold, regarding the porosity and pore size, should be carry out to increase the flexibility of the device;
- it would be interesting to perform the same diffusion testing inside the bioreactor using the as-synthesized Red-emitted CDs as carrier model, including a cytotoxicity test and bioimaging with a living cell line;
- a general experiment growing living cells into the porous polymeric matrix (not only cancer cell lines), grafting the nano-carriers with a potential drug and exploiting the perfusion system of the bioreactor should be finally performed.

With all these improvements in the entire apparatus, the goal of *in vitro* pre-screening tests of new drugs and development of new therapies is just around the corner.

CONCLUSION ET PERSPECTIVES FUTURES

L'objectif de ce travail a été la conception et le développement d'un appareillage in vitro pour des applications biomédicales et pharmaceutiques essayant de limiter l'abus massif des tests in vivo sur les animaux. Il ne fait aucun doute que l'utilisation des animaux en science et en médecine ait grandement bénéficié aux êtres humains. Cependant, tester d'abord certaines substances sur des modèles cellulaires, avant de passer à des modèles animaux, permet d'exclure directement certains composés si les résultats ne sont pas favorables, ou du moins de réduire le nombre d'expérimentations in vivo. Bien que la méthode de culture 3D n'ait pas encore remplacé les modèles 2D traditionnels à grande échelle, elle est devenue plus facile à utiliser et à appliquer en routine, permettant aux chercheurs de basculer vers cette technologie afin d'obtenir de meilleurs modèles de culture cellulaire et des alternatives in vitro plus bienfaisants et plus efficaces en termes de temps/coût que les modèles animaux.

Dans cette thèse, j'ai montré le développement et la validation d'un bioréacteur à perfusion double flux comme système potentiel de pré-criblage de tests *in vitro*. Sa conception originale offre plusieurs avantages significatifs par rapport aux bioréacteurs existants. Tout d'abord, le dispositif permet un contrôle séparé de deux flux de perfusion à travers un échafaudage poreux cylindrique creux « ad hoc ». Le flux de perfusion externe garantit à la fois une bonne recirculation et une bonne oxygénation du milieu, tandis que le flux de perfusion interne garantit une diffusion radiale dans tout le volume de l'échafaudage. La direction de ce flux radial et le débit de perfusion peuvent être réglés avec précision, selon l'application souhaitée. Par conséquent, la conception à double flux permet certainement de maximiser l'efficacité de la culture cellulaire dynamique de

perfusion à l'intérieur du dispositif 3D. De plus, grâce au flux radial réglable de la surface interne à la surface externe de l'échafaudage et vice versa, ce système est capable de contrôler la migration/diffusion des nanoparticules à travers un échafaudage creux, tout en imitant les conditions d'écoulement adaptées à la libération de médicaments à partir de nano-supports. Différents modèles de nano-porteurs ont été présentés dans ce travail. Des nanoparticules polymériques et à base de carbone ont été testées via des tests de diffusion dans le but de démontrer la flexibilité de l'appareil et la bonne diffusion des nano-systèmes à travers des structures microporeuses polymériques 3D.

De nos jours, le cancer est une des causes principales de décès dans le monde, avec près de 9,6 millions de décès en 2018, notamment en raison du manque d'approches efficaces pour la détection précoce des cancers et d'une connaissance approfondie de leur biologie. Dans cette thèse, pour rendre le système présenté adapté aux études de biologie du cancer, au pré-criblage chimiothérapeutique et au développement de nouvelles thérapies, des échafaudages PLLA ont été synthétisés via TIPS avec différentes architectures de la matrice poreuse. Un échafaudage avec une matrice poreuse hautement interconnectée, une taille moyenne des pores de 40-50 µm et un revêtement de collagène ont permis de soutenir de manière appropriée à la fois la croissance et la prolifération des cellules MDA-MB 231 (cancer du sein), induisant la formation d'agrégats tumoraux multicellulaires plutôt qu'un monocouche avec une morphologie tumoroïde typique.

Pour compléter les études, une synthèse facile, rapide et respectueuse de l'environnement des CD à émission rouge a été enregistrée. Les CD émettant dans le rouge présentent un potentiel prometteur dans l'imagerie cellulaire, l'imagerie *in vitro/in vivo*, et le marquage et le diagnostic *in vivo*, mais il est toujours très difficile de fabriquer des CD avec une forte émission à grande longueur d'onde avec une stratégie simple et rentable. Trois hétéroatomes différents ont été choisis pour préparer des CD dopés (N-CD, N, B-CD, N, Co-CD) qui présentaient une morphologie uniforme, des groupes fonctionnels abondants et une forte émission rouge avec une émission typique indépendante de la longueur d'onde d'excitation. Le co-dopage a amélioré le QY et la stabilité des CD, montrant une photostabilité élevée sous irradiation de lumière visible et différentes valeurs de pH. Dans l'ensemble, les CD tels que synthétisés présentaient des caractéristiques optiques prometteuses pour leur utilisation future en tant que sondes de

fluorescence alternatives aux colorants organiques conventionnels et en tant que nano-supports potentiels pour les futurs essais cliniques.

Cette thèse a démontré le grand potentiel du bioréacteur de perfusion à double flux en tant que dispositif polyvalent ayant un impact dans de nombreux domaines, y compris les applications biomédicales et pharmaceutiques. Cependant, des améliorations de la conception du système existant ainsi que de ses performances sont nécessaires pour avoir des opportunités majeures d'utilisations ultérieures. Quelques suggestions pour d'autres améliorations de l'ensemble de l'appareil sont énumérées ci-dessous :

- la conception du bioréacteur devrait être simplifiée en un réacteur à petite échelle avec plusieurs chambres de culture indépendantes pour réduire les coûts expérimentaux et d'exploitation;
- la mise en œuvre de certains capteurs, tels que la vitesse de mélange, la direction du flux de perfusion radiale, la concentration en oxygène, le contrôle du pH, pourraient être des solutions potentielles pour étendre le niveau d'information obtenu pour chaque expérience;
- une enquête plus approfondie sur la morphologie de l'échafaudage cylindrique creux, en ce qui concerne la porosité et la taille des pores, devrait être effectuée pour augmenter la flexibilité du dispositive;
- il serait intéressant d'effectuer le même test de diffusion à l'intérieur du bioréacteur en utilisant les CD synthétisés à émission rouge comme modèle de support, y compris un test de cytotoxicité et une bio-imagerie avec une lignée cellulaire vivante;
- une expérience générale faisant croître des cellules vivantes dans la matrice polymérique poreuse (pas seulement des lignées cellulaires cancéreuses), greffant les nano-supports avec un médicament potentiel et exploitant le système de perfusion du bioréacteur devrait enfin être réalisée.

Avec toutes ces améliorations apportées à l'ensemble de l'appareil, l'objectif des tests de présélection *in vitro* de nouveaux médicaments et du développement de nouvelles thérapies s’approche à grands pas.

CONCLUSIONI E PROSPETTIVE FUTURE

Lo scopo di questo lavoro di tesi è stato la progettazione e lo sviluppo di un sistema *in vitro* per applicazioni sia biomediche sia farmaceutiche cercando di ridurre l'abuso della sperimentazione animale. Non vi è alcun dubbio che l'uso degli animali ha apportato notevoli benefici nel mondo della scienza e della medicina. Tuttavia, testare alcune sostanze prima *in vitro* su modelli cellulari consentirebbe di escludere direttamente alcuni composti, nel caso in cui i risultati non fossero favorevoli, ancor prima di passare al modello animali, o almeno di ridurre il numero di sperimentazioni. Sebbene il metodo di coltura cellulare 3D non abbia ancora sostituito su larga scala i tradizionali modelli 2D, è diventato sempre più facile e applicabile, consentendo ai ricercatori di ottenere modelli cellulari migliori e alternative *in vitro* ai modelli animali, più umani e più efficienti in termini di tempo/costo.

In questa tesi si è discusso dello sviluppo e della validazione di un bioreattore a perfusione dotato di doppio flusso, proposto come potenziale sistema *in vitro*, in particolare, per il test di pre-screening di nuovi farmaci. Il suo design originale offre numerosi vantaggi rispetto ai bioreattori già esistenti. Il dispositivo, infatti, consente un controllo separato di due flussi di perfusione attraverso una matrice microporosa cilindrica cava, realizzata "ad hoc" per il sistema. Il flusso di perfusione esterno garantisce sia un buon ricircolo sia una buona ossigenazione del mezzo di coltura cellulare, mentre il flusso di perfusione interno garantisce una diffusione radiale attraverso l'intero volume poroso. La direzione di questo flusso radiale e la portata di perfusione possono essere facilmente regolati in base all'applicazione desiderata. Pertanto, il design a doppio flusso consente sicuramente di massimizzare l'efficacia della coltura cellulare tramite perfusione in

dinamico all'interno di matrici porose. Inoltre, grazie al flusso radiale regolabile dalla superficie interna a quella esterna del supporto poroso e viceversa, questo sistema è in grado di controllare la migrazione/diffusione di nanoparticelle, imitando le condizioni di flusso adatte per il rilascio di farmaci da nano-carrier. In questo lavoro sono stati presentati diversi modelli di nanocarrier. Sia le nanoparticelle polimeriche che quelle a base di carbonio sono state testate tramite test di diffusione con l'intenzione di dimostrare la flessibilità dell'apparato e la buona diffusione del flusso di nanosistemi attraverso strutture microporose polimeriche 3D.

Al giorno d'oggi, il cancro è una delle principali cause di morte in tutto il mondo, con quasi 9,6 milioni di decessi nel 2018, soprattutto a causa della mancanza di approcci efficaci per la diagnosi precoce e di una profonda conoscenza della loro biologia. In questo lavoro, per rendere il sistema presentato adatto anche a studi sulla biologia del cancro, pre-screening di chemioterapici e sviluppo di nuove terapie, sono stati sintetizzati supporti polimerici con diverse marfologie della matrice porosa. Il PLLA è stato utilizzato come biopolimero e la Separazione di Fase come tecnica di sintesi. La matrice con pori altamente interconnessi, una dimensione media dei pori di 50 μm e un rivestimento in collagene, si è rivelata il supporto appropriato per la crescita e la proliferazione delle cellule MDA-MB 231 (cancro al seno), inducendo la formazione di aggregati tumorali multicellulari con una tipica morfologia tumoroide.

Per completare la sperimentazione, sono stati sintetizzati Carbon Dots con emissione nel campo del rosso tramite una sintesi facile, rapida ed ecologica. I CDs con emissione rossa presentano un potenziale promettente nell'imaging cellulare, nell'imaging *in vitro/in vivo* e nella diagnosi *in vivo*, tuttavia è ancora molto difficile la loro sintesi attraverso una strategia facile ed economica. Sono stati selezionati tre diversi etero-atomi per preparare CD dopati (N-CD, N,B-CD, N,Co-CD) che hanno mostravano morfologia uniforme, abbondanti gruppi funzionali sulla superficie, e una forte emissione rossa indipendente dalla lunghezza d'onda di eccitazione. Il co-doping ha migliorato il QY e la stabilità dei CD, mostrando un'elevata fotostabilità sotto irradiazione con luce visibile e a contatto con diversi valori di pH. Nel complesso, i CD sintetizzati hanno mostrato caratteristiche ottiche promettenti per il loro uso futuro come sonde di fluorescenza, in alternative ai coloranti organici convenzionali, e come potenziali nano-carrier per futuri studi clinici.

Questa tesi ha dimostrato il potenziale del bioreattore a perfusione a doppio flusso come dispositivo versatile, con impatto su numerosi campi, comprese le applicazioni biomediche e farmaceutiche. Tuttavia, saranno necessari miglioramenti della progettazione del sistema esistente e delle sue prestazioni per ampliare le opportunità di applicazione. In questa sessione finale sono elencati alcuni suggerimenti per ulteriori potenziamenti dell'intero apparato:

- la progettazione del bioreattore dovrebbe prevedere una semplificata in un bireattore su piccola scala, con più camere di coltura indipendenti, per ridurre i tempi e i costi sperimentali e operativi;

- l'implementazione di alcuni sensori per la rilevazione della la velocità di miscelazione, la direzione del flusso di perfusione radiale, il livello di ossigeno nel mezzo di coltura, il controllo del pH, potrebbero essere potenziali soluzioni per espandere il livello di dati e informazioni ottenute per ogni esperimento;

- un'indagine più approfondita dovrebbe essere effettuata sulla morfologia dello scaffold cilindrico, per quanto riguarda la porosità e la dimensione dei pori della matrice, per aumentare la flessibilità del dispositivo;

- sarebbe interessante eseguire lo stesso test di diffusione, mostrato nel Capitolo 3-parte 4, all'interno del bioreattore utilizzando come modello di vettore i CD con emissione nel rosso, insieme a un test di tossicità e bioimaging con una linea cellulare vivente (oltre che tumorale);

- dovrebbe infine essere eseguito un test generale che preveda la crescita di cellule nella matrice polimerica porosa (non solo linee cellulari cancerose), utilizzando le nanoparticelle con un potenziale farmaco. Tutto questo sfruttando il sistema di perfusione del bioreattore.

Con tutti questi miglioramenti nell'intero apparato, l'obiettivo dei test di pre-screening *in vitro* di nuovi farmaci e lo sviluppo di nuove terapie è certamente dietro l'angolo.

REFERENCES

1. Zang R, Ding L, Tang I-C, et al (2012) Cell-Based Assays in High-Throughput Screening for Drug Discovery. Int J Biotechnol Wellness Ind 1:31–51. https://doi.org/10.6000/1927-3037.2012.01.01.02
2. Isgut M, Rao M, Yang C, et al (2018) Application of Combination High-Throughput Phenotypic Screening and Target Identification Methods for the Discovery of Natural Product-Based Combination Drugs. Med Res Rev 38:504–524. https://doi.org/10.1002/med.21444
3. Wildey MJ, Haunso A, Tudor M, et al (2017) High-Throughput Screening, 1st ed. Elsevier Inc.
4. Carnero A (2006) High throughput screening in drug discovery. Clin Transl Oncol 8:482–490. https://doi.org/10.1007/s12094-006-0048-2
5. Fox JT, Myung K (2012) Cell-based high-throughput screens for the discovery of chemotherapeutic agents. Oncotarget 3:581–585. https://doi.org/10.18632/oncotarget.513
6. Hung PJ, Lee PJ, Sabounchi P, et al (2005) Continuous perfusion microfluidic cell culture array for high-throughput cell-based assays. Biotechnol Bioeng 89:1–8. https://doi.org/10.1002/bit.20289
7. M Friedrich B, E Scully C, M Brannan J (2011) Assessment of High-Throughput Screening (HTS) Methods for High-Consequence Pathogens. J Bioterror Biodef 02: https://doi.org/10.4172/2157-2526.s3-005
8. Hackerman N (1988) Use of Laboratory Animals in Biomedical and Behavioral Research. National Accademy Press, Washington, D.C.
9. Henrique Franco N (2013) Animal experiments in biomedical research: A historical perspective. Animals 3:238–273. https://doi.org/10.3390/ani3010238
10. European Commission (2021) Report on the statistics on the use of animals for scientific purposes in the Member States of the European Union and Norway in 2018. Brussels
11. United States Department of Agriculture - Animal and Health Inspection Services (2021) Annual report animal usage by fiscal year 2019
12. Canadian Council on Animal Care (2021) CCAC Animal Data Report 2020. Ottawa, ON
13. Cao D (2018) Ethical Questions for Research Ethics: Animal Research in China. J Anim Ethics 8:138–149. https://doi.org/10.5406/janimalethics.8.2.0138

14. Takebe T, Imai R, Ono S (2018) The Current Status of Drug Discovery and Development as Originated in United States Academia: The Influence of Industrial and Academic Collaboration on Drug Discovery and Development. Clin Transl Sci 11:597–606. https://doi.org/10.1111/cts.12577

15. Balls M, Bailey J, Combes RD (2019) How viable are alternatives to animal testing in determining the toxicities of therapeutic drugs? Expert Opin Drug Metab Toxicol 15:985–987. https://doi.org/10.1080/17425255.2019.1694662

16. Beilmann M, Boonen H, Czich A, et al (2019) Optimizing drug discovery by investigative toxicology: Current and future trends. ALTEX 36:289–313. https://doi.org/10.14573/altex.1808181

17. Doke SK, Dhawale SC (2015) Alternatives to animal testing: A review. Saudi Pharm J 23:223–229. https://doi.org/10.1016/j.jsps.2013.11.002

18. Spielmann H (2006) Ethical Environment and Scientific Rationale Towards In-Vitro Alternatives to Animal Testing: Where Are We Going? In: Marx U, Sandig V (eds) Drug Testing in vitro: Breakthroughs and Trends in Cell Culture Technology, 2007th ed. Wiley-vch Verlag GmbH&Co., pp 251–267

19. Vinardell MP, Mitjans M (2008) Alternative methods for eye and skin irritation tests: An overview. J Pharm Sci 97:46–59. https://doi.org/10.1002/jps.21088

20. Antoni D, Burckel H, Josset E, Noel G (2015) Three-dimensional cell culture: A breakthrough in vivo. Int J Mol Sci 16:5517–5527. https://doi.org/10.3390/ijms16035517

21. Carter M, Shieh J (2015) Chapter 14 - Cell Culture Techniques. In: Guide to Research Techniques in Neuroscience, 2nd ed. pp 295–310

22. Langhans SA (2018) Three-dimensional in vitro cell culture models in drug discovery and drug repositioning. Front Pharmacol 9:1–14. https://doi.org/10.3389/fphar.2018.00006

23. Duval K, Grover H, Han LH, et al (2017) Modeling physiological events in 2D vs. 3D cell culture. Physiology 32:266–277. https://doi.org/10.1152/physiol.00036.2016

24. Markets and Markets (2019) Cell-based Assay Market by Product (Reagents, Microplates, Cell Lines, Assay Kits, Instruments, Services), Application (Drug Discovery, Research), End User (CROs, Biopharma Companies, Research Institutes), Geography - Global Forecast to 2024. https://www.marketsandmarkets.com/Market-Reports/cell-based-assays-market-119917269.html

25. Guzman-Rodriguez M, McDonald JAK, Hyde R, et al (2018) Using bioreactors to study the effects of drugs on the human microbiota. Methods 149:31–41. https://doi.org/10.1016/j.ymeth.2018.08.003

26. van Delft J, Mathijs K, Polman J, et al (2014) Hepatotoxicity Screening on In Vitro Models and the Role of 'Omics. Elsevier Inc.

27. Stacey G (2006) Primary Cell Cultures and Immortal Cell Lines. Encycl Life Sci 1–6.

https://doi.org/10.1038/npg.els.0003960

28. Sharma S V., Haber DA, Settleman J (2010) Cell line-based platforms to evaluate the therapeutic efficacy of candidate anticancer agents. Nat Rev Cancer 10:241–253. https://doi.org/10.1038/nrc2820

29. Rowe RG, Daley GQ (2019) Induced pluripotent stem cells in disease modelling and drug discovery. Nat Rev Genet 20:377–388. https://doi.org/10.1038/s41576-019-0100-z

30. Chaicharoenaudomrung N, Kunhorm P, Noisa P (2019) Three-dimensional cell culture systems as an in vitro platform for cancer and stem cell modeling. World J Stem Cells 11:1065–1083. https://doi.org/10.4252/wjsc.v11.i12.1065

31. Lv D, Hu Z, Lu LIN, et al (2017) Three - dimensional cell culture : A powerful tool in tumor research and drug discovery (Review). Oncol Lett 14:6999–7010. https://doi.org/10.3892/ol.2017.7134

32. Kapałczyńska M, Kolenda T, Przybyła W, et al (2016) 2D and 3D cell cultures – a comparison of different. Arch Med Sci 14:910–919

33. Friedrich J, Ebner R, Kunz-Schughart LA (2007) Experimental anti-tumor therapy in 3-D: Spheroids - Old hat or new challenge? Int J Radiat Biol 83:849–871. https://doi.org/10.1080/09553000701727531

34. Saji Joseph J, Tebogo Malindisa S, Ntwasa M (2019) Two-Dimensional (2D) and Three-Dimensional (3D) Cell Culturing in Drug Discovery. Cell Cult. https://doi.org/10.5772/intechopen.81552

35. Lee J, Cuddihy MJ, Kotov NA (2008) Three-dimensional cell culture matrices: State of the art. Tissue Eng - Part B Rev 14:61–86. https://doi.org/10.1089/teb.2007.0150

36. Jensen C, Teng Y (2020) Is It Time to Start Transitioning From 2D to 3D Cell Culture? Front Mol Biosci 7:1–15. https://doi.org/10.3389/fmolb.2020.00033

37. Hoarau-Véchot J, Rafii A, Touboul C, Pasquier J (2018) Halfway between 2D and animal models: Are 3D cultures the ideal tool to study cancer-microenvironment interactions? Int J Mol Sci 19:. https://doi.org/10.3390/ijms19010181

38. Fang Y, Eglen RM (2017) Three-Dimensional Cell Cultures in Drug Discovery and Development. SLAS Discov 22:456–472. https://doi.org/10.1177/1087057117696795

39. Katt ME, Placone AL, Wong AD, et al (2016) In vitro tumor models: Advantages, disadvantages, variables, and selecting the right platform. Front Bioeng Biotechnol 4:. https://doi.org/10.3389/fbioe.2016.00012

40. Sutherland RM, Inch WR, McCredie JA (1970) A multi-component radiation survival curve using an in vitro tumour model. Int J Radiat Biol 18:491–495

41. Sutherland RM (1988) Cell and Enrivonment Ineractions in Tumor Microregions : The Spheroid Model. Science (80-) 240:177–184

42. Abu-Absi SF, Friend JR, Hansen LK, Hu WS (2002) Structural polarity and functional bile canaliculi in rat hepatocyte spheroids. Exp Cell Res 274:56–67. https://doi.org/10.1006/excr.2001.5467

43. Kelm JM, Djonov V, Ittner LM, et al (2006) Design of custom-shaped vascularized tissues using microtissue spheroids as minimal building units. Tissue Eng 12:2151–2160. https://doi.org/10.1089/ten.2006.12.2151

44. Tseng TC, Wong CW, Hsieh FY, Hsu SH (2017) Biomaterial Substrate-Mediated Multicellular Spheroid Formation and Their Applications in Tissue Engineering. Biotechnol J 12:1–8. https://doi.org/10.1002/biot.201700064

45. Laschke MW, Menger MD (2017) Life is 3D: Boosting Spheroid Function for Tissue Engineering. Trends Biotechnol 35:133–144. https://doi.org/10.1016/j.tibtech.2016.08.004

46. Yoon HH, Bhang SH, Shin JY, et al (2012) Enhanced cartilage formation via three-dimensional cell engineering of human adipose-derived stem cells. Tissue Eng - Part A 18:1949–1956. https://doi.org/10.1089/ten.tea.2011.0647

47. Montani C, Steimberg N, Boniotti J, et al (2014) Fibroblasts maintained in 3 dimensions show a better differentiation state and higher sensitivity to estrogens. Toxicol Appl Pharmacol 280:421–433. https://doi.org/10.1016/j.taap.2014.08.021

48. Ota H, Kodama T, Miki N (2011) Rapid formation of size-controlled three dimensional hetero-cell aggregates using micro-rotation flow for spheroid study. Biomicrofluidics 5:. https://doi.org/10.1063/1.3609969

49. Lopa S, Piraino F, Kemp RJ, et al (2015) Fabrication of multi-well chips for spheroid cultures and implantable constructs through rapid prototyping techniques. Biotechnol Bioeng 112:1457–1471. https://doi.org/10.1002/bit.25557

50. Huang BW, Gao JQ (2018) Application of 3D cultured multicellular spheroid tumor models in tumor-targeted drug delivery system research. J Control Release 270:246–259. https://doi.org/10.1016/j.jconrel.2017.12.005

51. Fischbach C, Chen R, Matsumoto T, et al (2007) Engineering tumors with 3D scaffolds. Nat Methods 4:855–860. https://doi.org/10.1038/nmeth1085

52. Ho WJ, Pham EA, Kim JW, et al (2010) Incorporation of multicellular spheroids into 3-D polymeric scaffolds provides an improved tumor model for screening anticancer drugs. Cancer Sci 101:2637–2643. https://doi.org/10.1111/j.1349-7006.2010.01723.x

53. Drury JL, Mooney DJ (2003) Hydrogels for tissue engineering: Scaffold design variables and applications. Biomaterials 24:4337–4351. https://doi.org/10.1016/S0142-9612(03)00340-5

54. Lee SH, Shim KY, Kim B, Sung JH (2017) Hydrogel-based three-dimensional cell culture for organ-on-a-chip applications. Biotechnol Prog 33:580–589. https://doi.org/10.1002/btpr.2457

55. Hamidi M, Azadi A, Rafiei P (2008) Hydrogel nanoparticles in drug delivery. Adv Drug Deliv Rev 60:1638–1649. https://doi.org/10.1016/j.addr.2008.08.002

56. Maltman DJ, Przyborski SA (2010) Developments in three-dimensional cell culture technology aimed at improving the accuracy of in vitro analyses. Biochem Soc Trans 38:1072–1075. https://doi.org/10.1042/BST0381072

57. Gurski LA, Petrelli NJ, Jia X, Farach-Carson MC (2010) 3D Matrices for Anti-Cancer Drug Testing and Development. Oncol Issues 25:20–25. https://doi.org/10.1080/10463356.2010.11883480

58. Sultana N (2018) Mechanical and biological properties of scaffold materials. In: Functional 3D Tissue Engineering Scaffolds: Materials, Technologies, and Applications. Elsevier Ltd, pp 1–21

59. Campuzano S, Pelling AE (2019) Scaffolds for 3D Cell Culture and Cellular Agriculture Applications Derived From Non-animal Sources. Front Sustain Food Syst 3:1–9. https://doi.org/10.3389/fsufs.2019.00038

60. Eltom A, Zhong G, Muhammad A (2019) Scaffold Techniques and Designs in Tissue Engineering Functions and Purposes : A Review. 2019:

61. Unsworth JM (2004) NOVEL POROUS SCAFFOLDS FOR TISSUE ENGINEERING CARTILAGE. University of Nottingham

62. Plunkett N, O'Brien FJ (2011) Bioreactors in tissue engineering. Technol Heal Care 19:55–69. https://doi.org/10.3233/THC-2011-0605

63. Haycock JW (2011) 3D Cell Culture: A Review of Current Approaches and Techniques. In: 3D Cell Culture: Methods and Protocols, Methods in Molecular Biology. pp 1–15

64. Dhandayuthapani B, Yoshida Y, Maekawa T, Kumar DS (2011) Polymeric Scaffolds in Tissue Engineering Application : A Review. Int J ofPolymer Sci 2011:19. https://doi.org/10.1155/2011/290602

65. Ratner BD, Bryant SJ (2004) Biomaterials: Where We Have Been and Where We Are Going. Annu Rev Biomed Eng 6:41–75. https://doi.org/10.1146/annurev.bioeng.6.040803.140027

66. Garg T, Singh O, Arora S, Murthy RSR (2012) Scaffold: A Novel Carrier for Cell and Drug Delivery. Ther Drug Carr Syst 29:1–63. https://doi.org/10.1615/critrevtherdrugcarriersyst.v29.i1.10

67. Ige OO, Umoru LE, Aribo S (2012) Natural Products: A Minefield of Biomaterials. ISRN Mater Sci 2012:1–20. https://doi.org/10.5402/2012/983062

68. Ullah S, Chen X (2020) Fabrication, applications and challenges of natural biomaterials in tissue engineering. Appl Mater Today J 20:22. https://doi.org/http://dx.doi.org/10.1016/j.apmt.2020.100656

69. Rojo L, Vázquez B, San Román J (2014) Biomaterials for scaffolds: Synthetic polymers

70. Stratton S, Shelke NB, Hoshino K, et al (2016) Bioactive polymeric scaffolds for tissue engineering. Bioact Mater 1:93–108. https://doi.org/10.1016/j.bioactmat.2016.11.001

71. Jain A, Khan W, Kyzioł A (2019) Particulate systems of PLA and its copolymers. In: Materials for Biomedical Engineering: Thermoset and Thermoplastic Polymers. Elsevier Inc., pp 349–380

72. Farah S, Anderson DG, Langer R (2016) Physical and mechanical properties of PLA, and their functions in widespread applications — A comprehensive review. Adv Drug Deliv Rev 107:367–392. https://doi.org/10.1016/j.addr.2016.06.012

73. Guarino V, Raucci MG, Ronca A, et al (2014) Multifunctional scaffolds for bone regeneration. In: Bone Substitute Biomaterials. Woodhead Publishing Limited, pp 95–117

74. Samantaray PK, Little A, Haddleton DM, et al (2020) Poly(glycolic acid) (PGA): A versatile building block expanding high performance and sustainable bioplastic applications. Green Chem 22:4055–4081. https://doi.org/10.1039/d0gc01394c

75. Gavasane AJ, Pawar HA (2014) Clinical Pharmacology Synthetic Biodegradable Polymers Used in Controlled Drug Delivery System : An Overview. 3:. https://doi.org/10.4172/2167-065X.1000121

76. Tran TT, Hamid ZA, Cheong KY (2018) A Review of Mechanical Properties of Scaffold in Tissue Engineering: Aloe Vera Composites. J Phys Conf Ser 1082:1–7. https://doi.org/10.1088/1742-6596/1082/1/012080

77. Gunatillake PA, Adhikari R, Gadegaard N (2003) Biodegradable synthetic polymers for tissue engineering. Eur Cells Mater 5:1–16. https://doi.org/10.22203/eCM.v005a01

78. Chong EJ, Phan TT, Lim IJ, et al (2007) Evaluation of electrospun PCL/gelatin nanofibrous scaffold for wound healing and layered dermal reconstitution. Acta Biomater 3:321–330. https://doi.org/10.1016/j.actbio.2007.01.002

79. Salgado AJ, Coutinho OP, Reis RL (2004) Bone tissue engineering: State of the art and future trends. Macromol Biosci 4:743–765. https://doi.org/10.1002/mabi.200400026

80. Yang S, Leong KF, Du Z, Chua CK (2001) The design of scaffolds for use in tissue engineering. Part I. Traditional factors. Tissue Eng 7:679–689. https://doi.org/10.1089/107632701753337645

81. Mohseni M, Castro NJ, Dang HP, et al (2018) Adipose tissue regeneration: Scaffold-Biomaterial strategies and translational perspectives. In: Biomaterials in Translational Medicine: A Biomaterials Approach. Elsevier Inc., pp 291–330

82. Mi H-Y, Jing X, Turng LS (2014) Fabrication of porous synthetic polymer scaffolds for tissue engineering. J Cell Plast 51:165–196. https://doi.org/10.1177/0021955X14531002

83. Sola A, Bertacchini J, Avella DD, et al (2019) Development of solvent-casting particulate

leaching (SCPL) polymer sca ff olds as improved three-dimensional supports to mimic the bone marrow niche. Mater Sci Eng C 96:153–165. https://doi.org/10.1016/j.msec.2018.10.086

84. Huang R, Zhu X, Tu H, Wan A (2014) The crystallization behavior of porous poly(lactic acid) prepared by modified solvent casting/particulate leaching technique for potential use of tissue engineering scaffold. Mater Lett 136:126–129. https://doi.org/10.1016/j.matlet.2014.08.044

85. Li Z, Xie M Bin, Li Y, et al (2016) Recent progress in tissue engineering and regenerative medicine. J Biomater Tissue Eng 6:755–766. https://doi.org/10.1166/jbt.2016.1510

86. Şenel Ayaz HG, Perets A, Ayaz H, et al (2014) Textile-templated electrospun anisotropic scaffolds for regenerative cardiac tissue engineering. Biomaterials 35:8540–8552. https://doi.org/10.1016/j.biomaterials.2014.06.029

87. Fong H, Chun I, Reneker DH (1999) Beaded nanofibers formed during electrospinning. Polymer (Guildf) 40:4585–4592

88. Edwards J V., Goheen SC (2011) New developments in functional medical textiles and their mechanism of action. Woodhead Publishing Limited

89. Kulkarni AA, Rao PS (2013) Synthesis of polymeric nanomaterials for biomedical applications. Woodhead Publishing Limited

90. Shah T, Halacheva S (2016) Drug-releasing Textiles. In: Advances in Smart Medical Textiles: Treatments and Health Monitoring. Elsevier Ltd, pp 119–154

91. Gay S, Lefebvre G, Bonnin M, et al (2018) PLA scaffolds production from Thermally Induced Phase Separation: Effect of process parameters and development of an environmentally improved route assisted by supercritical carbon dioxide. J Supercrit Fluids 136:123–135. https://doi.org/10.1016/j.supflu.2018.02.015

92. Conoscenti G, Carrubba V La, Brucato V (2017) A Versatile Technique to Produce Porous Polymeric Scaffolds: The Thermally Induced Phase Separation (TIPS) Method. Arch Chem Res 01:10–12. https://doi.org/10.21767/2572-4657.100012

93. la Carrubba V, Pavia FC, Brucato V, Piccarolo S (2008) PLLA/PLA scaffolds prepared via thermally induced phase separation (TIPS): Tuning of properties and biodegradability. Int J Mater Form 1:619–622. https://doi.org/10.1007/s12289-008-0332-5

94. Alberti S, Gladfelter A, Mittag T (2019) Considerations and Challenges in Studying Liquid-Liquid Phase Separation and Biomolecular Condensates. Cell 176:419–434. https://doi.org/10.1016/j.cell.2018.12.035

95. Montesanto S, Mannella GA, Carfì Pavia F, et al (2015) Coagulation bath composition and desiccation environment as tuning parameters to prepare skinless membranes via diffusion induced phase separation. J Appl Polym Sci 132:1–10. https://doi.org/10.1002/app.42151

96. Carfì Pavia F, Palumbo FS, La Carrubba V, et al (2016) Modulation of physical and

biological properties of a composite PLLA and polyaspartamide derivative obtained via thermally induced phase separation (TIPS) technique. Mater Sci Eng C 67:561–569. https://doi.org/10.1016/j.msec.2016.05.040

97. Ghalia MA, Dahman Y (2016) Advanced nanobiomaterials in tissue engineering: Synthesis, properties, and applications. Elsevier Inc.

98. Vitrano I, Carfì Pavia F, Conoscenti G, et al (2018) Evaluation of hydroxyapatite distribution in a Poly-L-Lactic Acid (PLLA) scaffolds via Micro Computed Tomography (μCT). Chem Eng Trans 64:. https://doi.org/10.3303/CET1864033

99. Mooney DJ, Baldwin DF, Suht NP, et al (1996) Novel approach to fabricate porous sponges of poly (o , klactic-co-glycolic acid) without the use of organic solvents. Biomaterials 17:1417–1422

100. Sultana N (2013) Biodegradable Polymer Based Scaffolds for Bone Tissue Engineering. Springer

101. Ratheesh G, Venugopal JR, Chinappan A, et al (2017) 3D Fabrication of Polymeric Scaffolds for Regenerative Therapy. ACS Biomater Sci Eng 3:1175–1194. https://doi.org/10.1021/acsbiomaterials.6b00370

102. Raeisdasteh Hokmabad V, Davaran S, Ramazani A, Salehi R (2017) Design and fabrication of porous biodegradable scaffolds: a strategy for tissue engineering. J Biomater Sci Polym Ed 28:1797–1825. https://doi.org/10.1080/09205063.2017.1354674

103. Lam CXF, Mo XM, Teoh SH, Hutmacher DW (2002) Scaffold development using 3D printing with a starch-based polymer. Mater Sci Eng C 20:49–56. https://doi.org/10.1016/S0928-4931(02)00012-7

104. Li MG, Tian XY, Chen XB (2009) A brief review of dispensing-based rapid prototyping techniques in tissue scaffold fabrication: Role of modeling on scaffold properties prediction. Biofabrication 1:. https://doi.org/10.1088/1758-5082/1/3/032001

105. Abdelaal OA, Darwish SM (2011) Fabrication of tissue engineering scaffolds using rapid prototyping techniques. J World Acad Sci Eng Technol 59:577–585

106. Peltola SM, Melchels FPW, Grijpma DW, Kellomäki M (2008) A review of rapid prototyping techniques for tissue engineering purposes. Ann Med 40:268–280. https://doi.org/10.1080/07853890701881788

107. Bishop ES, Mostafa S, Pakvasa M, et al (2017) ScienceDirect 3-D bioprinting technologies in tissue engineering and regenerative medicine : Current and future trends. Genes Dis 4:185–195. https://doi.org/10.1016/j.gendis.2017.10.002

108. Hansmann J, Egger D, Kasper C (2018) Advanced dynamic cell and tissue culture. Bioengineering 5:5–7. https://doi.org/10.3390/bioengineering5030065

109. Rodrigues CA V, Fernandes TG, Diogo MM, et al (2011) Stem cell cultivation in bioreactors. Biotechnol Adv 29:815–829. https://doi.org/10.1016/j.biotechadv.2011.06.009

110. Merzari E (2011) Bioreactor Design for Dynamic Process Optimiization in Tissue Engineering. Unversity of Trento

111. Sailon AM, Allori AC, Davidson EH, et al (2009) A novel flow-perfusion bioreactor supports 3D dynamic cell culture. J Biomed Biotechnol 1–7. https://doi.org/10.1155/2009/873816

112. Perez RA, Riccardi K, Altankov G, Ginebra M (2014) Dynamic cell culture on calcium phosphate microcarriers for bone tissue engineering applications. J Tissue Eng 5:1–10. https://doi.org/10.1177/2041731414543965

113. Massai D, Isu G, Madeddu D, et al (2016) A Versatile Bioreactor for Dynamic Suspension Cell Culture . Application to the Culture of Cancer Cell Spheroids. PLoS One 5:1–16. https://doi.org/10.1371/journal.pone.0154610

114. Rinkenauer AC, Press AT, Raasch M, et al (2015) Comparison of the uptake of methacrylate-based nanoparticles in static and dynamic in vitro systems as well as in vivo. J Control Release 216:158–168. https://doi.org/10.1016/j.jconrel.2015.08.008

115. Ellis M, Jarman-Smith M, Chaudhuri JB (2005) Bioreactor systems for tissue engineering: A four-dimensional challenge. Bioreact Tissue Eng Princ Des Oper 1–18. https://doi.org/10.1007/1-4020-3741-4_1

116. Selden C, Fuller B (2018) Role of Bioreactor Technology in Tissue Engineering for Clinical Use and Therapeutic Target Design. Bioengineering 32:1–10. https://doi.org/10.3390/bioengineering5020032

117. Freshney RI, Obradovic B, Grayson W, et al (2007) Principles of Tissue Culture and Bioreactor Design. In: Principles of Tissue Engineering, 3rd ed. Elsevier Inc., pp 155–184

118. Salehi-Nik N, Amoabediny G, Pouran B, et al (2013) Engineering parameters in bioreactor's design: A critical aspect in tissue engineering. Biomed Res Int 2013:1–15. https://doi.org/10.1155/2013/762132

119. Pancrazio JJ, Wang F, Kelley CA (2007) Enabling tools for tissue engineering. Biosens Bioelectron 22:2803–2811. https://doi.org/10.1016/j.bios.2006.12.023

120. Wendt D, Riboldi SA (2009) Bioreactors in Tissue Engineering: From Basic Research to Automated Product Manufacturing. In: Fundamentals of Tissue Engineering and Regenerative Medicine. Springer, Berlin, Heidelberg, pp 595–611

121. Depprich R, Handschel J, Wiesmann HP, et al (2008) Use of bioreactors in maxillofacial tissue engineering. Br J Oral Maxillofac Surg 46:349–354. https://doi.org/10.1016/j.bjoms.2008.01.012

122. Yeatts AB, Fisher JP (2011) Bone tissue engineering bioreactors: Dynamic culture and the influence of shear stress. Bone 48:171–181. https://doi.org/10.1016/j.bone.2010.09.138

123. Sakamoto N, Saito N, Han X, et al (2010) Effect of spatial gradient in fluid shear stress on morphological changes in endothelial cells in response to flow. Biochem Biophys Res

Commun 395:264–269. https://doi.org/10.1016/j.bbrc.2010.04.002

124. Sharifi N, Gharravi AM (2019) Shear bioreactors stimulating chondrocyte regeneration, a systematic review. Inflamm Regen 39:1–8. https://doi.org/10.1186/s41232-019-0105-1

125. Lawrence BJ, Devarapalli M, Madihally S V. (2009) Flow dynamics in bioreactors containing tissue engineering scaffolds. Biotechnol Bioeng 102:935–947. https://doi.org/10.1002/bit.22106

126. Paez-Mayorga J, Hernández-Vargas G, Ruiz-Esparza GU, et al (2019) Bioreactors for Cardiac Tissue Engineering. Adv Healthc Mater 8:1–14. https://doi.org/10.1002/adhm.201701504

127. Korossis SA, Bolland F, Kearney JN, et al (2006) Bioreactors in Tissue Engineering. In: Eds. N. Ashammakhi & R.L. Reis (ed) Topics in Tissue Engineering. pp 1–23

128. Nichols DA, Sondh IS, Litte SR, et al (2018) Design and validation of an osteochondral bioreactor for the screening of treatments for osteoarthritis. Biomed Microdevices 20:1–8. https://doi.org/10.1007/s10544-018-0264-x

129. Pirosa A, Gottardi R, Alexander PG, Tuan RS (2018) Engineering in-vitro stem cell-based vascularized bone models for drug screening and predictive toxicology

130. Guller AE, Grebenyuk PN, Shekhter AB, et al (2016) Bioreactor-Based Tumor Tissue Engineering. Acta Nat 8:44–58

131. Bilodeau K, Mantovani D (2006) Bioreactors for tissue engineering: Focus on mechanical constraints. A comparative review. Tissue Eng 12:2367–2383. https://doi.org/10.1089/ten.2006.12.2367

132. Goldstein AS, Juarez TM, Helmke CD, et al (2001) Effect of convection on osteoblastic cell growth and function in biodegradable polymer foam scaffolds. Biomaterials 22:1279–1288. https://doi.org/10.1016/S0142-9612(00)00280-5

133. Levorson-Wright EJ, Santoro M, Kasper FK, Mikos AG (2017) 5.1 Scaffolds: Flow perfusion bioreactor design. In: Comprehensive Biomaterials II. pp 1–17

134. Glowacki J, Mizuno S, Greenberger JS (1998) Perfusion enhances functions of bone marrow stromal cells in three- dimensional culture. Cell Transplant 7:319–326. https://doi.org/10.1016/S0963-6897(98)00003-7

135. Santoro M, Lamhamedi-Cherradi S-E, Menegaz BA, et al (2015) Flow perfusion effects on three-dimensional culture and drug sensitivity of Ewing sarcoma. Proc Natl Acad Sci 112:10304–10309. https://doi.org/10.1073/pnas.1506684112

136. Fu L, Li P, Li H, et al (2021) The Application of Bioreactors for Cartilage Tissue Engineering: Advances, Limitations, and Future Perspectives. Stem Cells Int 2021:1–13. https://doi.org/10.1155/2021/6621806

137. Brady MA, Vaze R, Amin HD, et al (2014) The Design and Development of a High-

Throughput Magneto-Mechanostimulation Device for Cartilage. Tissue Eng - Part C 20:149–159. https://doi.org/10.1089/ten.tec.2013.0225

138. Thakurta SG, Kraft M, Viljoen HJ, Subramanian A (2014) Enhanced depth-independent chondrocyte proliferation and phenotype maintenance in an ultrasound bioreactor and an assessment of ultrasound dampening in the scaffold. Acta Biomater 10:4798–4810. https://doi.org/10.1016/j.actbio.2014.07.013

139. Bayda S, Adeel M, Tuccinardi T, et al (2020) The history of nanoscience and nanotechnology: From chemical-physical applications to nanomedicine. Molecules 25:1–15. https://doi.org/10.3390/molecules25010112

140. Gatoo MA, Naseem S, Arfat MY, et al (2014) Physicochemical properties of nanomaterials: Implication in associated toxic manifestations. Biomed Res Int 2014:. https://doi.org/10.1155/2014/498420

141. Ramos AP, Cruz MA e., Tovani CB, Ciancaglini P (2017) Biomedical applications of nanotechnology. Biophys Rev 9:79–89. https://doi.org/10.1007/s12551-016-0246-2

142. Saji VS, Choe HC, Yeung KWK (2010) Nanotechnology in biomedical applications: A review. Int J Nano Biomater 3:119–139. https://doi.org/10.1504/IJNBM.2010.037801

143. Whitman AG, Lambert PJ, Dyson OF, Akula SM (2008) Applications of Nanotechnology in the Biomedical Sciences : Small Materials , Big Impacts , and Unknown Consequences. In: Jotterand F (ed) Emering Conceptual, Ethical and Policy Issues in Bionanotechnology. Springer Science+Business Media, pp 117–130

144. Saallah S, Lenggoro IW (2018) Nanoparticles carrying biological molecules: Recent advances and applications. KONA Powder Part J 2018:89–111. https://doi.org/10.14356/kona.2018015

145. Heuer-jungemann A, Feliu N, Bakaimi I, et al (2019) The Role of Ligands in the Chemical Synthesis and Applications of Inorganic Nanoparticles. https://doi.org/10.1021/acs.chemrev.8b00733

146. Khan I, Saeed K, Khan I (2019) Nanoparticles: Properties, applications and toxicities. Arab J Chem 12:908–931. https://doi.org/10.1016/j.arabjc.2017.05.011

147. Chatterjee K, Sarkar S, Jagajjanani Rao K, Paria S (2014) Core/shell nanoparticles in biomedical applications. Adv Colloid Interface Sci 209:8–39. https://doi.org/10.1016/j.cis.2013.12.008

148. Liu KK, Song SY, Sui LZ, et al (2019) Efficient Red/Near-Infrared-Emissive Carbon Nanodots with Multiphoton Excited Upconversion Fluorescence (Supporting Information). Adv Sci 6:. https://doi.org/10.1002/advs.201900766

149. Rosenthal SJ, Chang JC, Kovtun O, et al (2011) Biocompatible quantum dots for biological applications. Chem Biol 18:10–24. https://doi.org/10.1016/j.chembiol.2010.11.013

150. Yadav HKS, Raizaday A (2016) Inorganic nanobiomaterials for medical imaging. In:

Nanobiomaterials in Medical Imaging: Applications of Nanobiomaterials. Elsevier Inc., pp 365–401

151. Pawar RS, Upadhaya PG, Patravale VB (2018) Quantum dots: Novel realm in biomedical and pharmaceutical industry. Elsevier Inc.

152. MELVILLE J (2015) Optical Properties of Quantum Dots. UC BERKELEY COLLEGE OF CHEMISTRY

153. Kumar DS, Kumar BJ, Mahesh HM (2018) Quantum Nanostructures (QDs): An Overview. In: Synthesis of Inorganic Nanomaterials. Elsevier Ltd., pp 59–88

154. Estupiñán-lópez C, Dominguez CT, Filho PEC, et al Chapter 7 Measured by Thermal Lens Spectroscopy. 1199:93–101. https://doi.org/10.1007/978-1-4939-1280-3

155. Mazumder S, Dey R, Mitra MK, et al (2009) Review: Biofunctionalized quantum dots in biology and medicine. J Nanomater 2009:1–17. https://doi.org/10.1155/2009/815734

156. Goreham R V., Ayed Z, Ayupova D, Dobhal G (2019) Extracellular vesicles: Nature's own nanoparticles. Compr Nanosci Nanotechnol 1–5:27–48. https://doi.org/10.1016/B978-0-12-803581-8.10412-6

157. Jamieson T, Bakhshi R, Petrova D, et al (2007) Biological applications of quantum dots. Biomaterials 28:4717–4732. https://doi.org/10.1016/j.biomaterials.2007.07.014

158. Alivisatos AP, Gu W, Larabell C (2005) Quantum dots as cellular probes. Annu Rev Biomed Eng 7:55–76. https://doi.org/10.1146/annurev.bioeng.7.060804.100432

159. Resch-Genger U, Grabolle M, Cavaliere-Jaricot S, et al (2008) Quantum dots versus organic dyes as fluorescent labels. Nat Methods 5:763–775. https://doi.org/10.1038/nmeth.1248

160. Farzin MA, Abdoos H (2021) A critical review on quantum dots: From synthesis toward applications in electrochemical biosensors for determination of disease-related biomolecules. Talanta 224:121828. https://doi.org/10.1016/j.talanta.2020.121828

161. Bhatia S (2016) Natural polymer drug delivery systems: Nanoparticles, plants, and algae. In: Natural Polymer Drug Delivery Systems: Nanoparticles, Plants, and Algae. Springer International Publishing, Switzerland, pp 1–225

162. Li L, Dong T (2018) Photoluminescence tuning in carbon dots: Surface passivation or/and functionalization, heteroatom doping. J Mater Chem C 6:7944–7970. https://doi.org/10.1039/c7tc05878k

163. Wang J, Zhu Y, Wang L (2019) Synthesis and Applications of Red-Emissive Carbon Dots. Chem Rec 19:2083–2094. https://doi.org/10.1002/tcr.201800172

164. Xu X, Ray R, Gu Y, et al (2004) Electrophoretic analysis and purification of fluorescent single-walled carbon nanotube fragments. J Am Chem Soc 126:12736–12737. https://doi.org/10.1021/ja040082h

165. Zhang Z, Yi G, Li P, et al (2020) A minireview on doped carbon dots for photocatalytic and

electrocatalytic applications. Nanoscale 12:13899–13906. https://doi.org/10.1039/d0nr03163a

166. Chung YJ, Kim J, Park CB (2020) Photonic Carbon Dots as an Emerging Nanoagent for Biomedical and Healthcare Applications. ACS Nano 14:6470–6497. https://doi.org/10.1021/acsnano.0c02114

167. Chan KK, Yap SHK, Yong KT (2018) Biogreen Synthesis of Carbon Dots for Biotechnology and Nanomedicine Applications. Springer Berlin Heidelberg

168. Fong JFY, Ng YH, Ng SM (2019) Recent Advances in Carbon Dots for Bioanalysis and the Future Perspectives. In: Carbon Nanomaterials for Bioimaging, Bioanalysis, and Therapy, First. John Wiley & Sons Ltd, pp 203–264

169. Chao D, Lyu W, Liu Y, et al (2018) Solvent-dependent carbon dots and their applications in the detection of water in organic solvents. J Mater Chem C 6:7527–7532. https://doi.org/10.1039/c8tc02184h

170. Meng X, Chang Q, Xue C, et al (2017) Full-colour carbon dots: from energy-efficient synthesis to concentration-dependent photoluminescence properties. Chem Commun 53:3074–3077. https://doi.org/10.1039/c7cc00461c

171. Yu P, Wen X, Toh YR, Tang J (2012) Temperature-dependent fluorescence in carbon dots. J Phys Chem C 116:25552–25557. https://doi.org/10.1021/jp307308z

172. Tachi S, Morita H, Takahashi M, et al (2019) Quantum Yield Enhancement in Graphene Quantum Dots via Esterification with Benzyl Alcohol. Sci Rep 9:1–7. https://doi.org/10.1038/s41598-019-50666-3

173. Gao D, Zhao H, Chen X, Fan H (2018) Recent advance in red-emissive carbon dots and their photoluminescent mechanisms. Mater Today Chem 9:103–113. https://doi.org/10.1016/j.mtchem.2018.06.004

174. Wang H, Sun C, Chen X, et al (2017) Excitation wavelength independent visible color emission of carbon dots. Nanoscale 9:1909–1915. https://doi.org/10.1039/c6nr09200d

175. Shi X, Meng H, Sun Y, et al (2019) Far-Red to Near-Infrared Carbon Dots: Preparation and Applications in Biotechnology. Small 15:1–17. https://doi.org/10.1002/smll.201901507

176. Xu Q, Cai W, Zhang M, et al (2018) Photoluminescence mechanism and applications of Zn-doped carbon dots. RSC Adv 8:17254–17262. https://doi.org/10.1039/c8ra02756k

177. Zhu Z, Zhai Y, Li Z, et al (2019) Red carbon dots: Optical property regulations and applications. Mater Today 30:52–79. https://doi.org/10.1016/j.mattod.2019.05.003

178. Sudolská M, Otyepka M (2017) Exact roles of individual chemical forms of nitrogen in the photoluminescent properties of nitrogen-doped carbon dots. Appl Mater Today 7:190–200. https://doi.org/10.1016/j.apmt.2017.03.004

179. Craciun AM, Diac A, Focsan M, et al (2016) Surface passivation of carbon nanoparticles

with: P -phenylenediamine towards photoluminescent carbon dots. RSC Adv 6:56944–56951. https://doi.org/10.1039/c6ra10127e

180. Jiang K, Sun S, Zhang L, et al (2015) Red, green, and blue luminescence by carbon dots: Full-color emission tuning and multicolor cellular imaging. Angew Chemie - Int Ed 54:5360–5363. https://doi.org/10.1002/anie.201501193

181. Tan C, Su X, Zhou C, et al (2017) Acid-assisted hydrothermal synthesis of red fluorescent carbon dots for sensitive detection of Fe(III). RSC Adv 7:40952–40956. https://doi.org/10.1039/c7ra06223k

182. Tan C, Zhou C, Peng X, et al (2018) Sulfuric Acid Assisted Preparation of Red-Emitting Carbonized Polymer Dots and the Application of Bio-Imaging. Nanoscale Res Lett 13:. https://doi.org/10.1186/s11671-018-2657-4

183. Kalaiyarasan G, Hemlata C, Joseph J (2019) Fluorescence Turn-On, Specific Detection of Cystine in Human Blood Plasma and Urine Samples by Nitrogen-Doped Carbon Quantum Dots. ACS Omega 4:1007–1014. https://doi.org/10.1021/acsomega.8b03187

184. Liu JJ, Li D, Zhang K, et al (2018) One-Step Hydrothermal Synthesis of Nitrogen-Doped Conjugated Carbonized Polymer Dots with 31% Efficient Red Emission for In Vivo Imaging. Small 14:1–10. https://doi.org/10.1002/smll.201703919

185. Miao S, Liang K, Zhu J, et al (2020) Hetero-atom-doped carbon dots: Doping strategies, properties and applications. Nano Today 33:100879. https://doi.org/10.1016/j.nantod.2020.100879

186. Du F, Zhang M, Gong A, et al (2017) Engineered gadolinium-doped carbon dots for magnetic resonance imaging-guided radiotherapy of tumors. Biomaterials 121:109–120. https://doi.org/10.1016/j.biomaterials.2016.07.008

187. Lin L, Luo Y, Tsai P, et al (2018) Metal ions doped carbon quantum dots: Synthesis, physicochemical properties, and their applications. TrAC - Trends Anal Chem 103:87–101. https://doi.org/10.1016/j.trac.2018.03.015

188. Barman MK, Jana B, Bhattacharyya S, Patra A (2014) Photophysical Properties of Doped Carbon Dots (N, P, and B) and Their In fl uence on Electron/Hole Transfer in Carbon Dots − Nickel (II) Phthalocyanine Conjugates. J Phys Chem 118:20034–20041. https://doi.org/10.1021/jp507080c

189. Xu Q, Kuang T, Liu Y, et al (2016) Heteroatom-doped carbon dots: synthesis, characterization, properties, photoluminescence mechanism and biological applications. J Mater Chem B 4:7204–7219. https://doi.org/10.1039/C6TB02131J

190. Xia C, Zhu S, Feng T, et al (2019) Evolution and Synthesis of Carbon Dots : From Carbon Dots to Carbonized Polymer Dots. Adv Sci 6:23. https://doi.org/10.1002/advs.201901316

191. Wang Y, Zhu Y, Yu S, Jiang C (2017) Fluorescent carbon dots: Rational synthesis, tunable optical properties and analytical applications. RSC Adv 7:40973–40989. https://doi.org/10.1039/c7ra07573a

192. Hu C, Li M, Qiu J, Sun YP (2019) Design and fabrication of carbon dots for energy conversion and storage. Chem Soc Rev 48:2315–2337. https://doi.org/10.1039/c8cs00750k

193. De Medeiros T V., Manioudakis J, Noun F, et al (2019) Microwave-assisted synthesis of carbon dots and their applications. J Mater Chem C 7:7175–7195. https://doi.org/10.1039/c9tc01640f

194. Xu M, Li Z, Zhu X, et al (2013) Hydrothermal / Solvothermal Synthesis of Hydrothermal/Solvothermal Synthesis of Graphene Quantum Dots and Their Biological Applications. Nano Biomed Eng 5:65–71. https://doi.org/10.5101/nbe.v4i3.p65-71.

195. Yang Y, Wu D, Han S, et al (2013) Bottom-up fabrication of photoluminescent carbon dots with uniform morphology via a soft-hard template approach. Chem Commun 49:4920–4922. https://doi.org/10.1039/c3cc38815h

196. Sharma A, Das J (2019) Small molecules derived carbon dots : synthesis and applications in sensing , catalysis , imaging , and biomedicine. J Nanobiotechnology 1–24. https://doi.org/10.1186/s12951-019-0525-8

197. Mohammadinejad R, Dadashzadeh A, Moghassemi S, et al (2019) Shedding light on gene therapy: Carbon dots for the minimally invasive image-guided delivery of plasmids and noncoding RNAs - A review. J Adv Res 18:81–93. https://doi.org/10.1016/j.jare.2019.01.004

198. Wei Z, Wang B, Liu Y, et al (2019) Green synthesis of nitrogen and sulfur co-doped carbon dots from Allium fistulosum for cell imaging. New J Chem 43:718–723. https://doi.org/10.1039/c8nj05783d

199. Yang M, Meng Y, Liu J, et al (2019) Facile Synthesis of Mg 2+ -Doped Carbon Dots as Novel Biomaterial Inducing Cell Osteoblastic Differentiation. Part Part Syst Charact 36:1–6. https://doi.org/10.1002/ppsc.201800315

200. Yang X, Cui F, Ren R, et al (2019) Red-emissive carbon dots for “switch-on” dual function sensing platform rapid detection of ferric ions and l-cysteine in living cells. ACS Omega 4:12575–12583. https://doi.org/10.1021/acsomega.9b01019

201. Wang C, Jiang K, Wu Q, et al (2016) Green Synthesis of Red-Emitting Carbon Nanodots as a Novel “Turn-on” Nanothermometer in Living Cells. Chem - A Eur J 22:14475–14479. https://doi.org/10.1002/chem.201602795

202. Li X, Shi L, Li L, et al (2019) Recent Advances in Carbon Nanodots: Properties and Applications in Cancer Diagnosis and Treatment. J Anal Test 3:37–49. https://doi.org/10.1007/s41664-019-00089-w

203. Jia Q, Zhao Z, Liang K, et al (2020) Recent advances and prospects of carbon dots in cancer nanotheranostics. Mater Chem Front 4:449–471. https://doi.org/10.1039/c9qm00667b

204. Sun S, Chen Q, Tang Z, et al (2020) Tumor Microenvironment Stimuli-Responsive Fluorescence Imaging and Synergistic Cancer Therapy by Carbon-Dot–Cu 2+ Nanoassemblies . Angew Chemie 132:21227–21234.

https://doi.org/10.1002/ange.202007786

205. Yue L, Li H, Sun Q, et al (2020) Red-Emissive Ruthenium-Containing Carbon Dots for Bioimaging and Photodynamic Cancer Therapy. ACS Appl Nano Mater 3:869–876. https://doi.org/10.1021/acsanm.9b02394

206. Ai L, Yang Y, Wang B, et al (2021) Insights into photoluminescence mechanisms of carbon dots: advances and perspectives. Sci Bull 66:839–856. https://doi.org/10.1016/j.scib.2020.12.015

207. European Parleament Commission (2021) Resolution on plans and actions to accelerate the transition to innovation without the use of animals in research, regulatory testing and education

208. de Boo MJ, Rennie AE, Buchanan-Smith HM, Hendriksen CFM (2005) The interplay between replacement, reduction and refinement: Considerations where the Three Rs interact. Anim Welf 14:327–332

209. MacArthur Clark J (2018) The 3Rs in research: A contemporary approach to replacement, reduction and refinement. Br J Nutr 120:S1–S7. https://doi.org/10.1017/S0007114517002227

210. Xu K, Ganapathy K, Andl T, et al (2019) 3D porous chitosan-alginate scaffold stiffness promotes differential responses in prostate cancer cell lines. Biomaterials 217:119311. https://doi.org/10.1016/j.biomaterials.2019.119311

211. Liu Z, Vunjak-Novakovic G (2016) Modeling tumor microenvironments using custom-designed biomaterial scaffolds. Curr Opin Chem Eng 11:94–105. https://doi.org/10.1016/j.coche.2016.01.012

212. Ferreira LP, Gaspar VM, Mano JF (2018) Design of spherically structured 3D in vitro tumor models -Advances and prospects. Acta Biomater 75:11–34. https://doi.org/10.1016/j.actbio.2018.05.034

213. Hinshaw DC, Shevde LA (2019) The Tumor Microenvironment Innately Modulates Cancer Progression. Am Assoc Cancer Res 4557–4567. https://doi.org/10.1158/0008-5472.CAN-18-3962

214. Balachander GM, Talukdar PM, Debnath M, et al (2018) Inflammatory Role of Cancer-Associated Fibroblasts in Invasive Breast Tumors Revealed Using a Fibrous Polymer Scaffold. ACS Appl Mater Interfaces 10:33814–33826. https://doi.org/10.1021/acsami.8b07609

215. Rijal G, Bathula C, Li W (2017) Application of Synthetic Polymeric Scaffolds in Breast Cancer 3D Tissue Cultures and Animal Tumor Models. Int J Biomater 2017:. https://doi.org/10.1155/2017/8074890

216. Polonio-Alcalá E, Rabionet M, Gallardo X, et al (2019) PLA electrospun scaffolds for three-dimensional triple-negative breast cancer cell culture. Polymers (Basel) 11:. https://doi.org/10.3390/polym11050916

217. Osuka S, Meir EG Van, Osuka S, Meir EG Van (2017) Overcoming therapeutic resistance in glioblastoma : the way forward Find the latest version : Overcoming therapeutic resistance in glioblastoma : the way forward. J Clin Invest 127:415–426

218. Kievit FM, Wang K, Erickson AE, et al (2016) Modeling the tumor microenvironment using chitosan-alginate scaffolds to control the stem-like state of glioblastoma cells. Biomater Sci 4:610–613. https://doi.org/10.1039/c5bm00514k

219. Girard YK, Wang C, Ravi S, et al (2013) A 3D Fibrous Scaffold Inducing Tumoroids: A Platform for Anticancer Drug Development. PLoS One 8:. https://doi.org/10.1371/journal.pone.0075345

220. Tostões RM, Leite SB, Serra M, et al (2012) Human liver cell spheroids in extended perfusion bioreactor culture for repeated-dose drug testing. Hepatology 55:1227–1236. https://doi.org/10.1002/hep.24760

221. Ginai M, Elsby R, Hewitt CJ, et al (2013) The use of bioreactors as in vitro models in pharmaceutical research. Drug Discov Today 18:922–935. https://doi.org/10.1016/j.drudis.2013.05.016

222. Parrish J, Lim KS, Baer K, et al (2018) A 96-well microplate bioreactor platform supporting individual dual perfusion and high-throughput assessment of simple or biofabricated 3D tissue models. Lab Chip 18:2757–2775. https://doi.org/10.1039/c8lc00485d

223. Schmid J, Schwarz S, Meier-Staude R, et al (2018) A perfusion bioreactor-system for cell seeding and oxygen-controlled cultivation of 3D-cell cultures. Tissue Eng Part C Methods 1–30. https://doi.org/10.1089/ten.TEC.2018.0204

224. Talò G, D'Arrigo D, Lorenzi S, et al (2020) Independent, Controllable Stretch-Perfusion Bioreactor Chambers to Functionalize Cell-Seeded Decellularized Tendons. Ann Biomed Eng 48:1112–1126. https://doi.org/10.1007/s10439-019-02257-6

225. Clift MJD, Doak SH (2021) Advanced In Vitro Models for Replacement of Animal Experiments. Small 17:2101474. https://doi.org/10.1002/smll.202101474

226. Lombardo ME, Carfì Pavia F, Vitrano I, et al (2019) PLLA scaffolds with controlled architecture as potential microenvironment for in vitro tumor model. Tissue Cell 58:33–41. https://doi.org/10.1016/j.tice.2019.04.004

227. Carfì Pavia F, La Carrubba V, Piccarolo S, Brucato V (2007) Polymeric scaffolds prepared via thermally induced phase separation: Tuning of structure and morphology. J Biomed Mater Res - Part A 86:459–466. https://doi.org/10.1002/jbm.a.31621

228. Mannella GA, Carfì Pavia F, La Carrubba V, Brucato V (2016) Phase separation of polymer blends in solution: A case study. Eur Polym J 79:176–186. https://doi.org/10.1016/j.eurpolymj.2016.04.025

229. Lombardo ME, Carfì Pavia F, Craparo EF, et al (2021) Novel dual-flow perfusion bioreactor for in vitro pre-screening of nanoparticles delivery: design, characterization and testing. Bioprocess Biosyst Eng 44:2361–2374. https://doi.org/10.1007/s00449-021-02609-

230. Shaikh A, Al-Dahhan M (2013) Scale-up of bubble column reactors: A review of current state-of-the-art. Ind Eng Chem Res 52:8091–8108. https://doi.org/10.1021/ie302080m

231. Craparo EF, Porsio B, Sardo C, et al (2016) Pegylated Polyaspartamide-Polylactide-Based Nanoparticles Penetrating Cystic Fibrosis Artificial Mucus. Biomacromolecules 17:767–777. https://doi.org/10.1021/acs.biomac.5b01480

232. Giammona G, Carlisi B, Palazzo S (1987) Reaction of α,β-poly(N-hydroxyethyl)-DL-aspartamide with derivatives of carboxylic acids. J Polym Sci Part A Polym Chem 25:2813–2818. https://doi.org/10.1002/pola.1987.080251016

233. Craparo EF, Porsio B, Mauro N, et al (2015) Polyaspartamide-Polylactide Graft Copolymers with Tunable Properties for the Realization of Fluorescent Nanoparticles for Imaging. Macromol Rapid Commun. https://doi.org/10.1002/marc.201500154

234. Sciortino L, Sciortino A, Popescu R, et al (2018) Tailoring the Emission Color of Carbon Dots through Nitrogen-Induced Changes of Their Crystalline Structure. J Phys Chem C 122:19897–19903. https://doi.org/10.1021/acs.jpcc.8b04514

235. Craparo EF, D'Apolito R, Giammona G, et al (2017) Margination of fluorescent polylactic acid-polyaspartamide based nanoparticles in microcapillaries in vitro: The effect of hematocrit and pressure. Molecules 22:. https://doi.org/10.3390/molecules22111845

236. Sciortino A, Mauro N, Buscarino G, et al (2018) β-C3N4 Nanocrystals: Carbon Dots with Extraordinary Morphological, Structural, and Optical Homogeneity. Chem Mater 30:1695–1700. https://doi.org/10.1021/acs.chemmater.7b05178

237. von Recum HA, Cleek RL, Eskin SG, Mikos AG (1995) Degradation of polydispersed poly(l-lactic acid) to modulate lactic acid release. Biomaterials 16:441–447. https://doi.org/10.1016/0142-9612(95)98816-W

238. Liu YS, Huang QL, Kienzle A, et al (2014) In vitro degradation of porous PLLA/pearl powder composite scaffolds. Mater Sci Eng C 38:227–234. https://doi.org/10.1016/j.msec.2014.02.007

239. Palumbo FS, Bongiovì F, Carfì Pavia F, et al (2019) Blend scaffolds with polyaspartamide/polyester structure fabricated via TIPS and their RGDC functionalization to promote osteoblast adhesion and proliferation. J Biomed Mater Res - Part A 107:2726–2735. https://doi.org/10.1002/jbm.a.36776

240. Renouf-Glauser AC, Rose J, Farrar D, Cameron RE (2005) A degradation study of PLLA containing lauric acid. Biomaterials 26:2415–2422. https://doi.org/10.1016/j.biomaterials.2004.07.067

241. Conoscenti G, Schneider T, Stoelzel K, et al (2017) PLLA scaffolds produced by thermally induced phase separation (TIPS) allow human chondrocyte growth and extracellular matrix formation dependent on pore size. Mater Sci Eng C 80:449–459. https://doi.org/10.1016/j.msec.2017.06.011

242. Bahcecioglu G, Basara G, Ellis BW, et al (2020) Breast cancer models: Engineering the tumor microenvironment. Acta Biomater 106:1–21. https://doi.org/10.1016/j.actbio.2020.02.006

243. Ghersi G, Carfì Pavia F, Conoscenti G, et al (2016) PLLA Scaffold via TIPS for Bone Tissue Engineering. Chem Eng Trans 49:301–306. https://doi.org/10.3303/CET1649051

244. Maddah HA (2016) Polypropylene as a Promising Plastic: A Review. Am J Polym Sci 6:1–11. https://doi.org/10.5923/j.ajps.20160601.01

245. Nájera-Aguilar HA, Mayorga-Santis R, Gutiérrez-Hernández RF, et al (2021) Aged Refuse Filled Bioreactor Using Like a Biological Treatment for Sugar Mill Wastewater. Sugar Tech 23:201–208. https://doi.org/10.1007/s12355-020-00881-4

246. Wang W, Yang Q, Zheng S, Wu D (2013) Anaerobic membrane bioreactor (AnMBR) for bamboo industry wastewater treatment. Bioresour Technol 149:292–300. https://doi.org/10.1016/j.biortech.2013.09.068

247. Martin I, Smith T, Wendt D (2009) Bioreactor-based roadmap for the translation of tissue engineering strategies into clinical products. Trends Biotechnol 27:495–502. https://doi.org/10.1016/j.tibtech.2009.06.002

248. Jasuja H, Kar S, Katti DR, Katti KS (2021) Perfusion bioreactor enabled fluid-derived shear stress conditions for novel bone metastatic prostate cancer testbed. Biofabrication 13:. https://doi.org/10.1088/1758-5090/abd9d6

249. Brancoft GN, Sikavitsas VI, Mikos AG (2003) Design of a Flow Perfusion Bioreactor System for Bone Tissue-Engineering. Tissue Eng 9:549–554. https://doi.org/10.1089/107632703322066723

250. Stephens JS, Cooper JA, Jr. FRP, Dunkers JP (2007) Perfusion Flow Bioreactor for 3D In Situ Imaging: Investigating Cell/Biomaterials. Biotechnol Bioeng 97:952–961. https://doi.org/10.1002/bit

251. Mandenius C (2016) Challenges for Bioreactor Design and Operation. In: Bioreactors: Design, Operation and Novel Applications. pp 1–34

252. Nasseri BA, Pomerantseva I, Kaazempur-Mofrad MR, et al (2003) Dynamic rotational seeding and cell culture system for vascular tube formation. Tissue Eng 9:291–299. https://doi.org/10.1089/107632703764664756

253. Koo MA, Kang JK, Lee MH, et al (2014) Stimulated migration and penetration of vascular endothelial cells into poly (L-lactic acid) scaffolds under flow conditions. Biomater Res 18:1–8. https://doi.org/10.1186/2055-7124-18-7

254. Anisi F, Salehi-Nik N, Amoabediny G, et al (2014) Applying shear stress to endothelial cells in a new perfusion chamber: hydrodynamic analysis. J Artif Organs 17:329–336. https://doi.org/10.1007/s10047-014-0790-0

255. Magrofuoco E, Flaibani M, Giomo M, Elvassore N (2019) Cell culture distribution in a

three-dimensional porous scaffold in perfusion bioreactor. Biochem Eng J 146:10–19. https://doi.org/10.1016/j.bej.2019.02.023

256. Pourchet L, Petiot E, Loubière C, et al (2018) Large 3D Bioprinted Tissue: Heterogeneous Perfusion and Vascularization. Bioprinting 13:1–7. https://doi.org/10.1016/j.bprint.2018.e00039

257. Egger D, Fischer M, Clementi A, et al (2017) Development and Characterization of a Parallelizable Perfusion Bioreactor for 3D Cell Culture. Bioengineering 4:51. https://doi.org/10.3390/bioengineering4020051

258. Nguyen BNB, Ko H, Fisher JP (2016) Tunable osteogenic differentiation of hMPCs in tubular perfusion system bioreactor. Biotechnol Bioeng 113:1805–1813. https://doi.org/10.1002/bit.25929

259. Navarro J, Swayambunathan J, Janes ME, et al (2019) Dual-chambered membrane bioreactor for coculture of stratified cell populations. Biotechnol Bioeng 116:3253–3268. https://doi.org/10.1002/bit.27164

260. Angeloni V, Contessi N, De Marco C, et al (2017) Polyurethane foam scaffold as in vitro model for breast cancer bone metastasis. Acta Biomater 63:306–316. https://doi.org/10.1016/j.actbio.2017.09.017

261. Liverani C, Mercatali L, Cristofolini L, et al (2017) Investigating the Mechanobiology of Cancer Cell–ECM Interaction Through Collagen-Based 3D Scaffolds. Cell Mol Bioeng 10:223–234. https://doi.org/10.1007/s12195-017-0483-x

262. Cailleau R, Young R, Olivé M, Reeves WJ (1974) Breast tumor cell lines from pleural effusions. J Natl Cancer Inst 53:661–674. https://doi.org/10.1093/jnci/53.3.661

263. Balachander GM, Balaji SA, Rangarajan A, Chatterjee K (2015) Enhanced Metastatic Potential in a 3D Tissue Scaffold toward a Comprehensive in Vitro Model for Breast Cancer Metastasis. ACS Appl Mater Interfaces 7:27810–27822. https://doi.org/10.1021/acsami.5b09064

264. Kenny PA, Lee GY, Myers CA, et al (2007) The morphologies of breast cancer cell lines in three-dimensional assays correlate with their profiles of gene expression. Mol Oncol 84–96. https://doi.org/10.1016/j.molonc.2007.02.004

265. Ariadna GP, Marc R, Teresa P, Joaquim C (2016) Optimization of Poli(ε-caprolactone) Scaffolds Suitable for 3D Cancer Cell Culture. Procedia CIRP 49:61–66. https://doi.org/10.1016/j.procir.2015.07.031

266. Senanayake KK, Fakhrabadi EA, Liberatore MW, Mukhopadhyay A (2019) Diffusion of Nanoparticles in Entangled Poly(vinyl alcohol) Solutions and Gels. Macromolecules 52:787–795. https://doi.org/10.1021/acs.macromol.8b01917

267. Craparo EF, Porsio B, Sardo C, et al (2016) Pegylated Polyaspartamide–Polylactide-Based Nanoparticles Penetrating Cystic Fibrosis Artificial Mucus. Biomacromolecules 17:767–777. https://doi.org/10.1021/acs.biomac.5b01480

268. Craparo EF, Licciardi M, Conigliaro A, et al (2015) Hepatocyte-targeted fluorescent nanoparticles based on a polyaspartamide for potential theranostic applications. Polymer (Guildf) 70:257–270. https://doi.org/10.1016/j.polymer.2015.06.009

269. Arefina IA, Khavlyuk PD, Stepanidenko EA, et al (2020) Influence of heteroatoms on optical properties and photoluminescence kinetics of carbon dots. J Phys Conf Ser 1461:. https://doi.org/10.1088/1742-6596/1461/1/012008

270. Jiang L, Ding H, Xu M, et al (2020) UV–Vis–NIR Full-Range Responsive Carbon Dots with Large Multiphoton Absorption Cross Sections and Deep-Red Fluorescence at Nucleoli and In Vivo. Small 16:1–9. https://doi.org/10.1002/smll.202000680

271. Myint AA, Rhim WK, Nam JM, et al (2018) Water-soluble, lignin-derived carbon dots with high fluorescent emissions and their applications in bioimaging. J Ind Eng Chem 66:387–395. https://doi.org/10.1016/j.jiec.2018.06.005

272. Dalmark M, Hoffmann EK (1983) Doxorubicin (adriamycin) transport in ehrlich ascites tumour cells: Comparison with transport in human red blood cells. Scand J Clin Lab Invest 43:241–248. https://doi.org/10.1080/00365518309168251

273. Jiang K, Feng X, Gao X, et al (2019) Preparation of multicolor photoluminescent carbon dots by tuning surface states. Nanomaterials 9:1–12. https://doi.org/10.3390/nano9040529

274. Kozák O, Datta KKR, Greplová M, et al (2013) Surfactant-derived amphiphilic carbon dots with tunable photoluminescence. J Phys Chem C 117:24991–24996. https://doi.org/10.1021/jp4040166

275. Papaioannou N, Marinovic A, Yoshizawa N, et al (2018) Structure and solvents effects on the optical properties of sugar-derived carbon nanodots. Sci Rep 8:1–10. https://doi.org/10.1038/s41598-018-25012-8

276. Jalilov AS (2020) Solvent effect on structural elucidation of photoluminescent graphitic carbon nanodots. ACS Omega 5:20409–20416. https://doi.org/10.1021/acsomega.0c02375

277. Liu JJ, Li D, Zhang K, et al (2018) Supporting Info-One Step Hydrothermal Synthesis of Nitrogen-Doped Conjugated Carbonized Polymer Dots with 31% Efficient Red Emission for In Vivo Imaging. Small 14:. https://doi.org/10.1002/smll.201703919

278. Shen C, Wang J, Cao Y, Lu Y (2015) Facile access to B-doped solid-state fluorescent carbon dots toward light emitting devices and cell imaging agent. J Mater Chem C 1:1–23. https://doi.org/10.1039/b000000x

279. Yao YY, Gedda G, Girma WM, et al (2017) Magnetofluorescent Carbon Dots Derived from Crab Shell for Targeted Dual-Modality Bioimaging and Drug Delivery. ACS Appl Mater Interfaces 9:13887–13899. https://doi.org/10.1021/acsami.7b01599

280. Huang S, Yang E, Yao J, et al (2019) Nitrogen, Cobalt Co-doped Fluorescent Magnetic Carbon Dots as Ratiometric Fluorescent Probes for Cholesterol and Uric Acid in Human Blood Serum. ACS Omega 4:9333–9342. https://doi.org/10.1021/acsomega.9b00874

281. Zhang HY, Wang Y, Xiao S, et al (2017) Rapid detection of Cr(VI) ions based on cobalt(II)-doped carbon dots. Biosens Bioelectron 87:46–52. https://doi.org/10.1016/j.bios.2016.08.010

282. Liu S, Tian J, Wang L, et al (2012) Hydrothermal treatment of grass: A low-cost, green route to nitrogen-doped, carbon-rich, photoluminescent polymer nanodots as an effective fluorescent sensing platform for label-free detection of Cu(II) ions. Adv Mater 24:2037–2041. https://doi.org/10.1002/adma.201200164

283. Liu JJ, Li D, Zhang K, et al (2018) One-Step Hydrothermal Synthesis of Nitrogen-Doped Conjugated Carbonized Polymer Dots with 31% Efficient Red Emission for In Vivo Imaging. Small 14:1–10. https://doi.org/10.1002/smll.201703919

284. Liu J, Lu S, Tang Q, et al (2017) One-step hydrothermal synthesis of photoluminescent carbon nanodots with selective antibacterial activity against Porphyromonas gingivalis. Nanoscale 9:7135–7142. https://doi.org/10.1039/c7nr02128c

285. Ganguly A, Sharma S, Papakonstantinou P, Hamilton J (2011) Probing the thermal deoxygenation of graphene oxide using high-resolution in situ X-ray-based spectroscopies. J Phys Chem C 115:17009–17019. https://doi.org/10.1021/jp203741y

286. Mondal S, Yucknovsky A, Akulov K, et al (2019) Efficient Photosensitizing Capabilities and Ultrafast Carrier Dynamics of Doped Carbon Dots. J Am Chem Soc 141:15413–15422. https://doi.org/10.1021/jacs.9b08071

287. Jana J, Ganguly M, Chandrakumar KRS, et al (2017) Boron precursor-dependent evolution of differently emitting carbon dots. Langmuir 33:573–584. https://doi.org/10.1021/acs.langmuir.6b04100

288. Bourlinos AB, Trivizas G, Karakassides MA, et al (2015) Green and simple route toward boron doped carbon dots with significantly enhanced non-linear optical properties. Carbon N Y 83:173–179. https://doi.org/10.1016/j.carbon.2014.11.032

289. Liu Y, Duan W, Song W, et al (2017) Red Emission B, N, S-co-Doped Carbon Dots for Colorimetric and Fluorescent Dual Mode Detection of Fe3+ Ions in Complex Biological Fluids and Living Cells. ACS Appl Mater Interfaces 9:12663–12672. https://doi.org/10.1021/acsami.6b15746

290. Yang J, Gao G, Zhang X, et al (2019) One-step synthesized carbon dots with bacterial contact-enhanced fluorescence emission property: Fast Gram-type identification and selective Gram-positive bacterial inactivation. Carbon N Y 146:827–839. https://doi.org/10.1016/j.carbon.2019.02.040

291. Lu W, Gong X, Yang Z, et al (2015) High-quality water-soluble luminescent carbon dots for multicolor patterning, sensors, and bioimaging. RSC Adv 5:16972–16979. https://doi.org/10.1039/c4ra16233a

292. Choi Y, Choi Y, Kwon OH, Kim BS (2018) Carbon Dots: Bottom-Up Syntheses, Properties, and Light-Harvesting Applications. Chem - An Asian J 13:586–598.

https://doi.org/10.1002/asia.201701736

293. Nie H, Li M, Li Q, et al (2014) Reply to comment on "carbon dots with continuously tunable full-color emission and their application in ratiometric pH sensing." Chem Mater 26:6084. https://doi.org/10.1021/cm503256m

294. Barati A, Shamsipur M, Abdollahi H (2016) Carbon dots with strong excitation-dependent fluorescence changes towards pH. Application as nanosensors for a broad range of pH. Anal Chim Acta 931:25–33. https://doi.org/10.1016/j.aca.2016.05.011

295. van Dam B, Nie H, Ju B, et al (2017) Excitation-Dependent Photoluminescence from Single-Carbon Dots. Small 13:1–5. https://doi.org/10.1002/smll.201702098

296. Wang H, Lu F, Ma C, et al (2021) Carbon dots with positive surface charge from tartaric acid and m-aminophenol for selective killing of Gram-positive bacteria. J Mater Chem B 9:125–130. https://doi.org/10.1039/d0tb02332a

297. Fang HY, Huang WM, Chen DH (2019) One-step synthesis of positively charged bifunctional carbon dot/silver composite nanoparticles for killing and fluorescence imaging of Gram-negative bacteria. Nanotechnology 30:. https://doi.org/10.1088/1361-6528/ab1fef

298. Jian HJ, Wu RS, Lin TY, et al (2017) Super-Cationic Carbon Quantum Dots Synthesized from Spermidine as an Eye Drop Formulation for Topical Treatment of Bacterial Keratitis. ACS Nano 11:6703–6716. https://doi.org/10.1021/acsnano.7b01023

299. Lin Z, Xue W, Chen H, Lin JM (2012) Classical oxidant induced chemiluminescence of fluorescent carbon dots. Chem Commun 48:1051–1053. https://doi.org/10.1039/c1cc15290d

300. Willander M, Adam R, Alnoor H, et al (2018) Optical and magneto-optical properties of zinc-oxide nanostructures grown by the low-temperature chemical route. 42. https://doi.org/10.1117/12.2288970

301. Stehr JE, Hofmann DM, Chen WM, Buyanova IA (2019) Electron paramagnetic resonance signatures of Co 2 +. Appl Phys Lett 119:1–13. https://doi.org/10.1063/1.5127651

302. Khan WU, Wang D, Zhang W, et al (2017) High quantum yield green-emitting carbon dots for Fe(III) detection, biocompatible fluorescent ink and cellular imaging. Sci Rep 7:1–9. https://doi.org/10.1038/s41598-017-15054-9

303. Han Z, He L, Pan S, et al (2020) Hydrothermal synthesis of carbon dots and their application for detection of chlorogenic acid. Luminescence 35:989–997. https://doi.org/10.1002/bio.3803

304. Liu C, Zhang F, Hu J, et al (2021) A Mini Review on pH-Sensitive Photoluminescence in Carbon Nanodots. Front Chem 8:1–9. https://doi.org/10.3389/fchem.2020.605028

305. Wang C, Xu Z, Cheng H, et al (2015) A hydrothermal route to water-stable luminescent carbon dots as nanosensors for pH and temperature. Carbon N Y 82:87–95. https://doi.org/10.1016/j.carbon.2014.10.035

306. Ye X, Xiang Y, Wang Q, et al (2019) A Red Emissive Two-Photon Fluorescence Probe Based on Carbon Dots for Intracellular pH Detection. Small 15:1–9. https://doi.org/10.1002/smll.201901673

307. Xiong Y, Schneider J, Reckmeier CJ, et al (2017) Carbonization conditions influence the emission characteristics and the stability against photobleaching of nitrogen doped carbon dots. Nanoscale 9:11730–11738. https://doi.org/10.1039/c7nr03648e

308. Mirza Z, Karim S (2021) Nanoparticles-based drug delivery and gene therapy for breast cancer: Recent advancements and future challenges. Semin Cancer Biol 69:226–237. https://doi.org/10.1016/j.semcancer.2019.10.020

309. Zhao D, Liu X, Wei C, et al (2019) One-step synthesis of red-emitting carbon dots: Via a solvothermal method and its application in the detection of methylene blue. RSC Adv 9:29533–29540. https://doi.org/10.1039/c9ra05570c

310. Ferrari SM, Elia G, Ragusa F, et al (2020) Novel treatments for anaplastic thyroid carcinoma. Gland Surg 9:S28–S42. https://doi.org/10.21037/gs.2019.10.18

311. Saini S, Tulla K, Maker A V., et al (2018) Therapeutic advances in anaplastic thyroid cancer: A current perspective 11 Medical and Health Sciences 1112 Oncology and Carcinogenesis. Mol Cancer 17:1–14. https://doi.org/10.1186/s12943-018-0903-0

312. Tiedje V, Stuschke M, Weber F, et al (2018) Anaplastic thyroid carcinoma: Review of treatment protocols. Endocr Relat Cancer 25:R153–R161. https://doi.org/10.1530/ERC-17-0435

313. Niu Y, Ding Z, Deng X, et al (2020) A Novel Multimodal Therapy for Anaplastic Thyroid Carcinoma: 125I Seed Implantation Plus Apatinib After Surgery. Front Endocrinol (Lausanne) 11:1–5. https://doi.org/10.3389/fendo.2020.00207

314. Lee H, Kim SY, Kim SM, et al (2020) Long-term survival of patients with anaplastic thyroid cancer after multimodal treatment. Transl Cancer Res 9:5430–5436. https://doi.org/10.21037/tcr-20-1364

315. Mao S, Pang Y, Liu T, et al (2020) Bioprinting of in vitro tumor models for personalized cancer treatment: a review. Biofabrication 12:1–16. https://doi.org/10.1088/1758-5090/ab97c0

316. Insua-Rodríguez J, Oskarsson T (2016) The extracellular matrix in breast cancer. Adv Drug Deliv Rev 97:41–55. https://doi.org/10.1016/j.addr.2015.12.017

317. Kitaeva K V., Rutland CS, Rizvanov AA, Solovyeva V V. (2020) Cell Culture Based in vitro Test Systems for Anticancer Drug Screening. Front Bioeng Biotechnol 8:1–9. https://doi.org/10.3389/fbioe.2020.00322

318. Prieto-Vila M, Takahashi RU, Usuba W, et al (2017) Drug resistance driven by cancer stem cells and their niche. Int J Mol Sci 18:. https://doi.org/10.3390/ijms18122574

319. Tomasello L, Coppola A, Pitrone M, et al (2019) PFN1 and integrin-β1/mTOR axis

involvement in cornea differentiation of fibroblast limbal stem cells. J Cell Mol Med 23:7210–7221. https://doi.org/10.1111/jcmm.14438

320. Rao X, Lai D, Huang X (2013) A new method for quantitative real-time polymerase chain reaction data analysis. J Comput Biol 20:703–711. https://doi.org/10.1089/cmb.2012.0279

321. Vinogradov S, Wei X (2012) Cancer stem cells and drug resistance: The potential of nanomedicine. Nanomedicine 7:597–615. https://doi.org/10.2217/nnm.12.22

322. Thi L, Phi H, Sari IN, et al (2018) Review Article Cancer Stem Cells (CSCs) in Drug Resistance and their Therapeutic Implications in Cancer Treatment. Stem Cells Int 2018:1–16

323. Lombardo ME, Zito G, Pavia FC, et al (2020) 3D polymeric supports promote the growth and progression of anaplastic thyroid carcinoma. Biochem Biophys Res Commun 531:223–227. https://doi.org/10.1016/j.bbrc.2020.07.062

324. Dowd KO, Nair KM, Forouzandeh P, et al (2020) Face Masks and Respirators in the Fight Against the COVID-19 Pandemic: A Review of Current Materials, Advances and Future Perspectives. Materials (Basel) 13:1–27. https://doi.org/10.3390/ma13153363

325. Choi S, Jeon H, Jang M, et al (2021) Biodegradable, Efficient, and Breathable Multi-Use Face Mask Filter. Adv Sci 8:1–8. https://doi.org/10.1002/advs.202003155

326. Armentano I, Barbanera M, Carota E, et al (2021) Polymer Materials for Respiratory Protection: Processing, End Use, and Testing Methods. ACS Appl Polym Mater 3:531–548. https://doi.org/10.1021/acsapm.0c01151

327. He H, Gao M, Illés B, Molnar K (2020) 3D Printed and electrospun, transparent, hierarchical polylactic acid mask nanoporous filter. Int J Bioprinting 6:1–10. https://doi.org/10.18063/ijb.v6i4.278

328. Shen H, Zhou Z, Wang H, et al (2021) Development of Electrospun Nanofibrous Filters for Controlling Coronavirus Aerosols. Environ Sci Technol Lett 8:545–550. https://doi.org/10.1021/acs.estlett.1c00337

329. Karabulut DF (2020) Melt-Blown Fibres vs Electrospun Nanofibres as Filtration Media. In: Innov. Text. https://www.innovationintextiles.com/

330. Essa W, Yasin S, Saeed I, Ali G (2021) Nanofiber-Based Face Masks and Respirators as COVID-19 Protection: A Review. Membranes (Basel) 11:250. https://doi.org/10.3390/membranes11040250

331. Fadare OO, Okoffo ED (2020) Covid-19 face masks: A potential source of microplastic fibers in the environment. Sci Total Environ 737:140279. https://doi.org/10.1016/j.scitotenv.2020.140279

332. Babaahmadi V, Amid H, Naeimirad M, Ramakrishna S (2021) Biodegradable and multifunctional surgical face masks: A brief review on demands during COVID-19 pandemic, recent developments, and future perspectives. Sci Total Environ 798:149233.

https://doi.org/10.1016/j.scitotenv.2021.149233

333. Zhang J, Gong S, Wang C, et al (2019) Biodegradable Electrospun Poly(lactic acid) Nanofibers for Effective PM 2.5 Removal. Macromol Mater Eng 304:1–8. https://doi.org/10.1002/mame.201900259

334. Lin CC, Fu SJ, Lin YC, et al (2014) Chitosan-coated electrospun PLA fibers for rapid mineralization of calcium phosphate. Int J Biol Macromol 68:39–47. https://doi.org/10.1016/j.ijbiomac.2014.04.039

335. Forrey C, Muthukumar M (2009) Electrostatics of capsid-induced viral RNA organization. J Chem Phys 131:1–10. https://doi.org/10.1063/1.3216550

336. Schoeman D, Fielding BC, Arias-Reyes C, et al (2020) Journal Pre-proof Does the pathogenesis of SAR-CoV-2 virus decrease at high-altitude? Does the pathogenesis of SAR-CoV-2 virus decrease at high-altitude? Corresponding authors. Cell Res 9:278–280. https://doi.org/10.3390/ijerph17082932

337. Palmieri S, Pierpaoli M, Riderelli L, et al (2020) Preparation and characterization of an electrospun pla-cyclodextrins composite for simultaneous high-efficiency pm and voc removal. J Compos Sci 4:1–11. https://doi.org/10.3390/jcs4020079

338. Li H, Wang Z, Zhang H, Pan Z (2018) Nanoporous PLA/(Chitosan Nanoparticle) composite fibrous membranes with excellent air filtration and antibacterial performance. Polymers (Basel) 10:10–12. https://doi.org/10.3390/polym10101085

339. Ullah S, Ullah A, Lee J, et al (2020) Reusability Comparison of Melt-Blown vs Nanofiber Face Mask Filters for Use in the Coronavirus Pandemic. ACS Appl Nano Mater 3:7231–7241. https://doi.org/10.1021/acsanm.0c01562

340. Hossain E, Bhadra S, Jain H, et al (2020) Recharging and rejuvenation of decontaminated N95 masks. Phys Fluids 32:1–7. https://doi.org/10.1063/5.0023940

341. Kravtsov A, Brünig H, Zhandarov S, Beyreuther R (2000) Electret effect in polypropylene fibers treated in a corona discharge. Adv Polym Technol 19:312–316. https://doi.org/10.1002/1098-2329(200024)19:4<312::AID-ADV7>3.0.CO;2-X

342. Yim W, Cheng D, Patel SH, et al (2020) KN95 and N95 Respirators Retain Filtration Efficiency despite a Loss of Dipole Charge during Decontamination. ACS Appl Mater Interfaces 12:54473–54480. https://doi.org/10.1021/acsami.0c17333

343. N95DECON (2020) Cloth Mask Breathability and Filtration Efficiency Technical Report. 1–40

344. Akduman C, Akcakoca Kumbasar EP (2018) Nanofibers in face masks and respirators to provide better protection. IOP Conf Ser Mater Sci Eng 460:. https://doi.org/10.1088/1757-899X/460/1/012013

345. Shen R, Xu W, Xue Y, et al (2018) The use of chitosan/PLA nano-fibers by emulsion eletrospinning for periodontal tissue engineering. Artif Cells, Nanomedicine Biotechnol

46:419–430. https://doi.org/10.1080/21691401.2018.1458233

346. Akbar K, Moretti E, Vomiero A (2021) Carbon Dots for Photocatalytic Degradation of Aqueous Pollutants: Recent Advancements. Adv Opt Mater 9:. https://doi.org/10.1002/adom.202100532

347. Vasiljevic ZZ, Dojcinovic MP, Vujancevic JD, et al (2020) Photocatalytic degradation of methylene blue under natural sunlight using iron titanate nanoparticles prepared by a modified sol-gel method: Methylene blue degradation with Fe2TiO5. R Soc Open Sci 7:. https://doi.org/10.1098/rsos.200708

348. Yao J, Wang C (2010) Decolorization of methylene blue with TiO2 sol via UV irradiation photocatalytic degradation. Int J Photoenergy 2010:1–6. https://doi.org/10.1155/2010/643182

349. Niazi Z, Goharshadi EK, Mashreghi M, Jorabchi MN (2021) Highly efficient solar photocatalytic degradation of a textile dye by TiO2/graphene quantum dots nanocomposite. Photochem Photobiol Sci 20:87–99. https://doi.org/10.1007/s43630-020-00005-7

350. Azeez F, Al-Hetlani E, Arafa M, et al (2018) The effect of surface charge on photocatalytic degradation of methylene blue dye using chargeable titania nanoparticles. Sci Rep 8:1–9. https://doi.org/10.1038/s41598-018-25673-5

351. Al-Hetlani E, Amin MO, Madkour M (2017) Detachable photocatalysts of anatase TiO 2 nanoparticles: Annulling surface charge for immediate photocatalyst separation. Appl Surf Sci 411:355–362. https://doi.org/10.1016/j.apsusc.2017.03.151

352. Xian T, Sun X, Di L, et al (2019) Carbon quantum dots (CQDs) decorated Bi2O3-x hybrid photocatalysts with promising NIR-light-driven photodegradation activity for AO7. Catalysts 9:. https://doi.org/10.3390/catal9121031

353. Peng Z, Zhou Y, Ji C, et al (2020) Facile synthesis of “boron-doped” carbon dots and their application in visible-light-driven photocatalytic degradation of organic dyes. Nanomaterials 10:1–17. https://doi.org/10.3390/nano10081560

354. Umoren SA, Etim UJ, Israel AU (2013) Adsorption of methylene blue from industrial effluent using poly (vinyl alcohol). J Mater Environ Sci 4:75–86

355. Alzahrani E (2015) Photodegradation of Eosin y Using Silver-Doped Magnetic Nanoparticles. Int J Anal Chem 2015:. https://doi.org/10.1155/2015/797606

356. Fernandes RJC, Magalhães CAB, Amorim CO, et al (2019) Magnetic nanoparticles of zinc/calcium ferrite decorated with silver for photodegradation of dyes. Materials (Basel) 12:. https://doi.org/10.3390/ma12213582

357. Houas A, Lachheb H, Ksibi M, et al (2001) Photocatalytic degradation pathway of methylene blue in water. Appl Catal B Environ 31:145–157. https://doi.org/10.1016/S0926-3373(00)00276-9

LIST OF PUBLICATIONS

1. Capuana E.; Carfì Pavia, F.; **Lombardo, M.E.**; Rigogliuso S.; Ghersi, G.; La Carrubba V.; Brucato V. Mathematical and numerical modeling of an airlift perfusion bioreactor for tissue engineering applications". *Biochemical Engineering Journal*, 178:1-14 (2021).
2. **Lombardo, M.E**; Carfì Pavia, F.; Craparo, E. F.; Capuana, E.; Cavallaro, G.; Brucato V.; La Carrubba V. Novel dual-flow perfusion bioreactor for in vitro pre-screening of nanoparticles delivery: design, characterization and testing. *Bioprocess and Biosystems Engineering*, 44: 2361-2374 (2021)
3. **Lombardo, M.E.**; Benetti D.; La Carrubba V.; Rosei, F. Heteroatom-doping for carbon dots: an efficient strategy to improve their optoelectronic properties". ECS Meeting Abstract, ECS-The Electrochemical Society. Volume MA 2020-01 D02: Nanoscale Luminescent Materials 6 (2020).
4. **Lombardo, M.E.**; Carfì Pavia, F.; Zito, G; Pizzolanti, G.; Giordano, C; Brucato, V.; La Carrubba, V. 3D polymeric supports promote the growth and progression of anaplastic thyroid carcinoma. *Biochem Biophys Res Commun*, 531:223-227 (2020)
5. **Lombardo, M.E.**; Carfì Pavia, F.; Vitrano, I.; Ghersi, G.; Brucato, V.; Rosei, F.; La Carrubba, V. PLLA Scaffolds with Controlled Architecture as Potential Microenvironment for in Vitro Tumor Model. *Tissue and Cell*, *58:* 33–41 (2019).
6. Vitrano, I.; Carfì Pavia, F.; Conoscenti, G.; **Lombardo, M. E.**; Carrubba, V. L.; Brucato, V. Evaluation of Hydroxyapatite Distribution in a Poly-L-Lactic Acid (PLLA) Scaffolds via Micro Computed Tomography (MCT). *Chemical Engineering Transactions*, *64* (2018).
7. **Lombardo, M.E.**; Benetti, D.; Lambert-Fliszar E.; Rajagopalan, S.; Rosei, F. Eco-friendly positively charged nanofibers for face masks (Manuscript in preparation)
8. **Lombardo, M.E.**; Benetti, D.; Rosei, F. Solar photocatalytic degradation of Methylene Blue dye using red-emitted doped CDs (Manuscript in preparation)

LIST OF CONFERENCE PRESENTATIONS

1. **Lombardo M.E.**; Carfì Pavia, F.; Sciortino, A.; Messina, F.; Brucato, V.; La Carrubba, V. "Dual-emission carbon dots in polymeric scaffold for biomedical applications" GRICU National Congress ("The contribution of Italian Chemical Engineering to global sustainability"). Palermo-Mondello, 2019 (poster)
2. **Lombardo M.E.**; Carfì Pavia, F.; Ghersi, G.; La Carrubba, V.; Brucato, V. "INFLUENCE OF PORE SIZE ON BREAST CANCER CELLS GROWTH IN PLLA SCAFFOLDS" abstract at the National Congress of Biomaterial. Rende (Calabria, Italy). June 2018
3. **Lombardo M.E.**; Vitrano, I.; Carfì Pavia, F.; Conoscenti G.; La Carrubba, V.; Brucato, V. "Double Flow Perfusion Bioreactor for dynamic 3D cell cultures and in vitro test of drug delivery" GRICU Ph.D. National School (Multi-scale modelling for chemical engineering; From research in the lab to profitable applications). Palermo, 2017 (poster)

APPENDICES

APPENDIX A

3D polymeric scaffold for studying anaplastic thyroid carcinoma (ACT) cells biology

A.1. INTRODUCTION

Among the deadliest human cancers and particularly the thyroid cancers, anaplastic thyroid carcinoma (ATC) represents a small subgroup of undifferentiated thyroid cancers (< 2%). However, it is highly aggressive and nearly incurable with a fast course of disease progression and high resistance to conventional treatments [310]. The current therapies for ATC include a primary surgical resection (Lobectomy or Total thyroidectomy), followed by cytotoxic chemotherapies of single-agent or a combination of drugs such as Doxorubicin, Cisplatin, Docetaxel, Paclitaxel and Platins [311]. Recently, other clinical trials are carrying on which involve targeted drugs such as BRAF, MEK and mTOR inhibitors [312, 313] and new treatments including gene therapy and immunotherapy [310]. Unfortunately, they have shown low performance status especially in ATC patients at a late disease stage and, so far, no unified treatment is established. Considering its malignancy, rarity and the several genetic mutations, it is still a big challenge the development of efficacy targeted therapy approaches and new treatment options in order to improve the quality of life in ATC patients with at least a favorable survival up to 13 months [314]. With the recent development and advances in biotechnologies, biomaterials and tissue engineering methods, studying tumor biology and evaluating the treatment effects with novel anticancer agents have gone through significant improvements [315]. It is well known that *in vivo* tumor microenvironment is a complex environment characterized by different cell phenotypes and the ECM which provides physical support to the malignant cells and it is also an important source of key growth factors [316]. As already mentioned in Chapter 1, the traditional 2D cell culture with

a monolayer growing on a flat surface provides a useless platform for imitating the cell microenvironment *in vivo*, especially for tumor cells, together with relevant differences in the phenotype, gene and protein expression, and drug sensitivity [31]. Additionally, preclinical *in vivo* testing on animal models is still an important tool for tumor research to assess the therapeutic efficacy of new compounds and the toxicity at specific doses before being admitted for human clinical trials. However, the use of animal models has disadvantages, such as ethical disputes, high cost and difficult operations, differential responses due to the genetic backgrounds different from humans', and restrictions in feasibility and availability of tests [317]. In the last decades, the choice of the 3D tumor cell culture and 3D tumor models at the stage of preclinical *in vitro* testing has provided the perfect bridge between the common 2D *in vitro* cell culture and the *in vivo* animal testing. This owned to the reduction in both financial and time costs due to the early pre-screening of inefficient compounds and to the decrease in number of animals used in tumor research and drug evaluation [31]. Among the various methods for 3D cell culture, scaffold-based models (matrices both natural and/or synthetic) have been widely used as sophisticated engineered platforms for anticancer studies, as already mentioned in Chapter 1. Starting from this knowledge, in this work a PLLA microporous scaffold produced via TIPS was used as support for the growth of human anaplastic thyroid carcinoma cell line C643. Cell viability and morphology were analyzed before and after treatment with one of the most active anticancer drugs for solid tumors, Doxorubicin (Dox). Furthermore, Cancer Stem Cells (CSCs) enrichment was investigated since many studies suggest them as the main source of tumor resistance, recurrence and metastasis [318]. This work wanted to propose a potential 3D *in vitro* model that can be used to understand the pathogenesis of this rare tumor and also to guide the future selection of the right therapy approaches for the ATC and maybe other treatment-resistant thyroid cancers.

A.2. MATERIALS AND METHODS

A.2.1. PLLA scaffold synthesis and characterization

The synthesis protocol carried out for the polymeric scaffold applied in this experimentation is the one already reported in Chapter 3: Materials and Methods, Part 1. Briefly, a HDPE cylindrical sample holder was filled with a ternary polymeric solution (PLLA/Dioxane/water) at

60°C and immersed into a thermostatic water bath at 20°C for 15 min, where the TIPS process takes place. In order to obtain the desired porous structure, the demixing was stopped by a quick pool immersion into a -20°C bath of the sample-older previously embedded in a PTFE coating. After washing in deionized water and drying under vacuum overnight, the morphology of the obtained scaffold was analyzed by SEM.

A.2.2. Cell culture and seeding

ATC cell line C643 were cultured in common tissue culture flasks with RPMI 1640 culture medium supplemented with 10% fetal bovine serum (FBS, Euroclone) and 1% (v/v) penicillin-streptomycin (P/S, Euroclone) and incubated at 37°C and 5% CO_2. After reaching 80%-90% of confluence, the cells were seeded on PLLA scaffold disks (thickness ~5mm), placed in a 24-well plate, at a concentration of 4 x 10^4 cell/ml and cultured for 9 days for all the next experiments.

A.2.3. Analysis of viability, proliferation and morphology of cells within the seeded scaffolds

Cell viability within the 3D scaffold was evaluated by AB assay kit by following the same steps described in Chapter 2: Materials and Methods, Part 4. At different time points (24 h, 3d, 4d, 6d, 7d, 9d) fresh complete culture medium with AB mixture (90/10 v/v) was added to each well in a 24-well plate. Then the cell-seeded scaffolds were incubated at 37°C for 3 hours and the fluorescence of the supernatant was measured with a microplate spectrophotometer. A scaffold without cells was used as control and all the tests were performed in triplicate.

For cell proliferation investigation, the dye DAPI was used and cell nuclei were stained. After 3d, 6d and 9d of culture, the C643 cells were fixed on the scaffold by applying 4% paraformaldehyde (PFA, Sigma-Aldrich) to each sample and kept for 30 min at 4°C. After washing with a complete PBS buffer solution several times, few drops of DAPI were added to each sample and kept for 5 mins at room temperature in the dark. The as-treated cell-seeded scaffolds were observed under a fluorescence microscope. All tests were performed in duplicate. Finally, the morphology of the tumor cells after the 3D culture was analysed by SEM as already described in Chapter 3: Materials and Methods, Part 3.

A.2.4. RNA extraction and quantification via real-time PCR before and after treatment with Doxorubicin

For the isolation of RNA and quantitative real-time PCR (qRT-PCR) analysis, C643 cells were harvested from PLLA scaffolds at 3 time points (3d, 6d and 9d). RNA extraction from the detached cells was performed with a RNeasy Mini Kit (Qiagen, Milan, Italy), following the manufacturer's protocol. RNA concentration was measured by UV spectrophotometry and 1 μg of total RNA was used for complementary DNA (cDNA) synthesis. cDNA synthesis was carried out using Reverse Transcriptase Rnase kit (Imporm II, Promega, Wisconsin, USA), as the manufacturer's protocol. Each cDNA sample was mixed with specific primer sets and gene expression analysis was assessed by qRT-PCR on the RotorGene Q Instrument (Qiagen), as previously described [319]. PCR primers used were *NANOG* (QT01844808), *OCT3/4* (QT00210840), *SOX2* (QT00237601), *ABCG2* (QT00095431), *SURVIVIN* (QT00081186), *BCL-2* (QT00025011) and were purchased from Qiagen (QuantiTect ®Primer Assays, Qiagen, Hamburg, Germany), while β-*Actin* (FORWARD: 5' -GGACTT CGA GCA AGA GAT GG-3' REVERSE: 5' -AGC ACT GTG TTG GCG TAC AG-3') was purchased from Invitrogen. Gene level quantification was performed normalizing expression levels to β-actin-mRNA levels and the relative gene expression levels were expressed as fold change according to the $2^{-\Delta\Delta Ct}$ algorithm [320]. The results were represented as histograms on GraphPad Software, Inc, California.

The next step was the investigation of cell-drug sensitivity of C643 cells grown within the 3D supports. For this reason, cells cultured onto PLLA scaffolds were treated with fresh culture medium supplemented with 5 mM of the Doxorubicin (Dox, Sigma-Aldrich) at three different time points (3d, 6d, 9d). First, cell viability was evaluated after 48 hours of treatment using the AB assay as previously described. A non-treated scaffold seeded with the same cell density was used as control and all the tests were performed in triplicate. At the same time, the gene expression levels and apoptotic markers were examined for the cells cultured onto the scaffold and treated with Dox by using qRT-PCR and following the protocol described above for RNA extraction, cDNA synthesis and quantification.

A.3. RESULTS AND DISCUSSION

For the present study, a biocompatible PLLA scaffold was used as a 3D platform for ATC *in vitro* cell culture and evaluation of its impact on the cell metabolic activity, cell-drug sensitivity

and resistance. As already demonstrated in Chapter 4: Results and Discussion, Part 1, a microporous 3D structure with a high interconnection and homogeneous pore size of about 40-50 μm is able to induce the formation of tumour-like *in vivo* cell aggregates. Therefore, we chose PLLA-50 scaffold as a starting point for carrying on the following experimental study. The SEM micrograph of the cross section of the as-mentioned scaffold is shown in Figure 4.1 E (Chapter 4: Results and Discussion, Part 1). The proliferation and morphology of C643 tumor cell line grown for 9 days onto the PLLA scaffold are reported in Figure A1. From DAPI staining it is possible to appreciate the full cell colonization of the 3D polymeric network since day 3 of culture (Figure A1 a). The morphology of the cells in the scaffold was evaluated via SEM (Figure A1 b). After 9 days of culture, the cells showed a tendency to form multicellular aggregates, potentially resembling *in vivo* solid tumor masses. Finally, the cell viability over time was determined using AB assay and the proliferation events promoted by the 3D culture were demonstrated. The curve depicted in Figure A1 (c) shows an increase in the cell number in the early culturing period (day 1 to day 4), followed by a reduction of the proliferation rate until day 7 of culture, and a final increment in the last portion of the curve.

As therapy resistance seems to be one of the biggest problems in ATC treatment [311] and it has been gradually accepted that the small population of CSCs in tumors might be responsible of cancer therapy failure due to their considerable chemo- and radio-resistance [318, 321, 322], the behavior of C643 cells grown in the PLLA supports was study in detail from a molecular perspective analyzing the expression of some CSCs markers. qRT-PCR data proved that stem cell markers, including the essential transcription factors Oct-4, Sox2 and Nanog, were highly up-regulated after 6 days of 3D *in vitro* culture onto the PLLA scaffold, compared with the early day 3 and the final day 9. Moreover, a similar but not so strong trend was found for pluripotent stem cells marker ABCG2 (Figure A2 a). These data suggest that CSCs persist in the C643 cells cultured into the PLLA scaffolds and, particularly, their intensification at day 6 might be associated with the reduction in cell proliferation detected between day 4 and 6 of culture with the cell viability assay. Subsequently, for testing the efficacy of the PLLA scaffold as *in vitro* platform for studying ATC biology and its resistance to the traditional therapy, C643 cells seeded onto the polymeric matrix were treated with 5mM of Dox, a dose higher than the common 2mM used for 2D monolayer cells, and the cell viability was first tested using AB assay after 48 hours of treatment

at three different time points. As shown in Figure A2 b (left), C643 cells developed a drug resistance after long time culture, specifically, the cell viability increased from 40% at day 3 to around 65% at day 6 and day 9. This result suggests that the ATC cells became resistant even to non-conventional doses of chemotherapics when they assumed a 3D structure inside the polymeric matrix, closer to an *in vivo*-like behaviour. To further investigate this resistant phenotype, the expression of apoptotic markers was observed at the same time points by qRT-PCR analysis. Interestingly, anti-apoptotic markers Bcl-2 and Survivin were strongly up-regulated at day 6 and day 9 (Figure A2 b, right) that might explain the C643 cell resistance to high doses of the anticancer drug. In addition, the expression of CSCs markers, including OCT-4, Sox2, Nanog and ABCG-2, was also studied performing qRT-PCR experiments. After 6 and 9 days of *in vitro* 3D culture, all the stem cell markers were strongly up-regulated (Figure A2 c), contemporary with the as-observed high resistance to Dox.

In conclusion, this investigation confirmed the aggressive nature of ATC and the high resistance to chemotherapeutic treatments. Although still preliminary, it provided the proof of concept that biocompatible PLLA scaffolds with high interconnected porous matrix and average pore size of 40-50 μm could represent a suitable 3D platform for *in vitro* preclinical studies on anaplastic thyroid carcinoma biology. All the findings provide encouragement and hope for the future research and suggest the necessity of further studies on 3D *in vitro* models, as engineering scaffolds, to improve knowledge about ATC biology and discover new efficient therapeutic approaches.

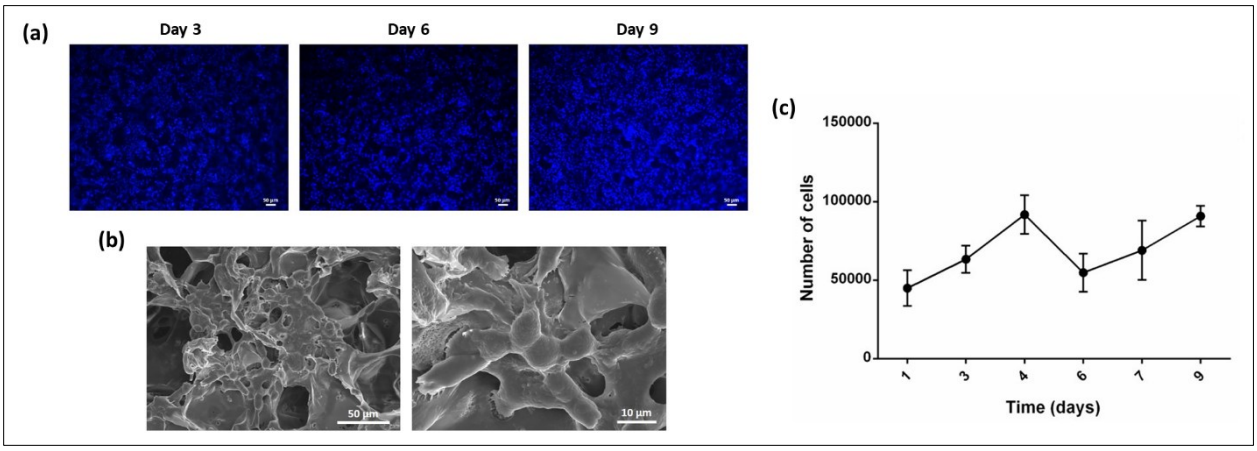

Figure A.1: (a) Fluorescence images of C643 cells grown on PLLA scaffold for 3, 6 and 9 days. Nuclei are stained blue with DAPI. Scale bar 50 µm. (b) SEM micrographs of C643 cells at 9 days post-seeding and culture on PLLA scaffold for 9 days at 37 °C and 5% CO_2. (c) C643 cell viability after 1, 3, 4, 6, 7 and 9 days of culture in PLLA scaffolds. D).[323]

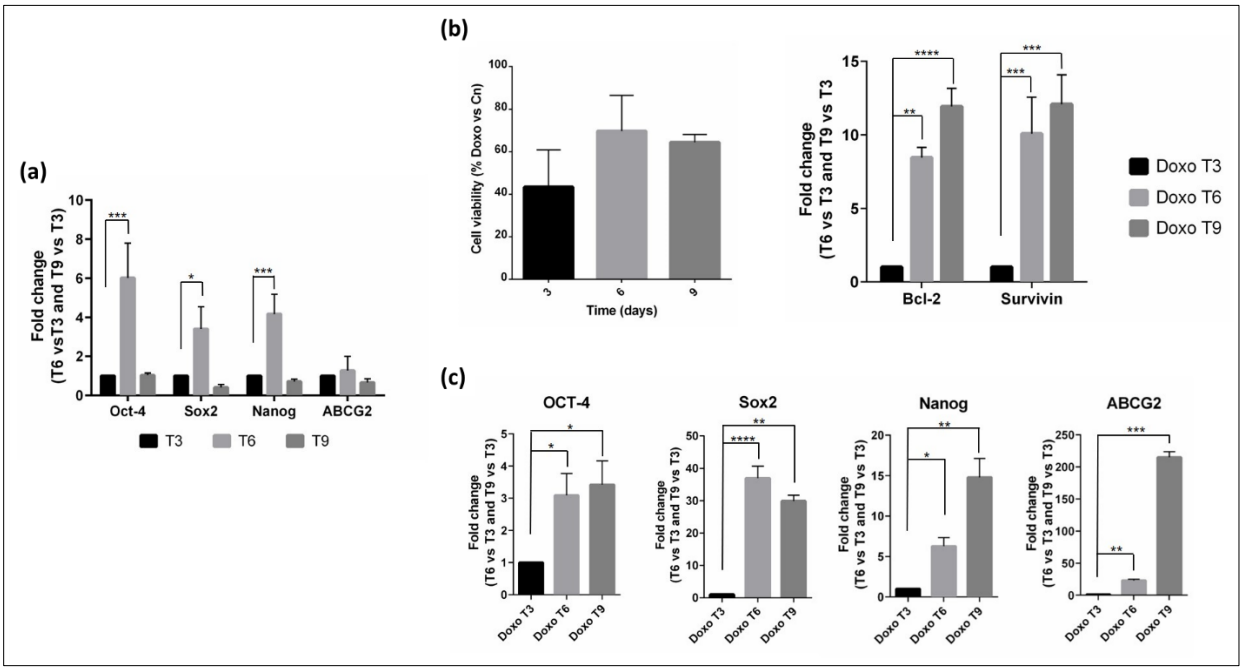

Figure A.2: (a) Expression of stem cell markers in 3D ATC cultures; (b) Acquisition of Doxorubicin and apoptosis resistance of C643 ATC cells after 3, 6, and 9 days of 3D culture; (c) Stem cell marker expression in Doxorubicin resistant 3D ATC cultures. [323]

The results presented in Appendix A have been reported in the paper "3D polymeric supports promote the growth and progression of anaplastic thyroid carcinoma" published by M. E. Lombardo, G. Zito, F. Carfì Pavia, G. Pizzolanti, C. Giordano, V. Brucato, V. La Carrubba in Biochemical and Biophysical Research Communications, August 2020.

APPENDIX B

Eco-friendly positively charged PLA/CS nanofibers for face masks

B.1. INTRODUCTION

Since the COVID-19 pandemic has spread around the world, face masks became one of the most important pieces among the Personal Protective Equipment (PPE) to protect people against the viruses and germs spreading through droplets in the air and to control public health concerns [324]. The World Health Organization (WHO) estimated that only in the last year 89 million medical masks are required every month, not only the highly efficient N95 masks but especially the daily disposable masks [325]. In general, good quality face-masks are made by 3-5 layers of nonwoven fabrics and the melt-blown (MB) is the process mostly used to develop fabrics in one-step starting from polymeric raw materials [326]. The obtained microsized fiber diameter and large pore size require an increase in thickness of the filter for a high filtration efficiency. This can cause difficulty to breathe and, as a consequence, unfiltered air will be inhaled through the edge of the mask [327]. Electrospinning is an emerging technique that permits fiber production with nanoscale diameter (10-2000 nm). It represents a valid alternative to MB due to the nanofibrous web characterized by smaller pore size, smaller fiber diameter and higher surface area. The reduced pore size can also capture small airborne particles less than 1 micrometre in diameter. Moreover, the well special organization and larger porosity can reduce the pressure drops and so improves the breathability [328]. Moreover, electrospun nanofibers (ES-NF) involve multiple filtration mechanisms in comparison with the conventional MB filters which are highly dependent on electrostatic adsorption. Unfortunately, the electrostatic charge can be lost due to the moisture of the environment or by disinfection processes using ethanol solution [329]. ES-NF allows electrostatic interactions with aerosol particles combined with a mechanical filtration due to the

small pore size and good pores' interconnectivity. It is well known that when the fibers are in the nanoscale, the aerodynamic airflow around nanostructured fibers can change and strong Van der Waals forces are able also to absorb submicron particles [330].

Face masks are usually developed from synthetic thermoplastic polymers such as Polypropylene (PP), polyurethane, polyacrylonitrile (PAN), polystyrene, polycarbonate, polyethylene (PET), or polyester. PP is widely used for developing filter layers thanks to its properties such as low melt viscosity, high electrical resistance and stability combined with low cost and versatility [324]. Nevertheless, all the conventional mask filters are not degradable and are usually buried in landfills which last for many years in the environment or incinerated after use. Moreover, some of these materials are often getting into waterways increasing plastics presence in the aquatic environment. This new emergence of face masks, as a source of plastic and plastic particle waste in the environment, is the evidence that the global pandemic has not reduced the challenge of increasing plastic pollution in the environment but is creating a massive waste crisis in the near future [331]. Hence, many engineering and scientific efforts have been carried out to use biodegradable and eco-friendly polymers and/or to produce reusable and recyclable face masks [325, 332].

Polylactic acid (PLA) is a linear aliphatic polyester made of starch raw materials derived from renewable plant sources such as corn or potato, tapioca roots, and sugarcane. In recent years, PLA has drawn research attention worldwide due to its biodegradability and biocompatibility and has been used for a wide range of applications from domestic applications (food packaging) to biomedical applications such as medical devices, scaffolds for tissue engineering and absorbable carriers for drug delivery. It can be completely degraded by microorganisms in nature after use under certain conditions, finally generating carbon dioxide and water, and so does not pollute the environment. It is recognized as environmentally friendly material and is the most popular material for FDM due to its easy processability and commercial availability [327]. Recently, Zhang et al. [333] proposed a biodegradable PLLA nanofiber-based filter as a promising device for air cleaning systems and air purifier devices. This electrospun filter showed enhanced filtering efficiency for removing small particulate matter due to the spontaneous polarization generated after electrospinning process.

Chitosan (CS) is a natural cationic polymer, which has attracted great interest as a new biomaterial because of its advantageous properties such as nontoxicity, biodegradability and biocompatibility in addiction with natural antimicrobial activity, being abundant and in-expensive [334]. Like other RNA viruses, COVID-19 consists of a negatively charged RNA enveloped inside a mostly positively charged capsid which plays a very important role in the virus infectivity [335, 336]. The idea to exploit positively charged polymers such as CS for preparing fibers possessing positive zeta-potential could provide an electrostatic virus repulsion and hence both decrease the viral load of those health-care instruments and increase the time of protection.

In this study, nanofibrous filters based on pure PLA and PLA/CS blend were fabricated by electrospinning and tested as potential filters for face masks. The morphology, composition and electrostatic surface charge of the obtained membranes were investigated before and after the deposition of chitosan nanoparticles on the fiber surfaces using scanning electron microscope (SEM), energy-dispersive X-ray spectrometer (EDX) and a surface voltmeter, respectively. The hydrophilic nature of the nanofibers was tested to evaluate their resistance to intrusion of droplets and so in deterring the virus. The filtration and breathability efficiency of the electrospun fibers and the commercially available PP melt-blown filter-based face masks were compared. Finally, the potential reusability of the nanofibrous PLA filter was discussed by testing the influence of the morphology, and the filter performance as a consequence, after cleaning them using 75% ethanol solution.

B.2. MATERIALS AND METHODS

B.2.1. Preparation of pure PLA and PLA/CS nanofibers

PLA nanofibers were prepared using a previously described electrospinning process with some modifications [337]. Pure PLA (Luminy® L 105; supplied by Total Corbion) (8% w/v) was dissolved into a DCM/DMF mixture (80/20 v/v) by stirring at room temperature to form a homogeneous solution. For the electrospinning process, the as prepared solution was placed in a 10-mL plastic syringe fitted to a 21G stainless needle (ID=0.5mm) and connected to a syringe pump for controlling a feed rate of 0.5 ml/h. Next, a fixed electrical potential of 16 kV was applied

using a high-voltage power supply (Spraybase, Projector Life Sciences electrospinning unit) across a distance of 10 cm between the syringe tip and the collector plate covered with aluminum foil. Electrospinning was carried out for 3 hours at room temperature and 30% of humidity. The resulting nanofiber mat was maintained under vacuum overnight to ensure complete solvent removal. Then CS (Millipore Sigma) (1% w/v) was dissolved in 70% Acetic Acid solution and electrospinned for 1 hour on the surface of PLA fibers using the same system and conditions applied before.

B.2.2. Characterization of the ES-NFs

The morphology of the composite electrospun nanofibers was observed by SEM (EOL JSM7401F FE-SEM) at an accelerating voltage of 10 kV. Each sample was cut into smallest pieces, mounted onto metallic stubs using a carbon tap and sputter-coated with 4-nm of Pt/Pd under nitrogen atmosphere for increasing the conductivity. The average diameter of PLA and PLA/CS fibers in SEM micrographs was analysed by using Image-J software. The presence of the CS in the composite samples was studied using the above instrument equipped with an Energy Dispersive X-ray (EDX) detector.

B.2.3. Hydrophobicity test

The hydrophilicity nature of the samples was measured by testing the water contact angle using a home-made video-based optical contact angle meter. Briefly, 1 x 1 cm samples were fixed on a glass microscope slide and then placed on the meter stage. 5 µL water was dropped onto the sample, and the droplet geometry was captured with the help of a camera placed in front of the sample holder. The contact angle on the left and on the right of the drop was measured in a software, and the average of 10 angles is reported.

B.2.4. Electrostatic Surface Charge

A Surface DC Voltmeter Model SVM2 (AlphaLab Inc.) was used to measure the electrostatic surface charge of the filter layer without contact. During the test, one side of the dried filter was isolated from the ground by an insulating surface. The sensing terminal of the voltmeter was put close to the filter layer and the free charge of 10 different spots was recorded. The PLA

and PLA/CS filters were both tested after the synthesis and after water dipping for 10 second and dried overnight. A commercial PP filter was used as reference.

B.2.5. Filtration/Breathability Test

To preliminary determine the filtration and breathability efficiency of the as-prepared filters a jet nebulizer spray technique was applied. Figure B1 shows the easy home-made set up using for the test: a nebulizer filled with an organic dye (methylene blue) is connected to a compressor which causes air, already dried through a dehumidifier, to flow at high velocity through the dye and turn it into an aerosol. All the tests were conducted with an airflow of around 24 l/m which is approximately the average breathing flow of humans in a resting position [327]. Then, the generated dyed aerosol is sprayed through the filter fixed between two "U" tubes which have small tapering at the substrate side to both receive and transmit the fine droplets. The amount of dye which passes through the sample in 5 min is finally collected and quantified via UV-vis spectroscopy at a wavelength of 664 nm. An amount of dye running without the filter is used as reference. The efficiency of the filter was determined from the difference in peak absorption value between the liquid collected with and without the filter, using Equation B1:

$$\text{Efficiency (\%)} = \left(1 - \frac{A_0 - A_1}{A_0}\right) * 100 \quad \text{(B1)}$$

where A_0 is the peak absorption of the reference liquid, A_1 is the peak absorption of the liquid tested using the filter.

In the meantime, in order to assess the breathability of the mask the ΔP gauge across the filter was also measured using a manometer and it is reported as the average value between the initial and final value recorded.

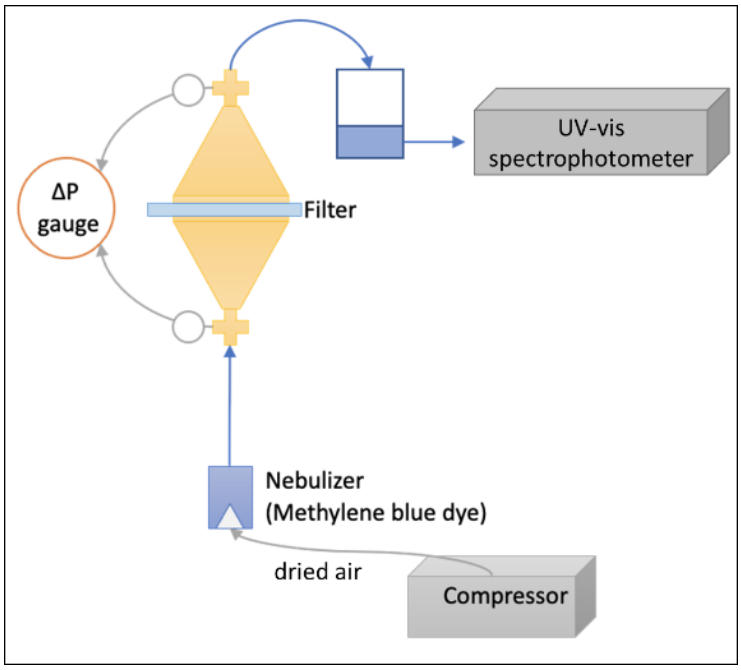

Figure B.1: Schematization of the home-made set up for the filtration/breathability test on filters.

B.2.6. Reusability Test

The filter layers of PLA were dipped into ethanol 70% for 1, 5 and 10 min to investigate any morphological changes. Then the samples were dried at 35°C in the air overnight and prepared for SEM observation, as described above. The same test was carried out for PP melt-blown fibers and the results were compared with PLA samples. For all the above tests, a three-layer non-woven surgical mask and a five-layer N95 mask were selected as representative commercial face masks because of their wide availability, extensive use, and already approved properties.

B.3. RESULTS AND DISCUSSION

B.3.1. Morphology and composition of pure PLA and PLA/CS fibers

Figure B2 shows the morphology and diameter distribution of the commercial PP melt-blown, pure PLA, and PLA/CS fibers. Comparing with the micrometer (~1.7 µm) irregular PP melt-blown commercial filter (Figure B2 a), the PLA electrospun fibers fabricated in this study

showed a uniform network with smaller fiber diameters and an average size of ~600 nm (Figure B2 b). After the chitosan deposition, particles of average size of ~200 nm were uniformly dispersed around each PLA fiber (Figure B2 c). SEM-EDX analysis was used to investigate the chemical composition and confirm the presence of the chitosan on the surface of PLA/CS nanofibers. As shown in Figure B3, the pure PLA fibers contained C and O, but not N. In the PLA/CS fibrous membranes N was detected, particularly the fibers containing around 6.5% of N, which confirmed a successfully loaded of the CS onto the PLA fibers [338].

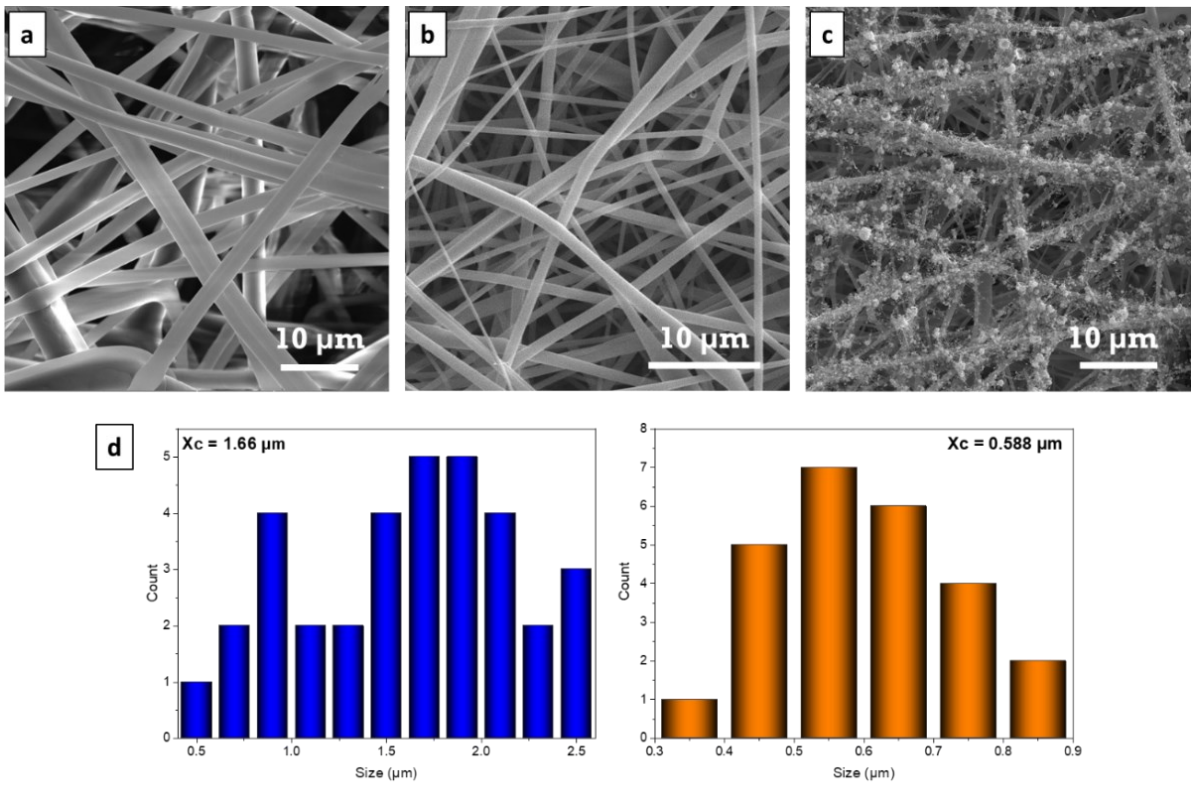

Figure B.2: SEM micrographs of PP melt-blown fibers (a), PLA electrospun fibers (b), and PLA electrospun fibers covered by CS particles (c). Scale bar 10 µm. Size distribution of PP melt-blown fibers (blue bars) and PLA electrospun fibers (orange bars) (d).

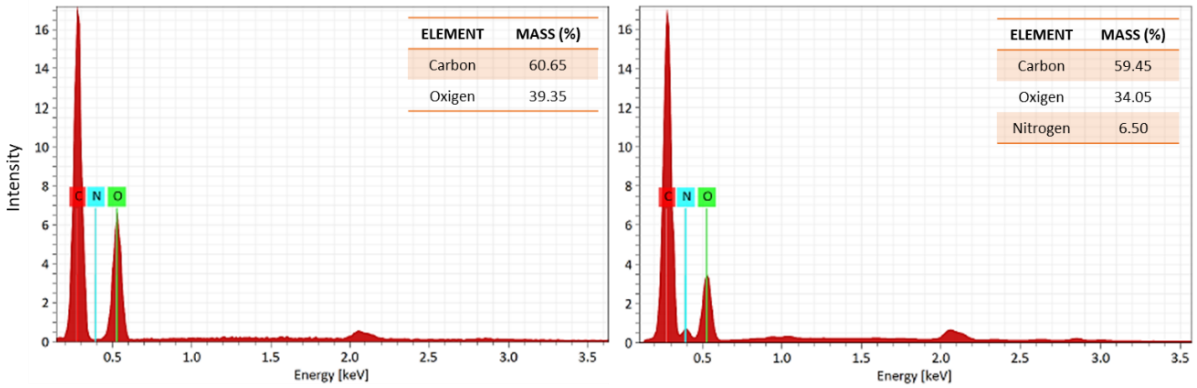

Figure B.3: EDX spectra of pure PLA electrospun fibers (left) and PLA fibers with CS coating (right).

B.3.2. Wettability of the fibers

The hydrophilic or hydrophobic nature of filter surfaces for face masks represents an important contribution in providing an environment favorable or unfavorable to different types of viruses [339]. It was observed that the pure PLA nanofibers showed a water contact angle of ~132° close to the value reported for the commercial PP melt-blown filter of both surgical and N95 masks (~140°). However, chitosan nanoparticles significantly reduced the water contact angle of the filter when dispersed on the surface of PLA (~110°), increasing the wettability (Figure B.4). The adhesion of chitosan on the fibers naturally increases the hydrophilicity of the material surface, but a value > 90° should be sufficient to prevent wetting by droplets of saliva and moisture and so to exclude not only pathogen transmission but also bacterial growing inside [339].

a

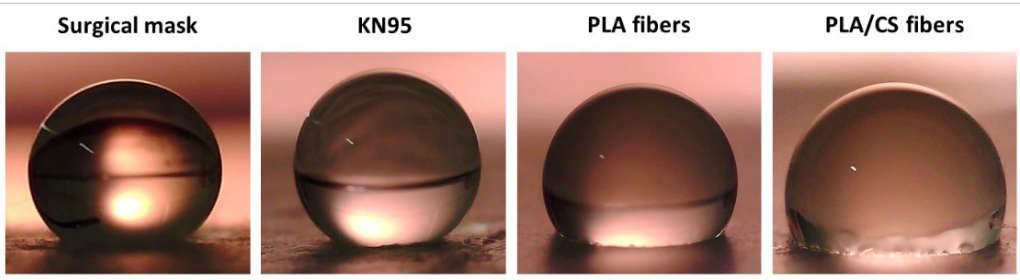

b

Sample	Average Angle (degree)
Surgical mask	140.2
KN95	140.8
PLA fibers	131.5
PLA/CS fibers	109.7

Figure B.4: (a) Images of water droplets on contacted surfaces and (b) calculated contact angles of commercial Surgical mask, KN95, pure PLA fibers and PLA/CS fibers.

B.3.3. Evaluation of the electrostatic surface charge

During a filtration process, particles can be captured by a filter layer either mechanically or electrostatically once in contact with the surface of the fibers [340]. Since the past few decades, it is well known that the presence of surface charges can significantly promote the filtration efficiency [328, 341, 342]. Here, all the synthesized electrospun filters showed a positive charge (+285V for pure PLA and +120V for PLA/CS) compared to the negative charge of the commercial PP melt-blown filters (-229V) (Table B1). Moreover, the electrostatic surface charge imposed during the production process decreased for all the samples after a water dipping treatment but remained over +50V for both PLA and PLA/CS filters.

B.3.4. Filtration and breathability efficiency

Filtration and breathability are two of the major testing methods used to evaluate the performance of face masks. In this work, a very easy apparatus was applied for a preliminary investigation on the filtration efficiency (FE) of the as-synthesized nanofibrous membranes. As

shown in Table B1, pure PLA electrospun samples achieved a FE more than 96%, while the composite PLA/CS samples were more than 98% efficient. One of the possible reasons for the increasing of the FE after CS deposition could be the decreasing pore size and porosity due to the presence of the nanoparticles onto the PLA fiber surface. Compared to commercial surgical (3-layers) and N95 (5-layers) masks, with FE ≥94% and ≥95%, respectively [343], the as-synthesised nanofibrous filters with smaller fiber diameter and pore size showed better performance in terms of filtration. Indeed, it is already well demonstrated that filtration efficiency becomes higher when fiber size is reduced due to the larger specific surface area available per volume for particle capture [344]. To form extremely small pores, nanoscale fibers need to be thickly stacked which bring to an uncomfortable human breathing due to the associated high-pressure differential [325]. However, in this work an interesting result emerged from the breathability test, as shown in Table B1. The composite PLA/CS membrane had a pressure drop of 190 Pa slightly lower than the 220 Pa of the pure PLA samples which is close to the 245 Pa evaluated for a commercial 5-layers mask [343]. From the above discussions it can be concluded that the electrospun nanofibers presented in this work could be a perfect candidate as filter for face masks allowing good filtration of droplets and tolerable breathability only using one layer, compared to the 3 or 5 layers needed for commercially available surgical masks and high performance N95.

Table B. 1: Breathability, filtration and surface charge (before and after water dipping) of pure PLA fibers, PLA/CS fibers and PP melt-blown fibers of commercial Surgical/KN95 masks.

Sample	Pressure (Pa)	Filtration (%)	Surface Charge (V)	Surface Charge after water dipping (V)
PLA fibers	220	≥96	+285	+56
PLA/CS fibers	190	≥98	+120	+51
Surgical Mask/KN95	65/245	≥94/≥95	-229	-70

B.3.5. Investigation of filter reusability

To evaluate the reusability of the pure PLA filters, a dipping in 70% ethanol was used up to 10 min as cleaning procedure. In the case of melt-blown filter, SEM analysis showed that even if the fiber diameters were found to be relatively unchanged, a nonuniform morphology was clearly observed, with fiber swelling and breaking, after 5 and 10 min of treatment (Figure B5 a). On the contrary, no significant change in morphology or fiber diameter, without any fiber deformation or matching, was noticed for the PLA electrospun fibers (Figure B5 b).

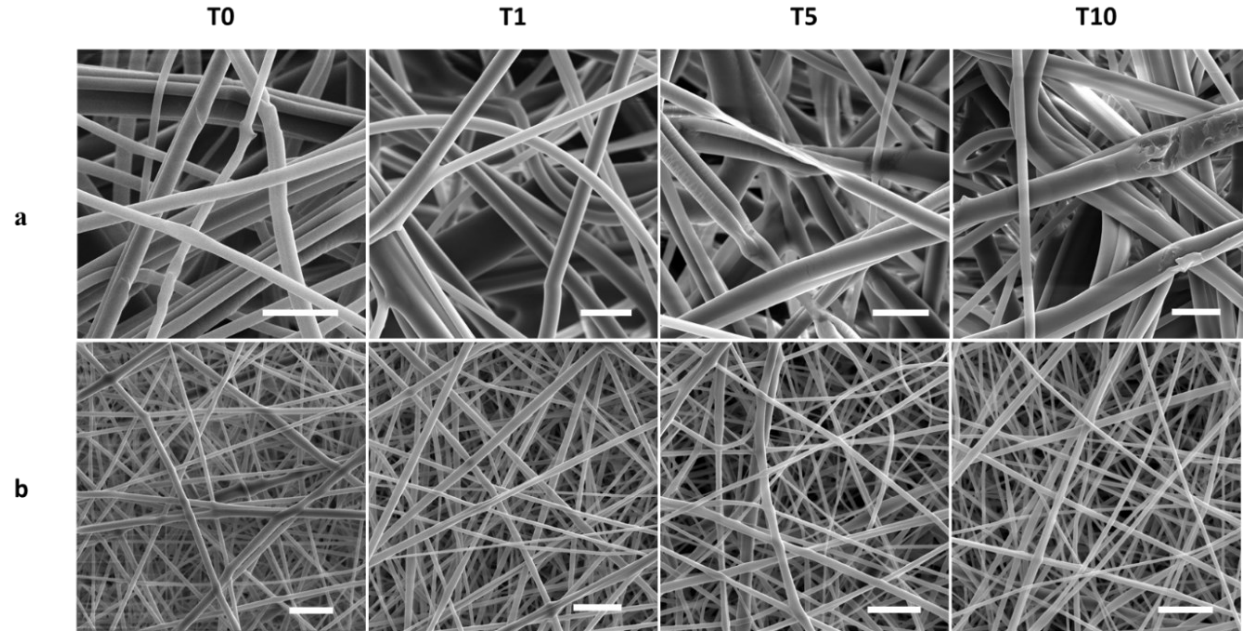

Figure B.5: SEM micrograph of PP melt-blown fibers (a) and pure PLA ES-NFs (b) before (T0) and after dipping treatment with ethanol 70% at different time points from 1 min (T1) to 10 min (T10).

B.4. CONCLUSION

The current pandemic has amplified the need for masks all around the world [329]. In this preliminary work, we focused the attention on the superiority of electrospun nanofiber compared to conventional MB microfibers in terms of filtration performance and reusability after simple cleaning with ethanol. The resulting structure of the as produced PLA filters was a uniform fishing network with fibers of 600-700 nm in diameter. The increase in efficiency is also attributed to the

charged fibers generated from the electrospinning process which can also allow the filtration of small particles via electrostatic interaction. Particularly, since a positive zeta potential has been identified in the spike proteins of Sars-Cov-2, the positively charged nanofibers, due to the addiction of CS nanoparticles, could lead to the electrostatic virus repulsion and hence decrease the viral load on those health-care equipment. Furthermore, unlike commercial disposable face masks, the developed PLA/CS filter is totally sustainable due to the high biodegradability of the synthetic polymer PLA combined with the natural polymer Chitosan. In a previous work [345], *in vitro* degradation nature of PLA/CS nanofibers was tested using a PBS solution. The presence of the CS together with shaking significantly increased the degradation rate of the nanofibers already after 7 days of testing. In addition, the filter is expected to exhibit anti-virus blocking properties due to the presence of CS that have been shown to exhibit direct antimicrobial and antiviral activity confirming its potential as a future helpful instrument in the treatment of the COVID-19 pandemic.

ACKNOWLEDGMENTS

This work has been done at INRS-EMT center of Varennes (Quebec, Canada) in collaboration with Bioastra Technologies Inc (Montreal, Quebec, Canada) (Sumitra Rajagopalan, Founder and CEO), in a framework of MITACS project about COVID-19 prevention in 2020/2021. An acknowledgment to the student Eve Lambert-Fliszar for the support during the entire project, especially for the filtration/breathability test, surface charge evaluation, and wettability.

The data showed in the APPENDIX B are present in the paper “Eco-friendly positively charged nanofibers for face masks”, co-authored by M.E. Lombardo, D. Benetti, E. Lambert-Fliszar, S. Rajagopalan, F. Rosei. (Manuscript in preparation)

APPENDIX C

Solar photocatalytic degradation of Methylene Blue dye using red-emitted doped CDs

C.1. INTRODUCTION

The rapid industrialization in the last decades has left a strong impression on the environment. It was estimated that tons of both industrial and domestic effluents are spilled each day without treatments into waterways which contain various dyestuff [346]. Organic dyes represent a significant part of the by-products in textiles, printing, plastic and food industry. Among the various pollutants of wastewater, they are identified as significant contaminants since they could damage aquatic life by suppressing light penetration and altering photosynthesis even if they are present at very low concentration. Moreover, most of the organic dyes are non biodegradable, highly toxic, carcinogenic and/or mutagenic leading to serious health issues to both humans and aquatic organisms, if ingested [347]. In recent years, much effort has been devoted to developing efficient and cost-effective methods for the treatment of pollutant dyes in water.

Conventional techniques combining physical, chemical and biological principles such as adsorption, ultrasonic decomposition, electrocoagulation, membrane process with nano filtration, advanced chemical oxidation (ACO), are currently employed for treatment of dye wastewater. Unfortunately, all of these processes are insufficient for an effective degradation of the dyes since they just transfer the compounds from aqueous to another phase creating a secondary pollution problem [348]. Recently, photocatalytic degradation was acting much interest as an efficient, green, advanced, clean and cost-effective method for removal of dye pollutants [349]. Titania nanoparticles (TiO_2) and all the nanomaterials derived from TiO_2 have been extensively investigated as photocatalyst for the decomposition of organic dyes due to their unique

characteristics, including low toxicity, low production cost, high physicochemical stability, strongly oxidizable, and biocompatibility [350]. Despite the excellent characteristics, there are two major drawbacks that represent an obstacle to a practical application of TiO_2 photocatalysis, and which are: (1) a wide band gap causing a poor visible-light absorption capacity, and (2) a rapid recombination rate of photogenerated electron/hole (e−/h+) pairs [351]. Thus, many studies have been published in attempt to overcome such limitations. Carbon Dots (CDs) are an important new class of nanocarbon materials which have been heavily investigated as promising candidates for driving photocatalytic redox reactions. Among their excellent properties including low toxicity, good water solubility and stability, ease of surface modification or functionalization, highly resistant to photobleaching, and unique high photoluminescence (PL), CDs exhibit a narrow band gap which promotes a greater absorption in the visible light, and abundant electrons acceptors and donors on the surface with high separation efficiency of photogenerated charges [352]. However, many papers reported a little activity of CDs alone toward the photocatalytic degradation of dyes suggesting metal/non metal-based hetero-doping to obtain an efficient removal of organic dyes [353].

In the present work, red-emitted doped and co-doped CDs were synthesized and explored as a potential photocatalyst material for the degradation of the organic dye Methylene Blue (MB) under exposure for 2 hours to sunlight irradiation. The degradation efficiency and adsorption kinetics of Nitrogen-doped CDs (N-CDS), Nitrogen-Boron co-doped CDs (N,B-CDs), and Nitrogen-Cobalt co-doped CDs (N,Co-CDs) has been investigated. The effect of operating parameters, such as the initial pH of the solutions, was also evaluated.

C.2. MATERIALS AND METHODS

C.2.1. CDs synthesis and characterization

N-CDs, N,B-CDs and N,Co-CDs were synthesized using *p*-phenylenediamine (*p*-PD) as carbon and nitrogen precursor, ultrapure water as solvent, 5% of doping for both non-metal (Boron) and metal (Cobalt) atoms, with a solvothermal/acid-assisted method as synthesis path. Morphology, chemical composition, optical properties and photostability were investigated.

Details of the synthesis procedure and all the characterizations are described in Chapter 3: Materials and Methods, Part 5. Zeta potential (ζ) was measured using BrookHaven ZetaPlus equipment for the CDs in aqueous solution prepared with both neutral pH (6.5) and alkaline pH (10) at room temperature.

C.2.2. MB photocatalytic experiments

The photocatalytic activity of the CDs was evaluated by the degradation of methylene blue (MB) aqueous solution under simulated sunlight irradiation (1 Sun, 1.5 AMG). In a typical process, 10 mg of CDs were added in 10 mL of aqueous MB (10 mg/L) solution and magnetically stirred in dark for 30 min, to achieve adsorption–desorption equilibrium between photocatalyst and dye. Subsequently, each solution was placed under the sun simulator with vigorous stirring at 200rpm. The experiments were carried out by two different initial pH values (6.5 and 10) and the temperature of the solution was kept in the range of 25-30°C. During each experiment, a fixed amounts of sample were collected in appropriate time intervals (up to 2h) and UV/vis absorption of the solution was recorded at a max wavelength of 664 nm by a UV–vis spectrophotometer. Similar experiments were also performed in the absence of the catalyst.

C.3. RESULTS AND DISCUSSION

In this experimentation, red-emitted doped and co-doped CDs were synthesized via a one-step solvothermal/acid assisted method using *p*-PD as precursor and carbon/nitrogen source. The results about morphology, chemical composition, optical properties and photostability are explained in detail in Chapter 3: Results and Discussion, Part 5. Their photocatalytic degradation activity was investigated by the degradation of the dye pollutant MB under simulated sunlight irradiation. MB is a well-known cationic dye employed especially in the textile industry for a variety of porpoises, and it is a heterocyclic aromatic chemical compound with a molecular formula $C_{16}H_{18}N_3SCl$. It may be responsible for permanent eye injury for both human and aquatic animals and can cause irritation to the skin after the contact as well as being highly toxic and carcinogenic [354].

Since the photocatalysis occurs on the NPs surface, determining the charge on the CDs surface during the photodegradation process, using solutions with different pH environment, is substantial to predict the surface ability to adsorb the pollutant and investigate the performance of the photocatalyst [350]. All the samples prepared at acid and neutral pH (3-6) carry on a positive charge, whereas, higher pH values promote the formation of negative charge on the CDs surface.

Photocatalytic degradation of MB in aqueous suspension of N-CDs, N,B-CDs and N,Co-CDs prepared at two different pH values (6.5 and 10) were performed to evaluate their photocatalytic activity and the dopant influence. The dye solution was first subjected to photolysis in the absence of the CDs at pH 6.5 and 10 under solar irradiation. The ratio of absorbance at time t and initial absorbance (At/A0) was plotted against irradiation time as reported in Figure C.1. The results show a gradual decrease with the reaction, especially for the alkaline conditions, with a degradation efficiency of 34% after 2 hours of sunlight irradiation. After the addition of the CDs to the dye solution (1 mg/ml), an adsorption/desorption equilibrium was first reached within 30 min under the darkness, which led to the enhancement of photodegradation of the dye. The UV/vis abs band of degradation of dye with the addition of N-CDs, N,B-CDs and N,Co-CDs under solar irradiation is shown in Figure C.2 (a-f). It is possible to notice that at neutral pH the absorbance for all the samples at the corresponding wavelength of MB (664nm) is unchanged with increasing irradiation time (Figure C.2 a,b,c). On the other hand, for pH 10 the absorbance rapidly decreases for N-CDs and N,B-CDs after 60 min of irradiation (Figure C.2 d,e), while a higher abs decreasing is evident for the N,Co-CDs immediately after 10 min of solar light irradiation (Figure C.2 f). The degradation efficiencies of MB after 2 hours of irradiation times using N-CDs, N,B-CDs and N,Co-CDs are 52%, 40% and 62%, respectively (Figure C.3 a-c). It should be noted that the curve of N,Co-CDs (Figure C.3 c) has not stabilized until 2 h of irradiation, suggesting that with a longer irradiation time, a higher degradation rate could be achieved.

The kinetic constant of dye photocatalytic degradation was estimated by following the simplified Langmuir-Hinshelwood (L-H) kinetic model for organic dyes in very dilute solutions based on a pseudo-first order kinetic equation (Equation C1) [349, 355, 356]:

$$\ln(C_t/C_0) = kt \qquad \text{Eq. C1}$$

where C_0 is the initial concentration of the dye and C_t is the concentration of the dye at different irradiation times t, and k is the apparent first-order reaction rate constant (min^{-1}). The reaction rates

for the three samples were calculated by plotting ln (C_t/C_0) versus t and recording the slope of the linear regression (Figure C.3 d-f). The kinetic curves in the case of N-CDs and N,B-CDs don't fit a pseudo-first-order kinetic model but present a sigma shape [357] with an inflection point corresponding to a reaction time of ca. 50 min. In the case of N,Co-CDs, the fit to a pseudo-first order kinetic model is clearly linear since the first 10 min of sunlight irradiation with a degradation rate of 0.007 min^{-1} (Figure C.3 f). According to these results the high degradation efficiency of the organic dye MB together with a good degradation rate have been achieved adding in solution the co-doped N,Co-CDs.

The high efficiencies of the CDs prepared at pH 10 could be attributed to the presence of negative charge on their surfaces. Thus, the cationic dye MB with a positive charge can be adsorbed on the negatively charged CDs surfaces through a strong electrostatic interaction, while the electrostatic repulsion between the positively charged CDs and the cationic dye maybe explain the lower degradation efficiency with neutral pH value [350].

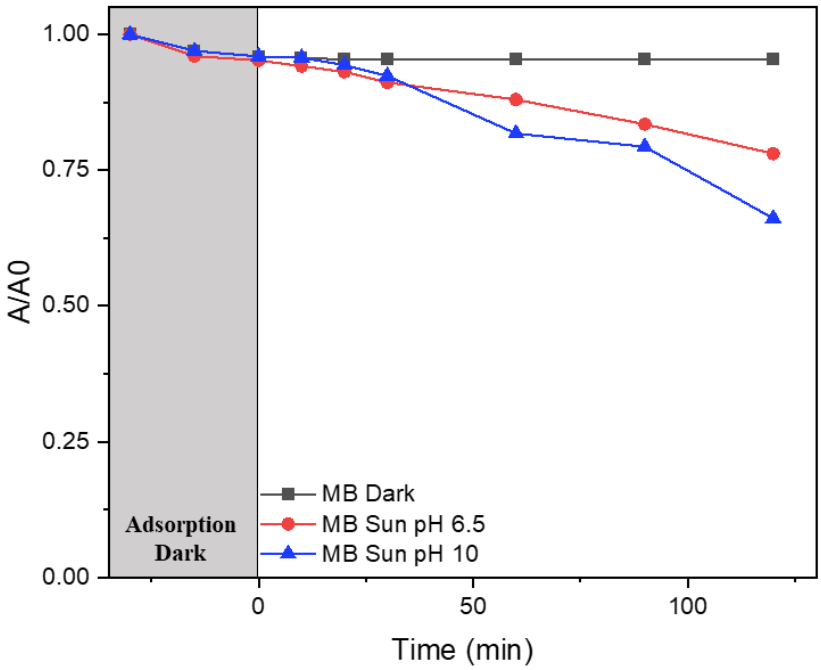

Figure C.1: At/Ao curves for photocatalytic degradation of MB in water in the absence of CDs under solar irradiation at pH values of 6.5 and 10.

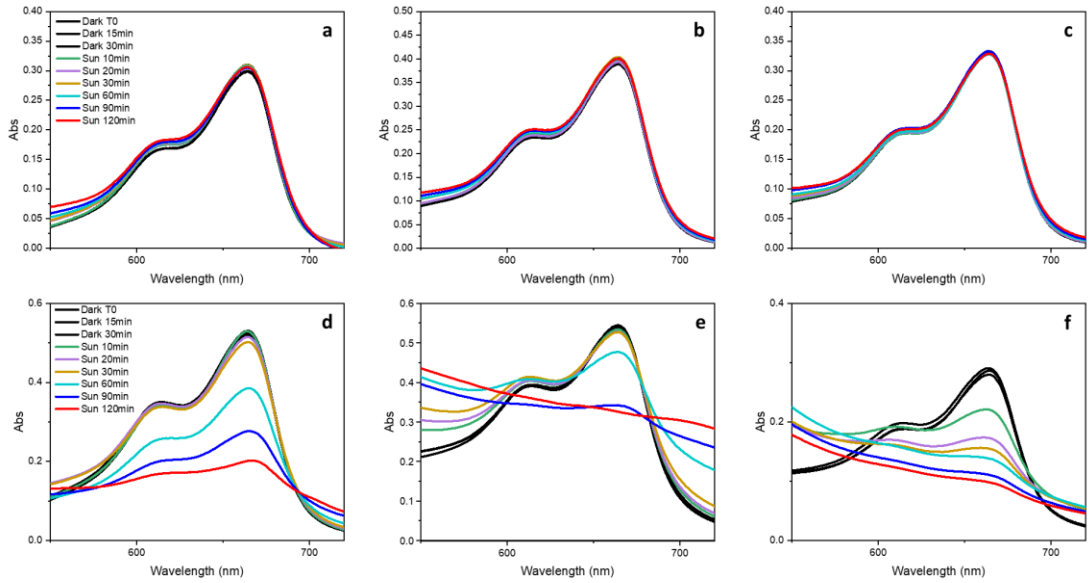

Figure C.2: UV-vis absorption spectra of MB degradation using N-CDs (a), N,B-CDs (b) and N,Co-CDs (c) at pH 6.5 (a-b-c) and 10 (d-e-f) and a concentration of catalyst 1mg/ml.

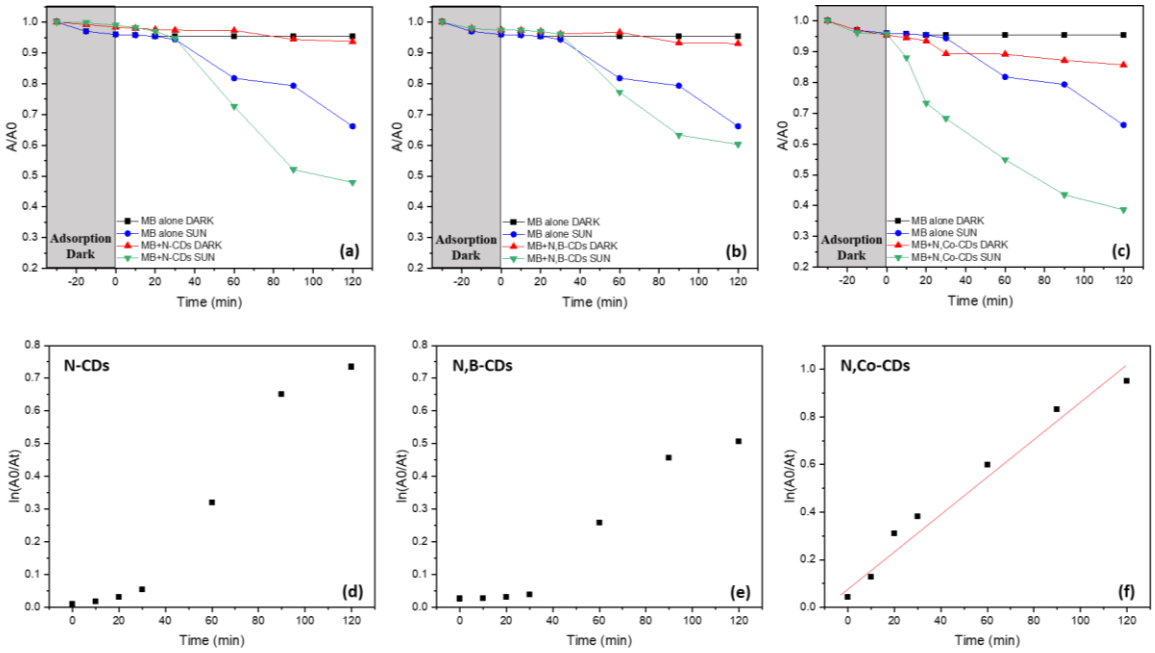

Figure C.3: Effect of N-CDs (a), N,B-CDs (b) and N,Co-CDs (c) on photodegradation of MB at pH 10 under simulated sunlight irradiation for 120 min. Plots of ln (Ao/At) vs. time of MB+N-CDs (d), MB+N,B-CDs (e), and M+N,Co-CDs (f) under solar irradiation.

C.4. CONCLUSIONS

Red-emitted doped and co-doped CDs were synthesized and applied as highly efficient photocatalysts for the photodegradation of the cation organic dye MB from aqueous solution under simulated sunlight irradiation. The impact of surface charge on CDs photocatalytic activity was investigated varying the pH of the solution. The optimum efficiency was obtained for the alkaline pH value for all the samples analysed. A good degradation rate was observed using the N,Co-doped CDs since the first 10 min of irradiation. Moreover, the co-doped N,Co-CDs which exhibited better performance for the dye degradation could be easily recovered by using an external magnet after the treatment [355, 356], taking advantage of their magnetic properties. In conclusion, the developed red-emitted CDs showed to be a promising economical alternative for simple removal of cationic dyes from wastewater and environmental protection.

The data showed in APPENDIX C are present in the paper “Solar photocatalytic degradation of Methylene Blue dye using red-emitted doped CDs”, co-authored by M.E. Lombardo, D. Benetti, F. Rosei. (Manuscript in preparation)